Contribution to the construction of the silicon pixel trajectometer of the ATLAS experiment for the high luminosity phase of the LHC

Yahya Khwaira

université PARIS-SACLAY

Contribution to the construction of the silicon pixel trajectometer of the ATLAS experiment for the high luminosity phase of the LHC

Contribution à la construction du trajectomètre en pixel au silicium de l'expérience ATLAS pour la phase haute luminosité du LHC

Thèse de doctorat de l'université Paris-Saclay

École doctorale n° 576, Particules, Hadrons, Énergie et Noyau, Instrumentation, Image, Cosmos et Simulation (PHENIICS)
Spécialité de doctorat: Physique des particules
Graduate School : Physique.
Référent : Faculté des sciences d'Orsay

Thèse préparée dans l'unité de recherche **IJCLab** (Université Paris-Saclay, CNRS), sous la direction d'**Abdenour LOUNIS**, Maître de conférences - classe exceptionnelle

Thèse soutenue à Paris-Saclay, le 27 Octobre 2023, par

Yahya KHWAIRA

Composition du jury

Membres du jury avec voix délibérative

Achille STOCCHI Professeur, Université Paris-Saclay, IJCLab (Orsay, France)	Président
Giovanni CALDERINI Directeur de recherche, Sorbonne Université, LPNHE (Paris, France)	Rapporteur et Examinateur
Didier CONTARDO Directeur de recherche, Université Claude Bernard Lyon 1,IP2I (Lyon, France)	Rapporteur et Examinateur
Koji NAKAMURA Chargé de Recherches, KEK (Tsukuba, Japon)	Examinateur
Mohsine MÉNOUNI Ingénieur de Recherches hors classe, Université d'Aix-Marseille,CPPM (Marseille, France)	Examinateur

THESE DE DOCTORAT
NNT : 2023UPASP139

université PARIS-SACLAY

ÉCOLE DOCTORALE
Particules, hadrons, énergie et noyau : instrumentation, imagerie, cosmos et simulation (PHENIICS)

Titre: Contribution à la construction du trajectomètre en pixel au silicium de l'expérience ATLAS pour la phase haute luminosité du LHC.

Mots clés: Détecteur de pixels en silicium, trajectomètre interne, dommages aux irradiations, electronique frontale en technologie CMOS 65nm.

Résumé: L'objectif de ce travail est la préparation du trajectomètre interne de l'expérience ATLAS pour la phase haute luminosité pour une recherche de nouvelles particules élémentaires ou découvrir des signes de nouvelle physique au delà du modèle standard. En effet, l'augmentation de la luminosité d'un facteur dix necessite, par conséquent, un refonte de l'ensemble des détecteurs de particules qui forment la partie interne de l'ensemble expérimental de l'expérience ATLAS. C'est au cœur de l'expérience, près du point de collision des protons incidents, que les doses de radiations seront les plus intenses. Les fluences très élevées en particules et rayonnement ionisants, jamais atteintes précédemment, feront subir des dommages considérables aux capteurs en siclicium, à l' électronique associée ainsi qu'à l'ensemble des matériaux et structures qui supportent mécaniquement ces dispositifs. Le détécteur de l'expérience ATLAS devra assurer, pendant une periode estimée entre cinq à dix ans, un fonctionnement nominal à plein régime sans perte de performances malgré cet environnement fortement hostile induit par les radiations. C'est pour cette raison, dû au cadre fortement contraint qu'il est absolument indispensable de préparer soigneusement et mettre en œuvre avec rigueur les modules pixel de détection ainsi que leur électronique associée qui seront installés dans le futur trajectomètre. A cette fin, um ensemble de travaux ont été entrepris; notamment la construction d'un démonstrateur au CERN qui represente à une échelle réduite le futur trajectomètre interne. Um ensemble de séries de mesures minutieuses de contrôle qualité à éte menée à bien sur les modules préalablement assemblés par différents laboratoires de la collaboration ATLAS. Une vérification des performances avant et après intégration sur les cellules du baril interne et les bouchons ont été soignement évaluées et ont prouvé la justesse de la stratégie de chargement des modules. Auparavant plusieurs campagnes d'irradiation à haut flux ont été mené à bien au CERN, visant à évaluer les performances des modules ainsi que des circuits intégrés de lecture. En particulier, un circuit spécialisé de monitorage des irradiations développé au laboratoire a été l'objet d'une attention particulière vu son importance pour réajuster, en temps réel, le cas échéant et rétablir les performances optimales de l'électronique de lecture des capteurs pixels pendant la prise des données. L'ensemble de ces travaux seront développés avec précison dans l'ouvrage écrit de la thèse.

université PARIS-SACLAY

ÉCOLE DOCTORALE
Particules, hadrons, énergie et noyau : instrumentation, imagerie, cosmos et simulation (PHENIICS)

Title: Contribution to the construction of the silicon pixel trajectometer of the ATLAS experiment for the high luminosity phase of the LHC.

Keywords: Silicon pixel detector, Inner Tracker, 65 nm CMOS front-end electronics, radiation damage.

Abstract: The goal of this work is to prepare the internal tracker for future challenging high luminosity working conditions of the HL-LHC. The ultimate goal of the ATLAS experiment is the search of investigation of rare decays and the search for signs of new physics beyond the standard model. Increasing the luminosity by a factor ten requires the complete redesign of the inner tracker and replacement with full silicon tracker and its associated readout electronics. Near the collision point, radiation fluence will be extremely high and will cause severe damage to the sensors and associated readout integrated electronics. The challenge is to build a robust internal tracker that will sustain high radiation doses during the entire period of operation time of more than five to ten years, without any major loss of performance. To face these predicted hostile working conditions, systematic studies on sensors, modules, and front-end electronics have been carried and in particular, their performance regarding their radiation tolerance is investigated in detail.
Furthermore, a demonstrator has been constructed at CERN and instrumented by barrel and endcap modules to verify and check in detail all the issues related to electrical and mechanical integration. Before installation in the demonstrator, quality control studies based on a series of criteria of modules have been performed as this will be detailed in a section of this manual. Moreover, X-ray and proton irradiation campaigns of sensors and integrated readout circuits have been carried out at CERN and CPPM for performance evaluation before and after irradiation. In particular, a section will be dedicated to describing the study under several tuning conditions of a specific radiation monitor circuit "Ring Oscillator" embedded in the main readout chip, designed in our laboratory.

بسم الله الرحمن الرحيم

﴿قُلْ سِيرُوا فِي الْأَرْضِ فَانظُرُوا كَيْفَ بَدَأَ الْخَلْقَ ثُمَّ اللَّهُ يُنشِئُ النَّشْأَةَ الْآخِرَةَ إِنَّ اللَّهَ عَلَىٰ كُلِّ شَيْءٍ قَدِيرٌ﴾
سورة العنكبوت ـ الآية ٢٠ ـ القرآن الكريم

In the name of God, the most gracious, the most merciful

"Travel in the land and see how (Allah) originated creation, and then Allah will bring forth (resurrect) the creation of the Hereafter (i.e. resurrection after death). Verily, Allah is Able to do all things."

Surah Al-Ankabut - Verse 20 - The Noble Quran

Dedication

فتحُ نظمي ومقالي حمدُ ربِّ العالمينا

وصلاةُ الله تالي تبلغ الهادي الأمينا

وعلى صحبٍ وآل وجميع التابعينا

ما بدا نور الوصالِ في وجوه الساجِدينا

أُهدي هذا العمل إلى أبي وأمي
د. أحمد خويرة، المُعلم الأول و سُهاد النابلسي، سِت الحبايب
إلى توأم الروح، زوجتي العزيزة ريما التميمي
إلى أخي يزن، ياسر وياسين. وأختي العزيزة يمان.

وإلى أهل مدينتي الحبيبة نابلس جبل النار
ولكل أهل فلسطين الصابرين الصامدين

Acknowledgement

Embarking on a captivating journey from engineering to physics, I am deeply grateful for the incredible support that shaped my path. At the forefront, I express my heartfelt thanks to the distinguished researcher, Dr. Abdenour Lounis, whose mentorship during my master's and Ph.D. significantly influenced my career. His immense support in aligning my focus with the ITk project and facilitating funding for my thesis at CERN has been invaluable.

I extend my appreciation to the ATLAS group members at IJC Lab, including Maurice-Cohen Solal, for their assistance in ring oscillator design. Special thanks to Abd Al-Ali Slimani, Jimmy Jeglot, Abood Falou, and Ana Torrento for their assistance. Gratitude also goes to the exceptional ATLAS group at CPPM: Mohsine Menouni, Pierre Barrillon, and Thomas Strebler—with whom I collaborated on significant irradiation campaigns.

Furthermore, I extend my appreciation to the ATLAS ITk test beam team at CERN for the enjoyable moments shared during long shifts. A special acknowledgment is reserved for Sejla Hadzic from ATLAS MPP, whose dedicated efforts facilitated my access to the Corryvreckan offline reconstruction software.

I would like to express my heartfelt gratitude to all my colleagues from the ATLAS Pixel-CERN group, particularly Susanne Kuehn and Benedikt Vormwald. Their support was instrumental in facilitating my seamless integration into the team. I appreciate their collaboration in module production and our joint participation in the delightful demonstrator in CERN-SR1.

To all these individuals, I owe a debt of gratitude for their unwavering support and collaborative spirit throughout my academic journey.

Moreover, pursuing a career in physics would have been inconceivable without the invaluable support and guidance provided by Ahmed Bassalat and Achille Stocchi. I established close connections with them through the wonderful association of SAPA and the Winter School in High Energy Physics in Palestine back in 2018. Their mentorship has played a pivotal role in shaping my journey in physics, and I am sincerely grateful for their unwavering encouragement.

Nevertheless, given that this thesis was conducted at CERN (Geneva) and IJC Lab (Paris-Orsay),

I extend my deepest gratitude to my limitless source of support, Reema Altamimi—my wife and constant motivator throughout this journey. Her steadfast encouragement has been the driving force behind my dedication and perseverance every day. Who was pursuing her master's in Paris and committed to taking weekly flights to Geneva. Your dedication and sacrifice added an extra layer of support. Thanks for being in my life!

Lastly, and with the utmost appreciation, I extend my acknowledgment (along with a heartfelt tip of the hat) to my family in Palestine—my parents, sister, brothers, Uncle Hazem Khwaira (my spiritual father), and my wonderful aunt Basma Khwaira (my personal life-consultant). Thank you all for consistently being there, despite the geographical distance spanning two different continents. Your unwavering support has served as a perpetual source of strength and encouragement throughout my entire journey.

Yahya يحيى
Paris, November 2023.

Synthèse en français

Cette thèse explore neuf chapitres, débutant par une introduction complète, motivant la poursuite de l'exploration scientifique. Elle trace le chemin évolutif de l'approche réductionniste à la compréhension de l'origine de la matière jusqu'au modèle standard actuel de la physique, soulignant ses défis et limitations actuels. Un point central est l'amélioration imminente de l'expérience ATLAS au CERN, prête à repousser les limites de la machine LHC dans la quête d'approfondir les connaissances.

Le troisième chapitre dévoile les intrications du complexe LHC, mettant l'accent sur les améliorations des systèmes sous-détecteurs de l'expérience ATLAS, avec une exploration détaillée du traqueur interne d'ATLAS en transition vers un détecteur entièrement en silicium. Ensuite, le quatrième chapitre plonge dans les bases de la technologie des détecteurs en silicium, élucidant les paramètres clés de détection.

Le cinquième chapitre élargit la portée, expliquant l'électronique de lecture des détecteurs développée pour le détecteur de pixels afin de résister à une irradiation accrue et à une élévation du nombre d'interactions. Il fournit un examen approfondi du traitement du signal et de l'architecture de l'interface avant analogique utilisée dans la construction de la puce de lecture de pixels RD53A, en vue de la soumission de la puce ITkPixV2 pour les nouveaux modules de détecteurs de pixels.

Le cœur de la thèse réside dans les chapitres suivants. Le chapitre six présente des mesures substantielles utilisant le dispositif de l'anneau oscillateur intégré dans la future puce de lecture de pixels. Des tests rigoureux et une caractérisation de l'oscillateur en anneau (ROSC) sont effectués, explorant les effets de fréquence sous différentes températures, tensions et irradiations, en particulier la dose totale d'ionisation (TID). Cette étude unique utilise un environnement contrôlé, soumettant la carte à puce unique ITkPixV1.1 à une TID allant jusqu'à 500 Mrad tout en surveillant simultanément la collecte de données, discernant ainsi les effets induits par la TID sur l'électronique en face avant. Le chapitre se conclut par un examen d'annealing à haute température, éclairant la récupération potentielle des performances de la puce en phase post-irradiation, pour imiter les conditions de prise de données de l'HL-LHC.

De plus, compte tenu du flux de particules élevé attendu dans l'environnement de l'HL-LHC, le

chapitre 6 aborde le défi des erreurs uniques dues aux particules (SEU) dans les éléments de stockage. La campagne menée dans le synchrotron à protons du CERN imite les flux de l'HL-LHC, évaluant la résilience de l'ITkPixV1.1 aux SEU. Un résultat crucial est l'efficacité observée des techniques d'atténuation pour contrer les dommages des SEU, assurant des performances électroniques robustes dans les conditions exigeantes de l'HL-LHC, en particulier dans la couche de détecteurs la plus interne. Les résultats présentés dans le chapitre 6 soulignent la résilience de la puce de lecture de pixels conçue en collaboration par RD53, confrontée à l'environnement radiatif exigeant prévu dans les futures conditions de l'HL-LHC. Une percée notable est l'utilisation innovante des oscillateurs en anneau (ROSC) en tant que capteurs de rayonnement, marquant une avancée pionnière dans l'exploitation des technologies existantes pour une fonctionnalité dans une dose totale d'ionisation sans précédent.

De plus, le chapitre 7 aborde la tâche cruciale du développement de capteurs de pixels adaptés aux exigences du nouveau traqueur interne. Compte tenu des conditions dépassant les seuils actuels des détecteurs, une approche innovante de recherche et développement a été adoptée pour concevoir un détecteur de pixels capable de gérer des scénarios d'interactions élevées, réalisés grâce à une granularité pixel améliorée.

Dans la recherche rigoureuse de la validation de la conception, une série de campagnes exhaustives de tests en faisceau ont été déployées au Super Proton Synchrotron (SPS) au CERN. Ces campagnes, utilisant des modules quad-pixels RD53A, ont été exécutées méticuleusement pour examiner les performances des modules dans diverses conditions. Les objectifs principaux étaient doubles : premièrement, évaluer l'efficacité des modules par rapport aux exigences de l'ITk, et deuxièmement, plonger dans les performances nuancées des modules irradiés et non irradiés.

À travers une analyse minutieuse des données, réalisée lors de périodes prolongées d'acquisition de données, le cadre de reconstruction des données du faisceau de test Corryvreckan a fourni des aperçus cruciaux. Les résultats confirment un succès retentissant, les modules testés satisfaisant aux exigences actuelles de l'ITk. Cela a été attesté par des performances robustes tant dans des états non irradiés qu'irradiés, évaluées par un examen minutieux des distributions résiduelles et de l'efficacité de suivi.

Le chapitre 8 constitue une exploration vitale des subtilités de la validation du prototypage, de la production de modules de pixels et du réseau complexe de mesures d'assurance qualité essentielles pour le bon fonctionnement des détecteurs à grande échelle. Les sections initiales plongent dans les analyses électriques nuancées cruciales pour caractériser les performances des modules de pixels. Avec le projet ITk prévoyant la production de plus de 4500 modules, ce chapitre souligne l'importance de l'expérience pratique de la production, garantissant des mesures d'assurance qualité et inspectant le rendement de la production pour répondre à des exigences strictes.

L'initiation du projet crucial du démonstrateur Outer Barrel émerge comme une pierre angulaire. Le projet du démonstrateur sert de terrain d'essai essentiel, non seulement pour la validation des

performances, mais aussi pour examiner les concepts de chargement, les nouvelles structures de support en fibre de carbone et le comportement thermique pour un refroidissement efficace. Tout au long de ce chapitre, la thèse présente méticuleusement des données collectées lors des différentes étapes du démonstrateur Outer Barrel, offrant une vue d'ensemble complète des aspects associés.

De plus, en prévision de la production de masse pour le traqueur interne, les 32 modules comprenant 114 puces jouent un rôle pivot. Cela marque le développement d'un outil innovant d'assurance qualité, une première du genre pour les modules de pixels du barillet externe. Grâce à la combinaison de scans électriques et d'un outil automatisé, les défauts sont identifiés, catégorisés et comptés, fournissant un moyen systématique et efficace d'évaluer le rendement global. Les résultats sont prometteurs, montrant que plus de 95 % des 8,75 millions de pixels fonctionnent parfaitement. L'outil, étendu pour évaluer la cohérence des défauts de pixels sur les 114 puces, offre des informations précieuses, telles que l'identification de défauts cohérents aux bords des modules. Ce chapitre se conclut par une approbation retentissante de l'efficacité de l'outil, démontrant son rôle crucial dans la filtration des pixels défaillants et facilitant le projet de production de masse d'ITk.

Cette thèse se conclut par une synthèse des efforts déployés pour faire progresser le développement de l'électronique de lecture pour le futur détecteur de pixels, avec les aspects discutés dans les chapitres précédents. Ils ont prouvé leur capacité à fonctionner dans l'environnement de radiation proposé et à relever les défis exigeants.

Table of contents

List of figures

List of figures

List of figures

List of tables

List of tables

1 Introduction

The mysteries surrounding the origin and composition of the universe have fascinated scientists, philosophers, thinkers, and even poets for ages. Questions such as how the universe began, how elementary particles give rise to the vast diversity we observe, and how the universe has evolved to its present state, including the formation of galaxies, stars, planets, and ultimately, life itself, have perplexed the curious minds of humanity.

Throughout different time periods, various answers and perspectives on the universe have emerged. Some explanations attributed natural phenomena to mythical forces, while others stood in awe of the magnificence of existence. In contrast, modern science, rooted in causality and reductionism, posits that all-natural phenomena can be broken down into interactions between particles and the exchange of forces between them. Quantum theory, in its attempt to elucidate the intricacies of physical structures and phenomena, reveals that nothing in existence is purely matter but rather composed of discrete quanta of energy. From the underlying structures of primary particles to the fields that give rise to electromagnetic forces, weak interactions, and strong nuclear forces, the intricate dance of mass, charge, spin, and confined energy in the form of particles or waves shapes the ingredients and hence the fabric of our universe. While there is still much to unravel, numerous theories endeavor to trace all-natural forces back to a single origin.

Through the interactions of elementary physical structures, atoms are formed, laying the groundwork for the creation of diverse chemical elements. From these elements, both organic and inorganic compounds emerge, with DNA and RNA playing a pivotal role in storing the genetic information vital for the reproduction of all living creatures. Examining this hierarchical structure, we come to appreciate that the existence of physical forms hinges upon the underlying order ingrained in the natural laws of physics. It is the fine-tuned nature of our universe that enables the support and sustenance

necessary for our existence that rests upon a meticulously prepared matrix of fundamental physical constants, testifying to the remarkable care bestowed upon this vast cosmos.

With mankind's remarkable mental capacity, physical capabilities, and the development of spoken language, social groups began to form, and technological advancements flourished. From basic tools like knives, axes, spears, and plows, to the advent of artificial intelligence, telescopes, subatomic particle colliders, and harnessing nuclear power for energy, humanity's progress has been astounding. Yet, what we know today pales in comparison to the knowledge possessed by previous eras of humanity. Even our understanding of the universe in the 1950s was limited. During that time, there was a lack of solid theoretical foundations or empirical evidence to construct a comprehensive vision of the universe. However, the knowledge of humankind experienced a remarkable leap in the 20th century.

Let us contemplate the shape of the universe during Aristotle's time, where the sun, moon, and Earth were perceived as the entirety of the universe. The human mind was unable to transcend this conceptual limit. However, during the Renaissance, figures like Kepler and Galileo challenged this notion, expanding our understanding of the solar system. As the 20th century unfolded, the Milky Way took center stage as the perceived universe. But even this idea was short-lived, as we soon discovered billions of galaxies, each housing billions of stars. Presently, scientists are delving into the intriguing question of the existence of multiple universes!

Witnessing these monumental leaps in human knowledge is truly awe-inspiring. Yet, we must acknowledge that there may never be definitive answers to all the complex questions we encounter in our quest for understanding. Science, research, and technology may not be sufficient to unravel the ultimate mysteries of the universe. Nonetheless, this does not diminish the wonder that drives humanity's fascination with the cosmos. What motivates us to set foot on the moon and collide particles at the speed of light is to continue our relentless exploration, a profound desire to comprehend the vastness, beauty, and mystery of the universe.

In this context, one organization stands out as a beacon of knowledge and innovation: the European Organization for Nuclear Research, known as CERN. With its cutting-edge facilities and brilliant minds from around the world, CERN has played a pivotal role in unraveling the mysteries of the subatomic world. At the heart of CERN's scientific endeavors lies the magnificent Large Hadron Collider (LHC), an engineering marvel that accelerates particles to extraordinary energies. Within its intricate network of tunnels stretching for tens of kilometers beneath the surface, particles are made to collide at the speed of light, providing a glimpse into the fundamental building blocks of the universe. Through the collective efforts of thousands of scientists, physicists, and engineers at CERN, groundbreaking discoveries have been made. From the momentous observation of the Higgs boson on 4th of July 2012, a particle that endows others with mass, to the exploration of dark matter and the search for new particles, CERN has pushed the boundaries of human knowledge to unprecedented levels.

As I embark on my academic journey, my aspiration is to contribute to the remarkable scientific community, drawing inspiration from CERN's dedication to expanding human knowledge through collaboration and innovation. Joining CERN's ATLAS group has provided me with a unique opportunity to make my own humble contribution to groundbreaking research, focusing on the ATLAS Inner Tracker (ITk), the innermost detector layer.

In this thesis, I delve into the ongoing research and development of a novel Silicon Pixel detector for the High-Luminosity phase of the LHC, specifically targeting the ATLAS ITk to several irradiation campaigns, test beams, and ITk proof-of-concept using demonstrator setups . The thesis encompasses various aspects, from the testing and production to the construction of the Outer Barrel (OB) demonstrator ITk section.

The thesis commences with an **introductory chapter:** that provides an overview of the subsequent chapters' content. The following chapters are outlined as follows:

Chapter 2: A comprehensive overview of the Standard Model SM history and content are presented, with key-enabling technologies related to advancing the SM.

Chapter 3: Focuses on the LHC machine, the ATLAS experiment, and includes a detailed description of the ATLAS detector's design and functionality with the upgrade plan for the HL-LHC with the ATLAS detector. This chapter will also highlight the challenges and detector requirements for the upgrade phase, and more particularly the ITk upgrade mediated with the Outer Barrel (OB) demonstrator project, is also discussed.

Chapter 4: Discusses the mechanisms of particle-matter interaction, semiconductor properties, and the application of semiconductor-based particle detectors in high-energy physics experiments. Additionally, the chapter addresses radiation damage in Silicon detectors and the resulting performance degradation.

Chapter 5: Presents the pixel detector technologies used in the ITk and its associated front-end readout electronics.

Chapter 6: Introduces simulation results by Cadence and experimental outcomes on radiation-induced damage using X-ray ionizing dose on the pixel readout chip ITkPixV1.1 Single Chip Card (SCC). In addition, the characterization of ring oscillators (ROSC) in the pixel read-out chip under different conditions is carried out while comparing the results with simulations. Besides, Single-Event Effects (SEE) induced by relativistic particles on semiconductor devices are explored to evaluate the expected soft errors in the HL-LHC phase, presenting experimental results from tests conducted at the IRRAD facility at CERN to assess the pixel read-out chip configurations.

Chapter 7: Focuses on the efficiency of pixel detector modules with relativistic particle beams at the Super Proton Synchrotron facility at CERN. The performance of the sensors is examined in various test beams, including an explanation of test beam principles, data monitoring, and offline analysis reconstruction with analysis results.

Chapter 8: Introduces the OB demonstrator project and the RD53a quad pixel modules electrical

tests with the module production stages at CERN including dedicated studies, analysis, and interpretations, are also covered. Moreover, the demonstrator setup and tests conducted are introduced, followed by a comprehensive introduction to the production of OB demonstrator modules, which involves examinations of potential degradation in the production line and highlights any issues before the final integration on the Outer Barrel demonstrator. The design qualifications of RD53a quad modules are studied with a novel quality control assessment developed exclusivly for the outer barrel demonstrator project, utilizing 32 RD53a quad pixel modules to identify and analyze Pixel failures and defect trends.

Chapter 9: Reflects the research findings presented through the thesis and summarizes the key contributions and implications for the ITk upgrade and the OB demonstrator project. In addition, an outlook for future work is also discussed within the prescriptive in constructing the ITk.

2

The Standard Model

The Standard Model (SM) is a triumph of theoretical and experimental physics. Nobel prize winner, physicist Gerard 't Hooft summarized the theory in [30] p. 50 as follows:

> *"This is a mathematical description of all known particles and all known forces between them, enabling us to explain all of the behaviour of these particles . . . As far as we know, there is no single physical phenomenon that cannot be regarded as some consequence of the Standard Model, and yet its basic formulae are not terribly complicated. We do admit that the model is not absolutely perfect . . . however, the degree of perfection reached is quite impressive."*

2.1 Historical overview

The last comprehensive theory of everything dates back to 2,500 years ago with Empedocle's concept of the four elements: earth, water, air, and fire. Aristotle later introduced a fifth element, quintessence. Showing that explaining everything was never easy. However, since then, the limitations of the four-element theory became evident in the fourth century BCE when alchemists discovered and isolated a wider range of substances. It was not until the eighteenth century that chemists realized that all substances are composed of a relatively small number of indivisible "elements" (initially believed to be less than a hundred) that could not be further broken down. This marked the beginning of the reductionist approach, seeking to understand complex phenomena by studying their fundamental constituents. Meanwhile, breakthroughs were made by connecting seemingly unrelated phenomena through common theories. Newton's discovery of gravity explained the motion of both falling rocks

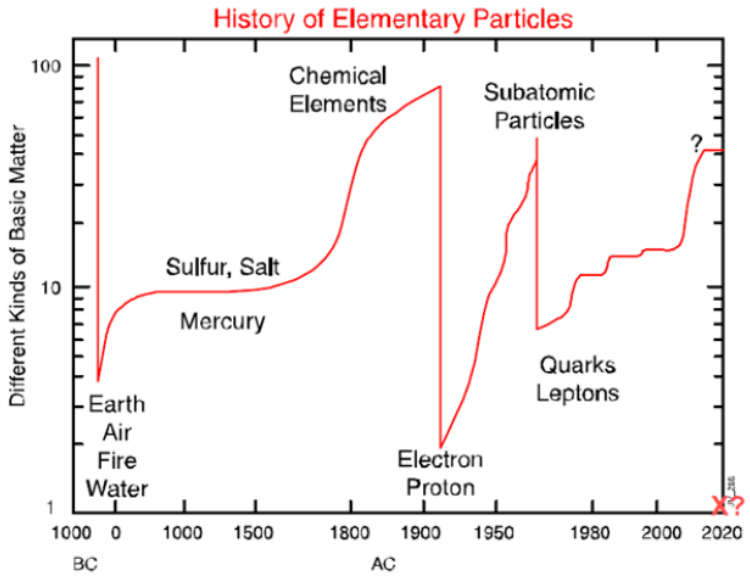

Figure 2.1: Number of elementary elements in nature varied during the development of knowledge [1].

and planets. Joule's work on heat revealed its connection to energy and atoms. J.J Thomson discovered the electron by cathode ray studies [31], showing discharge glow at a very low gas pressure. Hence, atoms are no more elementary. A few years later, natural radioactivity was discovered by Marie-Curie and Henri Becquerel. Paving the way for Ernest Rutherford to discover the atomic nucleus using α particles bombarding a thin gold foil. Now, an atom clearly consists of a nucleus surrounded by a cloud of electrons. Moreover, Maxwell's formulation of electromagnetism unified electricity and magnetism. These advancements led to new understandings and practical applications. In the late 19th century, the regularity of atomic spectra prompted the development of quantum mechanics, which explained atomic properties and chemical elements. By the 1930s, the discovery of neutrons, protons, and electrons within atoms marked another milestone in reductionism, unraveling the composition of matter at a smaller scale.

Later on, Einstein formulated special relativity by merging space and time, followed by general relativity, which incorporated gravity. The quest for unification led to addressing contradictions between quantum mechanics and special relativity, resulting in the successful quantization of electrodynamics. However, phenomena like radioactive decay remained unexplained until the introduction of the weak nuclear force.

As particle colliders probed higher energies, physicists encountered a complex array of particles, which were eventually simplified through the theory of the strong nuclear force and electroweak unification. The level of resolution achievable in particle accelerators is inversely proportional to the total energy of the colliding particles. For instance, an energy of 1 GeV corresponds to a resolved

distance of approximately 1 femtometer 10^{-15}m. Increasing the energy by an order of magnitude results in a decrease in distance by an order of magnitude. With a peak collision energy of about 10 TeV, the Large Hadron Collider (LHC) allows us to probe distances as small as 10^{-19}m, marking the shortest distance at which the laws of nature have been tested thus far.

Today, the Standard Model, together with general relativity, accounts for all known observations, augmented by the inclusion of dark matter and dark energy. While the microscopic structure of dark matter and dark energy remains unknown, it currently poses no significant challenge to the existing framework. More SM information with a detailed historical overview in [32].

2.2 Basis and foundations of the SM

The 1960s and 1970s were considered to be a golden age of particle physics. Back then, the commissioning of brand-new accelerators with high colliding energies was the beginning of an exciting journey into largely uncharted territory, populated by particles predicted by theoreticians, at best, only a few were detected.

SM consists of three types of Yang-Mills quantum field theories based on a principle called "Gauge symmetry". In the gauge group $SU(3)_C$ x $SU(2)_L$ x $U(1)_Y$, three generations of matter particles through three kinds of force, mediated by a collection of field particles or 'force carriers' are described.

An example of local gauge theory is **Quantum Electrodynamics** (QED), a quantum field theory for electromagnetic force. Mathematically, it involved phenomena related to electrically charged particles interaction by exchanging photons. QED is the unitary $U(1)$, Abelian gauge theory, that is expressed by one gauge field, the photon γ being the gauge boson. Hence, the photon couples to the electrical charge and, therefore, couples to the quantum number for QED. Moreover, the coupling constant determines the strength of electromagnetic interaction known as the fine-structure constant [**?**]:

$$\alpha = \frac{e^2}{4\pi\epsilon_o c} \tag{2.1}$$

Specifically, α is one of 20 empirical parameters in the SM that has to be computed experimentally, and found to be:

$$\alpha^{-1} = 137.035999074 \pm 0.000000032 \tag{2.2}$$

In more, considered to be the most precise measurement, QED is promoted to one of the most precise theories in physics up to date.

On the other hand, **Quantum Chromodynamics** (QCD) is represented by non-Abelian gauge theory, symmetry group $SU(3)_C$. In which the gauge group of the color triplets, and the gluon is the associated guage boson describing the strong interaction of colored particles. However, the gluons also carry color charges, which forbid adding a mass term for the gluon field of a non-broken gauge symmetry $SU(3)_C$. Hence, not invariant under the local transformation, therefore, gluons are

massless spin-1 particles. All interactions in QCD are based on a single universal coupling, the strong coupling constant g_s, defined as [33]:

$$\alpha_s = \frac{{g_s}^2}{4\pi} \tag{2.3}$$

Experimentally, the coupling constant value is determined at a fixed scale, for example, the Z boson mass ≈ 91 GeV in which the coupling constant can be found to be:

$$\alpha_s({M_Z}^2) = 0.1185 \tag{2.4}$$

The last term in Yang-Mills gauge theory is the **Weak interaction**. Distinguished from QED and QCD, Weak interaction poses properties like a lifetime, strength of coupling, cross-sections, and violation of symmetries. Mediated by $W^{\pm}$ bosons, charged current interaction involves only left-handed fermions. Neutral current interaction mediated by the Z boson, couples to both left- and right-handed fermions. However, to fully describe the weak interaction, one needs to elaborate the Electroweak EW theory to associate the weak isospin quantum number in the non-Abelian group $SU(2)_L$ to $U(1)_Y$ with the index Y hypercharge.

2.3 A Zoo of particles

The material world around us is intricately composed of atoms, which consist of a central nucleus housing protons and neutrons, encompassed by ghost-like electron wave-particles. However, the SM encompasses a rather extensive view of a fundamental number of particles, which may seem overwhelming. With six quark flavors and three-color values for each, we have 18 quark types. Including leptons (electron, muon, tau, and their neutrinos) brings the total to 24 fermions. Considering their corresponding antiparticles, we reach 48. Additionally, we account for the bosons as force carriers: the photon, W^+, W^-, Z^o particles, and eight types of gluons, totaling 60 particles. While all these particles were observed by the end of the 20th century, the Higgs boson has been successfully observed at the Large Hadron Collider (LHC) in 2012 by both ATLAS [34] and CMS [35] experiments, confirming its existence and completing the roster of observed particles in the Standard Model as summarized in Fig.2.2. With the inclusion of the observed Higgs boson, we now have a total of 61 particles in the SM framework. While this number may still challenge our notion of a truly fundamental theory, it represents the current understanding of particle physics.

These 61 particles are interrelated within a framework that necessitates 20 parameters, which cannot be derived solely from theory, but instead must be determined through experimental measurements. As Nobel prize winner physicist, Leon Lederman eloquently expressed in 1993 [36]:

> *"The idea is that twenty or so numbers must be specified in order to begin the universe. What are these numbers (or parameters, as they are called in the physics world)? Well,*

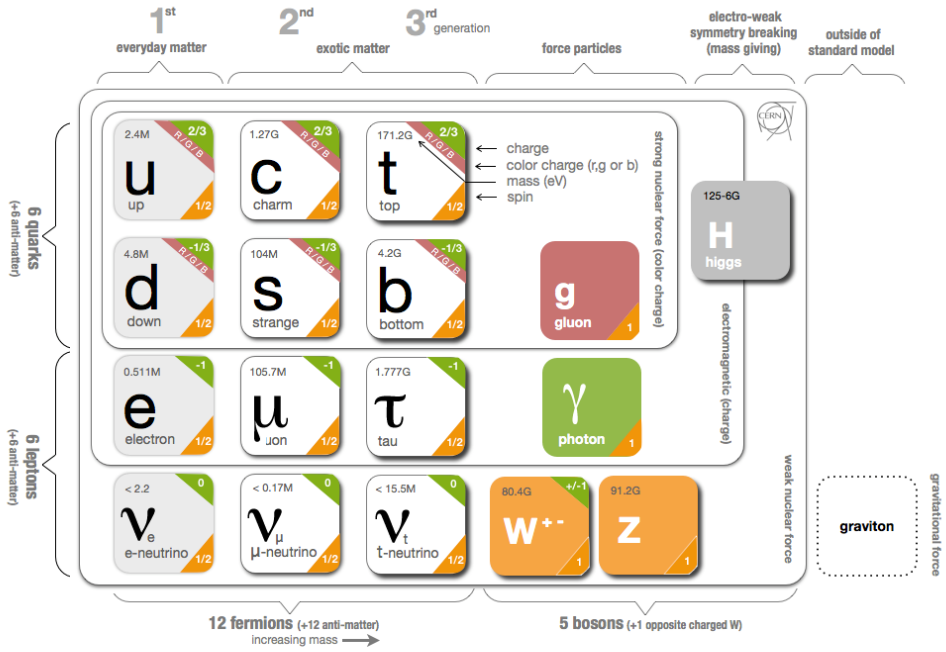

Figure 2.2: Elementary particles of the Standard Model: fermions consisting of quarks, leptons forming the building blocks of matter, subdivided into three generations. On the right, vector bosons represent the force carriers of the electromagnetic, weak, and strong forces. Higgs boson, is responsible for providing mass to all massive particles. Out of the chart resides the non-renormalizable gravitation force with spin -2 field boson, the graviton [2].

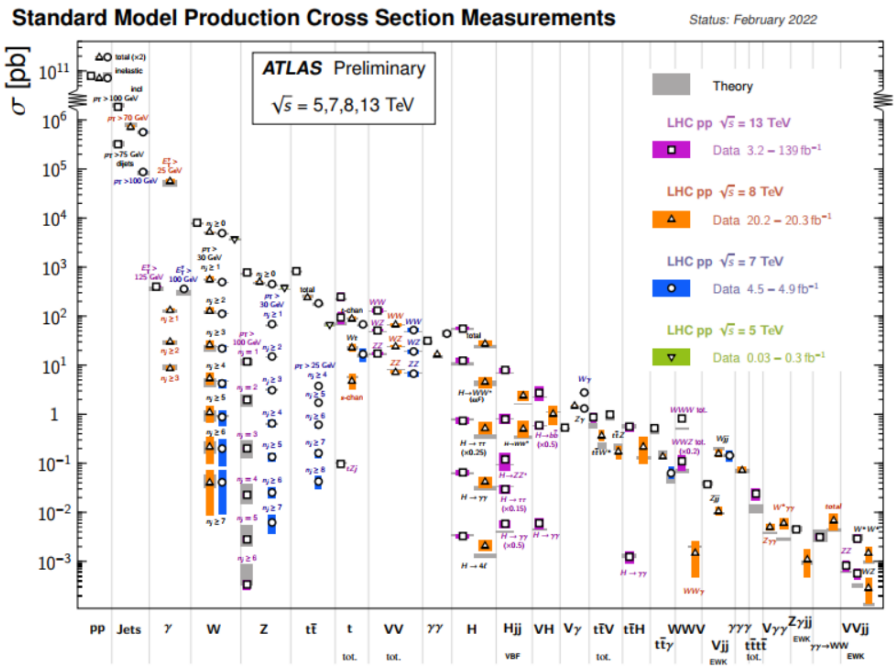

Figure 2.3: Summary of several Standard Model total and fiducial production cross-section measurements, corrected for branching fractions and compared to the corresponding theoretical expectations, highlighting the predictability power of the SM [3].

> *we need twelve numbers to specify the masses of the quarks and leptons. We need three numbers to specify the strengths of the forces . . . We need some numbers to show how one force relates to another. Then we need a number for how the CP-violation enters and amass for the Higgs particle, and a few other handy items."*

Within Lederman context, theoretical advancement necessitates precise measurements to develop further the SM predictions. The role of theoretical physicists is to discover the mathematical equations that effectively depict the results of particle collisions. When these calculations align with experimental data, it boosts our confidence in the theory. As our understanding of particle collisions improves, experimentalists can develop more efficient detectors, while advancements in accelerator technology provide theorists with better data. This collaborative approach has led to the remarkable success of the standard model of particle physics as in Fig.2.3, representing our most comprehensive understanding of the fundamental constituents of matter lineup with experimental findings, in which Fig.2.4 shows how experiment and theory advance together.

These particles as expressed in SM, including the up and down quarks (d), electron (e), and electron neutrino (υ_e), collectively form the first generation of matter particles in the SM. Remarkably, this ensemble of spin -½ fermions comprehensively accounts for our tangible experiences and phenomena.

Within the realm of particle physics, quarks exhibit distinct flavors: up (u) and down (d), each

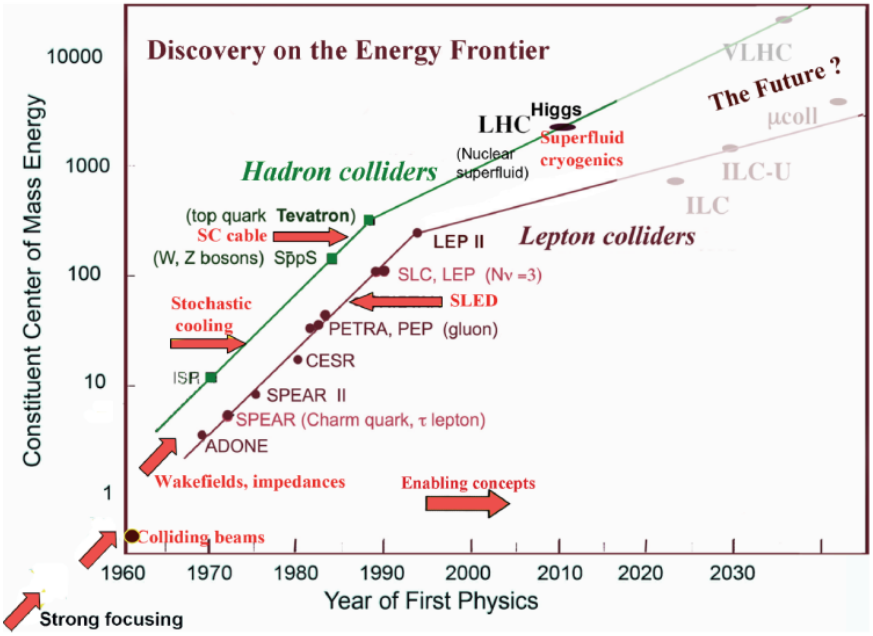

Figure 2.4: Livingston plot for constructed accelerators showing the maximum beam energy versus time. Whereas red arrows represent key features of technology development enabling breakthroughs related to setting precise measurements and particle discoveries with each commissioned accelerator and colliding machine [4]. An updated future colliding machines in [5].

existing in three different color variations—red, green, and blue. These quarks are perpetually bound together within protons and neutrons by the powerful strong force, which intensifies as attempts are made to separate them in distance. Consequently, quarks are forever "confined" and cannot manifest independently. Facilitating this interaction is the exchange of gluons (g) spin -1, particles mediate interactions among quarks as well as with one another.

Through the combination of up and down quarks with their corresponding anti-quarks, spin-0 pions (π^0) are formed. The positive pion (π^+), composed of an up quark (u) and an anti-down quark ($u\bar{d}$), and the negative pion (π^-), formed by a down quark and an anti-up quark ($d\bar{u}$), contribute to this family. However, the neutral pion (π^0) emerges as a superposition of $d\bar{d}$ and $u\bar{u}$ configurations. These relatively low-mass particles, discovered in the mid-20th century, possess characteristics related to pseudo-Nambu-Goldstone bosons. Their crucial role lies in mediating interactions between protons and neutrons, effectively binding them within atomic nuclei.

Beyond the first generation of matter particles, two additional generations exist, characterized by analogous patterns but heavier particle masses. The second generation encompasses the strange (S) and charm (C) quarks, along with the muon (μ) and muon-neutrino (ν_μ). The third generation comprises the top (t) and bottom (b) quarks, as well as the tau (τ) and tau-neutrino (ν_τ).

The strong nuclear force interacts with the colors of quarks, while the weak nuclear force, mediated by the spin-1 W and Z particles, acts on the flavors of quarks. An example of the weak force in action is Beta radioactive decay, where a down quark in a neutron converts into an up quark, causing the neutron to transform into a proton. This process involves the emission of a W^- particle, which subsequently decays into an electron and an anti-neutrino.

Weak-force interactions enable mixing between up and strange quarks, as well as between down and charm quarks. This mixing is quantified by the Cabibbo angle, named for the Italian physicist Nicola Cabibbo, with a measured value of approximately 13°. Additionally, CKM mixing [37], named after Cabibbo, Makoto Kobayashi, and Toshihide Maskawa, extends this concept to include transitions between up and bottom, down and top, charm and bottom, and strange and top quark.

The electromagnetic force, responsible for interactions between charged particles, is conveyed by photons, which are massless spin-1 gauge bosons. The discovery of photons dates back to Planck in 1900s and gained further prominence during Einstein's groundbreaking contributions in his "miracle year" five years later with the discovery of the photoelectric effect.

Lastly, deep within SM theoretical framework lies the enigmatic **Higgs field** [38], permeating the vacuum and permeating the entire universe. Through interactions with this field, massless particles acquire mass, with the degree of coupling determining the amount of mass obtained. At the heart of this field resides the spin-0 Higgs boson, often dubbed the "God particle" within the SM, as it is attributed with the responsibility of bestowing mass upon all other particles.

2.4 Cracks in the SM foundations

Physics, much like other scientific disciplines, has a propensity to transition from one crisis to another. Moments of brilliant insight can be succeeded by prolonged periods of perplexity and uncertainty. It could be contended that crisis is an inherent and desirable state, as it is only during such times that radical and audacious ideas are likely to emerge, propelling our comprehension of the world toward the next phase.

The particles introduced by the standard model, along with space and time, are currently regarded as fundamental entities, devoid of any further constituents. However, in the realm of fundamental physics, our quest is to determine if there exists an even deeper level of fundamentality yet to be discovered. In more, the most astounding discovery pertains to the prevailing source of gravitational force in the universe, which defies our prior understanding [39] p. 80. Referred to as "dark energy," this enigmatic form of energy constitutes a staggering 68.3% of the total matter-energy content. While we remain unaware of its microscopic structure, we are familiar with its impact. Dark energy propels the acceleration of the universe's expansion, necessitating its substantial presence. However, due to its sparse distribution, direct measurement is limited to larger scales, where its cumulative effect becomes apparent through accelerated expansion. On the other hand, approximately 26.8% is surprisingly, classified as "dark matter." Dark matter is characterized by its infrequent interactions with both itself and other forms of matter, and notably, it does not interact with light, hence its name. While certain supersymmetric particles exhibit behaviors consistent with dark matter, it remains uncertain if this provides the correct explanation.

Following this, Supersymmetry, a theoretical framework known as SUSY [40], introduces "super-multiplets" that connect fermions (matter particles) with bosons (force-carrying particles). It expanded the particle spectrum by proposing a massive supersymmetric partner with a spin differing by ½ for each particle in the standard model. For example, the electron's partner is the selectron, while quarks have squark partners. Photino, wino, and zino were predicted as supersymmetric partners of the photon, W, and Z particles, respectively. Despite theoretical predictions, these supersymmetric particles have yet to be observed at the TeV energy scale, for example, at the energy scale the LHC provides. However, none of SUSY particles have been found. Jonathan Ellis, a theorist at CERN, referred to the possibility that the LHC would find nothing but the Higgs boson as *"The real five stars disaster"* [41].

Moreover, SM does not provide a unified theory for the strong, weak, and electromagnetic forces, and it does not incorporate gravity, the fourth fundamental force [42]. Although gravity is weak in the context of particle interactions, it is always attractive and proportional to mass. As we scale up from quarks to atoms, molecules, and larger structures, the cumulative effect of gravity becomes significant and irresistible. In the absence of puzzling or unexplained experimental findings and with no theoretical predictions testable by experiments, there was a lack of direction in the development of

the Standard Model. The question arose whether it should be continued with further advancements or if an entirely different approach should be pursued instead. What we're certain about nowadays is that there is a lack of experimental data. Without experiment, theory risks a retreat into metaphysics due to mathematical speculations obscured by the language of the abstruse mathematics that is deployed.

Therefore, to sum up, observational guidance is necessary. Physics isn't math, it's choosing the right math. Hence, more data at higher energies is needed with more statistics or higher luminosity. For this, the High Luminosity Large Hadron Collider $HL-LHC$ is being built to assist theoreticians in digging deeper into the particle physics world, finding new particles, and searching for what is fundamental in nature. The Large Hadron Collider (LHC) complex will be introduced in Chapter 3, followed by the ATLAS detector, the largest multi-purpose detector ever built. Moreover, the physics demand will be presented, followed by the $HL-LHC$ upgrade.

3

The Large Hadron Collider and the ATLAS Experiment

Known as the *'Big Bang'* machine, the LHC is the largest accelerator and particle collider in the world. It accelerates proton beams in a ring capable of reproducing conditions that haven't existed in nature since the birth of our universe. The Conseil Européen pour la Recherche Nucléaire, shortly known as *CERN*, operates the largest particle collider in TeV scale. The LHC tunnel stretches along 27 km underground tunnel built 100m below ground level, with a treasury collection of machinery of superconducting magnets, an ultrahigh vacuum of 10^{-10} mbar, equipped with computer clusters that, during the experiment record 3 GB of data per second. Two opposing hadron beams of protons or Pb ion beams driven within the accelerator complex of the LHC are brought into collision at four interaction points as in Fig.3.1. Since the commissioning of the LHC in 2009, the first proton-proton collision occurred at a center-of-mass energy of $\sqrt{(s)} = 3.5$ TeV each. Progressively, the beam parameters were improved to reach center-of-mass energy of $\sqrt{(s)} = 13$ TeV with a $2 \times 10^{34} cm^{-2} s^{-1}$ peak luminosity [43].

Moreover, to increase the statistical sensitivity to specific rare processes, the LHC accelerator and detectors will undergo several upgrades in 2023 - 2025, to run with a ten times higher luminosity of $10^{36} cm^{-2} s^{-1}$ [44]. The High Luminosity HL-LHC upgrade plan will be discussed in Sec.3.5, highlighting the ATLAS detector upgrade, and the innermost detector layer the ITk will be presented in detail.

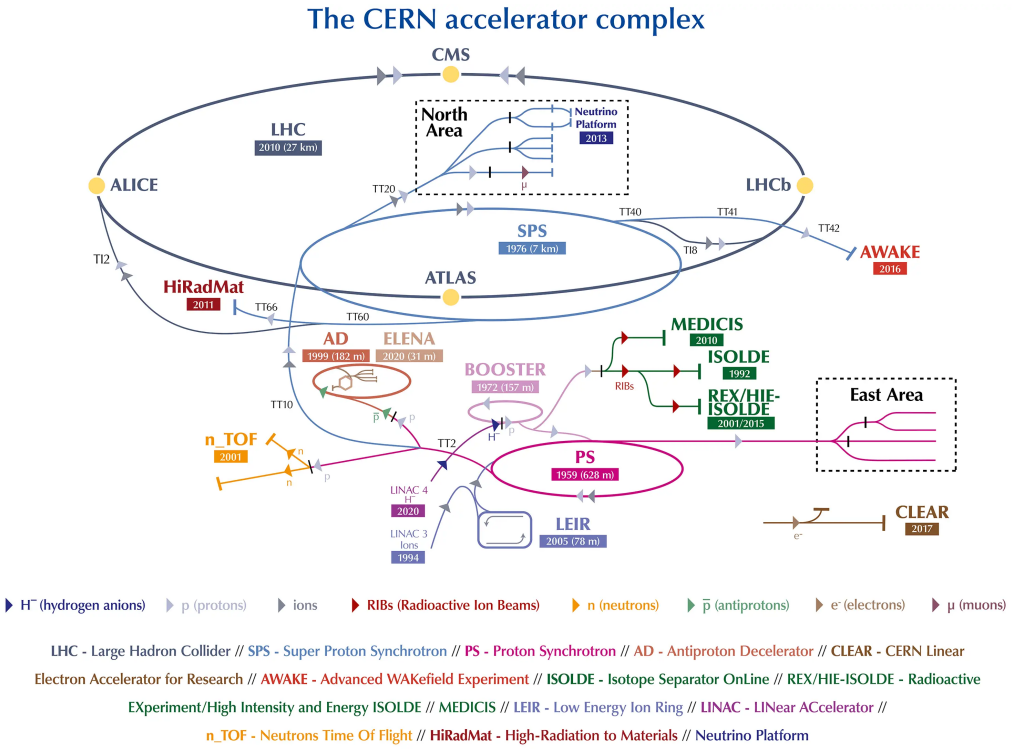

Figure 3.1: The CERN accelerator complex compromising the LHC ring with pre-accelerator stages. Four interaction points are shown in yellow where the two opposing particle beams collide [6].

3.1 The accelerator complex at LHC

A beam circulating in the LHC tunnel is injected into the ring using a hydrogen molecule tank were proton and electrons are separated by stripping foils and an electric field. The beam in the LHC ring is presented in the form of bunches, in which the LHC ring stores 2835 bunches per beam separated in time by 25ns, each bunch containing 10^{11} protons. The protons are accelerated by the LINAC 2, the first linear accelerator up to 50 MeV. The next step with the Proton Synchrotron (PS) booster, which increases the beam energy up to 1.4 GeV, followed by an injection of the beam to the Proton Synchrotron (PS) that raises up the energy to 26 GeV. The last step before entering the LHC tunnel is the Super Proton Synchrotron (SPS), which boosts the beam energy reach to 450 GeV. Lastly, the beam injected into the LHC ring will endure several intensification cycles of beam energy increment, while ramping up the LHC superconducting magnet's strength to keep the beam on track.

One of the key components of the LHC is its powerful magnets. The LHC accelerator complex structure includes thousands of superconducting magnets that guide and focus particle beams along a 27 Km circular tunnel. The niobium-titanium (NbTi) magnets can bear a magnetic field of 9 - 10 Tesla operating at $\approx$ 1.9K, hence, required to be cooled down with super-fluid helium, making the LHC one of the coolest places on earth.

Once the beam energies reach the desired center-of-mass collision energy, both opposing beams collide in four different interaction points (IP). The LHC complex comprises four different large-scale experimental instruments: ATLAS (*A Toroidal LHC ApparauS*), CMS (*Compact Muon Solenoid*), ALICE (*A Large Ion Collider Experiment*), and LHCb (*Large Hadron Collider beauty*). While each detector is meant for a specific physics study, ATLAS, and CMS are general-purpose detectors that aim to study a broad range of physics.

When the LHC was commissioned in 2009, Run1 lasted until 2013 remarking a historical milestone with the discovery of the Higgs boson at mass of 125 GeV [34]. Then, several shutdowns for the upgrade were performed until Run2 started in early 2015, to reach another peak of center-of-mass energy of $\sqrt{(s)}$ = 13 TeV, with a luminosity reached twice the design luminosity. Nevertheless, in Run3, LHC recorded another world record, colliding particles at $\sqrt{(s)}$ = 13.6 TeV in mid-2022, after a long period of shutdown.

3.2 The Luminosity and interaction rate

Luminosity is a key parameter of particle colliders that measures the number of collisions generated per surface area and per time. For instance, the total probability of interactions between colliding beams produces a number of events N_{tot}, expressed as the total interaction cross-section σ_{tot} jointly

with the time integral over the instantaneous luminosity defined as:

$$N_{tot} = \sigma_{tot} \int L(t)\, dt \tag{3.1}$$

In which, a differential form defining the collision rate $R(t)$ as a function of the number of collisions over time $R(t) = dN_{tot}/dt$ gives:

$$R(t) = L(t).\sigma_{tot} \tag{3.2}$$

Typically, particle colliders are expressed as the amount of data taking over time $\triangle t$, via the integrated luminosity:

$$\ell = \int_{\triangle t} L dt \tag{3.3}$$

With L being the instantaneous luminosity, the expression measures the collision event rate, a key parameter to identify the statistical yield for physics processes. In which the instantaneous Luminosity is expressed as [11]:

$$L = \gamma \frac{n_b N^2 f_{rev}}{4\pi\beta^* \varepsilon_n} R \quad , \quad R = \frac{1}{\sqrt{1 + \frac{\theta_c \sigma_z}{2\sigma}}} \tag{3.4}$$

Where γ is the relativistic gamma factor, n_b is the number of bunches per beam interaction at the collision point, N is the bunch population occupancy, f_{rev} is the revolution frequency, β^* is the beta function value at the collision point, ε_n is the normalized transverse beam emittance, R being the luminosity geometrical reduction factor from the crossing angle not including the Hourglass effect, θ_c is the full crossing angle between two colliding beams, σ, σ_z are the transverse and longitudinal r.m.s sizes, respectively. For example, in Run2, ATLAS and CMS $L_{Run2,\ max} \simeq 2 \times 10^{34} cm^{-2} s^{-1}$ enabled ATLAS and CMS to gain statistics as much as $\ell \approx 190 fb^{-1}$ [45]. In contrast, previous runs delivered $\approx 100 fb^{-1}$ on a yearly basis, indicating the integrated luminosity effect on the collider productivity.

To meet the physics program and to expand the discovery reach of the LHC, another Run is scheduled in 2027 during the high luminosity era of the LHC. As the names denote, more statistics are needed to reduce uncertainties of measured observed particles, like the Higgs boson, coupling strengths, constrain SM parameters range, and identify any BSM physics.

3.3 Physics Goals at the ATLAS Experiment

High-energy hadron colliders have played a crucial role in discovering new particles at the highest mass scales of the Energy Frontier. The discovery of the Higgs boson at the ATLAS experiment marked a significant milestone, opening up a new era in particle physics, and boosting our confidence with the detector technology implemented such as the ATLAS detector.

Observation and detection of particle properties occur through their interaction with the sur-

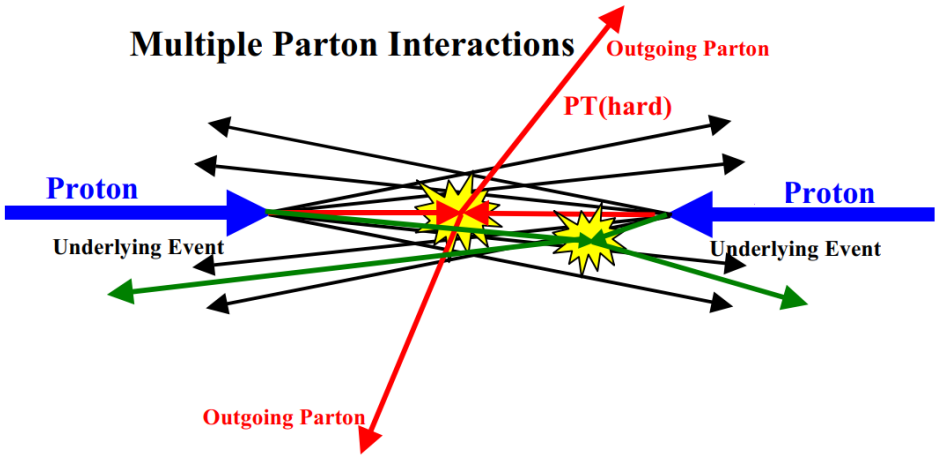

Figure 3.2: Illustration of Proton-Proton collision with an underlying event attributed to multiple patron interactions and several decay products. In addition to potential patron-patron interaction with transverse momentum [7], p. 1.

rounding matter, via elastic or inelastic collisions. However, by the nature of the experimental demand, the product of the elastic scattering escapes undetected and the interest in such interaction is limited. On the other hand, head-on hard scattering and inelastic collisions are within the physics interest, as such interactions could reveal unknown physics or provide precise measurements for rare physics processes.

The beam-beam remnants after a hard scattering interaction have a large transverse momentum outgoing, that manifests themselves as a cluster of particles or "Parton jets" traveling through active detecting material. The ultimate goal is to understand the physics of the underlying event through the hits and built trajectories in several detector layers. That is, a resulting event originating is mainly expressed as an *initial-state* and *final-state* in addition to the particles resulting from the break up of the *initial-state*. A typical hard scattering event has a distinct topology outcome of sub-processes exhibiting a collection of bursts or hadrons in the direction of the initial beams and two collections of jets with two large transverse momenta as back-to-back azimuth angle. As illustrated in Fig.3.3 three regions "towards", "transverse", and "away" might have a potential decay product. For instance, in proton-proton collisions, the "toward" region typically contains a leading charged particle jet, while the "away" region, on average, contains the "away-side" jet. The "transverse" region is perpendicular to the plane of the hard scattering and is therefore very sensitive to the “underlying event". Generally, in physics analysis, the missing transverse momentum E_T^{miss} is an essential part of many precise measurements and searches BSM. After a proton-proton hard scattering, the majority of particles predicted by the SM leave detectable traces, except for neutrinos and certain hypothetical BSM particles. These elusive particles evade detection and do not produce a measurable signal. However, by examining the momentum of colliding protons in the transverse direction, where their momenta are negligible compared to their boost along the beam direction, the presence of these

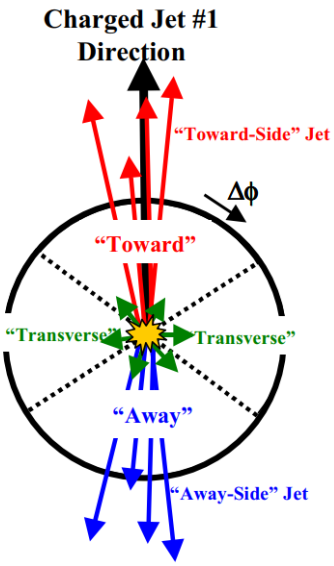

Figure 3.3: Topology illustration of average proton-proton collision linked to hard scattering interaction. Several regions of decay products or jets relative to the direction of colliding beams are presented. The transverse momentum region perpendicular to the plane of hard scattering interaction is very sensitive to an underlying event of a rare physics process. Through this region, measurements of missing transverse momentum E_T^{miss} are remarkably important for LHC physics analyses, including Higgs boson measurements and searches beyond the Standard Model (BSM) signatures such as supersymmetric or hidden sector particles [7], p. 3.

particles can be inferred from the resulting imbalance of momentum in the transverse plane. The E_T^{miss} is constructed and calculated from the reconstructed final-state particles and calibrated energy deposits inside many detector layers, including the calorimeters. If invisible particles with unknown properties are created, only the transverse momentum can be constrained as follows [46], p. 425:

$$E_T^{miss} = \Sigma \rho T(i) \tag{3.5}$$

Furthermore, once the decayed products in the form of charge, neutral particles, or hadronic jets are evaluated, the invariant mass can be calculated accordingly. If a missing transverse momentum is found, it could be constrained close to the mass of the unknown particle.

This strategy has proved historically the capabilities to identify many physics processes, such as the discovery of W and Z bosons [47],p. 157. But, this approach is susceptible to fluctuations caused by noise and unrelated collisions occurring within the same event. With the growing luminosity of the LHC, this effect of additional unrelated collisions has become increasingly significant and problematic. This imposes the need to expand the longitudinal sensitivity on the transverse region of the detection range for the detector, where extraordinary physics processes take part in.

Additionally, it's worth mentioning that detectors are generally considered a transducer, where the particles deposit energy in detector volume, and the detector converts it to measurable signals, usually in the form of an electric current. Furthermore, based on the decay products and energy deposits, the mass, electric charge, and final state kinematic properties could be identified. Apart from this, not all of the SM particles could be identified in the same manner. Instead, only $e^{\pm}$, $\mu^{\pm}$, and γ could be detected and observed directly. Other SM particles required different approaches for detection. Quarks for instance are detected through the interaction of stable or semi-stable hadrons as $\pi^{\pm}$, $K^{\pm}$, and K^0 due to the fact that quarks are always confined to a bound state.

What is more, the hadrons decay as the products of quarks have a short decay length from the vertex at the moment of creation, and are only detectable in the innermost detection layers closest to the IP, through the short tracks in the detecting volume. On the other hand, higher generation particles (2^{nd} or 3^{rd} type) have a shorter lifetime due to their own higher masses and, thus, are less stable in their own form. Lastly, Neutrinos are the trickiest to find and not observable directly, and a dedicated approach using large volume detectors is needed, such as the Super-Kamiokande [48].

To summarize, the properties of the Higgs boson align with those predicted by the SM, and understanding the true origin of electro-weak symmetry breaking is now the primary challenge. This challenge involves investigating the precision of the Higgs boson's behavior within the SM framework and identifying new particles at higher energies that could shed light on mysteries such as dark matter, matter-antimatter asymmetry, and neutrino masses.

In the following section, the ATLAS experiment is explained followed by the foreseen upgrade in the HL-LHC phase, to exploit the full potential of the ATLAS HL-LHC program.

3.4 The ATLAS Experiment

ATLAS detector system is one of the largest general-purpose hybrid cylindrical detectors ever built. Stretching to 44m long with 25m in diameter, it weighs ≈ 7000t. Occupying the ATLAS cavern in point 1, 100m below ground level, the ATLAS detector is arranged with its sub-detector systems to provide maximum coverage around the IP [9], p. 4.

To capture the beam collision events, multiple particle detectors are employed. A key requirement of a general-purpose detector system is the ability to be able to identify various particles simultaneously. These detectors are designed to serve the specific measurement requirements of each experiment and are composed of various sub-detector systems. For instance, the ATLAS experiment utilizes a barrel-type geometry, where the sub-detector systems are arranged in concentric cylindrical layers around the beam pipe. Each sub-detector system is responsible for the detection of specified particle properties to carry out a particular type of measurement and is strategically positioned within the experiment based on its unique properties.

For example, the first layer of sub-detecting layers compromises the highest granularity systems,

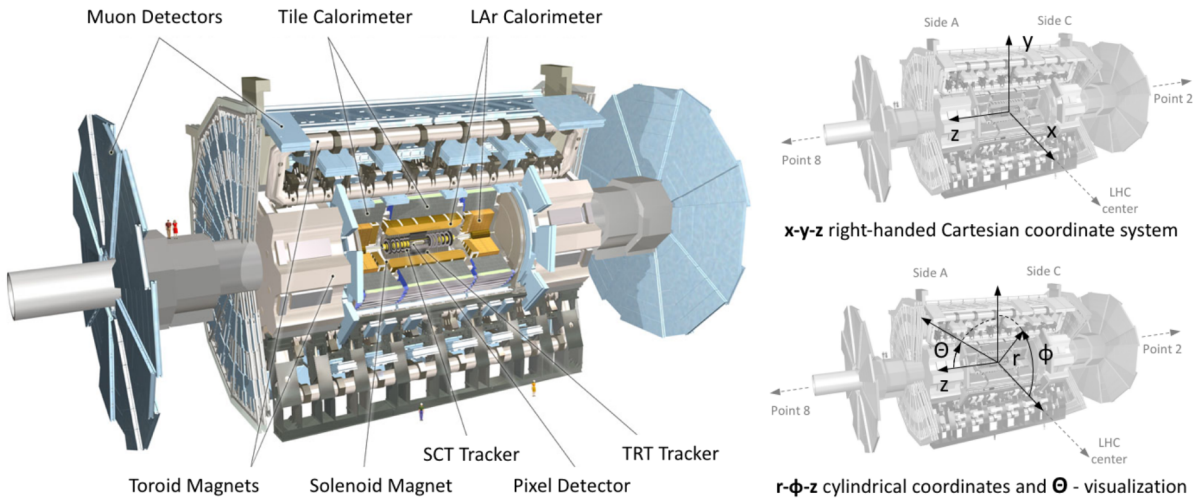

Figure 3.4: Illustration of the ATLAS detector, highlighting the main sub-detecting system. Two figures on the right side represent the ATLAS Cartesian and cylindrical coordinate system. ATLAS Experiment © 2021 cern.

mainly semi-conductor-based detectors, to enable Vertex and particles trajectory tracking, which plays a crucial role in accurately determining the positions of particles as they travel away from the collision point within the detector. To achieve precise measurements, detectors responsible for position tracking are positioned as close to the IP as possible. These detectors are specifically designed to minimize any disturbance to the particle's original trajectory, ensuring that their interactions with the detectors have minimal impact on their path.

Moreover, the most voluminous detectors, usually Calorimeters or muon chambers, serves the purpose of measuring the energy of particles, requiring the particle to transfer its energy entirely, or nearly entirely, to the detecting volume. Consequently, the particles effectively disappear within the detector, bringing their trajectory to a halt. To accommodate this requirement, calorimeters, or muon chambers, are typically positioned in the outer region of the experiment, surrounding the detectors responsible for position measurements and consisting of multiple layers of high-density energy-absorbing material. The role of the absorber material is to facilitate maximum momentum transfer interactions and effectively stop the particle within the volume of the calorimeter for detection.

By combining all data gathered from the tracks in sub-detector systems, a full picture of tracks reconstruction and identifying particles is attained, Fig.3.4 shows the ATLAS detector systems with their related coordination system. The main sub-detector systems in ATLAS detector include:

1. **The Inner Detector (ID):** Contributes to accurate measurements of particles trajectory and momentum, as it's the closest to the IP. The ID is composed of several sub-detecting systems, i.e., the inner-most section, the pixel detector, the semi-conductor tracker (SCT), and the transition radiation tracker (TRT), which will be introduced in detail in Sec.3.4.2.

2. **The Calorimeter system**, i.e., the ECAL and HCAL: Measures specific particle energy deposition and any missing transverse energies, i.e. ν, SUSY particles, if they exist. An example of ATLAS Calorimeter systems is the $ECAL$ and $HCAL$, which will be introduced briefly in Sec.3.4.3.

3. **The Muon Spectrometer (MS):** As the name sounds, it detects, measures, and identifies the μ interaction through the detector volume. Several layers are included within the MS, which will be discussed in Sec.3.4.4.

3.4.1 The ATLAS Coordination system

Measurements performed in ATLAS experiments are usually described between Cartesian, cylindrical, and spherical coordinates to parameterize the trajectory of the particle produced:

Cartesian is a right-handed based coordinate system, with the IP as the origin. The z-axis is along the beam direction, the positive z is defined counter-clockwise to the LHC ring. With two sides of the detector, side A had a positive z, and side c had a negative z coordinate. The $(x-y)$ planes are transverse to the beam direction, where positive z covers the region from the interaction point towards the LHC ring center, and positive y is defined from the ATLAS cavern towards the surface.

Cylindrical is a generalized form of the polar coordinates, where a plane along the the z-axis normal to the beam direction is introduced, with a rotation angle expressed as the azimuth angle ϕ around z. A projection of the Cartesian coordinates transverse to the beam direction gives the radial distances, $x = r\cos(\phi)$, $y = r\sin(\phi)$, and $z = z$.

Lastly, the **Spherical** coordinate is featured using the angle θ pointing from the positive z-axis towards the anti-clockwise on the LHC ring.

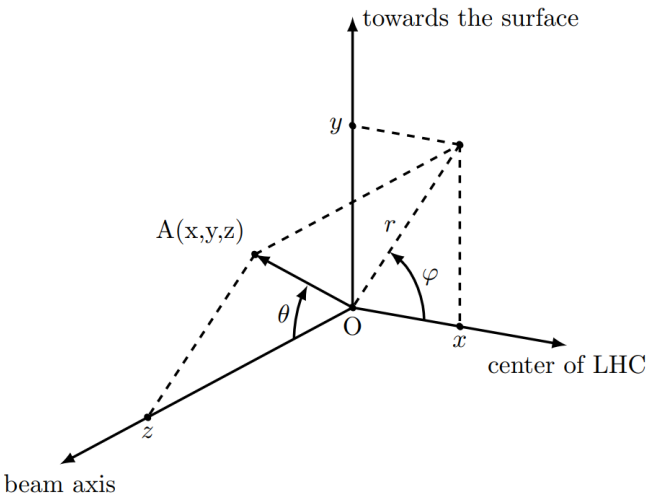

Figure 3.5: ATLAS coordinate system used to describe the position of any points using the Cartesian, polar, and Spherical coordinates, i.e. $A(x,y,z)$.

However, when particle kinematics are involved, the Lorentx invariant coordinate system is used. Typically, a specific coordinate called the Pseudorapidity (η) is introduced, expressed in terms of the polar angle θ measured against the beam axis [9], as:

$$\eta = -\ln\ tan(\frac{\theta}{2}) \tag{3.6}$$

that at very small θ, η goes to infinity. By relativistic translation of the origin, the center-of-mass coordinates could be obtained in terms of the particle momenta, for instance, η is related to $rapidity$ (y) and considered as its approximation if a zero-mass limit of a relativistic particle's rapidity $y(\lim_{M\to 0} y = \eta)$, both could be evaluated as:

$$\eta = \frac{1}{2}\ \ln(\frac{|\ p\ | + p_z}{|\ p\ | - p_z})\ \ ,\ \ y = \frac{1}{2}\ \ln(\frac{E + p_z}{E - p_z})\ \ and\ E = \sqrt{|\ \vec{p}^{\,2}\ | + M^2} \tag{3.7}$$

Where p_z is the momentum component parallel to the beam axis. It could be noted also from Eq.3.6 that η depends only on the polar angle of the particle trajectory and doesn't include the energy. Hence, $rapidity$ is often more used when describing the kinematics of heavy particles. Expanding the η notion between two particles leads to the η-azimuthal angle which is useful when finding out track isolation:

$$\triangle R = \sqrt{\triangle\eta^2 + \triangle\phi^2} \tag{3.8}$$

Moreover, due to the experimental constraints, an unknown portion of secondary particles escapes the detector geometry without leaving a track. However, based on the conservation of energy and momentum. It is possible to introduce the transverse momentum P_T and transverse energy E_T terms to evaluate the momentum or energy in the plane transverse to the beam axis, i.e. (x-y). The transverse variables in terms of the detector coordinates are expressed as:

$$p_T = \sqrt{p_x^2 + p_y^2} = |\ p\ |\ \sin\theta \tag{3.9}$$

In which the x and y components are further expressed as:

$$p_x = p_T\ \cos\phi\ ,\ \ p_y = p_T\ \sin\phi \tag{3.10}$$

In the case of the ATLAS detector, the particle's kinematics could be obtained with a high resolution in the transverse plane due to the detector's cylindrical shape. Following the introduction of the particle"s kinematics, detecting particles that don't leave or partially leave a track in the detector necessitates the introduction of missing transverse energy (E_T^{miss}). An invisible or semi-invisible final state particle contributes to the net energy of decay from an initial-state. Hence, the conservation of momentum is constrained in the transverse plane as the sum of all visible final states:

$$E_T^{miss} = -\Sigma(\sqrt{p_x^2 + p_y^2}) \tag{3.11}$$

For example, if a particle decays into two other particles, with one of them invisible, i.e. a neutrino. The transverse mass for the parent particle m_T has a maximum constrain in terms of its mass:

$$m_T^2 \equiv (E_{T1} + E_{T2})^2 - (p_{T1} + p_{T2})^2 \tag{3.12}$$

If the invisible particle with missing transverse energy is:

$$p_{T1} \equiv E_T^{miss} \tag{3.13}$$

where for the massless daughters ($m_1 = m_2 = 0$), the upper limit of mass $m = max(m_T)$ [2], p. 425.

$$m_T^2 = 2 \mid p_{T1} \mid \mid p_{T2} \mid (1 - \cos\phi_{12}) \tag{3.14}$$

Since the z longitudinal direction has resolution limitations, the neutrino z component, i.e., is effectively unknown. However, this quantity evaluation has been successfully used to measure the W mass at the Tevatron, as introduced in Sec.3.3.

3.4.2 The Inner Detector

At the ATLAS core, 20 collisions at each bunch crossing are expected, in 1 second, 40 million bunch crossing yields 1×10^9 collisions. This saturation of an enormous number of particles produced with its associated tracks, jets, and higher-order vertices, imposes a significant challenge for the detector tracking system in a very dense track environment. Vertex resolution, electronics triggering, momentum measurements, and timing constraints require high-granularity detectors capable of tackling a highly populated area of created particles showers, every $25nsec$ [49].

In ATLAS, high-resolution semi-conductor-based detectors made of multiple layers covering the forwards, back, and central regions around the IP are deployed. Extending as a cylindrical-based detector around the IP, the Pixel detector covers 2.7m in both directions from the IP, with a diameter of 2.1m, equipped with a high spatial resolution of $50 \times 250\ \mu m^2$ pixels, the first layer of the ID provides a very precise tracking measurement of the particles tracks. Outer layers are further composed of semiconductor detectors and gaseous straw tubes, known as the Transition Radiation Tracker (TRT), to offer cost-effective solutions while enabling specific particle pattern recognition .

The complete array of the ID extends to 6.2m in both directions of the beam axis, with 2.1m and η up to 2.5, as in Fig.3.6. The layout also shows different support structures for the detector modules and elements, to insure, as discussed in Sec.3.3, maximum geometrical acceptance reach. Introduced by two arrangements:

- **The Barrel section:** Covers the concentric layers around the IP, towards the outer regions equipped with a large number of detector modules for precise tracking.
- **The End-Cap section:** Located away from the IP and extended in both beam directions, the End-Cap covers the outer envelope in the shape of disks.

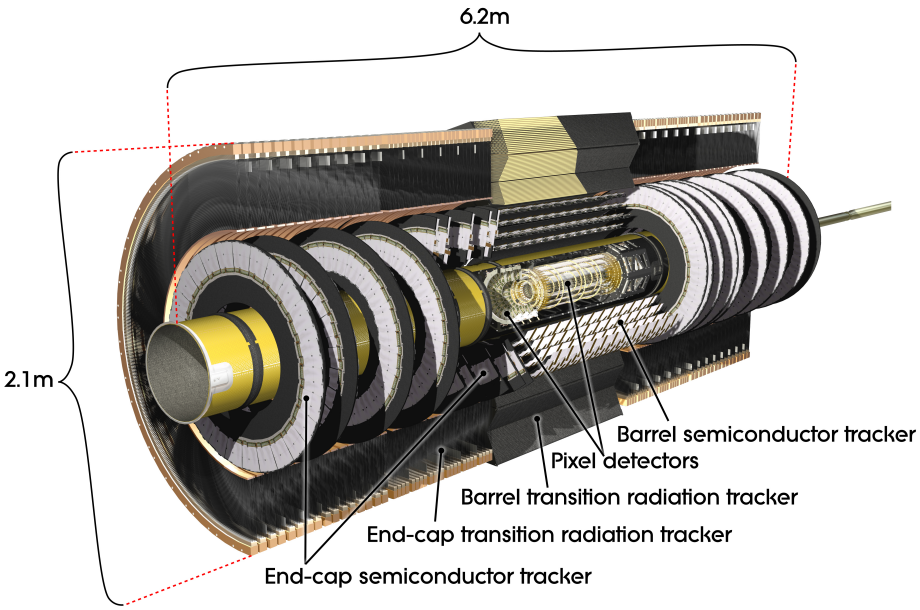

Figure 3.6: Cross-sectional view of the Inner Detector, showing different sub-detector systems which are complementary to each other. ATLAS Experiment © 2021 cern.

The ID in the ATLAS core is merged within a 2 T magnetic field induced by the ATLAS Solenoid [50], parallel to the beam pipe. For charged particles, momentum measurements and the charge sign identification are expressed by the Lorentz force mechanism. The magnetic field bends the charged particle's trajectories, hence the momentum could be evaluated from the curvature constructed using several detector layers. A uniform magnetic field of strength $B[T]$ in the z direction executes a force $F[N]$, that moves the charged particles in a helix. For simplification, if the particle tracks are considered circular, the motion that describes the measured particle momentum are expressed as:

$$F = m.a \quad where \quad a = w^2.R = \frac{v^2}{R} \quad that\ yields\ \ F = m.\frac{v^2}{R} \tag{3.15}$$

where $v\ [ms^{-1}]$ is the particle velocity, and $w[rad]$ is its related angular velocity. If we suppose the electric field $E = 0$ and the track is transverse to the magnetic field, we can equate the Lorentz force as:

$$p_{\perp} = q.R.B \tag{3.16}$$

In which e is a known parameter, with the given B as the detector magnet system, and R is evaluated from the induced track curvature due to particle interaction inside detectors.

3.4.2.1 The Pixel Detector

One of the most demanding requirements for HEP experiments is the simultaneous detection of particle tracks with micrometer spatial resolution, nanosecond timing precision, and in a hard radiation environment close to the IP. In HEP experiments, colliders usually generate particle collisions every $10-100MHz$, in the case of the LHC, $25nsec$ bunch crossing, corresponds to $40MHz$, lots of particles emerge from such a high interaction rate. While those particles live about 1 ps ($10^{-12}s$), they decay into other daughter particles. The topology of such decays is illustrated in Fig.3.7.

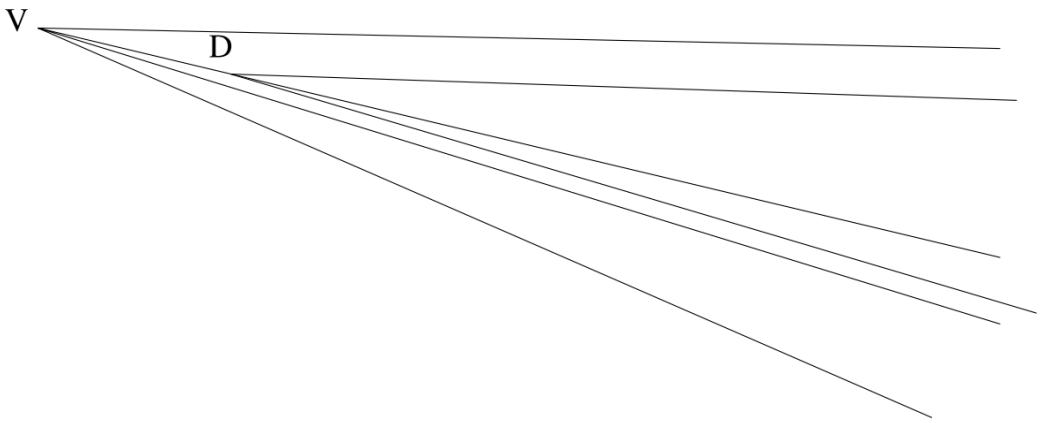

Figure 3.7: Short-lived particle decay topology. The collision vertex (V) results in decay products in the vertex (D), a few millimeters apart [8], p. 3.

Accuracy of tracking measurements as close as possible to the IP is necessary, in able to identify the collision vertex (V), and the decay vertex (D), up to an accuracy of $\approx 0.1\ c\tau$. In which τ is the particle's proper lifetime, and c is the speed of light, gives an order of picoseconds lifetime that requires measurements accuracy of $\leq 0.03mm$.

The development of highly segmented detectors with million pixels, each single pixel operating as an independent sensing element is a key parameter for tracking in dense environments around the beam pipe. The term "pixel", known typically as the picture element, in a given image process or device, is implemented in HEP experiments as a device able to detect and record the particle interaction through the Silicon bulk. The pixel size corresponds to the granularity of the image.

In the heart of the ATLAS detector, the Pixel detector is designed to provide a high granularity of identification for short-lived particles via various displaced vertices. Consisting of three barrels of staves, the pixel detector can provide three - at least - measured points for tracking reconstruction, with an acceptance angle of $|\eta| < 2.5$. The pixel detector is ≈1.3m long and ≈25cm in diameter

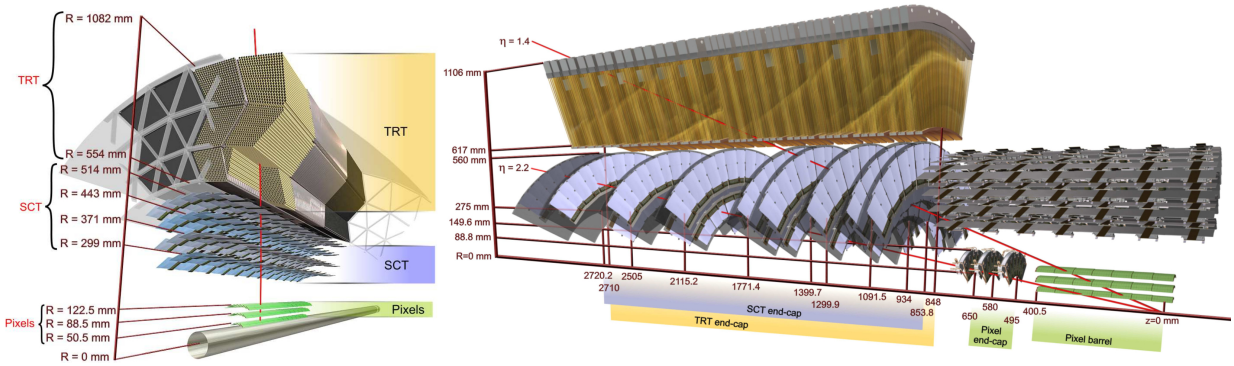

Figure 3.8: Illustration of the ATLAS ID positioning of detector barrel layers, with end-caps wheels. Several sensors and structure elements, with red lines indicating potentially charged particle interaction from the IP. The figure to the left indicates the transverse direction showing the barrel sections, with a particle track transversing the three pixel barrel sections, four Semi-conductor tracker (SCT) barrel layers, and ≈ 36 straw tubes of the Transition Radiation Tracker (TRT). The figure to the right shows a schematic drawing in the longitudinal direction, with two tracks red-colored, interacting with three cylindrical pixel layers in the barrel region, four SCT end-cap wheels, and ≈40 straw tubes of TRT subdetector. The track with a larger $|\eta|$, leads to less interaction with the ID detector. Showing interaction only with one pixel barrels section, two pixel end-cap wheels, and four SCT end-cap wheels, with no interaction through the TRT straw tubes [9], p. 55, 56.

shaped as a cylindrical structure around the beam pipe. The three barrel sections house 1456 pixel modules and the other three end-cap wheels host 288 modules. Totaling 1744 modules that compromise ≈4.7×10^4 Silicon pixels of 50x400 μm^2 in the outer three barrel layers, with three disks.

The innermost section of the Pixel detector, the Insertable B-layer (IBL) [51], was deployed specifically in 2014 before the LHC Run2, to replace the damaged innermost detector layer due to induced radiation damage, and to allow the detection of short-track particles, i.e., the B hadrons and $\tau^{\pm}$ leptons. Resolving close-by tracks in the core of high-transverse momentum jets is essential for excellent reconstruction performance of primary vertices from proton-proton collisions, and secondary vertices decay due to, i.e., the B, charmed hadrons, tau leptons, that is critical for flavor tagging capabilities. Those particles, i.e. decay before reaching the detector and could be identified through the secondary vertices decay products, only if a proper resolution for precise impact parameters [1] are available.

Moreover, the charge deposition due to particle-matter interaction in the pixel Silicon bulk triggers a hit in the intercepted pixel, due to the induced charge carrier's electron-holes pairs along the particle track as will be introduced in Sec.4.2. The pixel module consists of 16 front-end (FE) read-out chips, with one Module Control Chip (MCC) that is responsible for data, commands, and

[1] Tracing paths to the primary interaction point resulting from the decay of a relativistic particle are typically deviated from this vertex by an average distance denoted as "$c\tau$", which is referred to as the impact parameter.

trigger timing each 40MHz. While each module contains 47×10^3 pixels, each single pixel is driven with a single FE independent read-our electronics circuit. In which the FE chip is bump-bonded to the detector substrate. Two types of pixel module architectures are used in the pixel detector, the IBL includes planar sensors of 250x50 μm^2 pixel size with n^+-in-n doped Silicon in the central region, and possesses new architecture of slim edge sensor, to maximize the sensor active area, with a reduction of inactive sensor edge by $900\mu m$. The other pixel design includes the 3D sensors in the forward region, with $n^+ - in - p$ doped Silicon, with specific readout electronics, FE-I3, and FE-I4. In total, the pixel detector including the IBL, has 92.4×10^6 pixels covering a total active area of $1.88 m^2$.

The IBL is the closest part of the ATLAS detector to the IP. Only $3cm$ away from the beam pipe, charged and neutral hadrons are particularly important for Silicon radiation detectors. Usually expressed in units of the equivalent fluence of 1 MeV neutrons, IBL would receive a total fluence of $13.5 \times 10^{14} cm^{-2}$, translated into $790 kGy$ of ionizing dose, imposing a significant challenge to detector performance. Furthermore, the Pixel detector performance could be made more efficient by adapting, i.e., the CO_2 cooling plant by operating at low temperature to compensate the increased leakage current due to radiation damage on Silicon detectors, this will be discussed further in detail in Sec.4.3. However, the current ID will be replaced by its successor the Inner Pixel Tracker (ITk), which will need to cope with an order of magnitude due to high integrated luminosity.

3.4.2.2 The Semiconductor Tracker (SCT)

Surrounding the Pixel detector, the SCT [52] covers the outer radius around the beam pipe, to cover larger areas compared to the Pixel sub-detector. However, different technology of Silicon-based detectors is used, with a similar detection method. Equipped with a rectangular shape, inner-strip distance of 80 μm^2 pitch, $p - in - n$ Silicon doped sensor, the hybrid detector module is $285\mu m$ thick, glued with another identical module back-to-back with a stereo angle of $40 mrad$, which corresponds to about 2.3°. Hence, two active double-sided sensor areas are presented, in which a particle passing through the SCT will leave at least four hits per track. The SCT consists of four cylindrical barrel layers and 9 end-cap disks as in Fig.3.8, housing 4088 modules that cover 60 m^2 with 6.3 million active readout channels. The larger coverage area compared to the Pixel detector requires lower-cost detectors capable also to provide precise measurements in (R - ϕ). Which, the double-sided module of the SCT provides two two-strip hits, by exploiting the overlap angle, a space point created from the intersection of two hits provides a two-dimensional entity of $17\mu m$ precision in the $R - \phi$ tracking plane and a lower resolution of $580\mu m$ in the longitudinal direction along the beam axis. Moreover, the modules are designed to cope with a maximum fluence of $2 \times 10^{14} n_{eq}.cm^{-2}$, lower than the Pixel region as it's positioned away in the outer region around the beam pipe.

3.4.2.3 Transition Radiation Tracker (TRT)

TRT is the last sub-detector system in the ID, which utilizes a different approach for particle detection. As the name sounds, the TRT principle of identification is based on the transition radiation emitted, due to dielectric constants difference between two interface materials. When a relativistic charged particle passes through a solid-like material and gas, the drift tubes of $2mm$ radius and wall thickness of $35\mu m$ work as a drift chamber detector, filled with a mixture of non-flammable gasses Xe, CO_2, and O_2. Hence, the particle ionizes the oxygen inside the straw tubes and results in a measurable electrical signal by electron drifts. However, the drift distance of generated electrons is relatively short, due to the short time of bunch crossing each $25nsec$. The TRT implements calibration methods to meet the tracking resolution required, by estimating the distance of the closest approach of a charged particle to each wire in the TRT detector.

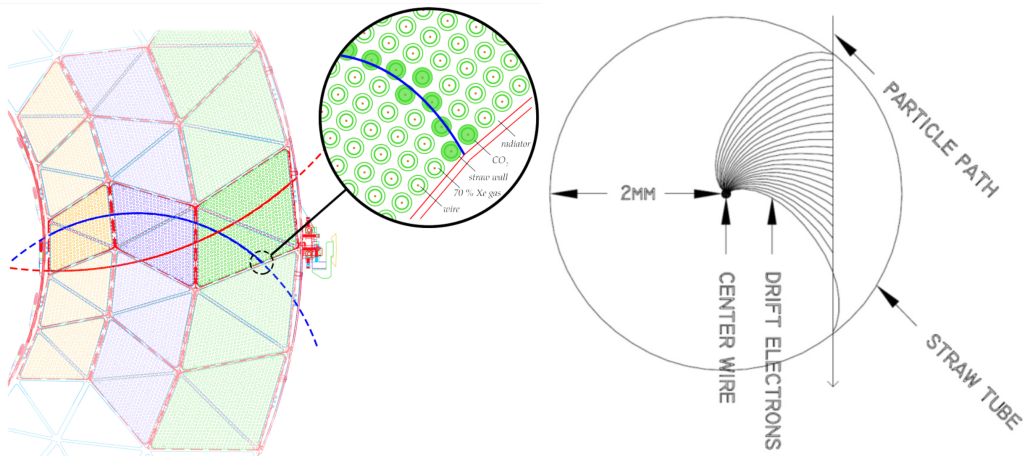

Figure 3.9: To the left a transversal TRT barrel cross-section of particle trajectory passes through straw tubes. The sketch to the right shows how the ionized electrons drift toward the electrode wire in the middle of the tube [].

Moreover, the detection method in TRT [53] is a key system in the ID, as of the ability to identify electrons. As the electron mass is light, they tend to emit more transition radiation at relativistic energies. Due to that, distinguishing electrons from hadrons, or heavier particles like pions is possible through the mean rate of energy loss that depends on the relativistic factor γ given by the Bethe-Bloch equation (Eq.4.8). Hence, the TRT can differentiate between electrons and pions, reaching electron identification of 90%, with misidentification of only 5% for pions. Therefore, the TRT is a unique detector in the ID that is equipped with 400 000 drift tubes organized in layers in the barrel and end-caps regions, covering up to $|\eta| < 2$. For tracking reconstruction, 36 space points are available for a single track with $p_T > 0.5$ GeV within the geometrical acceptance.

3.4.3 The ATLAS Calorimeter System

Calorimeters in HEP experiments are referred to detectors that are capable of not only measuring the position of the particle track but also the energy deposited by the means of absorption. When an incident particle transverses a large volume with an active medium, it generates secondary particles, that subsequently generate showers of particles in the Calorimeter. In contrast to the ID which provides crucial information on the particle momentum and secondary vertices associated with particle decays, the Calorimeter allows a better characterization of the incident particle properties by measuring the position and the direction of energy release while measuring it with a proper energy resolution. Although the measurement process is destructive, the particles are slowed down until they are absorbed, and the energy is converted to a measurable signal. The huge volume of Calorimeters as in Fig.3.10, is needed to stop the particles completely. However, only muons and neutrinos are an exception with other means of detection utilized for them [54].

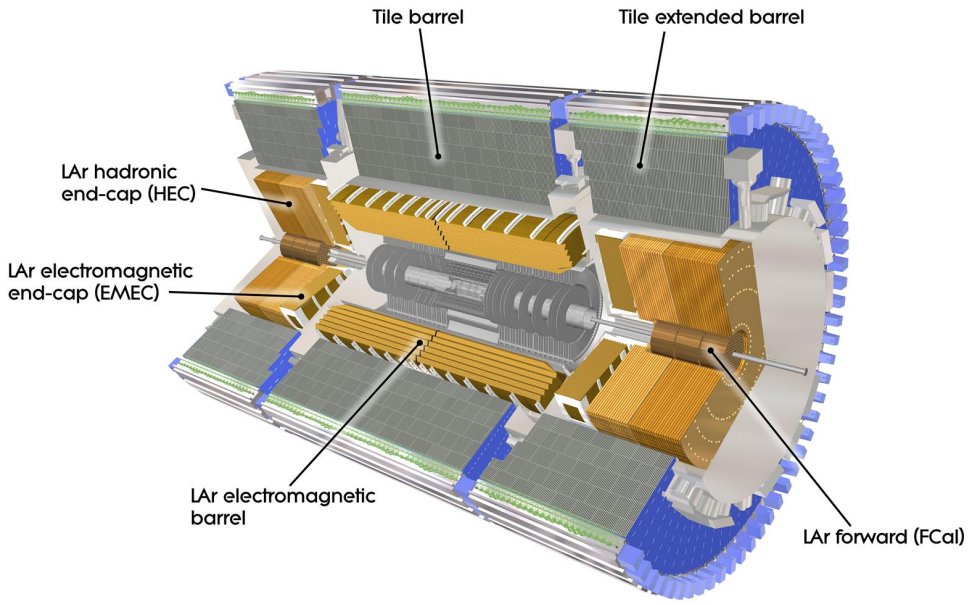

Figure 3.10: ATLAS Calorimeter cut-out view of different components.

Large hybrid detectors as the ATLAS detector are composed of two different types of Calorimeters. Outside of the solenoid reside the Electromagnetic and the Hadronic calorimeters, (ECAL) and (HCAL), respectively [55]. The ECAL measures the electromagnetic showers induced by electrons, photons, and the other measures created showers via the inelastic collisions of hadrons with the nuclei in the material volume. The main goals of ATLAS Calorimeters are summarized as follows:

- **Energy measurement and direction of deposition** of particles interacting with the Calorimeter active volume to measure and reconstruct the particle kinematic properties. In addition, it

separates the electrons and photons from the hadronic particles, while being more sensitive to neutral particles such as photons and neutrons by searching for hits with no correspondent track in the ID.

- **Missing transverse energy** (E_T^{miss}) measurement of weakly interacting particles in the transverse plane to the beam axis. As discussed previously in 3.3, the conservation of momentum could reveal any missing participation of unknown or invisible particles that could be identified in this manner.

The Calorimeters are composed of so-called sampling layers with alternating material composition and radiation length. Sampling layers made up of high-density passive material are implemented to slow down particles, with other active material layers playing the role of energy measurement and signal generation. In terms of pseudorapidity η coverage range, the Calorimeters extend beyond the ID reaching up to $|\eta| < 4.9$ around the beam pipe, allowing a significant contribution to the event construction. Fig.3.11shows the ATLAS Calorimeter system coverage as a function of pseudorapidity η.

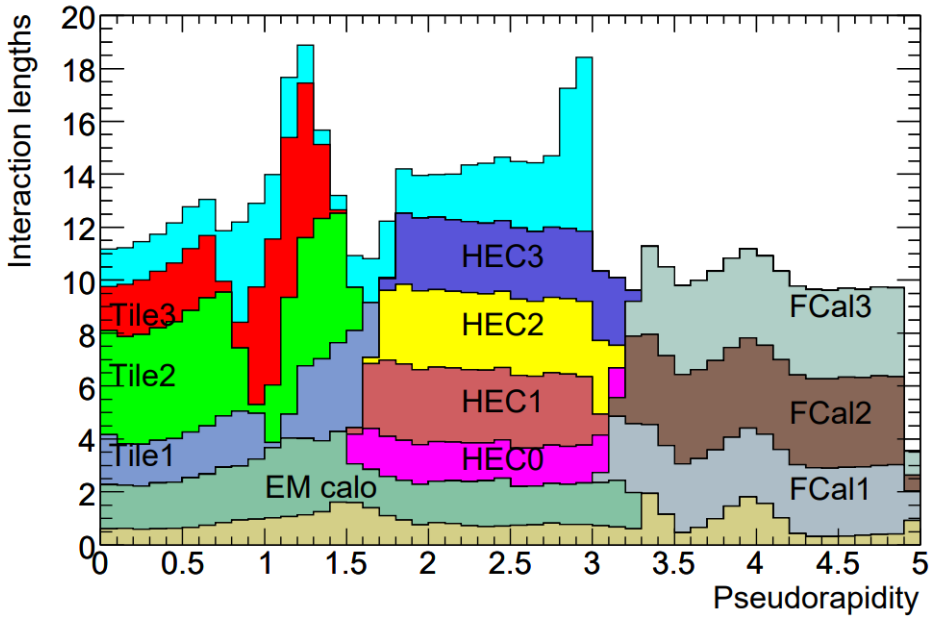

Figure 3.11: A display of the cumulative quantity of Calorimeter material, measured in units of interaction length, as a function of $|\eta|$. It illustrates the distribution of the material in different regions: in front of the electromagnetic calorimeters, within the electromagnetic calorimeters themselves, in each hadronic layer, and the total amount at the end of the active calorimetry. Additionally, for comprehensive information, the graph includes the total amount of material in front of the first active layer of the muon spectrometer, up to $|\eta| < 3.0$ [9], p. 112.

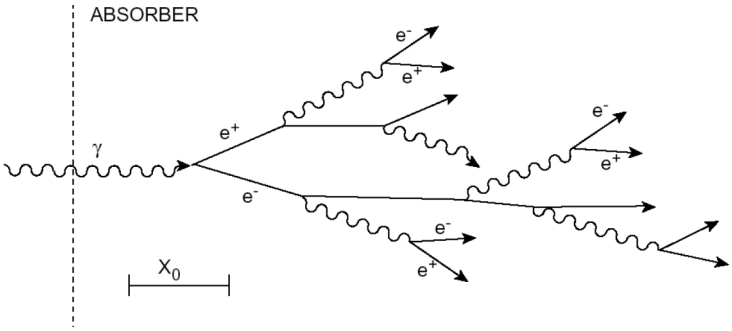

Figure 3.12: A simple model visually depicts the progression of an electromagnetic shower. The x-axis represents the depth of the shower, measured in units of radiation length (X_0). On the other hand, the y-axis illustrates the lateral expansion of the shower spreads, indicating the range of particle distribution [10].

The **Electromagnetic Calorimeter** (ECAL) is composed of absorbing layers with passive lead plates and interleaved with dedicated liquid argon (LAr) as an active material for particle detection. The shape of materials follows an accordion structure as in Fig.3.13, with more than twenty radiation lengths (X_0). When the primary particle interacts with the lead nucleus, secondary particle showers are induced and detected in the LAr active material via the copper grid that acts as an electrode, in which their energy is measured. The liquid argon was chosen for its good linearity as an ionization medium that withstands high voltage, with high radiation hardness and stability over the experiment running. However, the LAr must be maintained in a liquid state using a cryostat at -186.15 degrees Celsius. The key parameter of ECAL is its fractional energy resolution after eliminating the noise, the nominal resolution is [56]:

$$\frac{\sigma_E}{E} = \frac{10\%}{\sqrt{E}} \bigoplus \frac{170MeV}{E} \bigoplus 0.7\% \quad for\ electrons. \tag{3.17}$$

In the course of electromagnetic showers, Bremsstrahlung and pair production are the two main phenomena that characterize the shower's evolution in the Calorimeter. When a primary electron radiates a photon as a consequence of passing through an active material, the photon converts to e^- e^+ pairs, which in return interacts with the medium creating further branches of showers. The fingerprint trail of the primary particle of energy E_0 as it propagates in the calorimeter reveals the depth D in the detecting volume. Through this, the correspondent depth traveled is typically $\frac{E_0}{2^D}$ which becomes less than the required energy to create ionization or electron pairs, hence the showers stop. By this approach, the initial energies of primary particles in each shower branch create lower energy of e^- e^+, resulting in macroscopically observable effects of an event after reconstruction.

The ECAL is divided into different detecting structures, as in the ID. The barrel section has more than 22 radiation lengths and even more than 24 in the end-cap parts. Having an energetic particle

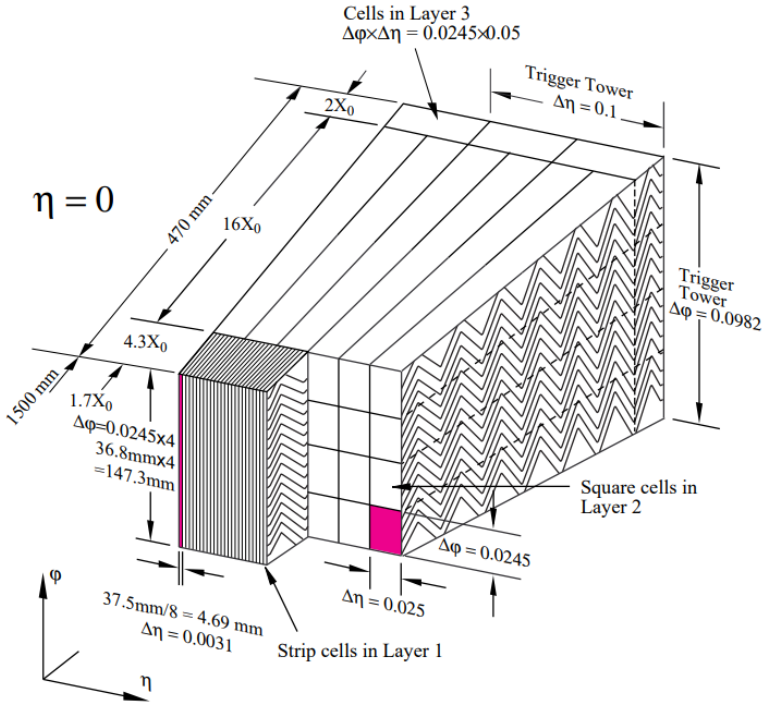

Figure 3.13: Illustration of the accordion-shaped barrel modules within the ATLAS ECAL. The diagram illustrates the granularity in $\eta - \phi$ for individual layers and the trigger tower [9], p. 114.

transversing the Calorimeter results in at least 10 interaction lengths, which leads to a high resolution for event reconstruction. As in Fig.3.11, the dependence of interaction length with $|\eta|$ is shown, where the Calorimeter reveals the largest possible range of measurement over $|\eta|$. The barrel is large in terms of geometry, stretching over 6.4m long, and weighs 114 tonnes, equipped with 110 000 read-out channels. The LAr and lead modules are arranged in an accordion shape, to maximize the absorbing surface.

In contrast, the **Hadronic Calorimeter** is dedicated to the series of hadronic showers created via the inelastic hadronic interaction, i.e. $\pi^{\pm}$, $K^{\pm}$, K^0 with the absorbing material. In the HCAL, secondary particles could undergo further interactions and produce more particles which have the additional complexity of generated hadronic, in addition to electromagnetic showers. This distinguished character of the hadronic showers requires more interactions to get developed.

Due to this, HCAL is considered thicker than the ECAL, and consequently, placed surrounding the ECAL. The barrel region utilizes steel as an absorber and scintillator tiles for detection, segmented into three layers. On the other hand, the end-caps region is less affected by the radiation environment with an active material made up of copper and LAr, with 11 interaction lengths (λ). The nominal resolution of the HCAL is [9], p. 5

$$\frac{\sigma_E}{E} = \frac{50\%}{\sqrt{E}} \bigoplus 3\% \tag{3.18}$$

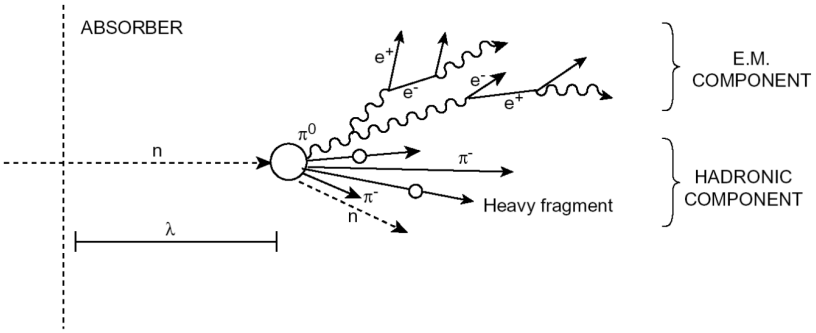

Figure 3.14: Conventional model of a hadronic shower that contains two components, an electromagnetic (EM) component, and a hadronic component. The π^0 decays into γ that create e^+ e^-pairs in the EM branch. The hadronic branch exhibits ionization by charged hadrons, i.e. $\pi^-$and contains invisible energy noted as n that includes nuclear binding energy, neutron scattering, and capture [10].

Furthermore, the HCAL consists of several layers as follows:

The Hadronic Tile Calorimeter (TileCal) [57] is positioned immediately adjacent to the ECAL, and divided into three main sections: a central barrel section covering the range of $|\eta| < 1.0$, and two extended barrel cylinders on each side, spanning the range of $0.8 < |\eta| < 1.7$. The TileCal utilizes steel as an absorber plate incorporates with an active scintillating material. The arrangement consists of three layers placed perpendicular to the beam direction, with a total thickness equivalent to 7.4 interaction lengths. When particles interact with the scintillator material, it generates light, which then passes through wavelength-shifting fibers attached to the scintillator tile. These fibers guide the light to a read-out photomultiplier for detection and data collection. The TileCal is constructed with 64 wedge-shaped modules, each measuring 5.60 meters in length and weighing 20 tonnes. A schematic representation of the module can be found in Fig.3.15(a). This configuration ensures efficient detection and measurement of hadronic particles in high-energy collisions.

The Hadronic Endcap Calorimeter (HEC) comprises two disks located directly behind the ECAL end-caps on both sides of the detector and accommodated within the same cryostat as the ECAL. The HEC extends the pseudorapidity range from $1.5 < |\eta| < 3.2$, overlapping with the forward calorimeter region. Similar to the ECAL, the HEC is designed with copper absorber plates, but with thicknesses of 25 mm and 50 mm instead of lead. These absorber plates are interleaved with 8.50 mm gaps filled with liquid argon (LAr). Each wheel of the HEC consists of 32 identical wedge-shaped modules, as in Fig.3.15(b). The inner radius of the wheel is 2.03 m, while the outer radius is 0.48 m. This configuration allows for effective measurement and detection of hadronic particles in the specified pseudorapidity range.

The LAr Forward Calorimeter (FCal) serves the purpose of measuring both hadronic and electromagnetic interactions. It is specifically designed to cover a high pseudorapidity range, spanning from $3.1 < |\eta| < 4.9$. The FCal has a considerable depth of approximately 10 interaction lengths. Utilizing

LAr technology, the FCal incorporates absorber plates made of copper and tungsten. These absorber materials are specifically optimized to effectively interact with hadronic particles. The combination of LAr technology and the choice of copper and tungsten absorbers allows for precise measurements of energy deposition and interactions in the high pseudorapidity region.

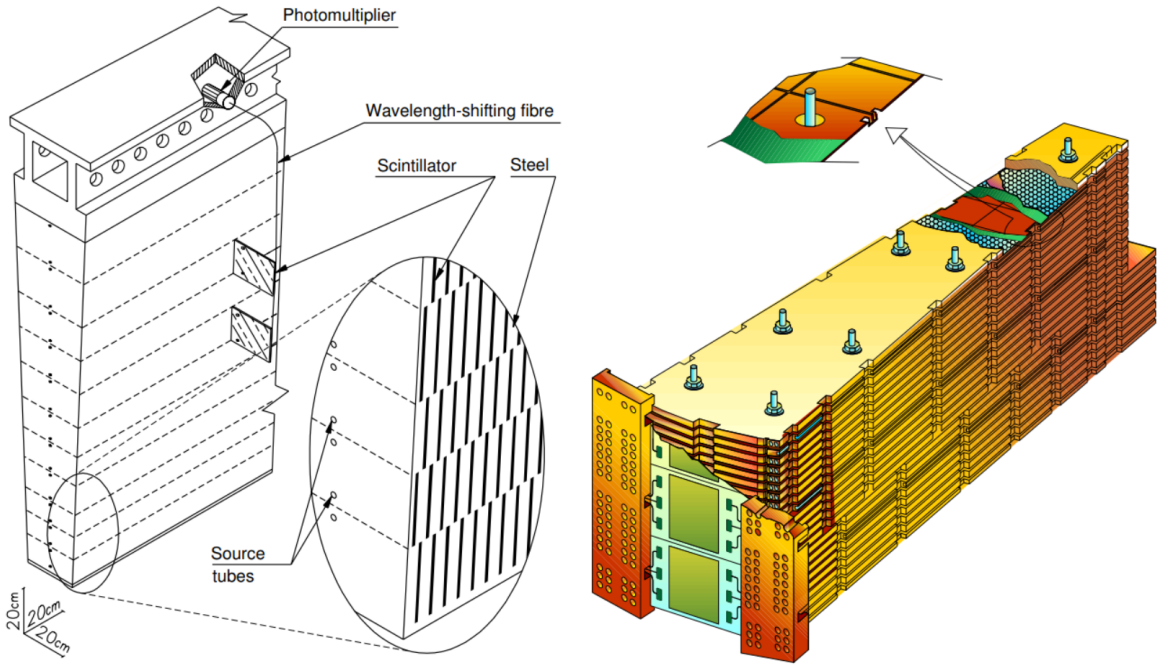

(a) TileCal module **(b)** HEC module

Figure 3.15: Figure A shows the schematic illustrates the integration of the mechanical assembly and the optical readout components of the tile calorimeter. It provides an overview of how the tiles, fibers, and photomultipliers are interconnected within the system. Figure b illustrates a view of an HEC module, showcasing its internal structure and the arrangement of the readout components and active-pad electronics [9], p. 122

3.4.4 The Muon Spectrometer

Most of the particles passing the ATLAS detector systems are either detected or absorbed by Calorimeter. However, muons and neutrinos are able to escape without being detected. Relativistic muons are charged particles heavier than electrons, due to this, they have a much lower energy loss rate and barely emit Bremsstrahlung radiation. They interact electromagnetically by leaving a track in the ID and don't generate any showers in the ECAL or the HCAL. Such a particle is classified as a *Minimum Ionizing Particle* (MIPs) as it loses about 1 MeV/mm in a medium-like steel - see [46] Chapter 30.6 for more information - combined with its long lifetime, and ability to escape the first layers of ATLAS detector, the Muon spectrometer (MS) is placed at the outermost region of the ATLAS detector.

The MS uses four different methods for muon detection. The Monitored Drift Tubes (MDT)

and Cathode Strip Chambers (CSC) are designed for setting precise measurements on the muon momentum with the Thin Gap Champers (TGC) and Resistive Plate Chambers (RPC) for triggering. The RPCs provide trigger identification to complement the other sub-detectors. Covering the barrel part of the MS, it provides pseudorapidity range coverage of $|\eta| < 1.05$ with a timing resolution of below 2nsec for excellent high-energetic muons triggering. On the other hand, TGCs are installed at the end-cap region $1.05 < |\eta| < 2.7$ to contribute to muon triggering at the azimuthal angle ϕ plane. The TGC uses multi-wire proportional chambers with a wire-to-cathode distance of 1.4 mm. The advantage of this detection method lies in the very high time resolution because of the small wire-to-wire distance in the end-cap region.

For track measurements, MDTs provide a coverage range over $|\eta| < 2.7$ with a measurement accuracy of < 50 using gas-filled aluminum tube sensors centered around high-voltage wires. Furthermore, CSCs are multi-wire proportional chambers with segmented cathode plates. Both sub-detector elements of the MS determine the high-p_T muons curvature to evaluate the momentum and charge sign, more information can be found in [9], p. 11,12.

3.4.5 Triggering system, DAQ, and Computing

By considering the LHC bunch crossing frequency of 40 MHz and the substantial number of channels readout channels spread over the ATLAS detector systems, it becomes evident that an enormous amount of expected data rate of ATLAS exceeds the capacity for offline storage. Therefore, an online decision-making system to correlate the detector signals is needed to select only interesting events for analysis and to reject the maximal amount of background. To achieve this, ATLAS employs a three-level trigger system [9], p. 218.

The ATLAS Level-1 (LVL1) trigger operates on a subset of information from the calorimeter, muon detectors, and front-end electronics of detectors. Within approximately two microseconds of latency after the event, a selection decision is made. This initial stage reduces the event rate from 40 MHz to around 75 kHz. Once a positive Level-1 (LVL1) decision is made, the full event data is transferred from the pipeline memories to the Level-2 (LVL2) buffers. The LVL1 trigger decision rate is limited to a maximum rate of 100 kHz, determined by the capabilities of the readout systems. The LVL2 trigger further reduces the trigger rate to approximately 1 kHz by analyzing the regions of interest (ROI) identified by the LVL1 trigger [58]. These ROIs include high-pT electromagnetic clusters, jets, and muons. Most of the sub-detectors and the full granularity of the data are utilized in this stage. With a latency of up to 10 ms, the LVL2 trigger performs complex processing tasks such as track finding in the Inner Detector, measuring their pT, and comparing the energies of the corresponding clusters in the electromagnetic calorimeter.

The events that pass the LVL2 trigger are directed to the LVL3 CPU processors farm for comprehensive event reconstruction, which is achieved within approximately 1 second. This process necessitates a computing performance of around 1 million instructions per second (MIPS). The

selected events are then stored at a rate ranging from 10 to 100 events per second, resulting in a data rate of 10 MB/s to 100 MB/s for an average event size of approximately 1 MB. Consequently, the accumulated data in the ATLAS experiment reaches approximately 1 petabyte (PB) in size.

3.5 The High Luminosity phase upgrades

The enhancement of the LHC luminosity holds significant potential for advancing the scientific capabilities of ATLAS and other LHC experiments. One of the primary objectives of these experiments is to investigate exceedingly rare phenomena, particularly novel indications of new physics. Additionally, the precision of SM measurements would be significantly augmented with increased statistical data as discussed in Sec.3.2. Hence, following the completion of Run3 and the accumulation of more than 300 fb^{-1} by ATLAS, the LHC will undergo an upgrade to start the High-Luminosity LHC (HL-LHC). The HL-LHC is anticipated to commence operations in 2027, marking a crucial milestone in scientific exploration.

To increase the luminosity in the HL-LHC, the LHC ring will undergo several upgrades [59]. The number of protons in the bunches is increased from 1.5×10^{11} to 2.2×10^{11}. Additionally, the beam size is reduced by implementing novel 11 T quadrupole magnets in the final focus systems. This reduction in beam size necessitates a larger crossing angle, resulting in a decrease in the geometrical factor. However, this reduction in R is mitigated by the implementation of crab cavities, which can rotate the bunches longitudinally, enhancing their overlap, see [60] for more information. These advancements in beam manipulation and management are essential for achieving the desired increase in luminosity in the HL-LHC, targeting an instantaneous luminosity of up to $7.5\times10^{34}\ cm^{-2}s^{-1}$ and collecting 4000 fb^{-1} of data in 10 years, ten times more than the total LHC lifetime.

However, such advancements in the accelerator reach create huge challenges for the detector operation. The biggest challenges are attributed to the higher number of interactions per bunch crossing, reaching a pile-up of 200 inelastic collisions with severe radiation levels compared to only 34 in Run2. Vertex trackers, i.e. the pixel detector are particularly very sensitive to the foreseen upgrade, as they are accommodated in the densest environment where radiation levels are at their most. For this reason, a correspondent upgrade on ATLAS ID is essential, as a new all-silicon tracker, called the ITk [12] will replace the existing detector equipped with radiation-tolerant electronics and finer pixels granularity extending the geometrical coverage up to $|\eta| = 4$. Also, trigger and data acquisition (DAQ) systems will be upgraded, to cope with the significant data capacity reach. The foreseen upgrades are planned at the long shutdown after Run3 between 2026 till the end of 2028 as Fig.3.16 illustrates.

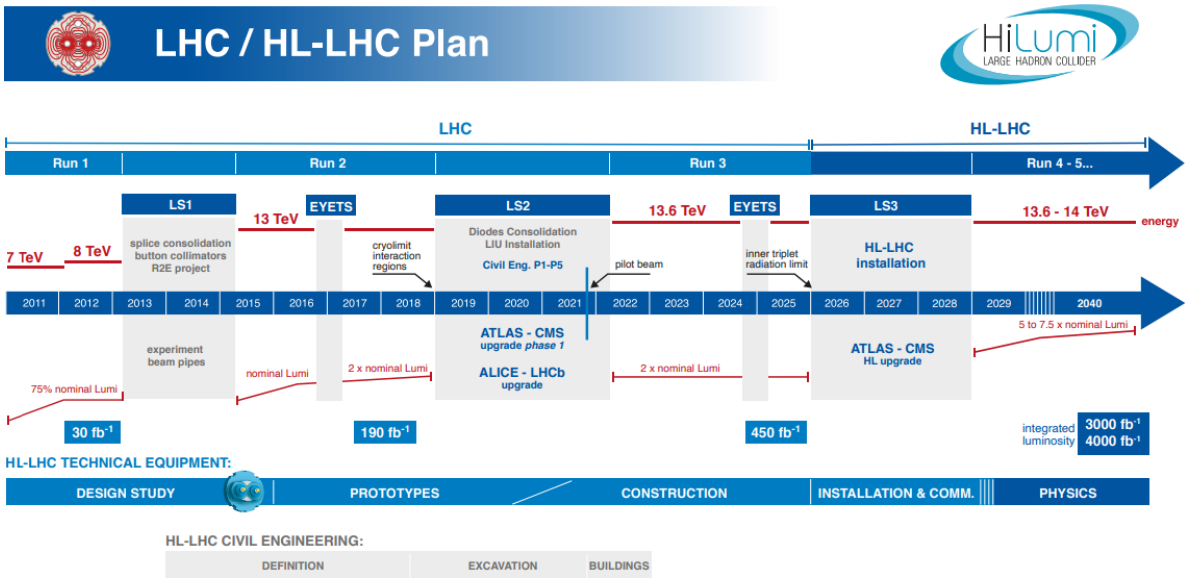

Figure 3.16: LHC road-map schedule and upgrades highlighting the delivered luminosity [11], p. 2.

3.5.1 ATLAS Inner-most detector upgrade for HL-LHC

As previously discussed in Sec.3.4.2, tracking and vertex detector have significant importance in dense particle environments as in ATLAS. However, to cope with the increased luminosity, data rate, and radiation damage in the ATLAS high-luminosity phase, a major upgrade is foreseen for the innermost detector layer located immediately around the LHC beam pipe. Briefly saying, the pixel detector is the only known detector technology presently capable of effectively being operational with high energetic particle densities, extreme radiation doses, and deals with immense data rates at each bunch crossing. The ITk will surpass the ID, with a higher number of readout channels, to cope with a five times higher pile-up than the ID was designed for. Finer Pixel size will be deployed in the new Pixel detector to obtain better tracking granularity by reducing the pixel pitch size from 400x50 μm^2 to 50x50 μm^2 or 25x100 μm^2, with more channels for readout while keeping a high signal-to-noise ratio, and design radiation-hard custom integrated circuits (IC) fast-read-out electronics fabricated in 65nm bulk CMOS technology. The ATLAS ITk pixel detector will be a handful of radiation-hard, high-rate, and granular pixel-size detectors ever built.

Moreover, a significant improvement in the ITk with respect to the ID is the material budget. The complexity of detector systems requires service connections to keep all detector systems operational. In the ATLAS HL upgrade, the material budget including cables, connections, patch panels, support structures, and inactive material will be notably reduced as in Fig.3.17 to comply with the high precision measurement requirements. Also, to remedy a large number of power cables necessary for modules inside the ITk, the read-out chips will be in serial power chains. Furthermore, operating

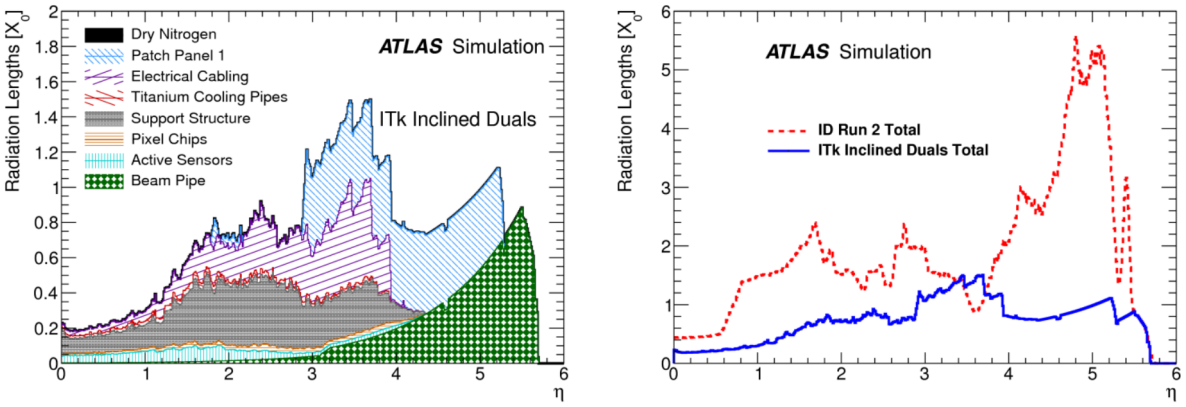

Figure 3.17: Material budget distribution illustrated to the left for the ITk as a function of pseudorapidity with radiation length X_0 of specified materials. The graph to the right compares the distribution of inactive material in the ID and its successor, the ITk, showing a significant reduction of inactive material [12]

within the intense radiation environment near the collision point poses significant challenges for the ITk modules. At an unprecedented rate of collisions, the ITk will be exposed to a dense flux of energetic particles capable of affecting its performance and longevity. Hence, exploring the radiation impact and the measures needed to be taken to address this formidable challenge is essential for ITk. Fig.3.18 presents fluences up to $1.3 \times 10^{16} n_{eq} cm^{-2}$ calculated with the PYTHIA 8 and FLUKA simulations for 2000 fb^{-1} integrated luminosity. Compared to the ID, the ITk will receive at least an order of magnitude more over its lifetime. To mitigate the impact of the high radiation fluence, a design feature has been implemented for the ITk barrel layers 0 and 1, along with their associated end-cap region. These components have been specifically designed to be easily replaceable. It is anticipated that an exchange of these components will likely occur after approximately half of the planned operational duration. In spite of that, outer detector regions have no foreseen replacements as they are not easily accessible and will accumulate only $3.8 \times 10^{15} n_{eq} cm^{-2}$ after 4000 fb^{-1} integrated luminosity.

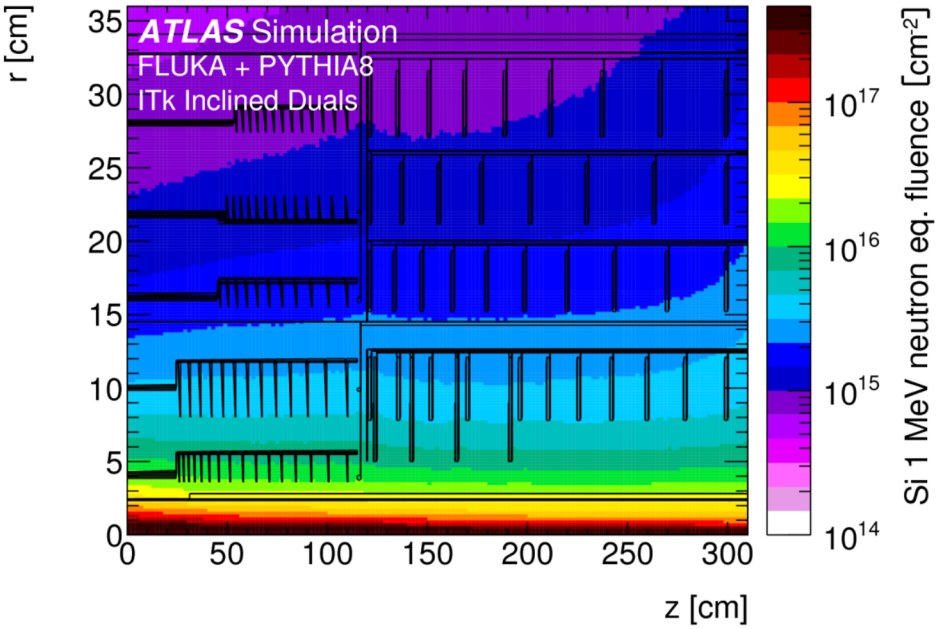

Figure 3.18: Radiation fluences in the ATLAS ITk HL-LHC simulated in terms of 1 MeV neutron equivalent fluence [12], p. 52.

Furthermore, the Pixel read-out chips developed by the RD53 collaboration for ATLAS and CMS experiments will be introduced in Sec.5.2. The ATLAS pixel front-end (FE) chip has been tested, developed, and validated progressively with different prototypes, RD53A, RD53B, and ITkPix chips. The last submitted version ITkPixV2 remarks a decade of continuous relentless research and development (R&D) to deliver a robust and reliable readout chip, to substitute the FE-I4 readout chip used in the ID. The final chip contains 400x384 pixels readout via a differential FE circuit covering ≈ 4x4 cm^2 of 50x50 μm² [61]. Moreover, to resolve data from each bunch crossing with the remarkable pile-up, the nominal bandwidth is extended to reach 1.28 $Gbit\ s^{-1}$ for each FE chip. While having each individual pixel cell read out by an independent electronics FE channel. Thus, the quad pixel module that is constituted of four FE chips reading the pixel detector active area will have 614400 pixels, for only the OB section as in Fig.3.19, made up of ≈4500 modules yields 2.7 billion pixels. Furthermore, scaling up the pile-up and interactions with the sensor active area requires scaling up the bandwidth, which requires in return more power and generates more noise. Hence, the FE digital/analog functionality within the pixels and the periphery must be reliable, and robust against single-event upsets (SEU). In Sec.6.3, tests of single latches within the pixel configuration memories are performed. Single latches are used, i.e., to store the bits within each pixel to adjust the threshold, assisted with redundant latches for recovery in case of SEUs. However, all of these designs require tolerance tests to any potential loss caused by a pile-up and region memory overflow or corruption. Nevertheless, the more stressful challenges in mass-production required for the ITk is the yield and testability of FE logic units first, and second for the bump-bonding between the sensor and read-out

chip. As any single defect found anywhere in the module could be translated into data losses, which is definitely unavoidable. This pressing challenge will be investigated in Sec.8.2 using the RD53A quad-pixel modules used for the outer-barrel (OB) demonstrator project .

Regarding radiation tolerance, the future pixel readout chip is designed to cope with more than 500 Mrad, compared to only 350 Mrad for the FE-I4 in the IBL. However, understanding and mitigating cumulative radiation effects as the total ionizing dose (TID) will be discussed in Sec.6.1.1 via the ring oscillator (ROSC) studies up to ≈ 500 Mrad, assisted with non-destructive single event effects (SEE) studies to examine the radiation hardness of FE electronics with fluences in accordance to the HL-LHC ATLAS innermost layer.

Table 3.1: Comparison between different pixel readout FEs [25], [26],[27].

	ID FE chip: FE-I3	IBL FE chip: FE-I4	ITk FE chip: ITkPixV2
Year	2003	2010	2020
Pixel size [µm^2]	50 x 400	50 x 250	50 x 50 or 25 x 100
Number of pixels	2880	26880	153600
Read-out data rate [$Mb\ s^{-1}$]	40	320	≈ 5120
Radiation tolerance [$Mrad$]	100	350	500
CMOS technology [nm]	250	130	65
Power [$per\ pixel$]		20µA	4µA
Chip size [mm^2]	7.6x10.8	20.2x18.8	20x21

In addition to the expected radiation effects on FE electronics, pixel sensors were designed to cope with a hard radiation environment. Sensor thickness in the ITk ranges from 100 μm in L_1 to 150 μm in the outer layers for planar sensors. Thinner sensors are deployed closest to the IP to allow efficient cooling while fully biased, to compensate for the dissipated power using CO_2 cooling plant. In addition, induced charge-trapping defects through radiation are also reduced by faster charge collection time with thinner sensors. Radiation-related effects such as increased leakage, and doping conversion are also tackled through the innovative design of$n-in-p$ doped sensors that features no type conversion. In addition, a unique property of new modules lies in the active edge technology by producing an edgeless sensor, the inactive material is further reduced allowing for higher tracking efficiency assisted with greater geometrical coverage in the overall detector.

In total, the future all-silicon ITk will consist of five barrel layers at each successive layers ranging from L_0 to L_4 as in Fig.3.19, with an inclined angle to increase the angular coverage. The ITk will house 10000 modules with an active area of $16m^2$, 10 times more than the current ID [43 tasnm] with an increased tracking coverage up to $|\eta| < 4$ as in Fig.3.19. The planar sensors of $100\mu m$ thickness will be used in L_1 and 150 μm for other layers. Moreover, 3D sensors will occupy exceptionally the innermost layer L_0.

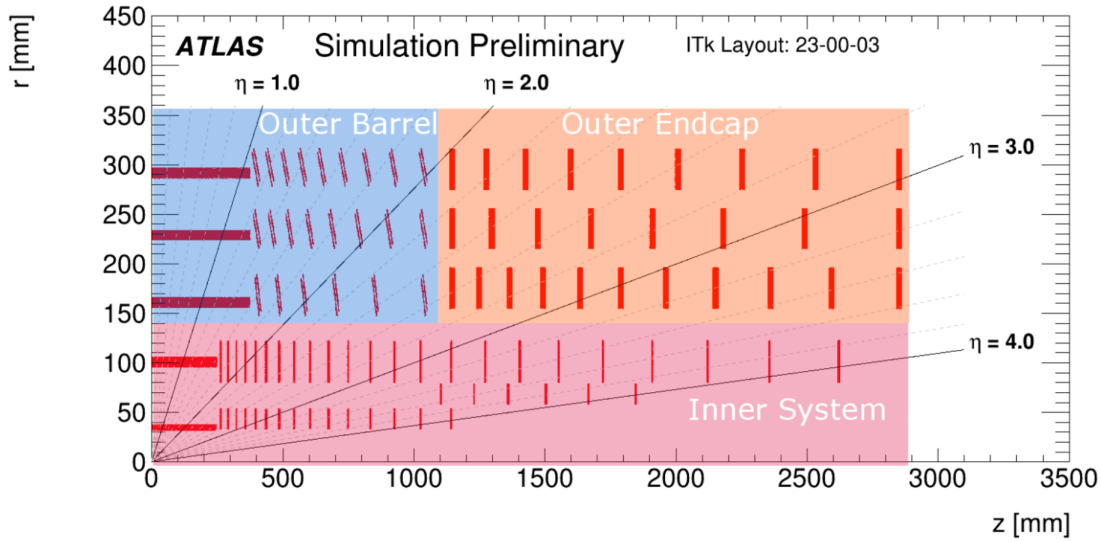

Figure 3.19: Schematic view of only one-quarter segment of the ITk. With zero being the IP, the Strip and Pixel systems extend up to $|\eta| < 4$ [12], p. 8.

3.5.2 The ITk demonstrator project

Large-scale experiments require a proof of concept to demonstrate the system's ability to function as needed. The ITk demonstrator project highlights the early preparation of getting hands-on detector construction, tooling, and quality assurance (QA) in addition to validating the cooling methods, powering chains, distributed control systems (DCS), and other system-related aspects and construction concepts to mimic the ITk detector.

For the ITk, the detector volume is partitioned into two distinct regions: the Inner System (IS) and the Outer System. The Inner System consists of the first two sensing layers (L_0 and L_1) and is designed to be replaceable. On the other hand, the Outer System comprises the remaining three layers and is further divided into a central Outer Barrel (OB) and two identical Endcaps (EC) situated on either side. Moreover, three separate demonstrators are being built for the underlined sections as in Fig.3.19.

The OB demonstrator is the scope of this thesis work focusing on quad-module testing and quality assurance in multiple production stages. Afterward, the module loading process with the design qualifications outlining the local loaded supports (LLS), cooling, and electrical services will be outlined in Sec.8.3. The main goals of the OB ITk project are summarized as follows:

- Validate the design performance of three main elements of the ITk stave. The quad-module, the functional local support, and the mechanical and thermal interface in between using the cell loading block.

- Authenticate the reliability of the cooling method using CO_2 cooling lines through the cell base blocks for each independent quad-module.
- Testify the two different functional local supports. A longitudinal beam-like structure coupled to the CO_2 cooling pipes known as the "Longerons" for the ITk flat section, in addition to the conical half arc known shortly as the inclined half ring (IHR) featured with semiannular cooling pipes in the inclined region.
- Test the on-detector system components with realistic powering supply units (PSUs), dedicated data acquisition system (DAQ), serial powering scheme (SLDO), system services associated with the interlocking functionality, data handling with the conversion from electrical to optical format via the so-called optical box (OptoBox).
- Nevertheless, the OB demonstrator project studies the integration of the cell-loaded module reliability adequately for specified module production stages. In more simplified words, a sophisticated electrical test comparison between single-module tests and an OB demonstrator is conducted to study any potential degradation of performance, as well as to validate the system test environment accordingly.

The OB demonstrator setup will be conducted at the SR1 facility lab at CERN. More details on the qualification of different concepts, while highlighting the experience outcomes in building, operating, and testing the OB demonstrator could be found in Chapter.8.

4

Silicon Pixel Detector Properties

Silicon has played a pivotal role in particle detectors since the 1960s, standing as a widely explored semiconductor across diverse technological domains in industry and has assisted the HEP community. This widespread research has led to a comprehensive understanding and characterization of silicon's electrical properties. In contrast to alternative particle detector technologies like gaseous detectors, boasting an ionization energy of around 30eV, silicon offers a distinct advantage. This advantage materializes in the form of superior energy resolution and a heightened signal-to-noise ratio (SNR), courtesy of its notably lower ionization energy of approximately 3.6eV for electron-hole pair generation.

These unique properties of low ionization energy and robust SNR culminate in the creation of ultra-thin sensors, as thin as 50 μm. This design minimizes the effects of multiple scattering due to lower budget material, rendering silicon detectors exceptionally adept at capturing particle tracks. Positioned in close proximity to the beam IP, these detectors provide unparalleled precision, making them an integral choice for tracing particle trajectories.

Particle detectors comprises several integral components, each playing a distinct role. To facilitate particle interaction and signal generation, a detection medium serves as the foundation. Subsequently, signal processing and conditioning is achieved through the utilization of amplifiers and shapers. Following this, analog-to-digital converters come into play for further signal processing, while digital logic digitizes the detector's read-out process. It's important to note that diverse experiment requirements may dictate varying detector architectures, shaping the integration of these components.

However, detectors can be categorized into hybrid and non-hybrid configurations. In hybrid detectors, the sensitive detection material and the read-out electronics are designed and produced

as separate layer entities on distinct physical devices. This strategy presents notable advantages, enabling optimization of sensor design with the read-out architecture. The flexibility to employ varying semiconductor technologies in sensor and read-out components enhances this approach's appeal. However, it's essential to acknowledge that there are potential drawbacks. Notably, the need for sensor/read-out integration introduces an additional step in joining the two layers to construct a detector within the construction process, translating into increased time and resource investments. As we navigate these considerations, the choice of detector architecture is decided on a careful balance between optimization, practicality, and cost.

In this chapter, we will explore the main enabling key figures of Silicon in the HEP semiconductor devices, and more particularly in the ATLAS ITk.

4.1 Basic Silicon Characteristics

Within lattice structures, the orbits of individual atoms converge, resulting in a phenomenon: shift of energy levels that spawns energy bands. Among these, the Fermi energy emerges as a key characteristic, defining the occupancy probability of energy states through the Fermi-Dirac distribution. A defining point, the Fermi energy corresponds to the energy at which occupancy probability reaches a midpoint. Notably, energy states up to the Fermi energy are fully occupied at an absolute zero temperature of $0K$.

At this juncture, the valence band takes prominence, representing the uppermost fully occupied energy band under $0K$ conditions. As temperature escalates, the potential for electrons to be thermally excited into the higher energy band—the conduction band—materializes, contingent on the energy band structure. Unlike the conduction band's partially occupied states, the lattice structure grants electrons in the conduction band freedom of movement.

A systematic classification based on energy band structure and Fermi energy level emerges and resulting in three main levels of conductivity, yielding: conductors, semiconductors, and insulators. In the world of conductors, the valence and conduction bands overlap, positioning the Fermi energy within the conduction band and allowing electrons to reside there.

Conversely, insulators exhibit a substantial energy gap between the valence and conduction bands, with a Fermi energy above the valence band and below the conduction band. Even at elevated temperatures, the energy gap remains formidable, preventing electron excitation into the conduction band.

Semiconductors, possessing a Fermi energy between the valence and conduction bands, exhibit intriguing behavior. At $0K$, they mimic insulators, but with a narrower energy gap. Silicon, a notable example, possesses an Energy Gap (E_g) of approximately $1.12eV$ [[16], p. 261]. Higher temperatures result in thermal electron excitation to the conduction band, leaving behind unoccupied states referred to as holes. These holes can interact with electrons, either through recombination or other

processes. The balance between the number of electrons in the conduction band (n) and holes in the valence band (p) is maintained for a given temperature, embodying a dynamic equilibrium that underpins the distinctive characteristics of semiconductors.

4.1.1 Silicon Doping

A well-established technique for fine-tuning the characteristics of a Silicon crystal involves the strategic introduction of impurities—a process aptly termed doping. By introducing an atom possessing five valence electrons, an additional energy level emerges in proximity to the conduction band. This supplementary electron, readily prone to excitation into the conduction band, gains the freedom to traverse the crystal with ease. This variant, known as $n-type$ silicon, emerges through the deliberate infusion of numerous donors—impurities that include Phosphorus atoms, often favored for this role.

In a contrasting scenario, a shift occurs when an atom endowed with merely three valence electrons is employed. This type, labeled $p-type$, comes into being through the utilization of elements like boron atoms. The outcome manifests as the creation of an energy level in close proximity to the valence band. An electron originating in the valence band can be nudged into this level, generating a void—a hole—in the valence band. This vacancy, displaying the freedom of movement, mimics an electron in a conduction band but carries a positive charge. Herein lies the essence of acceptor-infused Silicon—embracing a surplus of acceptors.

Through this interplay of these intriguing doping strategies, Silicon crystal engineering is intricately navigated. This manipulation not only enhances the crystal's properties but also paves the way for novel functionalities and tailored characteristics, offering a gateway to a diversified array of particle sensors technologies.

Moreover, the Silicon's electrical attributes through doping are generally expressed by the conductivity (σ) or its resistivity (ρ), as expressed in the following equation [8], p. 7:

$$\sigma = \frac{1}{\rho}, \quad where\ \rho = \frac{1}{q_e N \mu} \tag{4.1}$$

Within this context, the elemental charge is symbolized by q_e, with N representing the dopant concentration, and μ signifying the mobility of the prevalent charge carriers (electrons for $n-type$ silicon and holes for $p-type$ silicon). This mobility establishes a direct proportionality to the velocity at which charge carriers move within the silicon lattice—known as drift velocity—while inversely aligning itself with the electric field. Its value is contingent upon diverse factors, including temperature and the nature of the charge carriers (electrons or holes) in motion.

While an entire Silicon bulk can be doped (referred to as n or p), there exists an equally strategic avenue for localized, highly doped regions—a technique often termed implantation. The application of high implant doping results in n-type or p-type designation, correlating with the doping's nature.

This type of doping, distinguished by its polarity, plays a defining role in shaping the landscape of Silicon's electronic properties.

4.1.2 PN-Junction

In Silicon, the density of charge carriers far surpasses the levels anticipated from particle interaction within the material. Consequently, harnessing Silicon for particle detection necessitates the deliberate reduction of charge carriers. As expounded in the subsequent discussion, this imperative is achieved by a combination of union between n-type and p-type silicon, thereby giving rise to a pivotal pn-junction that forms a detection volume bulk in the Silicon sensor necessary for particle detection.

Within the focus of the pixel planar pn-junction, the fusion of n-type and p-type silicon, enables the dynamic interplay of charge densities. This union initiates electron migration from the n-type domain to the p-type, mirrored by the movement of holes from p-type to n-type territories, a purposeful response aimed at harmonizing disparate Fermi energies. A pivotal outcome emerges as electrons meld with holes in the p-type vicinity, while holes synchronize with electrons in the n-type vicinity, culminating in an expanse devoid of charge carriers and creating a depleted region. Dopant atoms, now settle as stationary charges within this region, acquire a negative charge in p-type silicon and a positive charge in n-type silicon. Within this, a subsequent potential difference materializes, exerting its influence against the diffusion of charge carriers and thus holds the expansion of the depleted region. Thus, the exerted potential in the formed junction is expressed via solving the Poisson distribution:

$$\Delta\phi = -\frac{\rho}{\epsilon_0 \epsilon_{Si}} = \frac{qN_{eff}}{\epsilon_0 \epsilon_{Si}}, \quad where\ N_{eff} = N_A - N_D \tag{4.2}$$

In this context, ρ represents charge density, ϵ_0 signifies vacuum permittivity, and ϵ_{Si}, rated at 11.75, corresponds to the dielectric constant for silicon. The effective doping concentration N_{eff} is characterized as the contrast between acceptor and donor concentrations within their respective regions. Moreover, an equilibrium materializes as the current stemming from charge carrier diffusion aligns with the current originating from the potential difference, establishing a state of thermal balance that signifies a significant juncture. As this is not in interest for particle detection, the pn-junction are typically operated in the so-called reverse-bias mode. In which, the n-type is connected to the positive node, and the p-type to negative one. When the bias is on, the exerted potential via this polarity induces a widening of the pn-junction and creating the desired free charge carriers region that a particle can freely interact with creating the tail of electron-hole pair. The expressions governing the depletion region width are expressed using the following equation [8], p. 41:

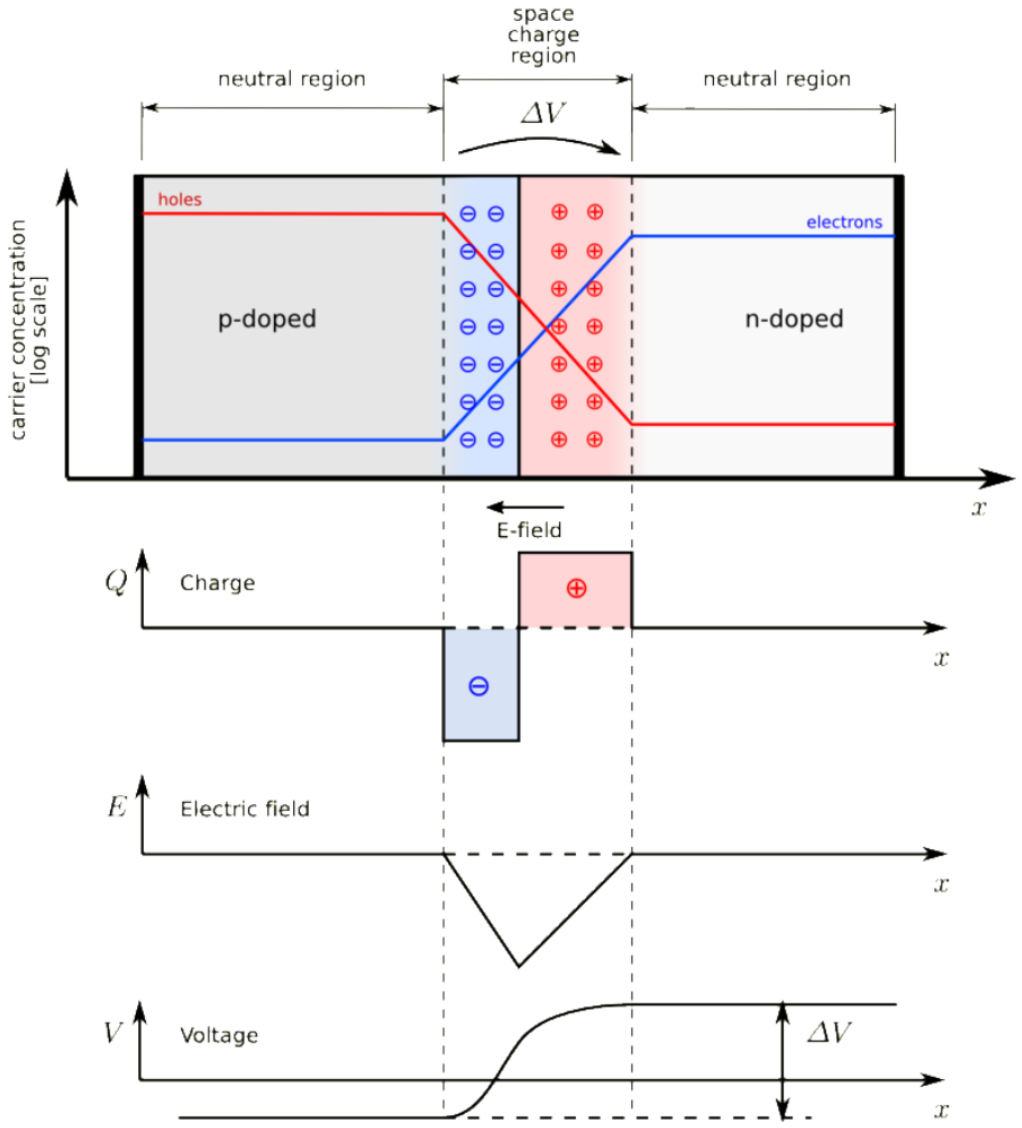

Figure 4.1: A pn-junction emerges at the interface of distinct doping regions. Holes migrate from the p-type material towards the n-region, and vice versa. On the p-side, a negative space charge accumulates, while a positive space charge builds up on the n-side. This interplay generates an electric field with a resultant potential difference known as the built-in voltage V_{bi}, hereby giving rise to a drift current. Within this boundary of doped regions, the depletion zone takes shape, characterized by an absence of free charge carriers [13], edited.

$$d(V_{bias}) = \sqrt{(V_{bi} + V_B \frac{2\epsilon}{e} \frac{(N_A + N_D)}{N_D N_A}} \tag{4.3}$$

Were ϵ represents electric permittivity, e signifies the electron charge, N_A, and N_D respectively denote the acceptor and donor concentrations, while V_{bias} stands for the bias voltage, and V_{bi} for the built-in potential. However, in case of a very high applied bias voltage, the width can be approximated based on the majority of charge carriers concentration in the junction, based on the following equation:

$$d = \sqrt{\frac{2\epsilon V_B}{eN_D}} \tag{4.4}$$

Concerning the sensor's capacity, it can be likened to a plate capacitor. The extent of the depleted sensor volume aligns with the dielectric, while the boundaries of the depleted region mirror the capacitor's plates. As the bias voltage increases, expanding the depletion zone, the capacitance diminishes. Moreover, the sensor capacitance can significantly impact the magnitude of the noise and the readout signal if the depletion zone shrinks. This methodology can potentially highlight defects in bump bonding as will be explained in Sec.8.5.2. However, increasing the bias tends to continue achieving full depletion, resulting in no further impact on capacitance. The distinct capacitance phases are explained in the following capacitance regimes:

$$C \approx \begin{cases} A\sqrt{\frac{\epsilon e N_D}{2|V_B|}} & \text{for } |V_B| \leq |V_{deplt}| \\ \frac{\epsilon A}{D} & \text{for } |V_B| > |V_{deplt}| \end{cases} \tag{4.5}$$

In which D is the depletion region thickness directly affected with bias voltage and A is the surface of the sensor. Moreover, the Silicon detectors exhibit a persistent current, termed as leakage current I_{leak} , which endures even in the absence of a signal. Grasping the nature of this leakage current is pivotal to assessing its impact on the detected signal and comprehending its role in noise generation. The primary source of the leakage current arises from liberated charge carriers generated via thermal excitations within the depleted region. As this effect is proportionate to the volume of the depleted area, it is denoted as volume current I_D, constituting a major portion of the overall leakage current using the following formula [16], p. 284:

$$I_{vol} \propto T^2 e^{\frac{-E_G(T)}{2KT}} \tag{4.6}$$

With T being the temperature, E_G the energy gap, and K the Boltzmann constant. The surface current component becomes apparent as the depleted region extends to the surface of the wafer, generally presenting a smaller magnitude compared to the bulk current. Elevating the bias voltage to significantly high levels initiates the generation of extra electron-hole pairs, triggering an avalanche effect. This phenomenon propels the leakage current to surge exponentially, culminating in a

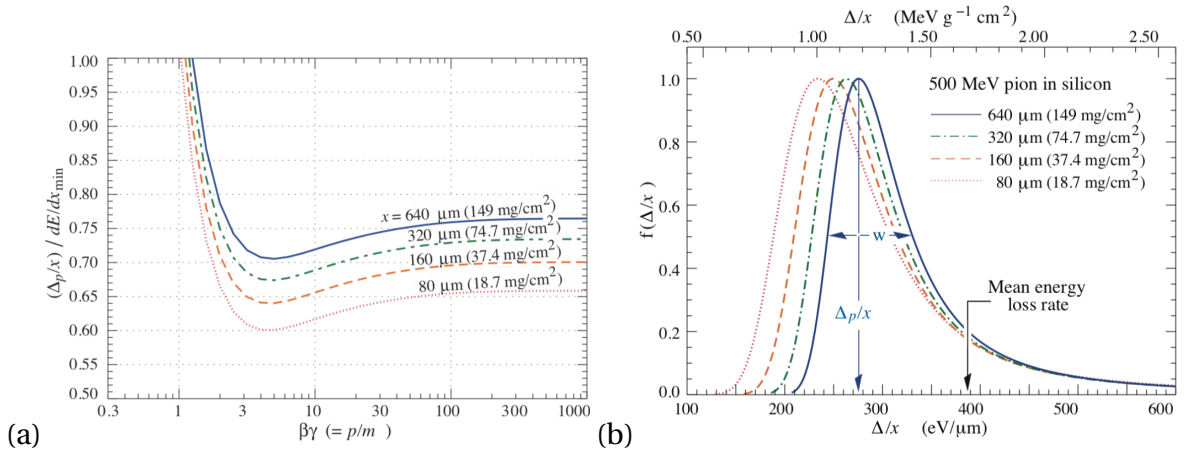

Figure 4.2: In (a), the graph presents the most probable energy loss observed in Silicon, scaled proportionally to the mean loss exhibited by a minimum ionizing particle (MIP), which is equivalent to $388eV\mu m$ ($1.66MeVg^{-1}cm^2$). In Figure (b), an illustration showcases the most probable energy loss resulting from $500MeV$ pions within silicon detectors featuring various sensor thicknesses. The values are normalized to unity at the peak most probable value p/x, while the parameter w denotes the full width at half maximum [14], p. 402, 403.

breakdown that establishes an upper limit on the operational voltage for a device. In addition, in case the sensor isn't fully depleted, the leakage current would scale up with the applied bias voltage and saturate at bias voltages larger than the full depletion voltage. The relation is generally expressed as:

$$I_{Leak} \propto W \propto \sqrt{Vbias} \tag{4.7}$$

4.2 Charge Generation and Particle-Matter Interaction

After introducing the main characteristics of Silicon-based detectors, the interaction within the interaction processes in the Silicon bulk exhibits variations according to particle types and their respective energies. The subsequent discussion generally focuses on generating signals within semiconductors based on many particle types, such as the light-charged particles encompassing electrons and positrons, photons, and heavy-charged particles including muons, and protons. As a charged particle traverses a semiconductor, it initiates the generation of electron-hole pairs along its path within the active detection material. At a temperature of 300K, the average energy required to produce a single pair within silicon amounts to $3.65eV$. When considering particles with intermediate energies, the mean energy reduction along the particle's trajectory within the material is captured by the Bethe-Bloch formula [14], p. 399:

$$-\frac{\mathrm{d}E}{\mathrm{d}x} = Kz^2\frac{Z}{A}\frac{1}{\beta^2}\left[0.5\ln\left(\frac{2m_ec^2\beta^2\gamma^2T_{max}}{I^2}\right) - \beta^2 - \frac{\delta(\beta\gamma)}{2}\right] \tag{4.8}$$

Here, K is defined as $4\pi N_A {r_e}^2 m_e c^2$, where N_A corresponds to the Avogadro constant. When considering an absorber material, the atomic number is denoted as Z, and the mass number is represented by A (for Silicon, $Z_{Si} = 14$ and $A_{Si} = 28$). The quantity $m_e c^2 = 0.511 MeV$ signifies the rest energy of the electron, while β symbolizes the velocity of the traversing particle in natural units. Additionally, $\gamma = \frac{1}{\sqrt{1-\beta^2}}$ embodies the Lorentz factor. The factor $\delta(\beta\gamma)$ captures the density effect correction pertaining to the ionization energy loss, while I denotes the mean excitation energy of $173eV$ for silicon.

Due to the inherently random nature of energy loss, there exists a finite probability that the incoming particle will engage with an orbital electron of an atom. This interaction can result in the ejection of an electron with considerable kinetic energy, triggering secondary ionizations, δ-electrons, or δ-rays. The quantity T_{max} signifies the maximum achievable energy transfer in a single collision event. Moreover, the signal generation for the majority of charged particles is approximated by the introduction of the MIP (Minimum Ionizing Particle) concept, characterized by a $\beta\gamma$ value of around 3 to 4. This specific particle type is capable of traversing the entire active thickness of a silicon tracking detector. Below this threshold, the term $1/\beta^2$ predominantly influences the process, leading to a decrease in mean energy loss as energy levels increase. Conversely, beyond this threshold, the logarithmic term introduces a gradual increase. An illustrative depiction of the most probable energy loss, scaled to the mean loss during minimum ionization, across various silicon sensor thicknesses is presented in Figure a. Moreover, the energy loss encounters substantial fluctuations, resulting in a probability distribution that characterizes the energy loss for a sensor with a thickness denoted as x. This distribution is approximated by the Landau-Vavilov distribution, highlighting the Most Probable Value (MPV) denoted as Δ_p [14], p. 402:

$$\Delta_p = \xi \left[\ln\left(\frac{2m_e\beta^2\gamma^2}{I}\right) + \ln\left(\frac{\xi}{I}\right) + 0.2 - \beta^2 + \delta(\beta\gamma) \right] \tag{4.9}$$

Within this equation, ξ signifies the ratio between the sensor thickness and β. The extended tail observed in the Landau-Vavilov distribution arises from the production of δ electrons, which are generally emitted in directions perpendicular to the trajectory of the incident particle. The release of these electrons results in an average energy loss exceeding the distribution's Most Probable Value (δ_p), contributing to the formation of substantial clusters that, in turn, adversely affect the detector's spatial resolution. Notably, thinner sensors exhibit greater fluctuations around the peak of this distribution.

4.2.1 Signal Formation

An overview of signal propagation and readout in Silicon is provided by examining the dependencies of relevant equations. The signal propagation due to the induced electron-hole pairs generated within the silicon sensor exhibits two modes of movement: drift and diffusion. Diffusion is characterized

based on the stochastic motion of charge carriers within silicon when the influence of the electric field $\vec{E}$ is negligible. During diffusion, charge carriers interact with the silicon lattice or impurity atoms, leading to scattering. A critical factor governing charge carrier diffusion is the mean free path length, which represents the average distance traveled between scatterings. In Silicon, the mean free path length for electrons and holes is approximately $0.1\mu m$ [8], p. 37.

Furthermore, the inherently random nature of diffusion leads to an equilibrium where the net distance traveled by charge carriers on average is zero. However, when a particle traverses the silicon, electron-hole pairs are generated, establishing a gradient of charge carriers. This gradient propels the stochastic diffusion of charge carriers, resulting in an average net distance traveled by charge carriers greater than zero. Consequently, an electric current opposing the charge carrier gradient is generated. However, the drift characterizes the supplementary displacement of charge carriers under the influence of an electric field. The drift velocity, denoted as v, can be defined as a function reliant on the mobility coefficient μ and the intensity of the electric field $\vec{E}$ as follows [[16], p. 98]:

$$\overrightarrow{v_{e,h}} = \mu_{e,h}\vec{E} \tag{4.10}$$

The combined current $J_{e,h}$, generated by the interplay of electron and hole drift and diffusion, can be expressed as a function encompassing various factors including the charge q, mobility coefficients $\mu_{e,h}$, charge carrier concentrations n_e and n_p, the electric field strength $\vec{E}$, and the concentrations of electrons and holes n_e and n_h as described by the following equation [8], p. 39:

$$J_{e,h} = q\mu_{e,h}n_{e,p}\vec{E} + qD_{e,h}n_{e,h} \tag{4.11}$$

The initial component elucidates the motion of charge carriers through drift, while the subsequent component delineates their motion through diffusion, contingent on the diffusion constant $D_{e,h}$. The diffusion constant can be characterized as a function involving the charge carriers' mobility and the temperature T, utilizing the relation [8], p. 37:

$$D_{e,h} = \frac{k_B T}{q}\mu_{e,h} \tag{4.12}$$

Incorporating the Boltzmann constant k_B, this relationship underscores the proportionality between the mobility of charge carriers and their diffusion. As depicted in Eq.4.1, the mobility manifests an inverse relationship with the charge of the mobile carriers, leading to a roughly threefold disparity between holes and electrons. Additionally, mobility is contingent on temperature, influenced by diverse scattering probabilities at different temperatures, as well as on the prevailing electric field. The impact of the electric field can be comprehended by referencing equation 4.10. At modest electric field strengths below $10^3\ V/cm$, mobility remains constant, since the drift velocity scales proportionally with the electric field in this range. As the electric field increases beyond this threshold,

the drift velocity reaches saturation, yielding a reduction in mobility. Standard figures for electron and hole mobility in Silicon are [16], p. 261 at $T = 300K$:

$$\mu_e \approx 1450 cm^2.V^{-1}.s^{-1}, \qquad \mu_h \approx 500 cm^2.V^{-1}.s^{-1} \tag{4.13}$$

Nonetheless, the mobility also hinges on the dopant concentration, resulting in variations across different Silicon materials. It's important to acknowledge that the introduction of a magnetic field alters the trajectory of charge carriers due to the influence of the Lorentz force acting upon them.

4.3 Radiation Damage in Silicon Detectors

As the tracking detectors are positioned adjacent and along the IP, detectors intended for the LHC and the prospective HL-LHC are engineered to sustain operation for approximately a decade within the challenging operational surroundings. A pivotal concern pertains to radiation exposure, which brings about alterations in Silicon properties and results in substantial performance deterioration over time. The impact of radiation damage influences numerous design considerations for detectors used in HEP applications. In Sec.7.4, an irradiated pixel module will be studied in detail compared to a non-irradiated one.

4.3.1 Bulk Damage

When a particle traverses a Silicon sensor, it can disrupt an atom from its lattice position. This displaced atom creates a vacancy within the crystal lattice and can also become an interstitial atom, positioned outside the crystal lattice. These vacancies and interstitial atoms are considered lattice defects. They have the potential to recombine and restore the structure of the Silicon lattice. However, defects can also interact with one another, resulting in the formation of more intricate defects. Additionally, defects can engage with impurities like doping atoms within the material. Moreover, distinct types of particles, each carrying varying energies, generate varying degrees of damage within the material bulk. The Non-Ionizing Energy Loss (NIEL)[1] hypothesis posits that the quantity of defects formed in the Silicon crystal is directly proportional to the energy lost in atom-displacing collisions. By employing the Lindhard partition function $P(E_R)$, it becomes possible to compute the cross section for displacement damage as follows [16], p. 344:

$$D(E)\sum_{\nu}\sigma_{\nu}(E)\int_0^{E_R{}^{max}} f_{\nu}(E,E_R)P(E_R)\,dE_R \tag{4.14}$$

[1]This concept is referred to as the Non-Ionizing Energy Loss (NIEL) equivalent fluence, denoted with units of a 1 MeV neutron flux: $1 MeV.n.cm^{-2}$, or as widely known, $n_{eq}.cm^{-2}$.

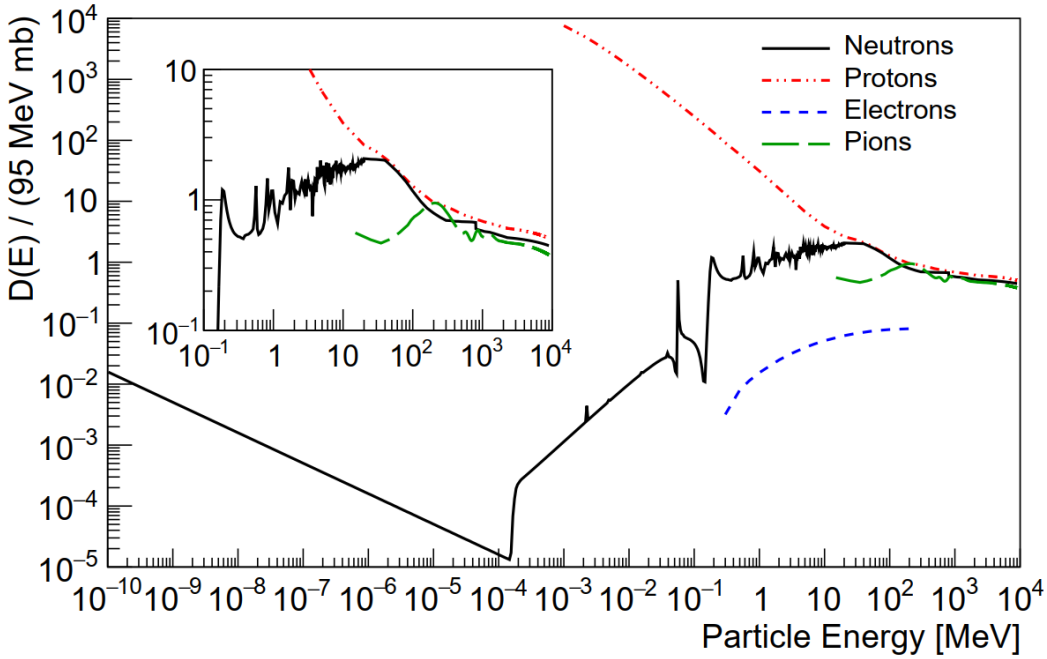

Figure 4.3: The hardness factor calculated for various particles and energies, with the displacement damage cross section $D(E)$ for neutrons at 1 MeV denoted as $95 MeV$ůmb [15] and [**?** **?**].

Here, ν encompasses all potential interactions between the particle and silicon atoms, σ signifies the interaction cross-section, E_R denotes the recoil energy of the Silicon atom, and f_ν represents the probability of displacing a silicon atom.

Utilizing the displacement damage cross-section enables the establishment of a parameter aimed at standardizing damage inflicted by diverse particles of varying energies. This parameter is referred to as the hardness factor k, establishing a connection between the displacement damage caused by a particle with an energy spectrum $\Phi(E)$, as Fig.4.3, and that induced by monochromatic neutrons at an energy of 1MeV as the following equation presents:

$$k = \frac{\int D_E \Phi(E)\, dE}{D(E_{neutron} = 1MeV) \int \Phi(E)\, dE} \tag{4.15}$$

Employing the hardness factor as defined in Eq.4.15, it becomes feasible to standardize the irradiation flux of any given source to the flux of 1 MeV neutrons that would generate an equivalent level of displacement damage []:

$$\Phi_{eq} = k\Phi = k \int \Phi(E)\, dE \tag{4.16}$$

4.3.2 Leakage Current

The detrimental impact of bulk damage on sensor performance manifests through various adverse effects. It results in the creation of deep defects situated near the center of the energy gap, as well as shallow defects positioned close to the valence and conduction bands. Defects located within the energy gap's central region can readily generate electron-hole pairs, consequently elevating the sensor's leakage current []. This increase in leakage current, brought about by bulk damage, exhibits a linear scaling relationship with the NIEL equivalent fluence [[[8], p. 70]].

$$\frac{I}{V_{ol}} = \alpha \Phi_{eq} \tag{4.17}$$

Where V_{ol} represents the volume of the silicon bulk and α is referred to as the current-related damage rate.

4.3.3 Full Depletion Voltage

The full depletion voltage primarily experiences the influence of defects located near the center of the energy gap. Illustrated in Fig.4.4, the full depletion voltage varies with the NIEL equivalent fluence in an n-bulk sensor. Initially, as the NIEL fluence rises, the full depletion voltage declines due to radiation-induced acceptor-like defects counteracting the n-type doping effect. Beyond NIEL fluences of $2 \times 10^{12} n_{eq}.cm^{-2}$, the bulk transitions to p-type, causing the full depletion voltage to rise in tandem with the NIEL fluence. For p-bulk silicon sensors, type inversion doesn't occur, and the full depletion voltage simply increases with the NIEL fluence.

To achieve full depletion in an irradiated Silicon sensor, a higher bias voltage is required. However, practical constraints exist on the maximum bias voltage that can be applied to a sensor. As a result, it might become necessary to operate highly-irradiated sensors with a bias voltage lower than the full depletion voltage. This approach diminishes the quantity of charge carriers collected within the depletion region, thus, declining the detector efficiency.

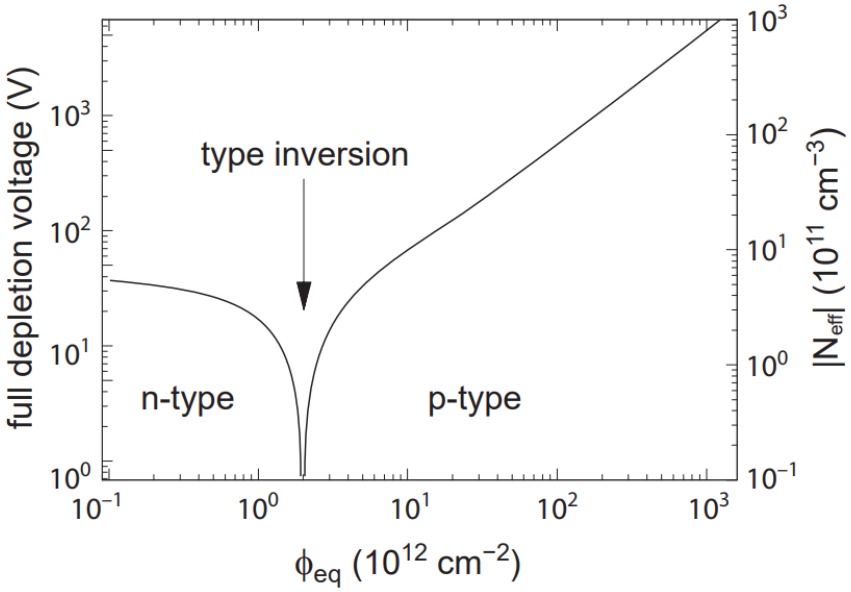

Figure 4.4: Graphing the full depletion voltage against the NIEL fluence in an n-bulk sensor also reveals the effective doping concentration, as indicated on the right axis [16], p. 350.

5

ITk Silicon Pixel Detector Technologies

The localization of positions using Silicon detectors relies on segmented implants, which can be either strip-like for one-dimensional positioning or pixel-like for two-dimensional accuracy, as briefly discussed in section 3.4.2.1. Each implant establishes an independent active sensing pn-junction within the sensor bulk adjacent in spacing between the centers of these implants to form the main key parameter of the Pixel sensor, known as the pixel pitch. Currently, two distinct technologies are utilized for manufacturing pixel detectors: monolithic and hybrid. In monolithic pixel detectors, the readout electronics are incorporated directly into the sensitive sensor volume, providing advantages such as reduced material usage and production expenses. A notable example of devices produced using this approach is the monolithic active pixel sensors (MAPS) [62], exemplified by the Mimosa26 sensors employed in EUDET-type Beam Telescopes in Chapter7.

In the ATLAS pixel Detector and the ITk hybrid pixel modules, layers of such detectors are employed, enabling precise tracking of particle trajectories [63]. Comprising a full hybrid pixel module is the bare module, which constitutes the sensor-readout-chip hybrid, coupled and wire-bonded to a flexible PCB (printed circuit board). Functioning as the connective tissue to the readout system and power supplies, the flexible PCB establishes the necessary links. Additionally, the aluminum wire bonds serve as conduits for signals between the flex and the sensor-readout chip. In the context of hybrid modules, it features a bump bond made up of indium conductive material that connects the sensor and the readout electronics layer. Due to this, the hybrid modules allow the optimization of the FE parts individually to reach the required demands before production. However, pixel segmentation within the sensor is achieved through specialized doping, resulting in each pixel hosting an independent pn-junction that necessitates a separate readout channel. Furthermore, a bump bond connects the gap between the bare sensor and the readout chip.

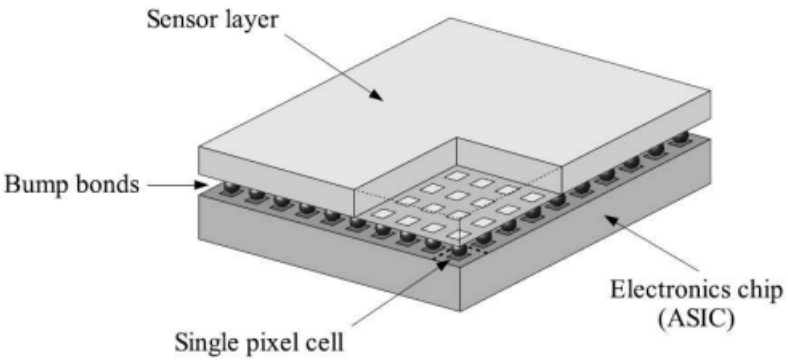

Figure 5.1: Hybrid pixel detector layout [8].

As the thesis covers the current ITk hybrid planar pixel modules attached to RD53A electronic, the following sections will highlight the main parts of ITk planner and 3D sensors, with the associated FE read-out electronics in Sec.5.2. Moreover, the sensor operates in a reverse bias mode to achieve a depleted pn-junction. When particles interact with the detector, electron-hole pairs are generated and subsequently separated, drifting toward the electrodes. This movement leads to the creation of a current, transmitted via the bump bond to the readout chip. The readout chip, in turn, processes and shapes the generated charges for each pixel individually.

The conventional readout chips utilized in pixel sensors, generally consist of a typical readout path that encompasses both analog and digital components. The analog segment includes an amplifier and a threshold discriminator, which yield a pulse whose duration corresponds to the charge signal's magnitude, see [8] Sec.3.1.3 for more information. To ensure consistency among pixels, despite each having its own readout, adjustments are made to the discriminator thresholds and the amplifier's return to baseline, aligning pixel responses. Therefore, one can envisage, for example, an incident X-ray photon that interacts with the detector, it deposits its energy within the sensor material via either the Compton or photoelectric effect. As a result of this interaction, an electron is liberated and gradually expands its energy within the sensor material. Upon reaching a sufficient energy loss, electrons from the valence band can be promoted to the conduction band, leading to the creation of electron-hole pairs. These charge carriers are then separated and guided toward the pixel electrodes via an externally applied electrical potential difference. Typically, a voltage of ≈ 90 V is needed to fully deplete a $150\mu m$ sensor.

On the side of the electrodes, as a consequence of the charge carrier's movement an electrical current is formed within the electrodes. The magnitude of this current can be determined by utilizing the concept of the weighting potential (Ramo Theorem) [13]. The integration over time of the current, shortly known as the time-over-threshold (ToT) within a pixel electrode corresponds to the quantity of

Table 5.1: Main features of the ITk pixel sensors with its related characteristics [12].

	Active Thickness [μm]	Pixel Pitch [μm^2]	Sensor size [cm^2]	Module Type	Position
Planar	100	50x50	4x4	Quad	L_1, R_1
Planar	150	50x50	4x4	Quad	L_{2-4}, R_{2-4}
3D	150	50x50	2x2	Triplets	$R_{0-0.5}$
3D	150	25x100	2x2	Triplets	L_0

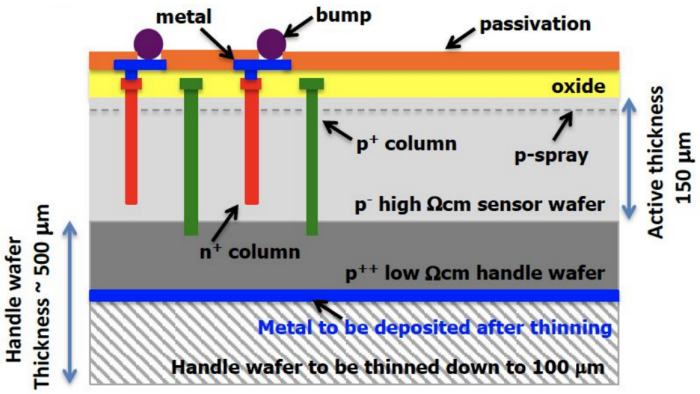

Figure 5.2: 3D sensor layout indicating the active detecting thickness of 150 μm with implemented n+ readout columns.

charge collected. In the case of hybrid modules, this current undergoes pre-amplification. Following this, the conversion of charge to voltage transpires within the preamplifier's integrating capacitance, with the result compared directly to an energy threshold. Moreover, if the pulse surpasses the threshold value, a counter is incremented. For the ITkPix chip, the hit is memorized in the periphery. When the trigger number corresponds to the trigger inside the pixel, the event is recorded and sent to the bottom chip and later sent to the optical link.

On the other hand, the digital portion focuses on measuring the pulse width. Processed data is then channeled to a shared buffer serving several pixels. Given the necessity for a high bandwidth within the detector, parallel readout implementation is imperative for the higher pile-up in the HL-LHC environment [64].

5.1 ITk Pixel Sensors

Two promising types of sensors have been developed for the ITk: 3D sensors and planar sensors, each with its own unique characteristics and manufacturing processes.

Planar sensors are a more traditional type of Silicon sensors, where the electrodes are located on the surface of the silicon wafer. Despite their conventional design, planar sensors have been optimized to withstand the high radiation environment of the HL-LHC. Moreover, two different

configurations of sensor thickness will be deployed at the ITk with 100 μm for the L1 and R1 to reduce the material budget and power consumption, while 150 μm to the outer ITk regions. Another particular significance of the planar sensor is n-in-p classification with p-bulk and n-implants, a strategic choice aimed at retarding degradation under the influence of irradiation. Unlike the n+-in-n sensor configuration adopted in the current ID pixel modules, the n-in-p design ensures that type inversion does not manifest at elevated irradiation doses as discussed in Sec.4.3.3, which will potentially extend the life expectancy of the operation.

The ITk planar sensors are structured with varying doping layers, organized from the sensor's rear side to its top. The bulk of the sensor typically contains one type of doping with concentrations around $\approx 10^{12} cm^{-3}$. Implants on the top and/or backside possess higher doping concentrations, usually exceeding $10^{18} cm^3$, and establish the pn-junction. Since the depletion region primarily extends into the less-doped side, it enables the depletion of the sensor's bulk volume.

For the ITk, planar sensors adopt an n-in-p configuration, where the Silicon substrate is a p-type crystal doped with boron [65]. N-type implants, coupled with aluminum readout pads, constitute individual pixels. An additional p-implant, known as p-stop or p-spray, depending on the type, provides inter-pixel resistance, isolating adjacent pixels. Another p+-doping at the sensor's backside enhances the ohmic contact with aluminum metallization. A passivation oxide layer is applied to the front side, serving as a protective barrier against scratches.

Pixel dimensions are (50×50) μm^2 for sensors with a thickness of 150 μm and (25×100) μm^2 for sensors with a 100µm thickness as in Tab.5.1, particularly in the outer layer of the inner system.

Prior to irradiation, the pixel sensors must exhibit a robust efficiency level exceeding 98.5%. This critical criterion serves as a prerequisite for their reliable performance. Furthermore, even after exposure to irradiation and the ensuing challenges, the pixel sensors are mandated to maintain an efficiency surpassing 97%. This is also needed as a post-irradiation threshold to underscore the durability and enduring functionality demanded of these sensors after a decade of operation, in 7, an evaluation of irradiated planar modules will be introduced. Moreover, to counter any degradation in module efficiency, the irradiated units will necessitate a higher bias voltage, potentially reaching up to 600V. This substantial potential difference between the sensor and the FE chip introduces the possibility of sudden discharges, particularly near the corners of the module that poses irreversible damage to the module. A proactive approach to mitigating this discharge risk involves the electrical insulation of the FE chip and the sensor through coatings of benzocyclobutene (BCB), polyimide, or Parylene. Notably, a coating with a thickness of 3 µm using BCB or polyimide can be seamlessly integrated during the wafer processing stage. A comprehensive characterization with a broad range of electrical scans, production, and testing of 150μm thick sensors will be discussed in 8.

3D sensors represent a groundbreaking advancement in sensor technology [66]. They employ a vertical integration approach, where the electrodes and sensing elements are embedded within the silicon substrate itself. This arrangement enables efficient charge collection and reduces the

distance between the charge carriers formed in the Silicon bulk and the electrodes, resulting in enhanced spatial resolution and reduced susceptibility to radiation damage, due to short travel distance and robustness against charge trapping. The 3D sensors are produced using a process called Deep Reactive Ion Etching (DRIE), which allows the precise creation of small, columnar electrodes that facilitate the vertical charge collection inside the Silicon substrate. In the context of the ITk, at its heart incorporates advanced 3D pixel sensor modules within its innermost layer L_0. These modules are characterized by their meticulously designed pixel cell dimensions, which will take on one of two forms: $25 \times 100 \mu m^2$ for the barrel configuration, and $50 \times 50 \mu m^2$ for the endcap arrangement. Within each pixel, a single read-out electrode will be centrally positioned, accompanied by four strategically placed bias electrodes at the corners. Furthermore, the 3D pixel sensors embrace the single-sided technology paradigm, wherein columns are etched into an active layer measuring $150 \mu m$ in depth made up of high-resistivity p-type material [67]. This active layer is then bonded to another one of low-resistivity (p++) handle wafer that spans 500 μm in thickness. After the process of dicing, the created sensor wafer is thinned down to approximately $100 \mu m$ before embarking on the flip-chip bonding phase with the FE readout chip.

The overall design incorporates ohmic (p+) columns that traverse the active layer and delve into the handle wafer, strategically facilitating the provision of bias from the backside. On the other hand, the readout (n+) columns are limited to approximately $20 \mu m$ length before reaching the end of the active layer. Ensuring isolation at the surface, a p-spray layer acts as a shield for the n+ columns, the overall 3D sensor layout is depicted in Fig.5.2.

5.2 ITk Pixel Front-End Electronics

Each pixelated channel of the sensor is read out by its corresponding FE electronics using a dedicated ASIC design that facilitated the integration of specified electronics in HEP experiments. One hardship in designs is generally attributed to power consumption, data bandwidth, noise, and radiation hardness to assist the measurement quality along the pixel sensors. In the context of this thesis, the ITk FE has been in development since decades to meet the required demands set by the HL-LHC challenges. Moreover, the RD53 collaboration comprising 24 research institutes from Europe and the United States, has been instrumental in the development of the FE readout chip. This chip serves as a shared platform for the pixel detectors in both the ATLAS and CMS experiments in CERN. The evolution of this chip traces its roots back to the RD53A prototype [10], which is the main research interest in module production for the OB demonstrator, and is encompassed by three distinct frontend flavors. This prototype subsequently evolved into ITkPix [11], dedicated to ATLAS with a layout of 400×384 pixels, leveraging the differential frontend approach. Additionally, another FE chip known as CROC was introduced for CMS, featuring 432×336 pixels and utilizing a linear FE design. Furthermore, the submission of version ITkPixV1 readout chip on SCC took place in

March 2020, marking a significant milestone in the development process. Currently, chapter6 will introduce several verification tests on the ITkPixV1.1 to ensure its functionality and performance. Looking ahead, the submission of the final iteration, ITkPixV2, is planned for Autumn of 2023. Moreover, the baseline of the pixel quad modules pre-production chip is ITkPixv1.1. A revised version, ITkPixv1.0, was produced due to imperfections in the chip design. The final chip for the ITk will be ITkPixv2. However, several improvements over the previous RD53a chip, including enhanced serial powering regulators, clocking, triggering and readout scheme, data encoding, and data merging were implemented. Data merging allows up to four ITkPix chips to be connected together to form a quad module.

This iterative approach to chip development reflects the advantages of the hybrid pixel architecture to tackle independently rising issues before flip-chip to pixel sensors. This collaborative effort underscores the shared advancements and testing campaigns to deliver a reliable and robust FE chip. In the context of this thesis, several irradiation campaigns to examine the reliability of ITkPixV1.1 against radiation-induced hard and soft errors are introduced in chapter6.

The **RD53a program** highlighted the main goals within the RD53 collaboration to address and achieve a comprehensive understanding of radiation effects in CMOS technology at the 65nm node, with the primary objective of establishing valuable guidelines for enhancing radiation hardness. The project encompasses several crucial aspects, including the design of a shared radiation-hard intellectual property (IP) library, the meticulous design and characterization of a full-sized pixel array chip, and the development of innovative tools and methodologies to effectively tackle the challenges associated with designing large and complex mixed-signal chips on a large scale.

The project's scope is aligned with addressing the challenges that future pixel upgrades will confront. These challenges encompass various aspects, such as the integration of small pixels with dimensions of 50x50μm^2 (and 25x100μm^2 for larger pixels), accommodating expansive chip sizes of approximately 2x2cm^2 housing an impressive array of around 10^9 transistors, managing high hit rates reaching up to 3 $GHz.cm^{-2}$, accounting for prolonged radiation exposure totaling 500Mrad and 2×10^{16} $neutrons.cm^{-2}$ over a span of 5 years, accommodating a trigger rate of 1 MHz with a 10μs time window requiring efficient buffering and readout mechanisms, and adopting a serial powering approach to optimize power management and reduce multiple scattering and material budget.

Within the RD53A SCC, three different analog frontends (AFEs) are featured as follows [68]:

1. Synchronous Frontend (Syn AFE): This employs a telescopic cascode charge-sensitive amplifier (CSA) featuring Krummenacher feedback. This design facilitates linear Time Over Threshold (ToT) measurements. The chip integrates a synchronous hit discriminator with track-and-latch compensation, ensuring accurate event detection. Additionally, autozeroing circuitry is incorporated to enable precise threshold trimming. The chip's functionality includes a versatile 40-to-320 MHz Fast ToT counter, realized through a latch mechanism. This comprehensive

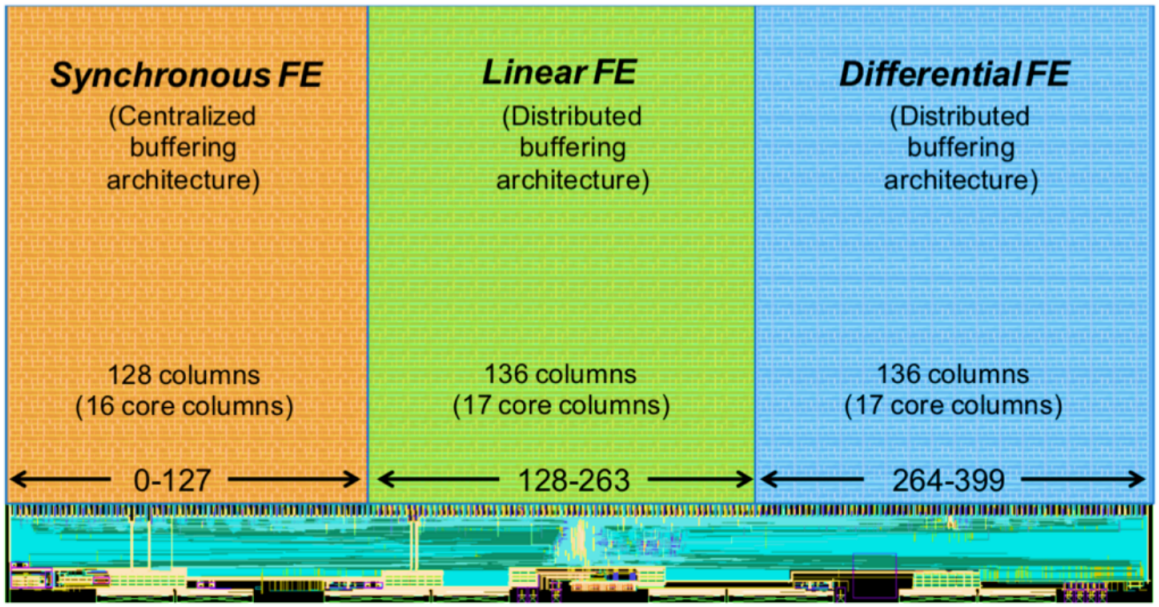

Figure 5.3: Three different analog FE designs for performance comparisons with the same layout area [17].

design enhances the pixel readout chip's performance by enabling synchronous operation, precise event detection, and efficient threshold calibration, all crucial elements for advancing pixel detector capabilities.

2. **Linear Frontend** (Lin AFE): features a single-stage amplification to minimize power usage. It incorporates Krummenacher feedback to handle an anticipated rise in detector leakage current effectively. The chip includes a high-speed, low-power current comparator, along with a 4-bit local DAC for threshold adjustment.

3. **Differential Frontend** (Diff AFE): Is similar to the FE-I4 AFE which utilizes a continuous reset integrator, a two-stage open loop, a fully differential input comparator, leakage current compensation, and threshold adjusting. The continuous reset integrator integrates the charge from the pixel and then compares it to a threshold voltage. The two-stage open loop, fully differential input comparator compares the output of the integrator to a reference voltage and generates a digital output signal. Leakage current compensation compensates for leakage current by adjusting the threshold voltage of the comparator. Threshold adjusting allows for fine-tuning of the threshold voltage for each pixel.

Fig.5.4 provides both the layout and a functional view of the RD53A floorplan. The chip's sensitive region occupies the top section, forming a matrix of 192x400 pixels, each measuring 50x50μm^2 with the three introduced sections of AFEs in Fig.5.3. Positioned at the chip's uppermost part is a row of test pads primarily intended for debugging purposes. Meanwhile, the peripheral circuitry is situated

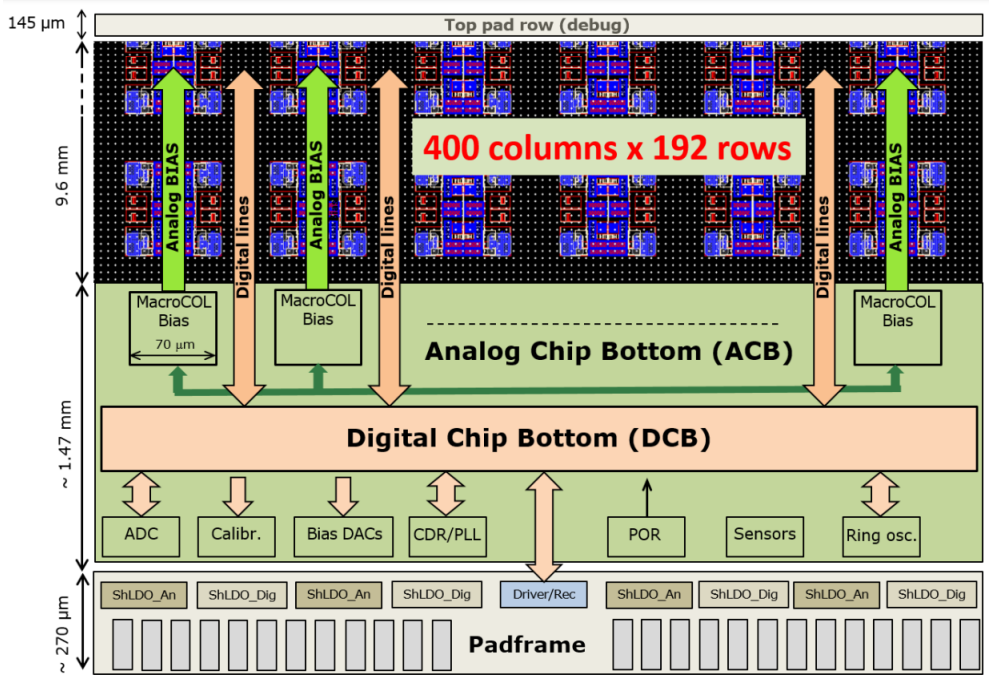

Figure 5.4: The floorplan of main RD53A readout chip components [18].

at the chip's lower portion, encompassing all the necessary global analog and digital components essential for chip biasing, configuration, monitoring, and readout. Besides, the DAC's to characterize the chip performance with the ring oscillators (ROSC) for radiation monitoring purposes are located at the chip bottom. The ROSCs will be studied intensively in 6.

Furthermore, the wire bonding pads are neatly arranged in a single row along the bottom edge of the chip. Notably, these pads are intentionally separated from the initial row of bumps by a distance of $1.7mm$, allowing for wire bonding following the sensor flip-chip process.

Regarding chip power supply, the RD53A hosted an innovative powering scheme for future ITk chips incorporating the shunt-LDO (SLDO) regulators. These regulators are instrumental in maintaining a consistent voltage supply to individual power domains, namely the analog and digital sections, within a serial power chain. This setup is achieved by delivering a constant current to all arranged chips in a single serial powering line. In case of any chip failures, the SLDO shunts the excessive current, hence the name comes from the "shunty" behavior. Nevertheless, since RD53A serves as a prototype requiring flexibility for various measurements, there is also the option to power the chip by directly providing the internal rail voltages, bypassing the regulation stage. Within the chip, two internal voltage rails, namely analog (VDDA) and digital (VDDD), are available for powering the core functions. Moreover, a more detailed behavior of chip powering performance during irradiation, using RD53B prototype, can be found in Sec.6.1.5.

6

Radiation cumulative effects and Single Event Effects (SEEs) studies

Chapter 4 discussed the interaction of particles with materials used in the fabrication of electronic devices, leading to various types of radiation effects. Extensive studies have been conducted to understand these effects across different materials, fabrication processes, and technology nodes in semiconductor electronics.

Effects arise from energy deposited during the interactions between the energetic particles and the materials as in the ITk readout chip. This energy deposition occurs through direct or indirect processes as the particles traverse through the materials. In semiconductor materials, this energy is converted into electron-hole pairs and atomic dislocations as previously discussed in Sec.4.3.1.

However, radiation effects can generally be classified into two categories as in Fig.6.1: cumulative effects on the long-term, and single-event effects (SEE) which are transient effects caused by a single energetic particle event and either temporarily or permanently destructive. Through comprehensive research and analysis, insights into the radiation effects encountered in the readout electronic devices are gained for the future Pixel ITk readout chip, facilitating the development of mitigation strategies and improved designs for enhanced radiation tolerance over the produced prototypes as mentioned in Sec.5.2

Cumulative effects are related to long-term exposition to the radiation environment. This particular effect is dependent on the exposed particle's characteristics and directly influences the charge distribution within a device, resulting in an effect known as total ionizing damage (TID). This phenomenon results in a direct degradation of the device application performance and can shorten the expected lifetime.

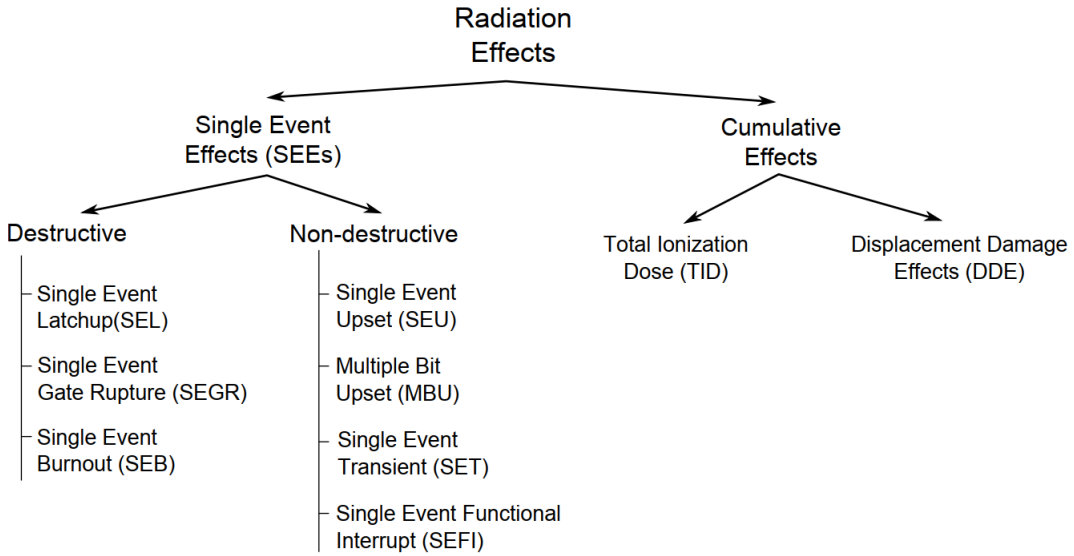

Figure 6.1: Classification of radiation effects in semiconductor-based electronics.

The interaction between ionized particles and semiconductor materials generates electron-hole pairs, which can result in a gradual deterioration of devices. In CMOS transistors, the presence of these newly generated carriers causes a redistribution of charges within the structure. This occurs due to the trapping of carriers at interfaces and gate oxides, leading to alterations in threshold voltages [69].

The cumulative effect of TID also manifests in the progressive degradation of devices. However, it is important to note that TID-induced degradation is often reversible to some extent through the application of annealing techniques [16], p. 358. These thermal processes facilitate a partial recovery of device performance by mitigating the effects of carrier trapping and charge redistribution. By utilizing annealing methods, it becomes possible to alleviate the degradation caused by TID and enhance the overall functionality of semiconductor devices, Sec.6.1.5 will discuss the annealing effect. This underscores the significance of incorporating appropriate thermal treatments to counteract the detrimental impacts of ionizing radiation on semiconductor materials. In this context, TID effects on the ITk Pixel readout chip using the impeded ring oscillators (ROSC) radiation monitoring device will be studied. Assisted with experimental and simulation outcomes to emphasize the temperature, voltage, TID long-term effects, and annealing effects to characterize the Pixel readout chip performance in the ATLAS experiment high luminosity upgrade.

In contrast, the non-long-term degradation effects observed in electronic devices are related to **Single Event Effects (SEEs)** that encompass various phenomena resulting from the impact of individual energetic particles on semiconductors utilized in integrated circuit fabrication. However, Single Event Upset (SEU) is our scope of study in this chapter. SEUs are caused by a soft error that

occurs when a radiation particle impacts a storage element, resulting in its modification that is either a charge or discharge in that element [70]. SEUs can be caused by two different phenomena. Firstly, if the impact takes place in a sensitive node of the storage element, the accumulated charge may be sufficient to alter the value of the stored bit. Secondly, a SEU can occur through the propagation of a Single Event Transient (SET). If a SET arises in a combinational path that terminates in a register, and the clock edge coincides with this SET, the induced pulse is stored and converted into a soft error [71].

The rate of SEUs is influenced by various factors in the electronic device characteristics and the radiation environment related particle properties and fluence. Furthermore, electronic device characteristics including the technology employed, the circuit topology, the design of storage elements, and the system's frequency are important to mitigate the radiation effects [72]. Besides, since SEUs primarily affect memory elements, studies on SEUs predominantly focus on the Pixel registers of the readout chip. These investigations aim to understand and mitigate the impact of SEUs on these critical components, which are fundamental to the reliable operation of Pixel detector and data taking. In that regard, Sec.6.3 will endorse the expected soft errors in the HL-LHC fluence and the experiment conducted at the IRRAD facility using a highly energetic proton beam.

6.1 The Ring Oscillator device

A Ring Oscillator (ROSC) device serves as a fundamental component for radiation monitoring in high-energy experiments (HEP) and read-out chips. The oscillating frequency signal within the ROSC ring plays a crucial role in assessing the impact of external factors such as temperature variations, voltage changes, and irradiation during experimental data acquisition. It provides valuable insights into the overall behavior of the chip in response to these external influences.

The purpose of this study is to evaluate the performance of the ITkPixV1.1 SCC, which is a prototype readout chip for the pixel detector at the ATLAS experiment conducted at CERN. The anticipated upgrade to the High Luminosity Large Hadron Collider (HL-LHC) necessitates higher luminosity conditions ($5 \times 10^{34} \mathrm{cm}^{-2}\mathrm{s}^{-1}$) and an expected total ionizing dose (TID) of 0.5 $Grad$ accumulated in the electronics [73]. Consequently, the electronics in the innermost detector layer of ATLAS will undergo long-term radiation effects and degradation over time. These effects include threshold shifts, increased leakage current, and elevated power consumption, among others.

The focus of this study is on the ROSC block device, which will experience degradation over time due to radiation-induced changes in the propagation delay of the signal within the ROSC ring gates. As the ROSC serves as a radiation sensor, it provides insights into the operational performance of the read-out chip [27], p. 90. By analyzing the behavior of the ROSC, valuable information can be obtained regarding the impact of radiation on the overall functionality of the readout chip.

The upcoming sections will present the methodology for testing the ROSC block and acquiring

valuable information under controlled conditions to study the three variables that affect the ROSC frequency: temperature, voltage, and TID (Total Ionizing Dose). Additionally, the chip undergoes a post-annealing at high temperatures to observe any relaxation effects. The ITkPixV1.1 SCC is subjected to testing in a climate chamber, allowing for evaluation across various temperature ranges while maintaining controlled biased voltage.

To further assess the chip's performance, it is subjected to X-ray irradiation of 16 Krad/min delivering a dose rate over a period of 25 days, resulting in an accumulated dose of 540 Mrad. Subsequently, the chip undergoes annealing for 62 days at high temperatures. To complement the experimental study, detailed simulations using Cadence are conducted to characterize the ROSC's frequency dependency on voltage, temperature, and TID.

Sec.6.1.1 will provide a description of the ROSC device and its associated devices in the ITkPixV1.1 chip. Afterward, Sec.6.1.3 highlights the ROSC circuit simulated using Cadence electronic design automation (EDA) with the results of the frequency dependency analysis with respect to voltage, temperature, and TID presented. Sec.6.1.4 compares the simulation outputs with pre-irradiation experimental data, while Sec.6.1.5 outlines the X-ray irradiation setup, testing methodology, and analysis of TID results. Finally, Sec.6.4 concludes the study by summarizing the findings.

6.1.1 Ring Oscillator Basis in a Nutshell

A Ring Oscillator (ROSC) is a circuit configuration that generates a periodic waveform output. It consists of a series of inverting gates, such as NAND or NOR gates as in Fig.6.2, connected in a closed loop or ring structure. The output of the last gate is fed back to the input of the first gate, forming a feedback loop. The operation of the ring oscillator involves the continuous propagation of a signal through the gates in the ring, with each gate inverting the signal. The inverted signal then proceeds to the next gate, and the process repeats. The period of the oscillator is the time it takes for the signal to complete one full cycle around the ring.

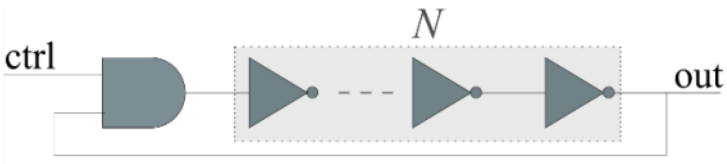

Figure 6.2: Basic ROSC circuit with N number of gates.

The frequency of the oscillator, which represents the number of cycles per unit of time, is the reciprocal of the period. It can be expressed as the inverse of the period:

$$f = \frac{1}{2NT_{pd}} \tag{6.1}$$

Where f is the frequency of the oscillator that can be determined by the number of gates in the ring N, the propagation delay through each gate T_{pd}, and the factor of 2, which accounts for both the low-to-high and high-to-low transitions required for a complete cycle. It is important to note that this equation is valid only when the signal rise time t_r and fall time t_f satisfy the following condition [74], p. 33:

$$2NT_{pd} >> t_r + t_f \tag{6.2}$$

Furthermore, the propagation delay T_{pd} through each gate depends on various characteristics, including the gate's size and threshold voltage. It can be approximated using the following equation:

$$T_{pd} = (K)(C_{load})(\frac{w}{l})(V_{dd} - V_{th})^2 \tag{6.3}$$

While K is a technology-dependent constant, C_{load} is the load capacitance seen by the gate output, w and l are the width and length of the gate, V_{dd} is the supply voltage, and V_{th} is the threshold voltage of the transistors. It's important to note that this equation provides a simplified approximation and does not account for all parasitic capacitances and resistances introduced by interconnections between the gates, which may impact the gate delay. Furthermore, the threshold voltage (V_{th}) at which the transistor starts to conduct relative to the supply voltage can be described by the following equation [75]:

$$T_{pd} = (K)\frac{C_{load}\ V_{dd}}{(V_{dd} - V_{th})^{\alpha}} \tag{6.4}$$

In which α is the power law model, where the equation represents the relationship between the V_{th} and the V_{dd}. This decrease in threshold voltage can lead to faster propagation delays and higher frequency outputs in the circuit.

However, variations in environmental temperature can impact the frequency of the ROSC as they induce alterations in the material properties employed during fabrication. The velocity v of charge carriers within the transistor channels is directly proportional to the applied electric field E between the source and the drain. The mobility μ of carriers within the transistor's bulk region is determined by the equation:

$$\mu = \frac{v}{E} \tag{6.5}$$

Furthermore, the carrier mobility in the transistor bulk expressed as a function of temperature is given by [76]:

$$\mu(T) = \mu(T_0)(\frac{T}{T_0})^{-k_\mu} \tag{6.6}$$

In which k_μ is a fitting factor dependent on the transistor characteristics ranging from $-1.2 \approx -2$, T is the absolute temperature, and T_0 is the reference temperature. It should be noted also that the V_{th} is related to temperature using [77]:

$$V_{th}(T) = V_{th}(T_0) + k_{V_{th}}(T - T_0), \quad k_{V_{th}} = 1 - 2\ mV/K \tag{6.7}$$

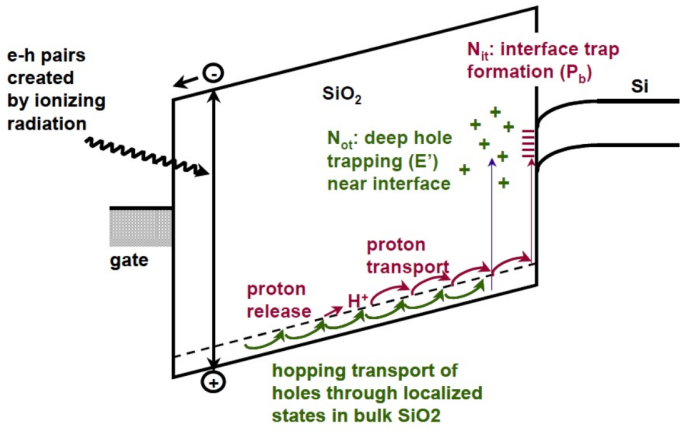

Figure 6.3: Band diagram for a positive gate bias showing a radiation-induced electron-hole pair generation with bulk hole and interface trapping [19].

Consequently, with an increase in temperature, both the mobility (μ) of charge carriers and the threshold voltage (V_{th}) decrease. This leads to a higher propagation delay (T_{pd}) according to Eq.6.6, resulting in slower transistor switching speeds. As a result, the increased propagation delay T_{pd} leads to a decrease in the frequency of the ROSC. Nevertheless, in the context of Pixel detector modules and the associated operation of FE readout electronics in the presence of radiation-induced damage caused by high-energy particles, such as protons, neutrons, electrons, or heavy nuclei, poses a significant challenge [12], Sec. 4.3.1. In the case of the HL-LHC, the proton-proton collisions are expected to result in such radiation effects due to accumulated TID of 0.5 $Grad$, which can lead to changes in the threshold voltage, carrier mobility, and oxide charge trapping, ultimately degrading the performance of the ROSC.

In our study, we will focus on the interaction of photons with the Silicon transistor bulk, aligning it with the experimental setup involving an X-ray tube. This will allow us to investigate the major TID damage mechanisms associated with photon interactions. When photons interact with the oxide gate and the isolation dielectrics, they generate electron-hole pairs. These pairs can either recombine or become trapped within the transistor. The extent of recombination depends on the applied electric fieldIn the absence of supply voltage offsets to counteract TID-induced degradation over long-term exposure, cumulative radiation doses can lead to charge-trapping phenomena, further affecting the performance of the ROSC.

During irradiation, holes can become trapped in micro-structural defects or pre-existing traps within the oxide layer, resulting in two main charge-trapping mechanisms [78]: changes in the total oxide-trapped charge ΔV_{ot} and the total interface-trapped charge ΔV_{it}. The accumulation of positive oxide-trapped charges ΔN_{ot} is attributed to the shift in the Fermi level to the mid-gap ΔV_{mg}, which can be expressed as [79]:

$$\Delta V_{ot} = \Delta V_{mg} \tag{6.8}$$

Hence, the total increase of Oxide-trapped numbers at the mid-gap is given by:

$$\Delta N_{ot} = -C_{ox}\frac{\Delta V_{ot}}{qA} \tag{6.9}$$

Where C_{ox} represents the oxide capacitance and A denotes the gate metal contact area. However, the presence of interface-trapped charge ΔN_{it} depends on the position of the Fermi-level within the band-gap. The assessment of the increased number of interface traps between mid-gap and flat-band voltages ΔN_{it} can be calculated as follows:

$$\Delta N_{it} = C_{ox}\frac{(\Delta V_{fb} - \Delta V_{mg})}{qA} \tag{6.10}$$

Finally, the voltage threshold shift ΔV_{th} caused by TID effects [80]:

$$\Delta V_{th} = \Delta V_{ot} + \Delta V_{it} \tag{6.11}$$

$$\Delta V_{ot,it} = \frac{-1}{C_{ox}t_{ox}}\int_0^{t_{ox}} \rho_{ot,it}(x)\,x\,dx \tag{6.12}$$

$\rho_{ot,it}(x)$ represents the charge distribution of the radiation-induced oxide-trapped holes or the interface-trapped charges, while t_{ox} denotes the oxide thickness.

6.1.2 ITkPixV1 Single Chip Card ROSC's

The ITkPixV1.1 SCC incorporates 42 ring oscillators with a diverse range of digital gates technologies and gate lengths, distributed across 6 banks as indicated in Tab.6.1. The purpose of the ROSC block is twofold: to perform radiation monitoring and to evaluate the impact of pixel injection capacitance on the output frequency using capacitive-loaded ROSC. Additionally, the ROSC drives a 12-bit counter, capable of recording output values up to 4095 counts, with an additional 4 bits allocated for start/stop pulses. More information can be found in RD53B manual [27].

6.1.3 ROSC's Simulations with Cadence

In order to comprehensively study and accurately assess the performance of the ROSC, the Cadence software was employed for designing, implementing, and simulating the analog circuits. The wide range of simulation options offered by Cadence allows for the inclusion of layouts, schematics, and verification tools. Through these simulation tools, the performance of the ROSC can be thoroughly verified by measuring key parameters such as frequency and propagation delay, as presented in this section. Temperature, voltage, and TID will be evaluated in Cadence, with a full consideration that in real experiments, the three effects with annealing would contribute collectively to the ROSC output.

Table 6.1: ROSC technologies type with number of gates for each block in RD53b chips [27].

ROSC Number	ROSC type	Number of gates	Bank group
0&1	Strgth. 0 Inv. Clk Driver	38.2	B Left & right
2&3	Strgth. 4 Inv. Clk Driver	44.5	B Left & right
4&5	Strgth. 0 Inverter	38.1	B Left & right
6&7	Strgth. 4 Inverter	44.3	B Left & right
8&9	Strgth. 0 4-Input NAND	12.6	B Left & right
10&11	Strgth. 4 4-Input NAND	16	B Left & right
12&13	Strgth. 0. 4-Input NOR	14.5	B Left & right
14&15	Strgth. 4. 4-Input NOR	14.5	B Left & right
16&17	Strgth. 0. Scan D-flip-flop	6.1	FF Left & right
18&19	Strgth. 1. D-flip-flop	6.2	B Left & right
20&21	Strgth. 1. Neg. edge D-flipflop	5	FF Left & right
22	Strgth. 9 LVT inverter	40.6	LVT
23	Strgth. 4 LVT inverter	56	LVT
24	Strgth 0 LVT 4-input NAND	16.5	LVT
25	Strgth 4 LVT 4-input NAND	22.8	LVT
26-33	Strgth. 4 Inj-Cap 4-input NAND	16.8	CAPA
34	Strgth. 0 inv. Clk. drvr.	55	Bank A
35	Strgth. 4 inv. Clk. drvr.	51	Bank A
36	Strgth. 0 inverter	55	Bank A
37	Strgth. 4 inverter	51	Bank A
38	Strgth. 0. 4-Input NAND	19	Bank A
39	Strgth. 04 4-Input NAND	19	Bank A
40	Strgth. 0. 4-Input NOR	19	Bank A
41	Strgth. 4. 4-Input NOR	19	Bank A

Additionally, simulations are conducted to investigate the effects of supply voltage variations, V_{dd}, in the typical range of the ITkPixV1.1 SCC, ranging from 0.9V to 1.2V with a step of 0.1V. These simulations also take into account temperature variations within a wide range, covering -20°C to 60°C, considering the low expected operating temperature as mentioned in Sec.6.1.4. Two simulation approaches are employed, where one parameter is kept constant while analyzing the effects of the other factors on the threshold voltage, propagation delay, and frequency of the oscillator.

Furthermore, TID simulations are conducted using the available TSMC 65nm process design kit (PDK) tools, employing the Radiation Model 2019 developed by CERN [81]. These simulations are based on testing approximately 100 devices designed in a special test chip with different sizes per type for linear and enclosed gate transistors, using X-ray irradiation. A summary of the model capabilities is shown in Tab.6.2. However, it's important to note that the scope of our simulation analysis does not include the consideration of annealing effects.

TID modeling will focus on a standard V_{th} with a Typical process corner. The effects of TID

Table 6.2: Available simulation approaches for the ROSC device.

Transistor	Layout	Process	V_{th}	Temp. [C°]	TID [Mrad]
p,nMOS	Enclosed, Std. gate	Typical, fast, slow	Low, Std. , High	-30, 0, 25	100, 200, 500

will be examined while varying the temperature with V_{dd} fixed at 1.2V. As depicted in Fig.6.4, the simulation shows the pre-irradiation at 0 TID, the accumulated dose causes a degradation in the frequency output. Notably, the output degradation is more pronounced at 25°C.

6.1.4 Pre-irradiation Experimental validation

To corroborate the simulation outcomes obtained through Cadence, we conducted an irradiation campaign in collaboration with CPPM, at the Institute Materials Microelectronics Nanoscience of Provence (IM2NP) on two ITkPixV1.1 SCCs. In this section, we will outline the essential pre-irradiation tests utilizing the SCC within a climate chamber and elaborate on the irradiation campaign plan. Additionally, we will present post-irradiation annealing at low temperatures to deduce the ROSC performance, as expected in the HL-LHC.

6.1.4.1 Temperature Tests

The ITkPixV1.1 SCC is biased with 1.22V and placed inside a climate chamber as in Fig.6.5 to facilitate temperature dependency tests. The ROSC outputs were acquired using a Keithley data acquisition system in addition to supply voltage V_{dd} sensing lines were fed back to the power supply to ensure stable bias conditions. ROSC readings were obtained in steps of 10°C, covering a range from -40°C to 60°C. A selection of ROSC was analyzed to investigate the output's dependence on temperature. The simulation results, represented by dashed lines, were compared with the experimental data for several ROSC in bank A of the ITkPixV1.1 SCC. As in Fig.6.6, the decrease in frequency with increasing temperature was observed in both simulation and experimental data, showing a consistent trend for all ROSC. It's important to note that the offset between simulation and experimental data was attributed to a mismatch in the supply voltage, where a higher bias was applied during the experiment, compared to 1.2V acquired with Cadence simulation.

6.1.4.2 Supply Voltage Tests

Proper device bias is crucial in assessing the overall performance, particularly since the ROSC is utilized in the ITkPixV1.1 for radiation monitoring. The supply voltage V_{dd} plays a significant role in determining the output, as represented in Eq.6.4. Addressing the frequency-to-bias dependency and sensitivity is vital to mitigate the effects of TID accumulation during prolonged operation, such as

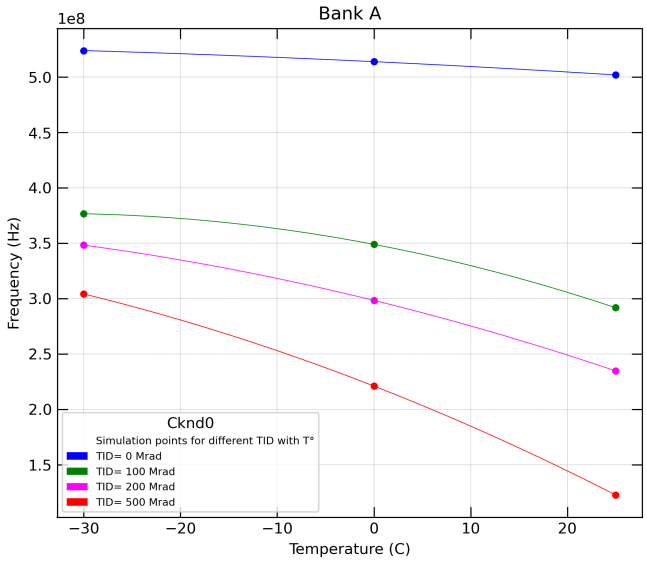

(a)

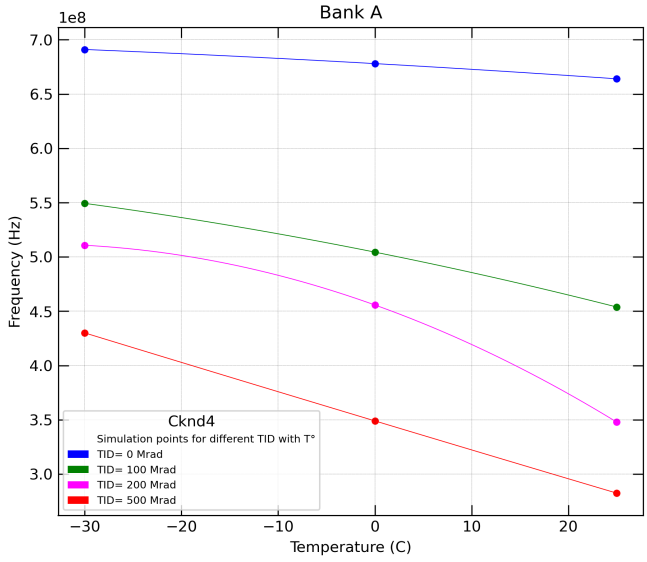

(b)

Figure 6.4: (a) Simulated frequency output of Cknd0 ROSC from bank A. The figure shows the evolution of frequency in terms of temperature and TID. Pre-irradiation value at 0 TID reveals a slight decrease in frequency as the temperature increases. However, at higher TID values frequency decreases significantly at 25°C. (b) On the other hand, Cknd4 ROSC shows higher frequency output due to lower number of gates as in table xyz. Moreover, the frequency declines with increasing temperature and TID.

(a) a (b) b

Figure 6.5: (a) ITkPixV1.1 SCC test bench. (b) Climate chamber for low-temperature testing, with the SCC inside.

in the HL-LHC. Experimental data obtained from various ROSC, alongside Cadence simulations at the same temperature, are evaluated in Fig.6.7 to gain insights into this frequency-to-bias relationship. Furthermore, previous studies have indicated that the bias-to-frequency sensitivity undergoes changes between pre and post-irradiation conditions. Fig.6.8, reveals the V_{ddd} and V_{dda} voltage sensitivity by modifying the corresponding register value for pre-irradiation. Moreover, this study [82] indicates that sensitivity changes with irradiation.

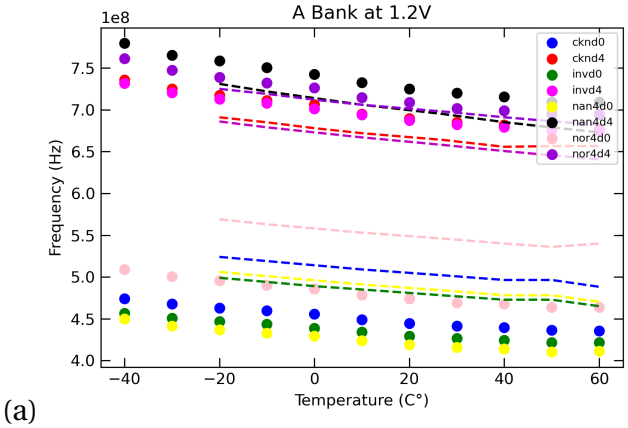

(a)

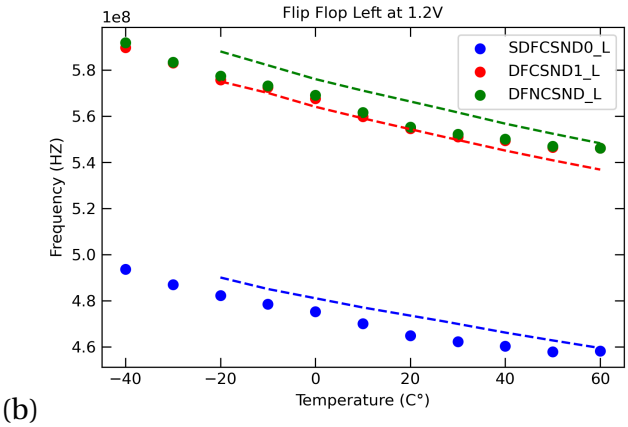

(b)

Figure 6.6: (a) Bank A ROSC's frequency evolution as a function of temperature changes with a constant V_{dd}. Experimental data acquired inside the climate chamber are presented as solid points. In addition, dashed lines represent simulated ROSCs with Cadence. Comparison between simulation and data shows an offset between Strgh. 0 and 4 ROSCs. (b) Flip Flop ROSC's block biased at 1.2V with frequency evolution plotted using experimental data and simulated by Cadence.

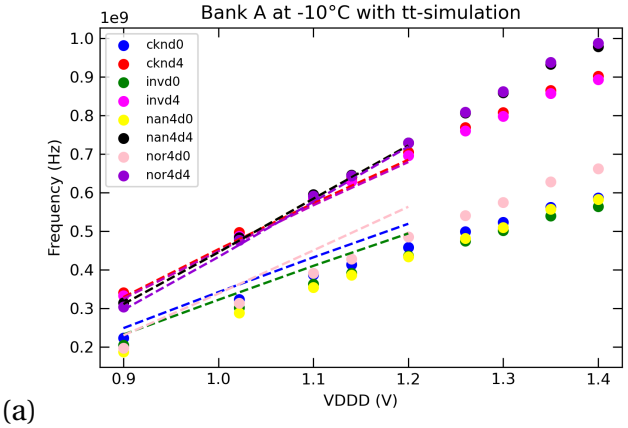

(a)

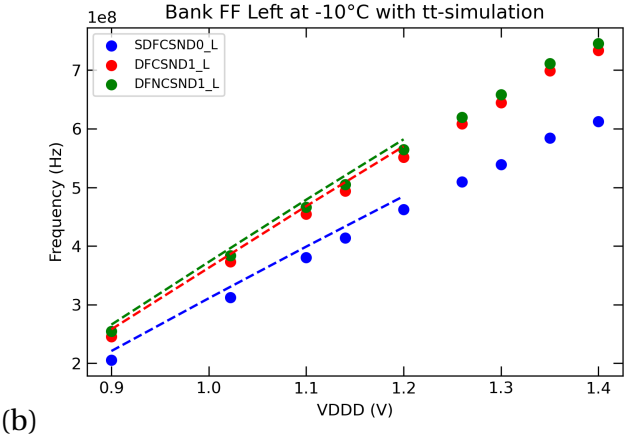

(b)

Figure 6.7: (a) Bank A ROSCs voltage evolution while ramping up the voltage up to 1.4V. Frequency dependency with V_{dd} shows linearity both in data and simulation. However, simulation points are covering the range between 0.9V and 1.2V. (b) Flip Flop bank ROSCs frequency evolution with respect to bias. As already seen in bank A, the dependency shows a linear relation with simulation dashed points matching data outcomes.

6.1.5 Irradiation Setup and Test Results

Fig.6.10 (a) shows the irradiated sample mounted for irradiation using the X-ray gun generator with specifications listed in Tab.6.3 facilitating the delivery of a high dose rate (HDR) to the region of interest (ROI). The measuring system ensures precise and accurate operating conditions, with voltage bias controlled using feedback sensing lines to prevent any undesired discrepancies from the power supply. Additionally, to maintain a stable temperature environment, a Peltier cooling system developed at CPPM is employed, ensuring the experiment runs smoothly and consistently at -10°C. Fig.6.10 (b) summarizes the setup layout of interconnections, DAQs, and control systems for the SCC while irradiated.

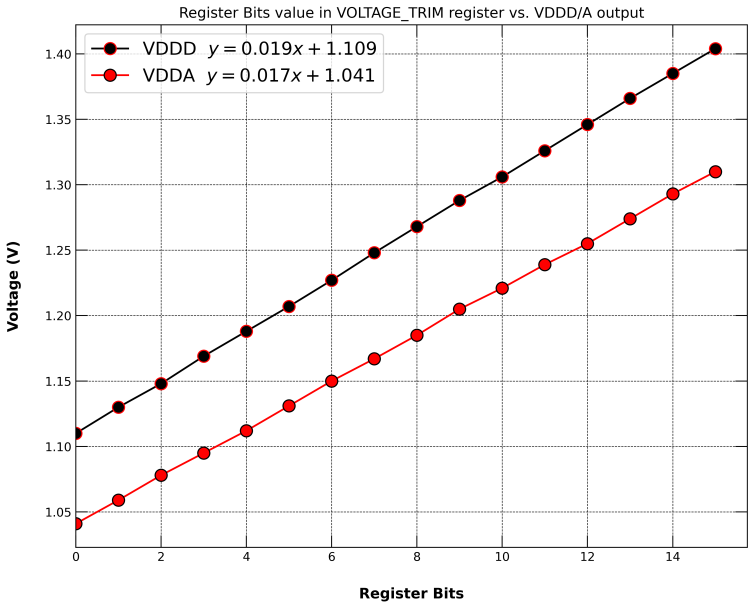

Figure 6.8: Register bit to voltage sensitivity before irradiation.

Table 6.3: main features x-ray irradiation tube.

Target Material	Dose Rate	Supply Voltage	Tube Current	Al filter
Tungsten (Peak at 20KeV)	1.3Mrad/Hour (SiO_2)	Max. 20KV	Max. 20mA	120μm

Moreover, the irradiation campaign included two SCCs for irradiation independently. The first chip was irradiated with 16 $Krad/min$ as Fig.6.9 illustrates the x-ray beam intensity as a function of distance to ROI, taking into account the beam profile. Consequently, an accumulated dose of 540 Mrad over 21 days was delivered to the SCC. Afterward, post-irradiation measurements included two periods of annealing while SCC was biased, starting with 20 days at 0°C, and followed with chip power-off for 20 days, ending with another 8 days of 0°C annealing.

For the whole duration of the 1st irradiation campaign, the reference and supply voltages are monitored along with temperature and BJTs radiation sensors, and certainly the ROSCs banks. In addition to this, it must be noted that loss of temperature and data acquisition control occurred twice after at 200, and 240 hours for a short time, but later restored and well maintained for the entire campaign. However, the drawn-up conclusion from Sec.6.1.4.1 on the temperature effects is seen on the ROSC T_{pd}.

Fig.6.12 (a) demonstrates that the time propagation delay T_{pd} for multiple ROSC devices, exhibits a rapid increase during irradiation. The lower axis summarizes the temperature and supply voltage at the moment of ROSCs data acquisition. As can be seen, the temperature was well maintained except for a temporary power cut. However, V_{ddd} shows prior to the initial state of bias an increase with irradiation. At the end of the TID accumulation process, a maximum delay change of 40% is observed

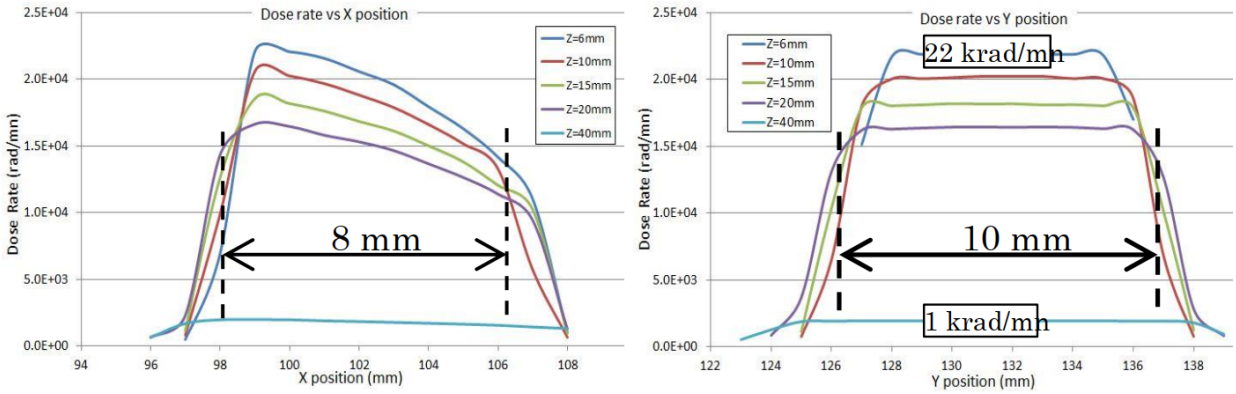

Figure 6.9: X-ray beam profile in x and y direction as a function of the dose rate. The distance of the irradiation tube towards the SCCs is also characterized in terms of distance.

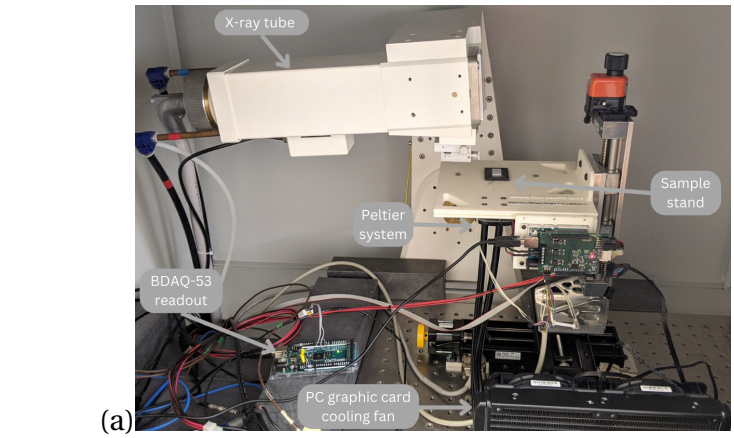

(a)

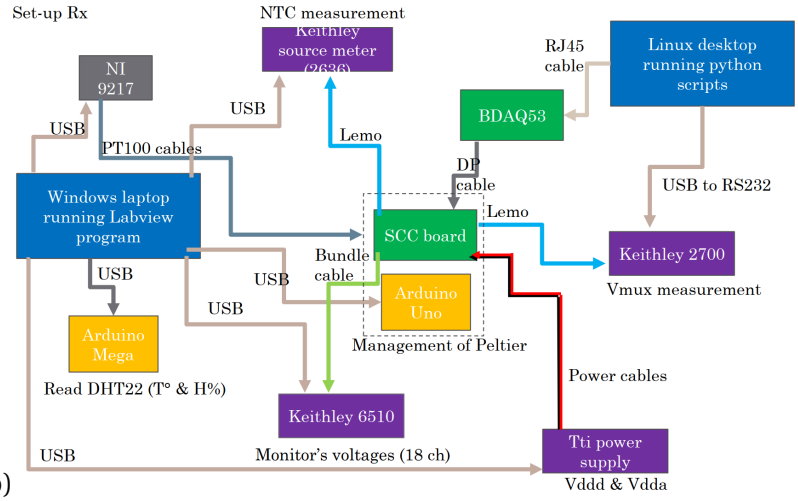

(b)

Figure 6.10: (a) Irradiation setup with X-ray gun generator and the cooling system at IM2NP. (b) Measuring system layout for the irradiation experiment showing the connections, sensors, and data acquisition systems.

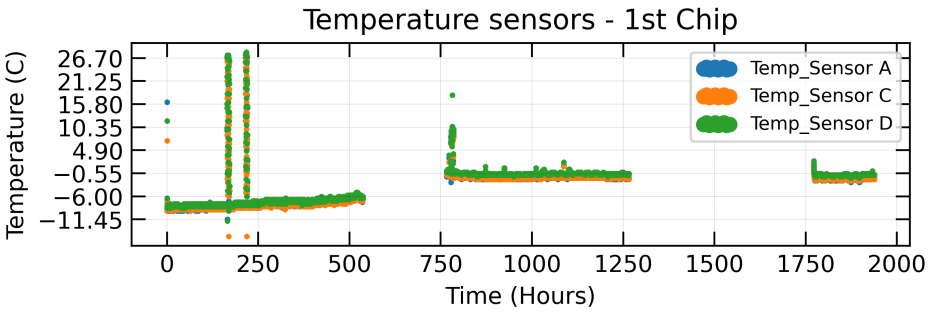

(a)

Figure 6.11: Temperature sensors illustrate well controlled conditions in the experimental setup. The plot shows three different regions for the entire experiment, including the irradiation process up to 500h for chip 1, and 210h for chip 2. After some time, the chips are powered on once again to undergo an annealing procedure at 0°C.

compared to the pre-irradiation state, expressed as the relative gate delay change (GDC):

$$GDC = \frac{T_{pd} - T_{pd_0}}{T_{pd_0}} \tag{6.13}$$

Furthermore, an increase of 40.2mV in the supply voltage V_{dd} power domain was observed prior to the initial conditions due to irradiation. This increase in V_{dd} is correlated with the decrease in T_{pd} as characterized previously in pre-irradiation voltage tests, Sec.6.1.4.2. To address this undesired V_{dd} increase and deliberate the TID effects, an absolute correction extracted from the supply voltage tests in Sec.6.1.4.2 is applied to adjust the bias to the starting conditions of the test using the following formula:

$$GDC_{After\ correction} = GDC_{Before\ correction} + (Slope_{\frac{T_{pd}}{V_{dd}}})(1.24 - V_{dd}) \tag{6.14}$$

Fig.6.12 (b) clearly illustrates that after applying correction, the GDC exhibits a linear relationship with the accumulated TID dose. The smoother performance obtained after eliminating bias inconsistencies is evident compared to Fig.6.12 (a). Hence, a 48% GDC was observed at the end of the irradiation phase highlighting the empirical evidence of TID damage on ROSCs. Furthermore, the annealing process took place aimed at restoring partially the induced TID damage after irradiation. A continuous slight drop in GDC during the 1st annealing phase is noticed, followed by another significant drop in ROSCs GDC at the 2nd annealing phase. Overall annealing effects restore in the long-term the ROSCs performance. However, it's worth mentioning that ROSCs with strength 0 driver experience lower GDC after annealing.

In more, the ITkPixV1.1 SCC power domains in LDO mode, scales with radiation-induced effects that could be measured as voltages and current variations. Fig.6.13 underlines the SCC reference voltages change in the presence of irradiation activity. Nevertheless, the observed V_{dd} increase is also

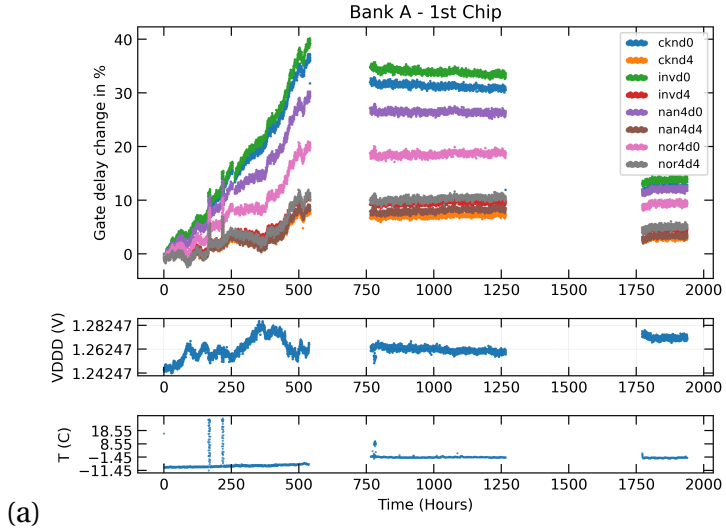

(a)

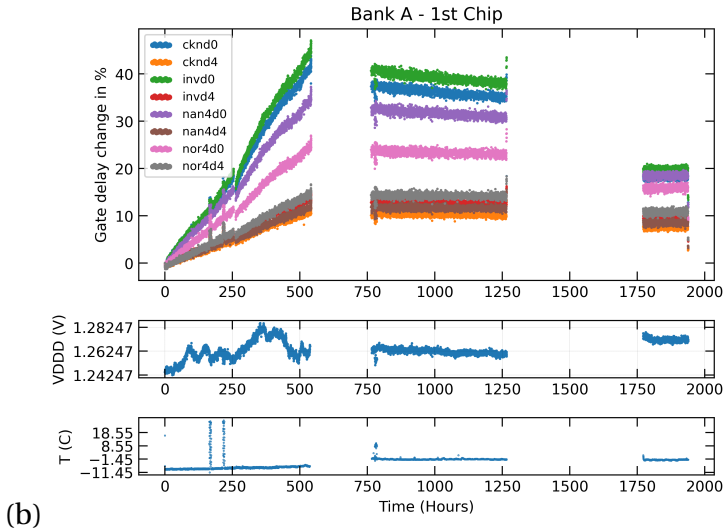

(b)

Figure 6.12: (a) Bank A ROSCs with X-ray irradiation up to 540Mrad. In the first 500h, the GDC is observed to be increasing in time with respect to the pre-irradiation measurement. Furthermore, observing the V_{dd} evolution is linked to a decrease in ROSCs *GDC* as discussed in section xyz. (b) GDC evolution with absolute correction for V_{dd} fluctuations. The GDC curves show a linear dependency with irradiation and a higher relative delay the expected end of the irradiation campaign.

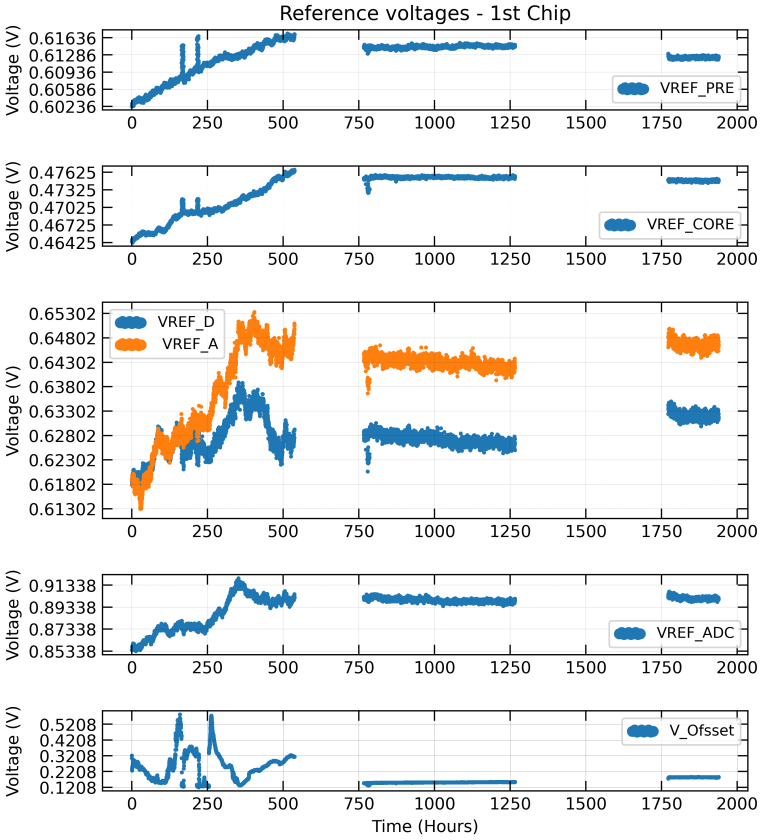

(a)

Figure 6.13: Reference voltages evolution along the irradiation phase and two annealing phases

seen for the analog power domain V_{dda} as in Fig.6.14, it must be noted that the enlarged increase of the analog power domain over the digital, is attributed to the irradiation spot on the SCC. That is, V_{dda} experienced more irradiation that led to inducing parasitic current due to charge trapping.

Furthermore, the second irradiated SCC reached up to 210Mrad in 9 days of irradiation. Afterwards, annealing was conducted in two steps as in Chip1 including the first period of 15 days at 0°C and ending with 4 days at 0°C. Irradiation and annealing temperature measurements for both SCCs are conducted and analyzed in a similar approach. Relative GDC for chip 2 is depicted in Fig.6.15 (a) without V_{dd} correction and (b) taking into account the absolute correction.

6.1.5.1 Dose Rate-Related Effects

The various time-dependent effects and trapping dynamics present serious challenges in testing. To obtain reliable estimates for device behavior in the actual radiation environment, a methodology is needed to address these complexities.

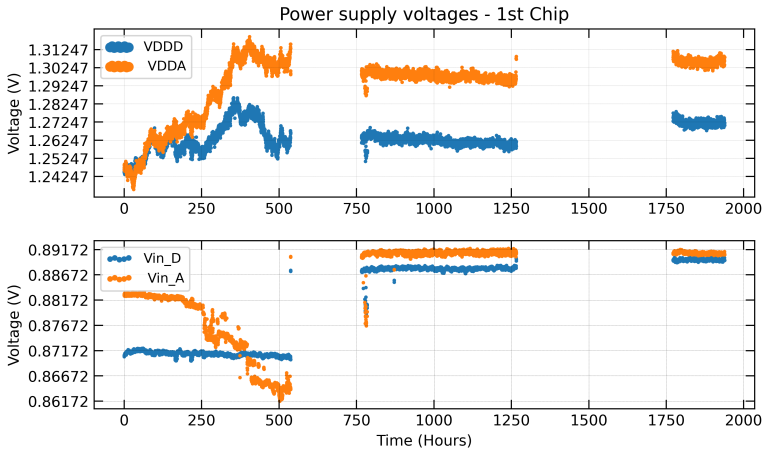

(a)

Figure 6.14: Power supply voltages V_{dda} and V_{ddd} evolution along the irradiation and two annealing phases.

The real radiation environment typically involves a very low dose rate, and the TID accumulates gradually over a long period, e.g., 10 years in the case of LHC's high luminosity phase. Conducting tests in the laboratory with such prolonged durations is impractical, necessitating a significant acceleration of the dose deposition. Moreover, in practice, the anticipated TID for LHC is deposited in a few hours of a day or continuously for a certain period of days, but not uninterrupted over the entire planned run.

An ideal methodology should include dose rates at which expected in real conditions. But, as for experimentalist this is not possible, addressing the component's qualifications for different dose rates is necessary. For CMOS technologies, such qualification is possible. In this section, a comparison of low dose rate (LDR) and high dose rate (HDR) is presented. Using the previous data obtained from the irradiation campaign at 16Krad/min, it can be considered up to an extent as LDR compared with the HDR data taken from the ATLAS group at Oxford University, with a dose rate of 66.6Krad/min.

As mentioned before, the SCC for the irradiation campaign at IM2NP was in LDO mode. However, at Oxford, the SCC was in Shunt-LDO (SLDO) mode. Both measurements utilize X-rays as a source of TID with the dose rates mentioned before. It should be noted also that bias voltage V_{dd} at IM2NP and Oxford are different, Fig.6.16 shows the frequency evolution as a function of TID, including the temperature and voltage supply for each measurement.

Furthermore, to be able to quantify the performance of a selected number of ROSCs from bank A in two different dose rates, both voltage and temperature conditions have to be similar. As evident, the supply voltage measurements are distinct. Therefore, both ROSCs V_{dd} must be corrected to an equivalent bias to inspect the dose rate effects. Fig.6.17 (a) and (b) demonstrate Cknd0 and Cknd0 ROSCs relative GDC as a function of two different dose rates at similar bias.

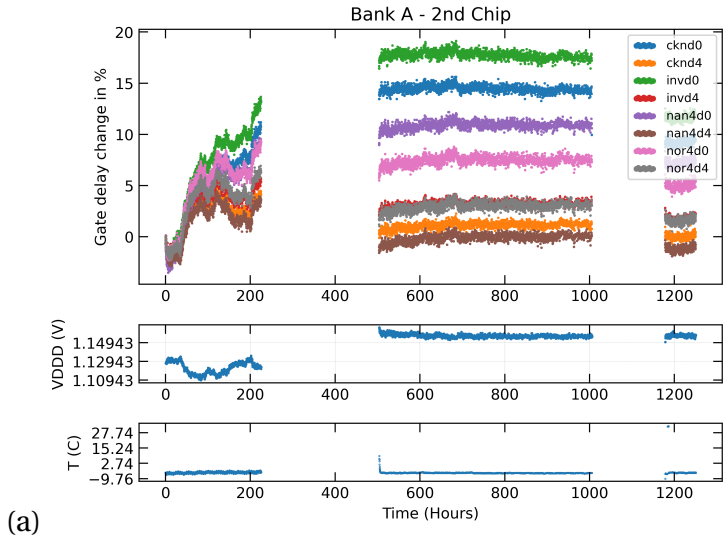

(a)

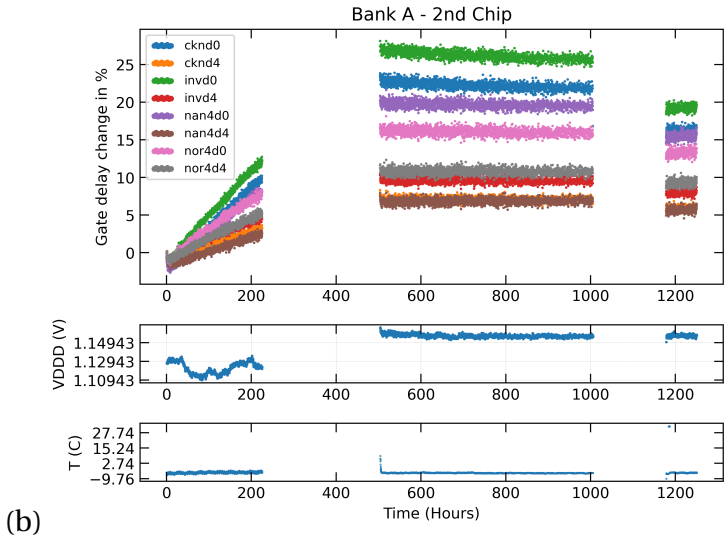

(b)

Figure 6.15: (a) Bank A ROSCs with X-ray irradiation up to 210Mrad. In the first 500h, the GDC is observed to be increasing in time with respect to the pre-irradiation measurement. Furthermore, observing the V_{dd} evolution is linked to a decrease in ROSCs *GDC* as discussed in section xyz. (b) GDC evolution with absolute correction for V_{dd} fluctuations. The GDC curves show a linear dependency with irradiation and a higher relative delay the expected end of the irradiation campaign.

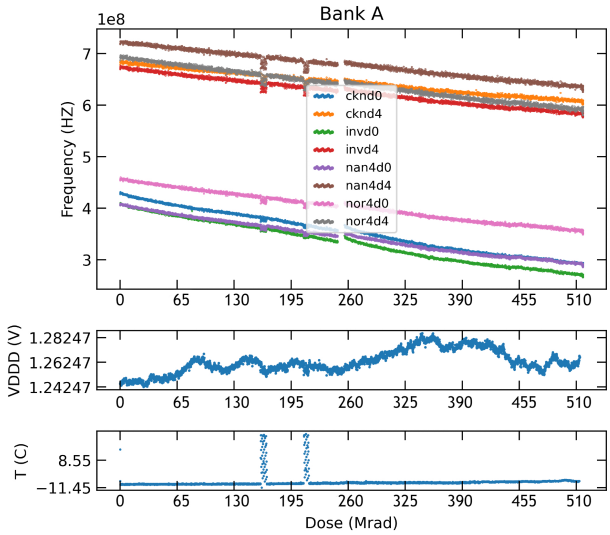

(a) a

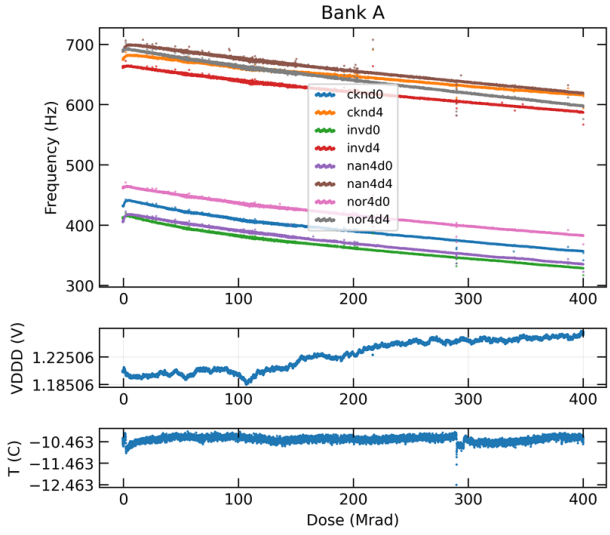

(b) b

Figure 6.16: (a) Frequency evolution with 16Krad/min (LDR) at IM2NP Marseille for bank A ROSCs, including the temperature control performance at -10°C with supply voltage growth. The frequency output is corrected prior to the initial conditions of the experiment. (b) Oxford's irradiation campaign with 66.6Krad/min (HDR), reaching an accumulated TID of 400Mrad. The corresponding temperature and voltage measurements are indicated while taking into account the voltage growth correction.

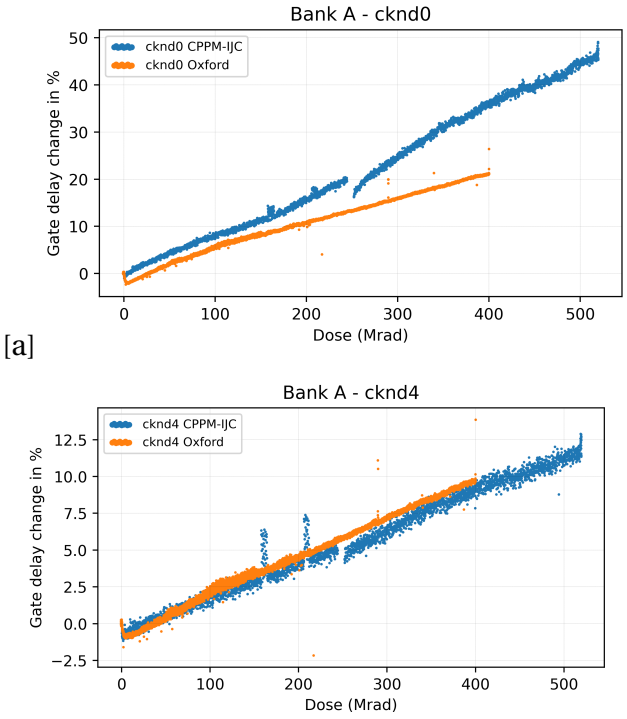

[a]

(a) b

Figure 6.17: (a) CkndO ROSC GDC evolution due to two different dose rates with the same bias voltage. It could be seen that over the course of irradiation, LDR effects cause more degradation on the T_{pd}. (b) Cknd4 ROSC GDC as a function of total accumulated TID of LDR and HDR. According to the results, both dose rates have a tendency to match even at higher accumulated doses.

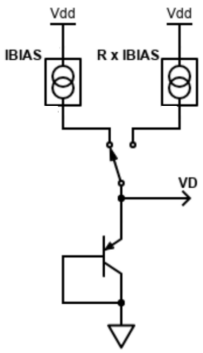

(a)

Figure 6.18: Diagram of BJT radiation sensor with supply voltages.

As previously discussed, the charge-trapping process influences the time propagation delay. It is illustrated that dose rate (DR) related effects vary between HDR and LDR, as measured by Cknd0 relative GDC, and for the same level of TID accumulated, LDR experiments provoke a much more severe degradation than HDR irradiation.

6.2 BJT as radiation sensors

Bipolar Junction Transistor (BJT) typically consists of three types of semiconductor materials, such as NPN configuration. In this setup, the base (B) is made of a P-type semiconductor, sandwiched between two N-type semiconductors known as the collector (C) and emitter (E). The BJT can be biased using a current source at the base-emitter junction and a voltage source applied to the collector and emitter electrodes, determining its operating point, VCE. For radiation detector applications, the BJT operates in the forward-active region. Its compact size makes it suitable for implementation in Application-Specific Integrated Circuits (ASICs) for radiation monitoring purposes. In the case of the RD53B chips, three radiation sensors are implemented at different locations, Fig.6.18 shows the BJT sensor layout. The basic device characterization formula from transistor theory indicates dependency on temperature, as follows [27]:

$$T = \Delta V_D \times \frac{q}{N_f \times k_B \times ln(R)} \tag{6.15}$$

Whereas the voltage applied across the diode V_d is readable via the VMUX port. N_f ideality factor equaled to 1.008, and k_B, q is the Boltzman constant and the electron charge, respectively. The sensors have a voltage output that is an input to the VMUX, readable with other voltages as indicated previously in the ROSC studies.

As shown previously in the ROSC performance, the accumulation of space charge is linked to

mechanisms that hinder hole transport. This effect can be attributed to the presence of a high density of trap centers in the parasitic oxide. These trap centers tend to capture radiation-generated holes, leading to a reduction in hole mobility. As the irradiation continues, an increasing number of holes become trapped within these centers, eventually forming a "wall" of potential that restricts additional holes from being captured by deeper trap centers. As the BJTs have Silicon bulk properties, they are not immune to TID. The TID effects are linked to the degradation of BJT sensors impacting more specifically, the base current and current gain factor, as will be shown in the two irradiation campaigns.

In Fig.6.19, the two TID campaigns illustrate an increase in the measured voltage across the BJT sensors viewed on a logarithmic scale that saturates the end of the TID process. As seen before for the ROSC performance, both temperature and bias voltage affect the T_{pd}. However, for the BJT sensors, the outcomes of irradiation highlight that the temperature control loss has an associated increase in the voltage measured as evident in Eqn.6.15 and seen in the 1st irradiation campaign. Moreover, as presented in the ROSC voltage effects increase related to TID and the necessity to apply an absolute correction, the BJT sensors are not affected by bias inconsistencies.

6.3 Single Event Effects (SEE)

Single Event Effects (SEE) encompass a broad category of effects that can be induced in semiconductor devices when ionizing particles pass through them as in Fig.6.20. In high-energy physics experiments, Single Event Upset (SEU) is a major effect that is particularly important to understand, in order to harden the electronics used. Temporary malfunctions or soft-error induced are related to a flip of a 'bit' in the Flip-Flop or memory cell leading to a change and corrupting the digital state of the circuit. Nevertheless, such corruptions might lead to direct unreliability of the readout chip, viewed as failures to read appropriately an individual pixel, or group of pixels in addition to corrupting triggers and data as presented in [83] in the IBL FE-I4 readout chip. Such reduction of readout chip efficiency must be encountered by robust electronic circuit design and gradual reconfiguration during data taking. This section will endorse the SEU rate and the soft errors induced in the Pixel registers matrix for the Pixel readout chip, ITkPixV1.1 using the proton beam at the IRRAD facility in CERN. Featuring custom-designed SEU-hardened memory cells, known as Triple Modular Redundancy (TMR) memories [21].

6.3.1 SEU mechanism

The production of single event effects (SEEs) in microelectronic devices involves three main consecutive steps. First, energetic particles deposit charge as they strike the sensitive region. Second, the

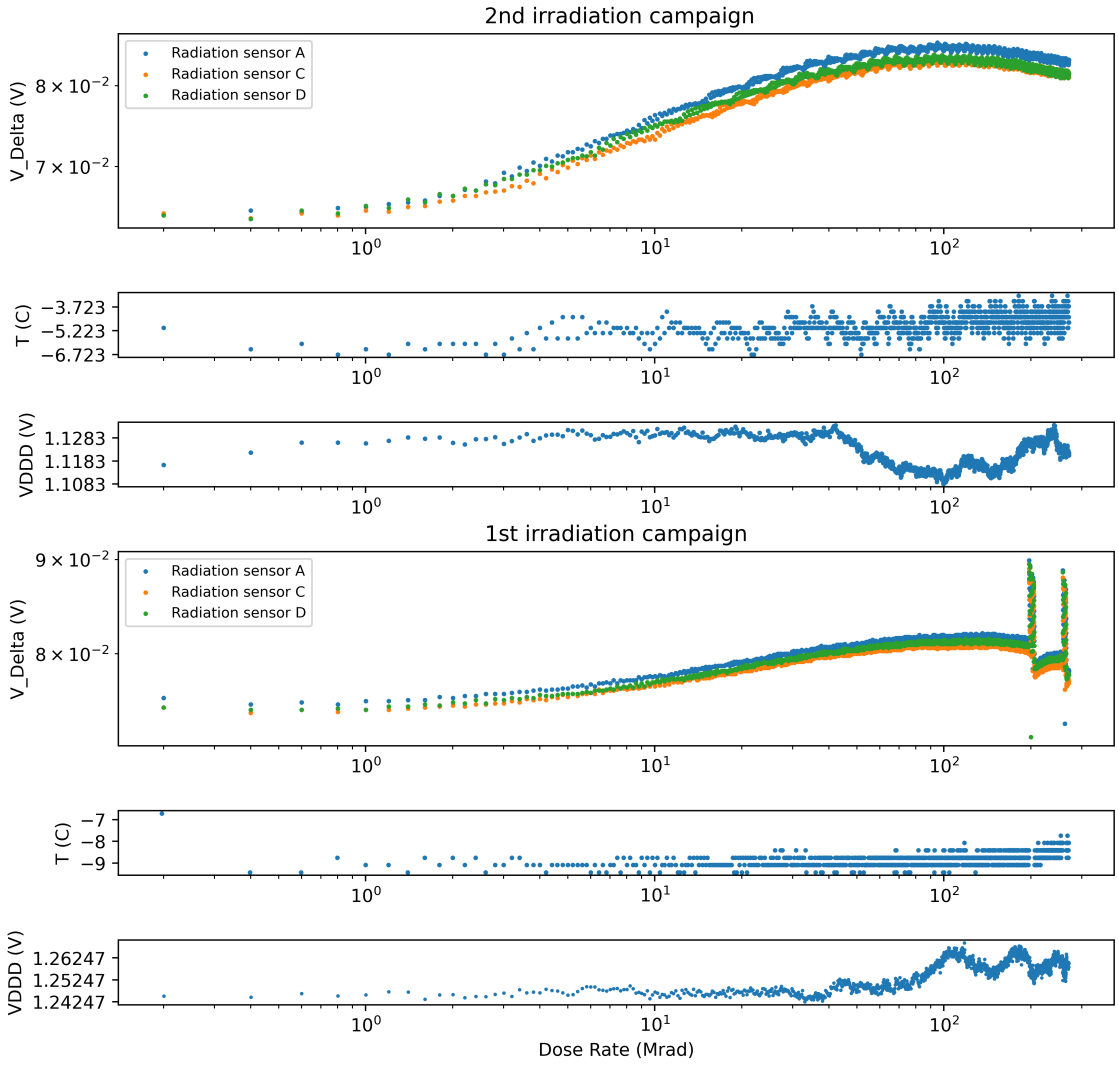

Figure 6.19: BJT radiation sensors V_{Delta} evolution with the two irradiation campaigns. The logarithmic shows indicate an increase in the measured voltage that saturates along the irradiation process. Moreover, as noted before for the 1st irradiation campaign, the temperature loss control significantly the voltage output.

released charge is transported within the device. Finally, the charge converges in the sensitive region of the device.

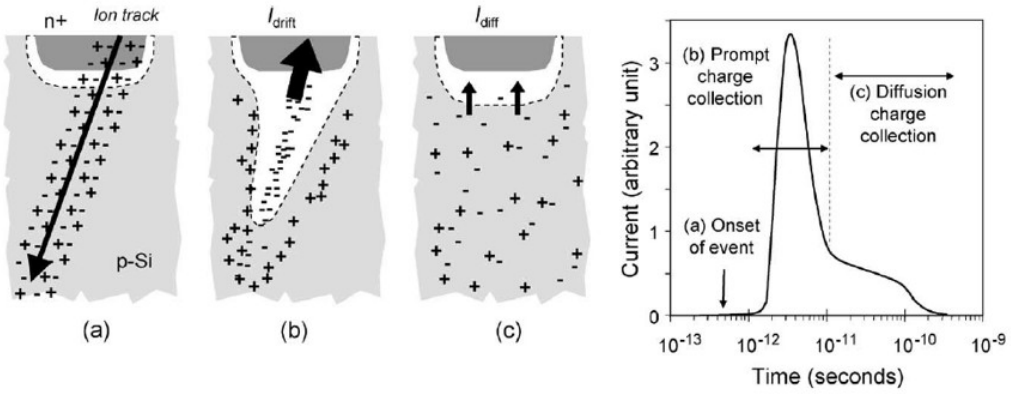

Figure 6.20: The passage of a high-ionization particle through a semiconductor device leads to the generation of a resultant current pulse [20].

The interaction of ionizing particles with a microelectronic device leads to the generation of charges, which in turn causes a parasitic current transient as in Fig.6.20. Furthermore, a portion of the charge gathered at the drain builds up on the capacitive load of the affected node, leading to a state alteration. This capacitive load is mainly associated with the input of the second inverter. When the charge collection process is rapid and the accumulated charge is sufficiently significant, it causes a change in the potential of the impacted drain. Consequently, the second inverter switches, amplifying the state change at the output of the affected inverter, resulting in an upset of the memory cell content. Hence, SEU effects due to ionizing radiation vary depending on the intensity of the current transient and the number of impacted circuit nodes. Accordingly, the possibility to trigger SEU events is therefore expressed as the critical charge ($Q_{critical}$) generated by high-ionization particles are calculated using the following equation:

$$Q_{critical} = \eta \; q_e \; \rho \; l \; \frac{LET}{E_{eh}} \tag{6.16}$$

In which η is the charge absorption efficiency, q_e represents the electron change, ρ is the target density, l is the particle travel path in the material, LET is the linear energy transfer of the particle energy per unit distance, and E_{eh} is the ionization energy. Kindly note the deposition of the critical charge to cause SEU has to occur in the proximity of the collecting node volume known as the sensitive volume (SV). Moreover, the evaluation of the SEU in the presence of a particle beam is expressed as the cross-section for an upset event [70]:

$$\sigma \; [cm^2] = \frac{SEU_{events}}{\Phi \; [N_{particles}.cm^{-2}.s]} \tag{6.17}$$

Where Φ is the total fluence calculated from the known amount of particles delivered as bunches within the exposure time, given that:

$$\Phi = Flux \times T_{exposure} \tag{6.18}$$

and SEU_{events} is the total number of observed upsets counted during the experiment. Furthermore, to quantify the σ_{SEU} for a selected bits architecture per FE, as in the case for the Pixel readout-chip, the overall equation becomes:

$$\sigma_{SEU}\ [cm^2/bit] = \frac{SEU_{events}}{Total\ \#\ of\ bits/type/FE \times \Phi\ [N_{particles}.cm^{-2}.s]} \tag{6.19}$$

6.3.2 SEU Mitigation Techniques

As discussed before, SEU events happen as a result of the corruption of the information stored in a memory element. To mitigate SEUs, an intuitive idea of making redundancies or copies of the correct data stored resolves the SEUs expected errors. This classic solution is widely used as an effective error mitigation mechanism in the microprocessor industry. In our case, triple modular redundancy (TMR) can provide more reliability against high hadron flux at the HL-LHC. The TMR block is composed of three replicated components with a voter of three inputs, A, B, and C. The boolean function of the three logic units for the outputs is given by:

$$Voter_{output} = AB \cup BC \cup AC \tag{6.20}$$

Based on the inputs to the voter, a voter logic gate serves the purpose of determining the correct output among multiple inputs. Specifically, the majority gate functions in the following way: its output is 1 when two or more of its inputs are 1, and the output is 0 when two or more of its inputs are 0. In worst cases, the voter could fail and duplication of errors due to SEUs arise in the registers. To counter this, the duplicated clocks in each replicated component must introduce a delayed latency Δ_t on each clock that is determined from the impulse response of combinational logic elements due to Single Event Transient (SET) glitches, the Δ_t is set to 250 ps according to the SET prototype test results [84].

Moreover, the introduction of redundant elements brings higher reliability as a trade-off with more micro-circuits that comes with more power cost and area for the small pixels. However, due to these constraints, other SEUs mitigation techniques and TMR topologies are implemented for critical parts of the configuration memories and pixel configuration registers. In addition to the conventional TMR topology with a voter. The second topology includes along with the triplication of memory elements, an auto-correction mechanism. In this configuration, if an upset occurs in any of the registers, it will be automatically corrected in the next clock cycle due to the redundant triple

Table 6.4: ATLAS Pixel configuration bits for RD53B [27].

Bit Number	Bit name	Description of bit function
0	Enable	Include the pixel in the DAQ data path
1	Enable Calibration Dig/Ana	Turn on charge injection
2	HitOr enable	Add the pixel to its wired OR core col. hit line
3,4,5,6	TDAC value	Value for in-pixel threshold trim DAC
7	TDAC sign	Selects differential branch set to TDAC value

configuration. Fig.6.21 presents the latches and TMR topologies used for SEU mitigation. Moreover, in case no external refresh of the logical state default values is done, the SEU is considered permanent. In addition to the discussed TMR topologies and the mentioned fact that SEU is a temporary event when refreshing the logical units is done to counteract SEUs, the reset or reloading of the proper information to the logic units mitigates the data corruption. Undoubtedly, while the pixel memory cells are in read mode, this method of recovery isn't accessible, and external re-configuration is only possible a few times.

To elaborate on SEU mitigation to the performance of the pixel readout chip, the design of the pixel configuration memories and registers for each pixel in the front end differs based on the sensitivity of malfunction to the reliability of chip performance. Each pixel has a dedicated 8 configuration bits that are not equal in terms of the criticality of pixel functionality. As Tab.6.4 indicates, the first 2 bits are arbitrary and the latch isn't protected. At an incidence of bit flip, no significant effect on the chip arises. In contrast, the later 6 bits, including the 5 of the threshold DAC (TDAC) are protected with TMR classical topology as in Fig.6.21 (b).

Moreover, Tab.6.22 summarizes the expected SEE rate with a hadron flux of $10^9 p.cm^{-2}.s^{-1}$ in the context of the ATLAS ITk at the HL-LHC. The simulations estimate more SEUs in the innermost layer and gradually decrease away from the IP. Hence, the impact on memories and TMR topologies differ on the basis of SEE flux and memory architecture, as indicated in higher events of bit flip for the unprotected latch, compared to the triplicated latch and auto-correction mitigation methods.

					Pixel Conf.	Pixel Conf.	Global Conf.
Layer	Location	R (cm)	Z (cm)	SEE-Flux ($cm^{-2}.s^{-1}$)	Unpr. latch (flip/FE)	TMR latch* (flip/FE)	TMR w/corr (flip/FE/hour)
0	L0 rings	3.6	114	1.0×10^9	230	7	0.2
2	L2 rings	15.6	286	0.82×10^8	19	0.095	1.7×10^{-2}
4	Outer Endcap	274.6	286	0.35×10^8	8	0.022	7.2×10^{-3}

*Based on external re-configuration time interval of 50 seconds

Figure 6.22: ATLAS Pixel detector SEU error rate estimation [21].

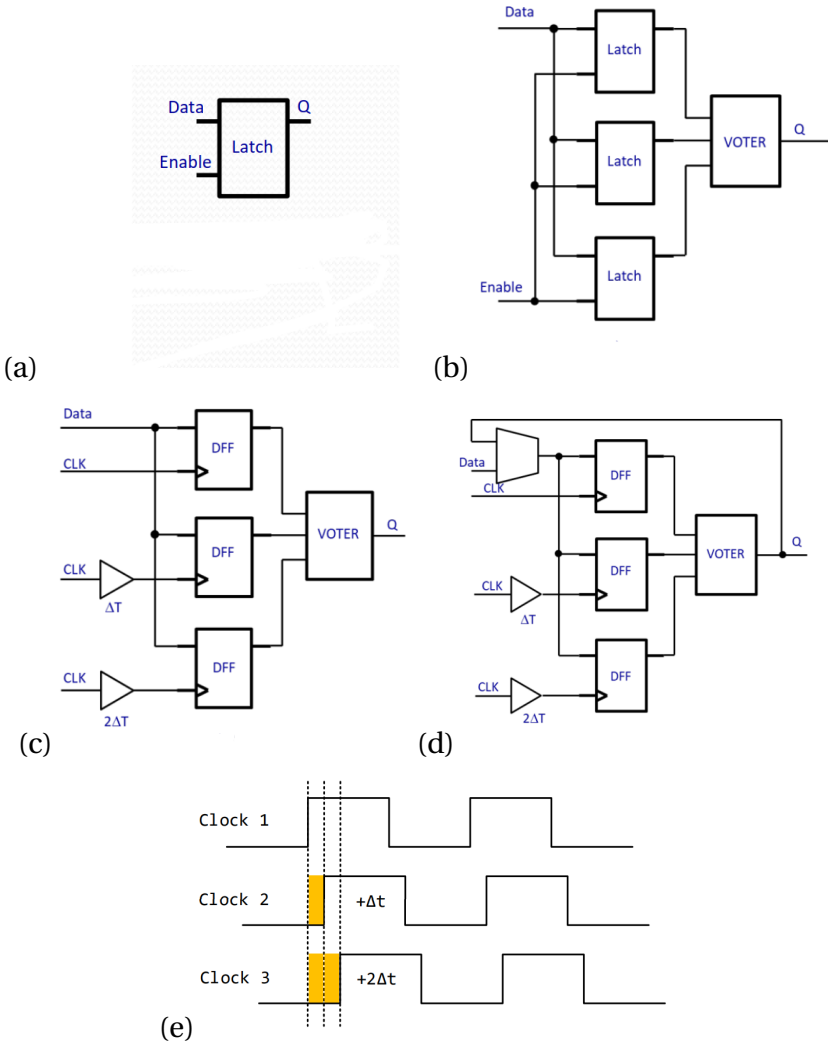

Figure 6.21: (a) Unprotected latch with no voter or auto-correction. (b) TMR without auto-correction. (c) TMR D flip-flop (DFF) triplicated with three delayed latencies skewed clocks. (d) TMR protection with auto-correction. (e) The triplicated skewed clocks schedule with Δ_t set to 200ps [6.20].

6.3.3 PS-IRRAD SEU Campaign

Testifying the performance of the ITkPixV1.1 readout chip against SEUs involves conducting an SEU campaign with hadron flux similar to what will be foreseen in the HL-LHC. The objective of the following experimental setup with the proton-synchrotron (PS) at the IRRAD facility is to examine the SEU cross section (σ_{SEU}) for the pixel configuration memories.

6.3.3.1 Experimental Setup and Testing Strategy with Results

The IRRAD facility at CERN features unique beam properties to inspect SEUs, similar to the environment at the HL-LHC. Beam properties include a proton beam energy of 24 GeV with a flux 40 times higher than in the HL-LHC. The protons are delivered in spills of 5×10^{11} p in a specific time window of the PS cycle. With each cycle containing 3 spills within a duration of 30 seconds. To inspect the beam profile, a beam position monitor (BPM) is used to survey the beam intensity. Ideally, the standard size of the beam is 12x12 mm^2 full-width half-maximum (FWHM).

The IRRAD facility consists of two main zones for conducting the SEU campaign. Firstly, the irradiation zone where the SCCs are accommodated in parallel to the PS proton beam at ambient temperature. Secondly, the control room that houses the test bench setup. Both zones are linked through a shuttle system that moves the irradiated samples in and out of the beam to configure the pixel memory registers. Fig.6.24 shows the floor plan of the IRRAD facility in addition to the BPM associated with the second zone.

Besides, as the irradiation zone is prohibited from entering in the presence of a beam, an interlink between both zones is used. The patch panel is connected to the power supply cables, display ports, and other necessary wiring to operate the two SCCs. One of the configurations to pilot one SCC was based on having the BDAQ53 in the irradiation zone. Unfortunately, within less than an hour, the connection was lost, and the BDAQ53 failed to operate afterward. The setup layout used to acquire the SEU data is illustrated in Fig.6.23.

The methodology of studying the σ_{SEU} for the pixel configuration memories involves writing a decimal value of 85 that corresponds to $0b1010101$ in binary, to the 8-bit memory for the 400x384 pixel matrix. The SCC is then moved to the beam in which if any SEU event erupts in a single, or multi-bit it will be registered when that memory is read, for a given time duration of SCC exposure. Using this, it will be possible to measure with an equivalent value for the 1.228 Mbits/FE in which pixel the SEU happened, for which bit in the memory, and in case there is a multiple-bit flip in a single SEU case.

A selected sample of results will be discussed to elaborate on the σ_{SEU}. Fig.6.26 shows the SEUs on the pixel matrix of the ITkPixV1.1 chip highlighting more upset events in the highest-intensity regions of the beam. At the beam halo, fewer SEUs are observed. However, the legend indicates more than a single-bit flip in the middle of the beam. The imposed number of SEUs histograms in the x

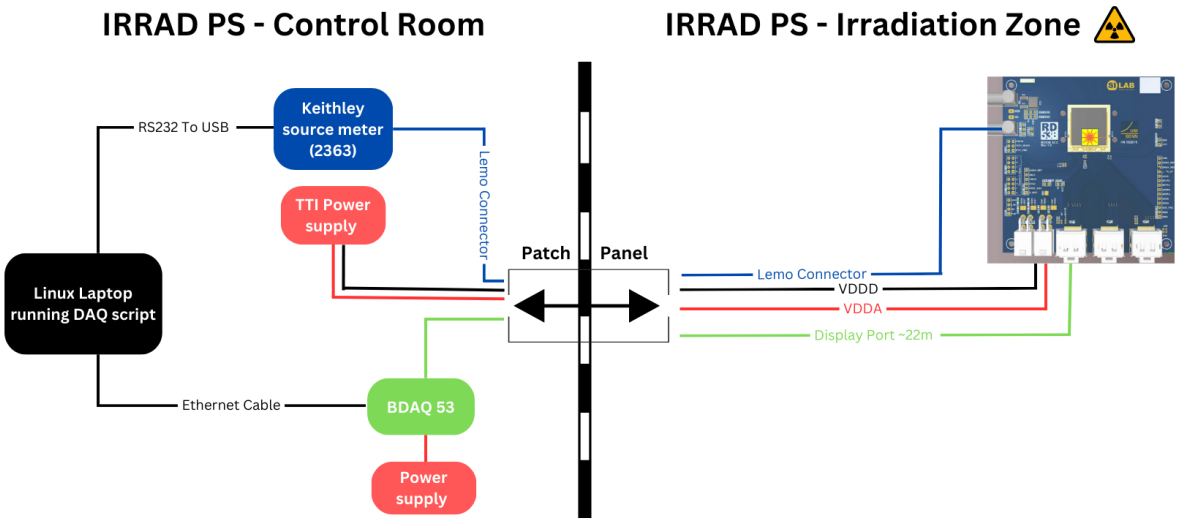

Figure 6.23: SEU system test setup layout.

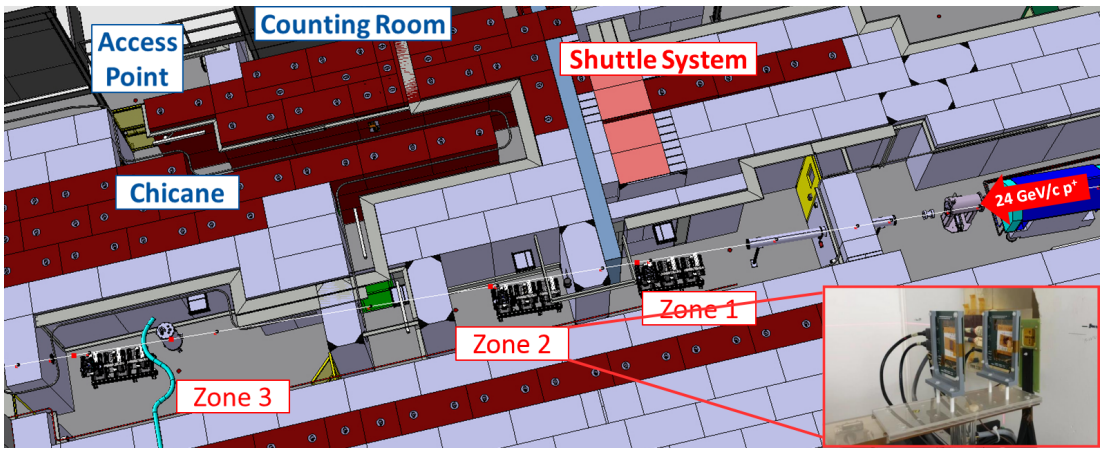

Figure 6.24: Floor plan of the IRRAD facility highlighting the location of the two SCCs used for the test at the second irradiation zone of which the SEU campaign has been conducted.

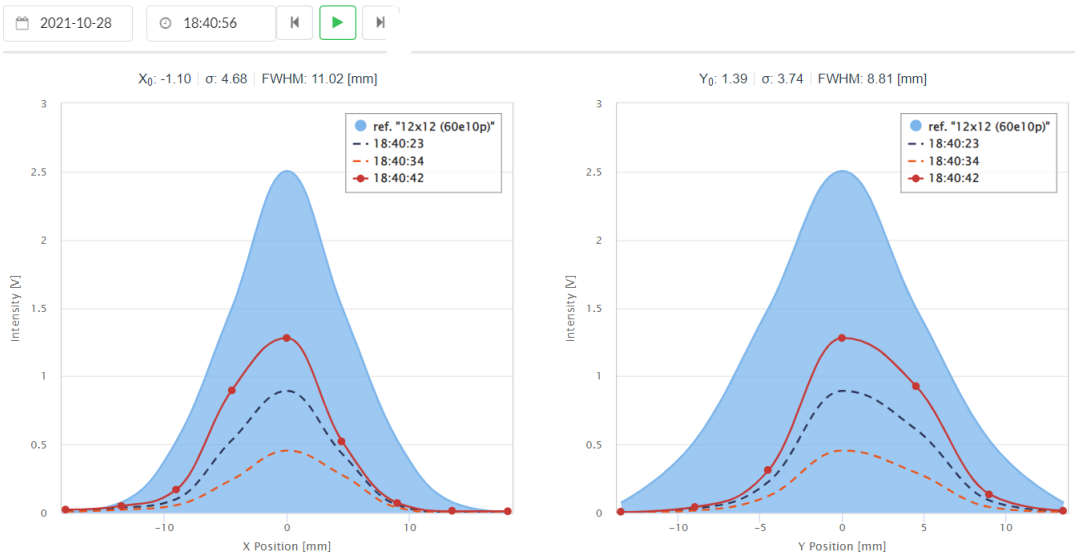

Figure 6.25: Monitoring of the beam profile seen by the BPM in the second zone just before hitting the SCC pixel matrix. At the time of measurement, the estimated hadron flux is $6.2 \times 10^{15} p.cm^{-2}$ with beam FWHM of 11x8.8 mm^2.

and y directions also illustrates the beam shape as seen in Fig.6.30. In this run, an accumulated 41200 SEUs were observed in which multiple-bit flips are observed at the same instance.

Moreover, as previously indicated not all bits have similar memory architecture. Therefore, a separation is based on the type of bit, whether it isn't a protected latch with an abbreviation of StandAlone Bit (STD Bit) and TMR protection without correction bit (TMR Bit). The bar chart.6.27 demonstrates the total number of bit flips categorized for the pixel configuration memories, clearly indicating more bit flips state from zero → one, rather than one → zero. In other words, it's more probable to charge the storage elements compared to discharge them. In addition to that, the 6 TMR-protected storage element bits are more immune to SEUs, in contrast to the unprotected 2 bits, taking into account the difference in bits number. Furthermore, Fig.6.28 (a) shows different categories of SEU, and Fig.6.28 (b) indicates the total number of upset events proportion for each bit flip in the 8-bit register of each pixel. As shown, bit number 2 accounts for the majority of bit flips as an unprotected latch. Other portions are distributed evenly on the rest of the bits.

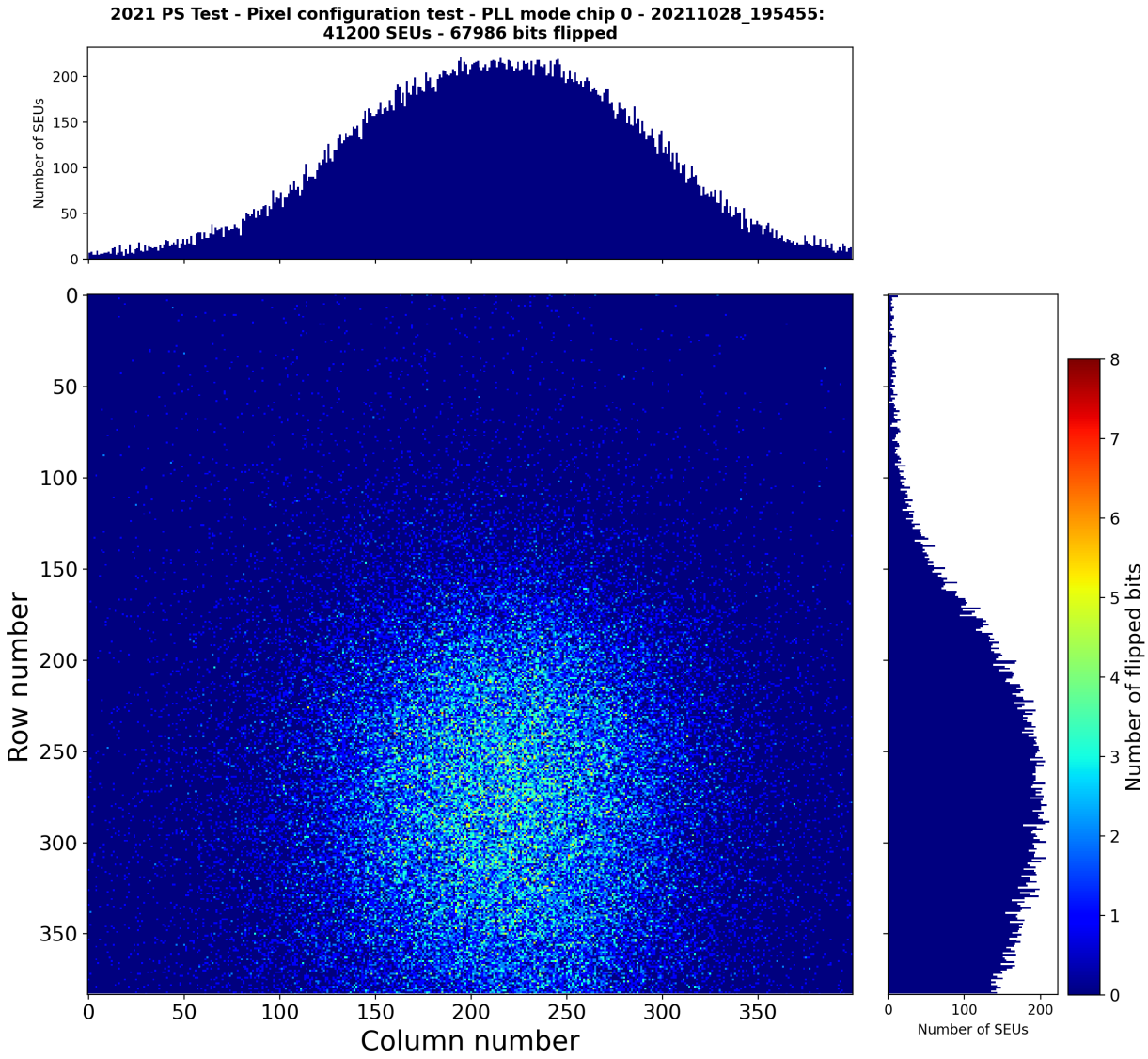

Figure 6.26: SEUs map for ITkPixV1.1 pixel readout chip

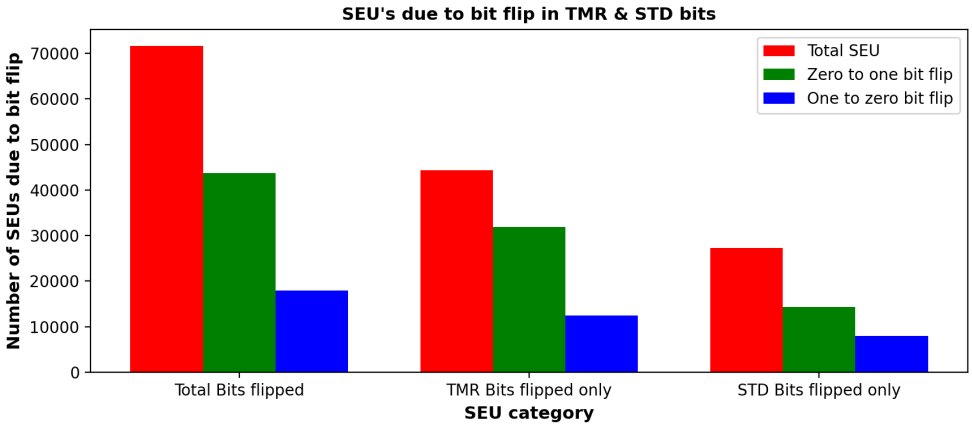

Figure 6.27: Bar chart of the total number of SEUs, indicating the bit flip state and the register memory device type.

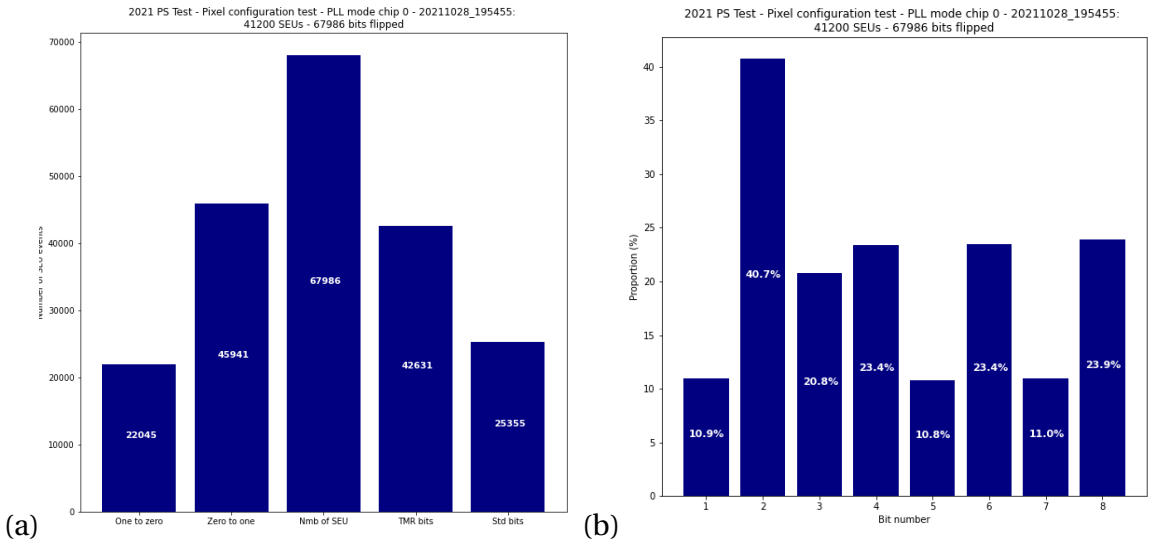

Figure 6.28: (a) Different categories of upset events for the pixel configuration memories. (b) The bit flip segments for each bit in the storage elements disregarding the bit flip state.

Furthermore, the inspection of bit flip state occurrence and multiple-flip bits are illustrated in Fig.6.29 (a) and (b). Again, the likelihood of many bit-flips in a single upset event is related to the flux intensity, correlated to the beam shape live from the beam position monitor in Fig.6.25. In Fig.6.29 (a), multiple bit-flips from zero → one are seen in a single pixel, and moving away from the beam center decreases the number of associated multiple-event upsets. However, in (b), fewer multiple-event upsets from one → zero are observed. With a reduction factor of 2. To sum up, the outcomes of how many bits flipped at a single SEU, Fig.6.29 clarifies the dominance of single-bit flips in the pixel registers memory, followed by fewer multiple-bit flips.

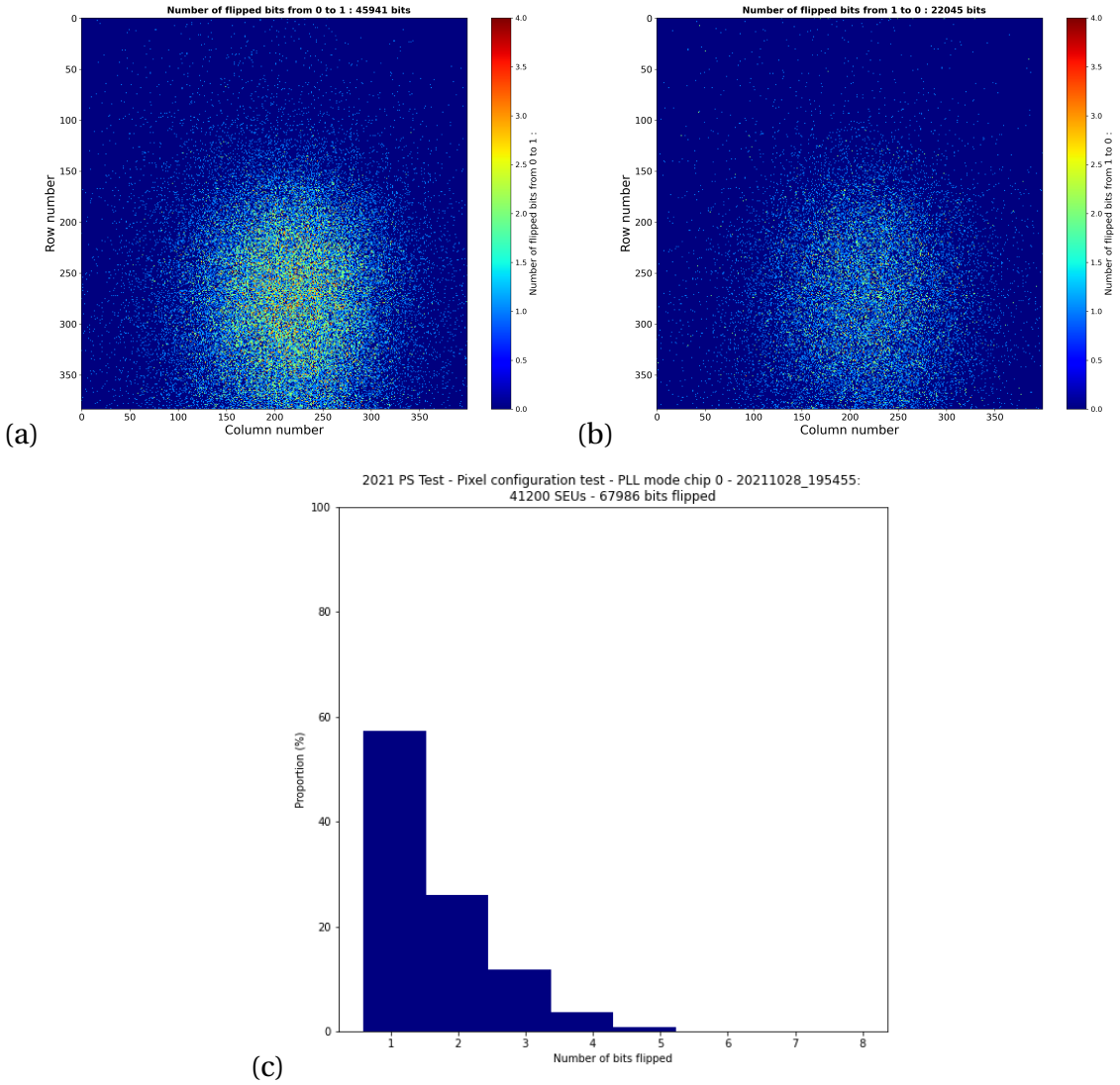

Figure 6.29: (a) SEU bit-flip from zero to one with the incident $24GeV$ proton beam. (b) SEU bit-flip as a discharge of the storage elements from one to zero. (c) Bar chart indicates the majority of SEUs to be a single-bit flip with a limited number of high bit-flip in multiple register indexes.

Table 6.5: SEU Cross Section for STD and TMR bits.

Bit number	Latch	# of bits	Total # of bits/FE	# of SEUs	$\sigma_{SEU}[cm^2/bit]$
0,1	Unprotected (STD)	2	307200	25355	3.86×10^{-16}
2,3,4,5,6,7	Protected (TMR)	6	921600	42631	2.16×10^{-16}

Moreover, as we have observed a fascinating correlation between the distribution of SEU events and the beam shape. Fig,6.30 shows a 3D map of SEU events that strikingly resembles the beam shape, implying a direct link between the intensity of the beam and the occurrence of SEUs in our Pixel storage elements. This remarkable finding demonstrates that the beam shape exerts a profound influence on SEU behavior, providing compelling evidence of the direct impact of the beam spatial profile, representing the intensity or density of particles across the area of the beam. This strong correlation between the beam shape and SEU events uncovers a crucial aspect of SEU behavior, shedding light on the likelihood of SEU occurrence.

Now it is evident that non-protected STD and TMR-protected bits response are poles apart. The σ_{SEU} will be calculated separately based on the formula introduced in Eq.6.19, taking into account the exposure time of 356 sec with $60 \times 10^{10} p.cm^{-2}$ proton beam flux. Hence, leading to a fluence of $2.13 \times 10^{14} p.cm^{-2}.s$ that induced the SEU cross-section finding in Tab.6.5.

6.4 Conclusion and Remarks

Experimental validation of ITkPixV1.1 ROSC functionality included tests using both Cadence simulations and irradiation campaigns. Prior to the irradiation experiments, assessments were conducted on the ROSC's performance concerning temperature and bias dependencies. The temperature dependency test revealed a consistent reduction in frequency as temperature increased across all ROSC variants within the ITkPixV1.1 chip, aligning with simulation results. Furthermore, investigations into bias dependency demonstrated the substantial influence of supply voltage on ROSC output, emphasizing the importance of addressing sensitivity to bias when monitoring Total Ionizing Dose (TID) accumulation during extended operation. During the irradiation campaign, a cumulative dose of 520 Mrad was administered, revealing a progressive increase in T_{pd} with accumulating radiation dose. Throughout the irradiation, an unintended rise in V_{dd} was observed. Consequently, absolute corrections were applied to the results, mitigating bias fluctuations and allowing for the observation of the TID effect on GDC independently of other factors.

Additionally, the post-irradiation phase introduced well-adjusted high temperature annealing, effectively compensating for the rapid increase noted after 25 days of irradiation. However, the study also unveiled a significant decline in performance following prolonged annealing.

In summary, the findings from the irradiation campaign were substantiated by ROSC simula-

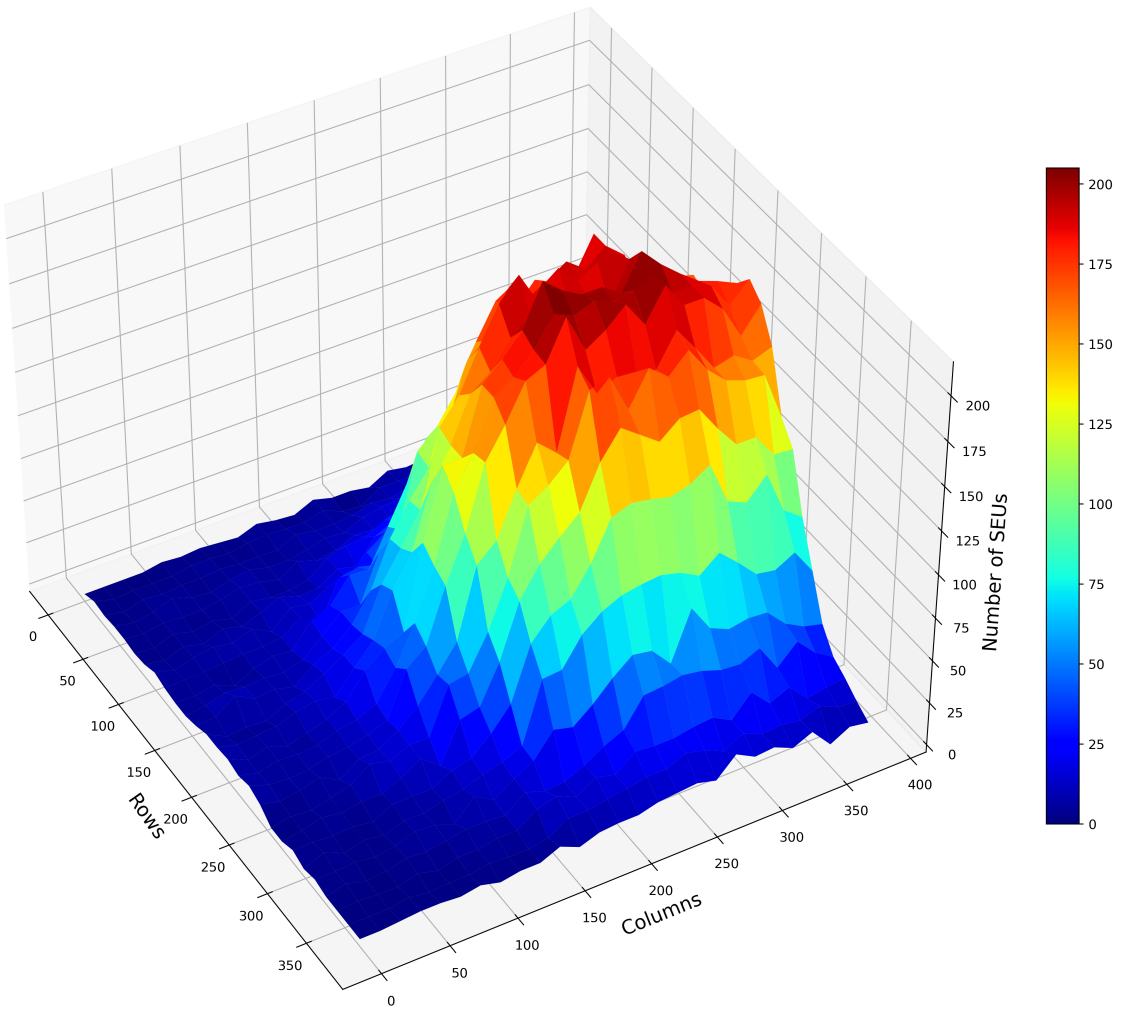

Figure 6.30: SEUs map for ITkPixV1.1 pixel readout chip

tion outcomes. The tests examining temperature and bias dependencies yielded critical insights into ROSC behavior under varying conditions, providing valuable information for optimizing its performance in future applications. Moreover, addressing the bias sensitivity to irradiation is crucial and future studies needs to include the bias corrections every few Mrads and avoid applying an absolute correction. However, post-irradiation annealing studies underscored the importance of comprehending the radiation-induced detrapping process, offering potential enhancements to the ROSC's resilience against TID accumulation.

Regarding SEU, the introduced study represents a significant step towards understanding the impact of high-flux proton beams on single-event upsets (SEUs) in electronic devices. Through comprehensive investigations, we have explored the effects of beam shape and intensity on SEU occurrence, shedding light on the spatial distribution of ionizing particles and their influence on vulnerable regions of the chip.

Our findings have highlighted the crucial role of beam shape in determining the occurrence of SEUs. The non-homogeneous nature of the beam shape has significant implications on the spatial distribution of ionizing particles, leading to the identification of "hotspots" where SEUs are more likely to occur. Consequently, the SEU cross section derived from the experiment may be slightly overestimated, emphasizing the need for corrections based on the actual beam shape.

Moreover, we have evaluated the effectiveness of protective measures with the Triple Modular Redundancy (TMR) in parallel to the non-protected latches. It was evident that the σ_{SEU} is lower for TMR bits, highlighting its importance in mitigating SEU effects. One also has to note that in addition to the reduced SEUs in the TMR, the external re-configuration isn't used in our test, proving that the σ_{SEU} would be much lower, and the high cross section found with the presented fluence is because of error-accumulation.

7

Pixel Quad Modules Performance through Test Beam

The test beam concept plays a crucial role in the field of particle physics detectors and more particularly, semiconductor-based detector technology. A comprehensive understanding to evaluate and characterize the performance of detector systems, particularly pixel modules is essential in the R&D phase. The beam tests involve exposing the detectors under test (DUT) to intense particle beams, typically high-energy protons or electrons, to examine the spatial resolution, tracking efficiency, and other critical characteristics of particle detectors. As the DUT performance is still to be determined in beam tests, it will be required to implement other high-precision detectors to play the role of a reference in evaluating the DUT performance. Hence, the notion of a telescope emerges as a sequence of reference planes surrounding the DUT, to provide a reference to reconstruct the tracks of the incident particles. In all of the beam test facilities, the detector under test (DUT) is placed within a tracking detector that is connected to a special data acquisition system (DAQ) and trigger logic unit (TLU) for data decoding and storing. Furthermore, to analyze the performance of the DUT, an offline reconstruction framework is used to examine the DUT properties through track reconstruction.

In this chapter, several test beam campaigns have been carried out since June 2021, for the first time using irradiated and non-irradiated RD53A quad modules, using the Super Proton Synchrotron (SPS) beam test facility. The DUTs performance evaluation has been carried out using energetic pion beams of 120 GeV energy. In the following sections, the SPS beam test facility at CERN is described in Sec.7.1, followed by the key features of the test beam concepts, DUT, and telescope sensor characteristics in Sec.7.2. The offline reconstruction framework with Corryvreckan will be highlighted in Sec.7.3, followed by analysis results for the RD53A quad modules in Sec.7.4.

7.1 SPS Test Beam Facility

The SPS plays a critical role in particle physics experiments as a versatile accelerator facility at CERN. One of its essential functions is to serve as a test beam facility for particle detector development and validation. As a test beam facility, the SPS provides high-energy particle beams that can be directed toward various particle detectors for comprehensive testing and calibration. These beams typically consist of charged particles, such as protons, pions, kaons, and electrons, with energies ranging from a few GeV up to several hundred GeV.

The following test beam results presented in this chapter are evaluated using the SPS pion beam at H6 beam line. In which, a focused proton beam is skillfully guided towards one of three accessible targets, namely T2, T4, or T6. Upon reaching the T4 target, the primary protons undergo interactions that yield two distinct beams: H8, characterized by high energy, and H6, featuring medium energy. The flexibility in beam energy selection is achieved through precise adjustments made using a set of three strategically positioned magnets encircling the T4 target, known as T4 wobbling [85]. This sophisticated setup enables the production of high-energy focused Pion beams of maximum flux 10^7 to 10^8 particles per extraction, rendering them suitable for an array of experiments and tests along the extraction beam line. Fig.7.1 illustrates the CERN-SPS North Area beam line.

7.2 Introduction to Test Beam Setup

In test beam experiments, a widely employed setup known as a test beam telescope plays a crucial role in evaluating and characterizing DUT. The telescope configuration typically consists of upstream and downstream telescope detector planes with a central testing area, as depicted in Fig.7.2. The beam telescope's mechanical frame is rigidly mounted, while the DUT box is positioned on a remote-controlled table for precise adjustments. Through controlled movements of the DUT box perpendicular to the beam, the beam spot can be accurately aligned to the region of interest (ROI) for test beam studies.

The experimental setup includes six telescope planes composed of MIMOSA-26 MAPS silicon sensors, featuring a $(2\times1)\ cm^2$ active area [86]. These reference planes are strategically aligned before and after the DUT, which is the focus of the performance investigation. The MIMOSA-26 sensors employ a rolling shutter readout mode, sequentially capturing rows of the pixel array, resulting in an integration time of 115.2 μs to read out the entire pixel matrix. In addition to the MIMOSA-26 planes and DUTs, reference planes are implemented in the test beam setup, similar to the technology used for the DUTs in order to evaluate the sensor properties. In our case, RD53A SCC is used as a spatial reference plane just after the second telescope plane. Additionally, another timing-reference module equipped with an FE-I4 readout chip operating at 25 $nsec$ sets a timestamp. In addition, just at the start and end of the test beam setup, a photomultiplier tube scintillator (PMT) is armed in front of

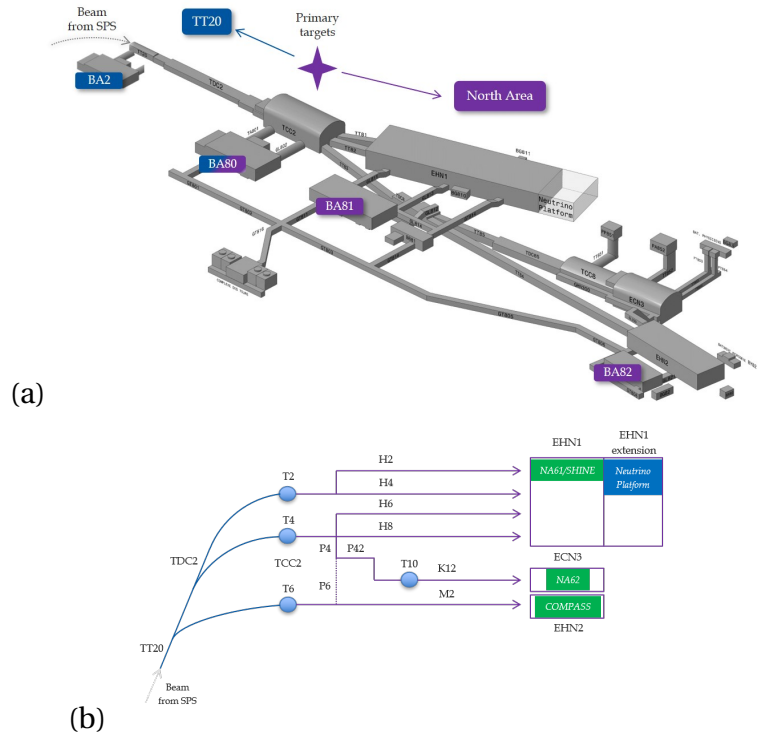

Figure 7.1: (a) TT20 and North Area Facilities showing the extraction point of SPS beam towards EHN1 building for test beam studies. (b) Primary beams extracted from SPS towards the main three targets T2, T4, T6, and afterward towards the experimental zones. Images taken from CERN © 2023.

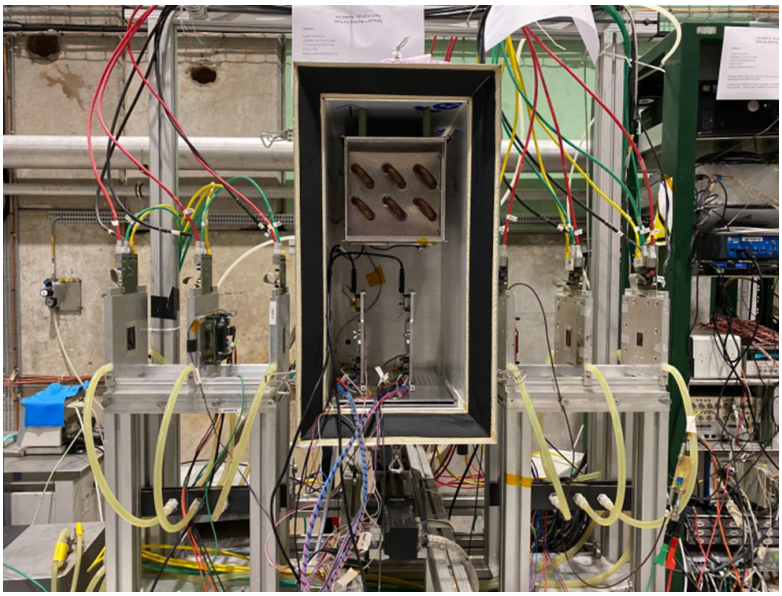

Figure 7.2: Beam telescope setup consists of 6 MIMOSA-26 detector planes, while the DUTs are placed inside the cooling box.

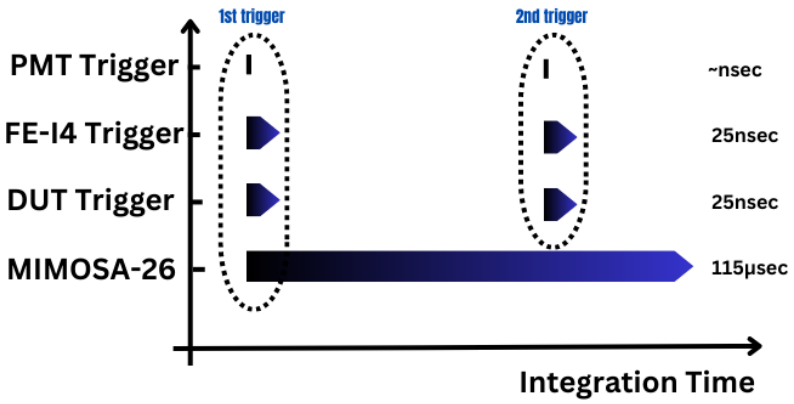

Figure 7.3: The integration time of multiple sensors in the test beam setup. As illustrated, the time resolution provided by the timing reference is far better than the telescope planes. One can envisage multiple triggers arriving by the PMTs, the majority of them are recorded by the FE-I4 and DUT, but only a few are detected by the telescope plane after the first incident track is recorded, and the integration time is refreshed.

Table 7.1: Main features of test beam setup telescope planes, references, and DUT [28].

Detector	# of Pixels	Pixel Size	Intrinsic resolution	Timing resolution	Role
MIMOSA-26	1152x576	18.4x18.4 μm	5.2x5.2 μm	115 μsec	Telescope plane
RD53A SCC	400x192	50x50 μm	14.4x14.4 μm	-	Reference (spatial)
RD53A Quad	764x800	50x50 μm	14.4x14.4 μm	-	DUT
FEI-4 SCC	80x336	250x50 μm	-	25 $nsec$	Reference (timing)

the first telescope plane, to trigger and synchronize the DAQ system on particle passage. However, as previously mentioned, the telescope planes, DUT, and reference plane don't match in the timing resolution.

Due to this, one can imagine that due to the long integration time of the MIMOSA-26 plane ($115 \mu sec$), multiple triggers could arrive from the PMTs within the MIMOSA-26 integration time window, but only 1 hit is registered in the DUT. As will be discussed in the reconstruction method section, an implementation of a high-time-resolution plane is needed to verify that the reconstructed track is relevant to an event that was read out by the DUT. In our setup, the FE-I4 is the timing-reference plane to distinguish track events with a trigger time of $25 nsec$. Tab.7.1 summarizes the main features of the test beam setup planes, pixel size, and roles.

Moreover, as the DUTs are biased, a passive cooling method is used to maintain a temperature range of approximately -20°C to -40°C to compensate for the leakage current I_{leak}. In addition to this, as discussed before in Sec.4.3.2, the irradiated modules suffer from further increased I_{leak}. Irradiated modules are cooled down to a very low-temperature value. Hence, to compensate for increased I_{leak} a sealed cooling box was designed at the Max-Planck-Institut für Physik (MPP) to accommodate

Table 7.2: Materials radiation length X_0 for the setup consisting of Silicon sensors and other contributing materials along the tracks reconstruction [29].

Material Name	Radiation Length (cm)
Silicon	9.37
Kapton	28.57
Air	3.039×10^4
Aluminium	8.897

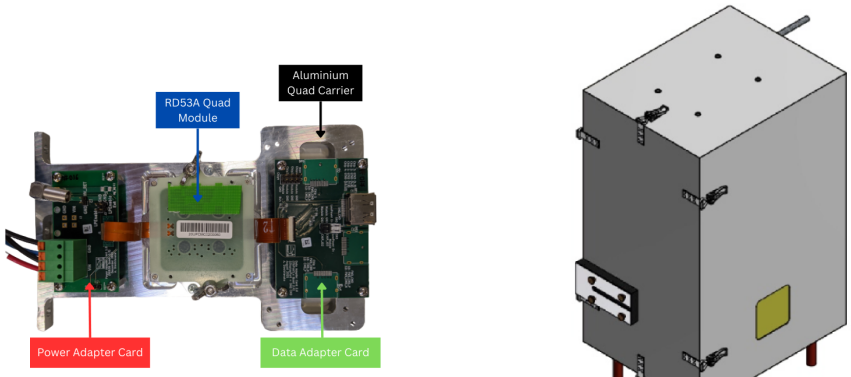

(a) (b)

Figure 7.4: (a) RD53A quad modules placed on a rigid Aluminium holder with data and power adapter cards. (b) The MPP cooling box used for the test beam setup in the H6A beam line.

multiple modules. The cooling box wall is built with two layers of 1.5mm aluminum sheets, filled in between with 46mm of Polyurethane insulating thermal material. Besides, to facilitate track reconstruction, the material budget is minimized as much as possible to reduce multiple scattering. Tab.7.2 summarizes the radiation length of each material in our test beam setup. Backstage, the EUDAQ software, YARR [87], and USBpix [88] DAQ systems interplay the architecture of data acquisition with the Trigger Logic Unit (TLU) [89]. The TLU arranges the trigger signals from the PMT at the up and downstream, which initiates triggering at the other planes. Each trigger responds to track passage once all triggers with a timestamp of each plane are acquired, a global event is constructed. However, EUDAQ is the main interface for controlling other DAQ systems by initializing, configuring, and controlling the readout. For the DUT, a unique software data manager, known as the YarrProducer is used to shape the DUT and manage the reception of tracks, and incident location, and integrate the DUT into the chain of planes in the setup. All of the producers in the setup contribute to the event builder, by consolidating event data collected from multiple detectors triggered by the same event. This merging process takes place in real-time during data acquisition,

carried out by the Data Collector software. The Data Collector gathers information from all Producers and amalgamates them into a unified file, which is then stored in a native raw binary format on disk.

During test beam data taking, it is possible to observe and track the evolution of runs by processing them online. The online monitor tool enables the shifters to check the quality of the runs, examine the position of the beam on the required ROI, and inspect any failure in the overall planes, due to increased noise, miss-alignment, regional pixel failures, and take measures to ensure high-quality data taking over the campaign.

7.3 Corryvreckan and Test Beam Analysis

Corryvreckan [90] is a powerful and versatile C++ software tool developed for the offline analysis of test beam data for track reconstruction, cluster finding, calibration, and alignment algorithms, all tailored to optimize the analysis process. By seamless integration of various detector geometries and sensor technologies, it provides extensive friendly-user tools to conduct test beam data analysis.

Via Corryvreckan, handling raw data is possible to be directly implemented into the framework for analysis. In which a series of progressive steps are required to be inspected and checked for proper result outcome. The analysis flow of test beam data is as follows:

1. **Data input**: Using the EventLoader by EUDAQ converter, that handles the raw data to perform an initial reconstruction of the hit map to its corresponding detector plane. Taking into account, the pixel geometry provided by the user configuration file, and the Producer.

2. **Mask creation**: Executes the raw data file to look for any over-firing pixels, which potentially indicate noisy pixels. The function method of doing so is based on determining noisy pixels by looking over any pixels that pose over the average of the pixels, a defined cut value, multiplied by the average. Afterward, if a pixel cross that limit, it will be masked, and a created mask file will be used for upcoming steps. Note that, similar masking of pixels is done before, by tuning the detector.

3. **Spatial clustering**: One can imagine that an incident particle passes through multiple numbers of the pixel, in which charge will be collected due to the particle passage in different pixels along the track. The charge collected at each pixel will correspond to the incident angle, position, and track depth in that pixel. This concept, known as charge sharing between different pixels due to the same particle is admired in HEP experiments. That is, charge sharing enables the sensor to go even higher spatial resolution by weighting the amount of charges in neighboring pixels. In multiple pixel channels charge sharing, an interpolation using relative energy to charge distribution measured by the electrodes gives better resolution. For MIMIOSA-26 sensors, the intrinsic resolution of $5.2\mu m$, goes down to $3.4\mu m$. The charge-sharing relation is

expressed using the η distribution [91] as follows:

$$\eta = \frac{Q_L}{Q_L + Q_R} \tag{7.1}$$

Therefore, a shared charge measured at the left pixel Q_L and right pixel Q_R will define a cluster seed. And based on the charge weight collected at each pixel, the track impact point can be deduced. Figure xyz visualizes the charge-sharing process. Consequently, all adjacent pixels sharing a common particle event will form a cluster. In Corry, the clustering center is calculated using the charge-weighted center of gravity (COG) method using:

$$\overline{n} = \frac{1}{Q} \sum_{i=1}^{N} n_i . q_i \tag{7.2}$$

In which $\overline{n}$ is the index of cluster center, n_i and q_i represent the column index (commencing from zero) and the recorded charge of the $i-th$ pixel within the cluster, respectively. Q denotes the total charge, and N signifies the cluster size.

4. **Correlation**: During test beam data taking, the online monitor performs correlation histograms to visualize the orientation between two detectors. In the analysis, the correlation of any detector is compared to the reference plane, in our case, the RD53A SCC. Correlation is done by taking the measured hits at one axis and comparing it to the reference plane axis. Positive overlapping in correlation plots indicates matching in sync with two detector planes and insures well-aligned planes, both in rotation, position, and entered dimension in config files in the direction of the beam. However, failing to have a positive correlation either during data taking means that desynchronization is present. In analysis, if a positive correlation of a diagonal line originating from the point-of-origin and stretching to 45° isn't present. One has to refer back to the config files to obtain proper results.

5. **Prealignment**: Achieving precise reconstruction of tracks in offline analysis imposes the need to perform multiple steps of refining the sensor planes position in the x and y axis, perpendicular to the beam. In the test beam setup, acquiring level of millimeters, down to micrometers of spatial resolution in lining up the setup is impractical. However, based on the information provided by the previous analysis steps, the cluster position in the telescope reference plane resolves the position of clusters formed on other sensors based on the same particle passage event. Therefore, repositioning of the misaligned planes are done, similar to the method of checking the correlation agreement, using the following shift procedure :

$$\Delta x = x_{ref} - x \quad , \quad \Delta y = y_{ref} - y \tag{7.3}$$

Moreover, multiple refining steps can gradually obtain prealignment to a few hundred of μm.

Nevertheless, misalignment down to the pixel pitch sizes still exists, and in order to resolve optimum track reconstruction, extra steps of alignment exclusively for the telescope planes, using the reconstructed tracks, will grant an accuracy for aligning the DUT afterward. Hence, the following two steps will pave the way, with several iterations, to obtain the best possible alignment.

6. **Alignment**: Using the updated config file with prealignment findings and spatial clustering, a simultaneous alignment of the telescope planes takes place to reconstruct tracks. This step is iterative, where constrained cut values are gradually increased to reach the residual distribution of well-aligned telescopes that matches the expected sensor binary resolution performance, expressed as [8], p. 62:

$$\sigma^2_{intrinsic} = \int_{\frac{-p}{2}}^{\frac{p}{2}} \frac{x^2}{p}\, dx = \frac{p^2}{12} \rightarrow \sigma_{intrinsic} = \frac{p}{\sqrt{12}} \tag{7.4}$$

Therefore, the tracks fitting algorithm within the Corry framework utilizes an iterative approach to refit individual tracks, aiming to minimize their χ^2 values using Minuit2 [[92]] and using the global broken line algorithm (GBL) [93]. This iterative process involves optimizing the detector positions and orientations while progressively reducing the spatial matching criteria until achieving sub-micron precision in the alignment procedure. Once all telescope planes are properly aligned, the alignment of the DUT is carried out using the reconstructed telescope tracks. This is achieved by minimizing the distance between the position of a DUT cluster assigned to the track and the track intercepts with the DUT plane. Hence, good alignment would be achieved when narrow Gaussian distribution set around zero is achieved. This simply means that the distance between a reconstructed track x_{track} on the telescope planes, and its associated cluster center x_{hit} in the DUT are well aligned in x and y directions, as the following equation states:

$$x_r = x_{track} - x_{hit} \quad , \quad y_r = y_{track} - y_{hit} \tag{7.5}$$

7. **Track Association on DUT**: Following the alignment of the telescope planes and DUT, track association based on the spatial clusters is executed. This step also requires multiple iterations to reach the spatial limits of assigning a track to the cluster's nearest pixel. For track association, the spatial limitations are gradually decreased to achieve the following condition:

$$\frac{x^2_{dist}}{x^2_{limit}} + \frac{y^2_{dist}}{y^2_{limit}} \leq 1 \tag{7.6}$$

Where x_{limit} and y_{limit} are the spatial limits and x_{dist} and y_{dist} are the distance between the track intercept on DUT and the nearest pixel cluster.

8. **DUT efficiency calculation**: This is the final step of the analysis which deduces the DUT

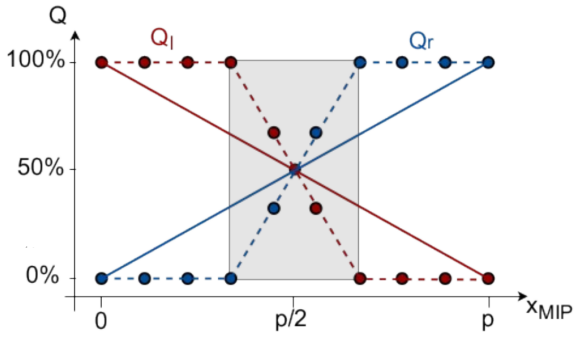

Figure 7.5: Charge sharing between two adjacent pixels. The y-axis shows the percentage of charge collected based on the incident particle location at the x-axis. left pixel is denoted as position 0 of the MIP passage and $p/2$ is the edge of both pixels. Finally, p is the right pixel. Based on the incident location, an extrapolation based on the COG charge sharing increases the intrinsic resolution.

performance by evaluating if the reconstructed tracks on the reference plane, found their matching associated clusters on the DUT. The hit efficiency ϵ_{eff} defines the detector properties between clusters on DUT, which are assigned to the reconstructed tracks if they are within twice the pixel pitch in both directions. Hence, ϵ_{eff} is computed using:

$$\epsilon_{eff} = \frac{Number\ of\ associated\ clusters\ on\ DUT}{Number\ of\ tracks\ intersecting\ reference\ plane} \tag{7.7}$$

7.4 Experimental Setup and Results

Several test beam campaigns have been conducted for the first time using RD53A quad-module prototypes, with three main DUTs since 2021. A subset of results is introduced to highlight the main sensor properties figures. The performance of these DUTs is evaluated to investigate the potential impact of voltage bias and irradiation on the desired pixel-hit efficiency requirements, using a Pion beam of E = 120GeV. The test beam setup schematic is illustrated in detail in Fig.7.6. Several consecutive runs with similar setup conditions are performed and joined as batches for offline analysis, and compared in hit-efficiency, and intrinsic resolution at different campaigns for the RD53A quad-modules DUTs. As depicted in Figure xyz, the telescope planes are distanced along the direction of the beam, with the RD53A reference plane positioned just after the second MIMOSA-26 plane. In addition, the cold box accommodates two DUTs at low temperatures with the beam positioned only on a portion of the sensor size. The FE-I4 timing reference is positioned after the cold box, behind the fourth MIMOSA-26 in the downstream region. The total length of the telescope's two arms is approximately one meter, Tab.7.3 summarizes the distance between the planes that is

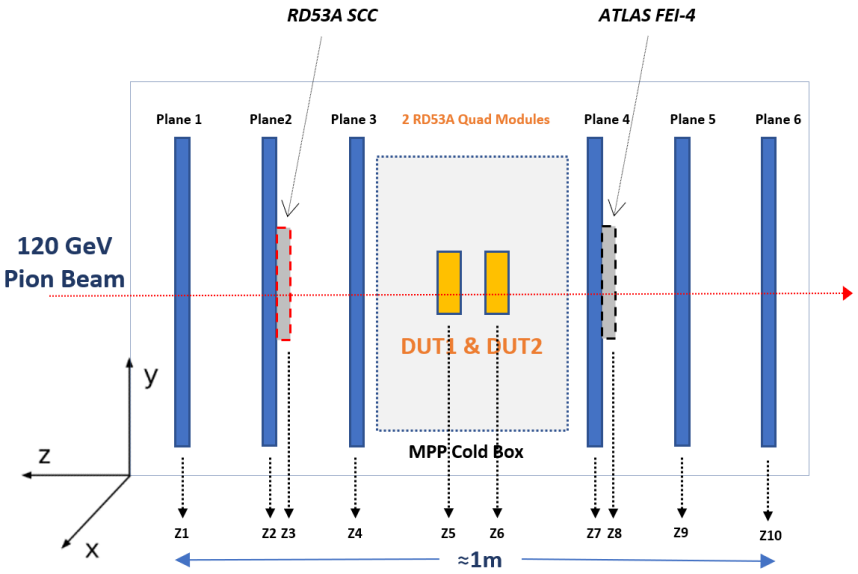

Figure 7.6: Test beam setup sketch summarizing the telescope planes position with the two reference planes, the RD53A spatial reference and the FE-I4 timing reference. The cold box is centered in between the two telescope arms and cooled down to -40°C.

implemented in the offline analysis.

Table 7.3: Test beam setup detector planes distances in mm along the beam direction as indicated in Fig.7.6.

Tele-1	Tele-2	RD53A SCC	Tele-3	DUT1	DUT2	Tele-4	FE-I4 SCC	Tele-5	Tele-6
Z1	Z2	Z3	Z4	Z5	Z6	Z7	Z8	Z9	Z10
0	152	182	304	469	569	763	790	915	1067

The test beam has been conducted on an unirradiated Q8 RD53A quad module of 150μm sensor thickness, which will be referred to as DUT1. In addition, another unirradiated Q2 RD53A quad module was accommodated in the cold box, of 150μm thickness manufactured with Micron vendor, which will be known as DUT2. Lastly, in another test beam campaign, an irradiated module up to $\phi_{eq} = 5 \times 10^{15} n_{eq}.cm^{-2}$ of HPK vendor, 150μm Q4 RD53A quad module was studied to conduct an investigation into the effect of long-term irradiation on the pixel-hit efficiency. The unirradiated quad modules were cooled down to 0°C, while relatively having good IV curve performance compared to the irradiated module that suffered from high leakage current. In order to compensate for this, an additional cooling using dry ice inside the cold box was implemented to reach -40°C. Tab.7.4 summarizes the operational conditions for the three different DUTs.

Table 7.4: Operational conditions for three DUTs in different test beam campaigns.

DUT	Batch Number	V_{bias} [V]	I_{leak} [μA]	T [°C]	Tuning Threshold [e]	ϕ [$n_{eq}.cm^{-2}$]
Q8	19	-130	-0.2	20	1500	0
Q2	19	-100	-4.8	25	1500	0
Q4	9, 12	-200, -600	1900,100	-5, -30	1500	5×10^{15}

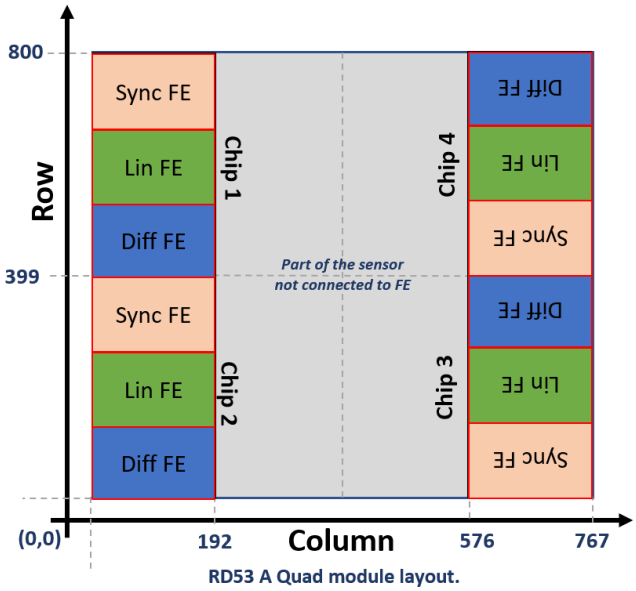

Figure 7.7: The layout of the RD53A quad module in which the central region is not connected to the sensor.

In Fig.7.8 (a), the hit map of the RD53A reference plane RD53A is shown. In which the beam is positioned on the linear FE of the SCC while having the syn AFE disabled. Moreover, as the RD53A quad modules are larger, only the part where the beam is positioned poses more hits. As seen in Fig.7.8 (b), the cold box is positioned so that the beam is focused on the third chip. However, not all of the pixels are uniform in pixel size. In our quads, the inter-chip region between different chips is 50x100 μm^2 for rows 398 and 399. By zooming in at Fig.7.8 (c) at the inter-chip region of our quad, it could be seen that larger pixels pose at least twice the number of hits compared to 50x50 μm^2 pixels. Those hit maps are performed for the spatial clustering, just after the masking of noisy pixels. As mentioned in the previous section, the created masking files, including Q2 and Q8 will be used for the entire offline analysis. As batch 19 includes a large data set of several runs it accumulates over 1.9 M events, a proper cut-off value for noisy pixels was chosen to discard unwanted discrepancies for the purpose of achieving accurate telescope alignment and reliable track fitting. Moreover, based on the offline reconstruction analysis steps, a good prealignment gives correlation plots that indicate proper overlapping in rotational and translation motion. As seen in Fig.7.8 (d), the difference in

cluster positions for the x-axis between the third telescope plane and DUT1 after prealignment marks a synchronization of alignment.

Furthermore, iterative refinements for telescope plane alignment and track fitting procedures using the GBL algorithm are done. After an initial alignment, an inspection of the expected intrinsic resolution indicates the quality of accurate track fitting. As seen in Fig .7.9 (a), the distribution of residuals in the x-direction after telescope alignment meets the desired mean intrinsic resolution for the six sensors discussed in Eq.7.4, while keeping in mind that six clusters per track were set to construct the tracks in all telescope planes. Simply meaning that to construct a track it is essential to find its corresponding cluster in all telescope planes.

Additionally, a second cross-check of the telescope plane alignment is to examine the spatial resolution that is quantified by the breadth of the impartial residual distributions. Here, impartial implies that these detectors are excluded from the track fitting process. The spatial resolution's extent, and consequently its measurement, is derived from the root mean square (RMS) of the residual distribution, as Fig.7.9 (d) indicates for DUT2. If the reconstruction is successful, the residual conforms to a Gaussian distribution centered around zero, with a characteristic width close to the pixel pitch.

Ultimately, the analysis afterward aims to check the RD53A quads hit efficiency. To perform this, the clusters found on the DUTs must be assigned to the reconstructed tracks with the telescope planes. The boundaries of spatial association between a single DUT cluster and track are explored using two non-irradiated quad modules for the default size of 50x50 μm^2 pixels as well as for the inter-chip area. The unirradiated DUT1 and DUT2 ϵ_{eff} are evaluated using many runs within the batch 19 data set to assess hit efficiency individually. In which the quad module with all functional chips enabled are subjected to testing using the beam spot positioned on various chips. Moreover, it could be seen that not all runs when analyzed individually have similar efficiency. Collectively joining all runs in one batch gives the efficiencies indicated in Fig.7.10 (a) and (b) for both unirradiated DUTs. Based on the ITK planar sensors requirements a non-irradiated 150 μm thick sensor must score ϵ_{eff} $\succ$ 98.5%, and $\epsilon_{eff} \succ$ 97% for -600 biased irradiated modules with a fluence of $\phi_{eq} = 5 \times 10^{15} n_{eq}.cm^{-2}$. Moreover, by assuming uniform behavior among pixels with the same geometry, hits, and tracks from all pixels are projected onto the coordinates of a single pixel. This process yields the in-pixel efficiency map, enabling a comprehensive analysis of hit efficiencies across different positions within the pixel. For DUT1, ϵ_{eff} clearly indicated high pixels reconstruction efficiency compared to our reference plane. In Fig.7.11 (a), this is indicated in the in-pixel hit efficiency considering a bias of V_{bias} = -130V. In contrast, DUT2 as shown before poses less ϵ_{eff} with V_{bias} = -100V, this could be also seen in significantly lower efficiencies at the sensor edge regions with pixel hit efficiencies in Fig.7.11 (b).

For the third irradiated DUT two different operational V_{bias} at -200V and -600V were tested. Following the same analysis procedure for the previously introduced DUTs, with -200V the ϵ_{eff} has

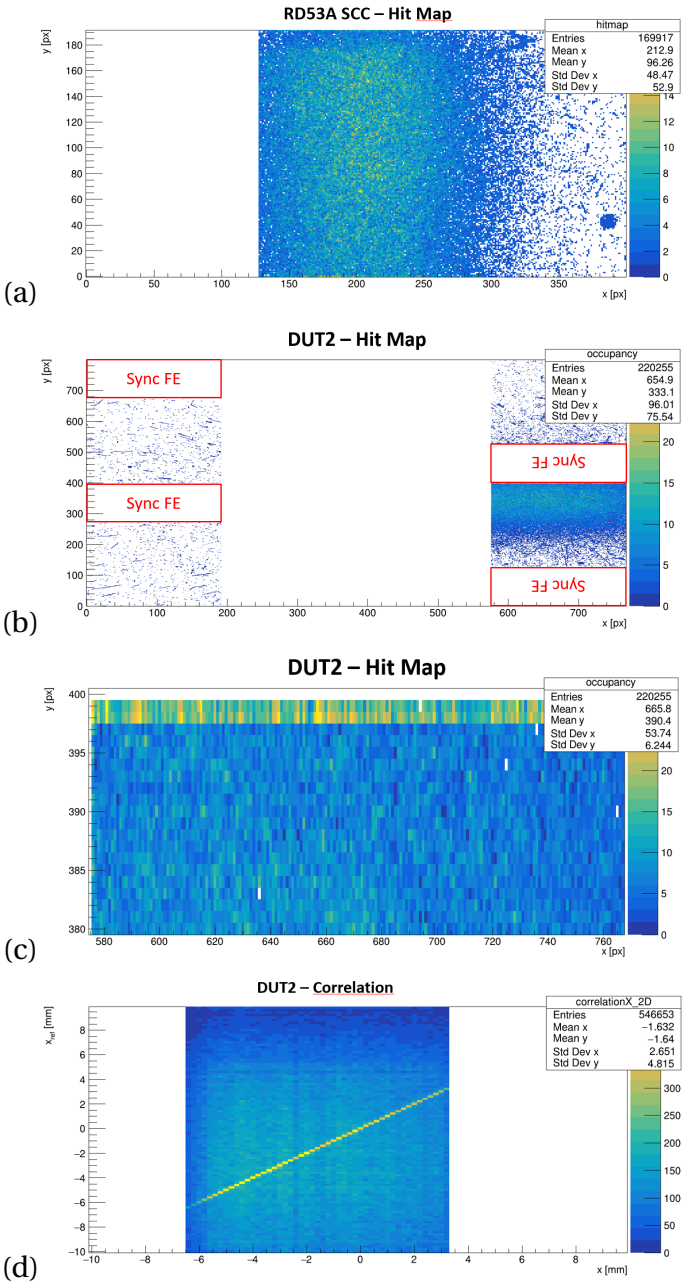

Figure 7.8: (a) RD53A SCC hit map clearly indicates the beam positioned in the center of the linear FE. (b) The quad module hit map shows a higher number of hits on chip3. Moreover, syn FE is disabled in all chips. (c) The inter-chip region between chip3 and 2 exhibits twice the number of hits compared to the average pixel matrix as seen in the top edge of the sensor. (d) Correlation plot between the third telescope-plane and DUT2. The diagonal line indicates that both sensors overlap in the beam and sync with each other. It could be seen also that hits due to multiple scattering or out of time will not be on this diagonal line, and straight lines in either horizontal or vertical directions emerge from noisy pixels.

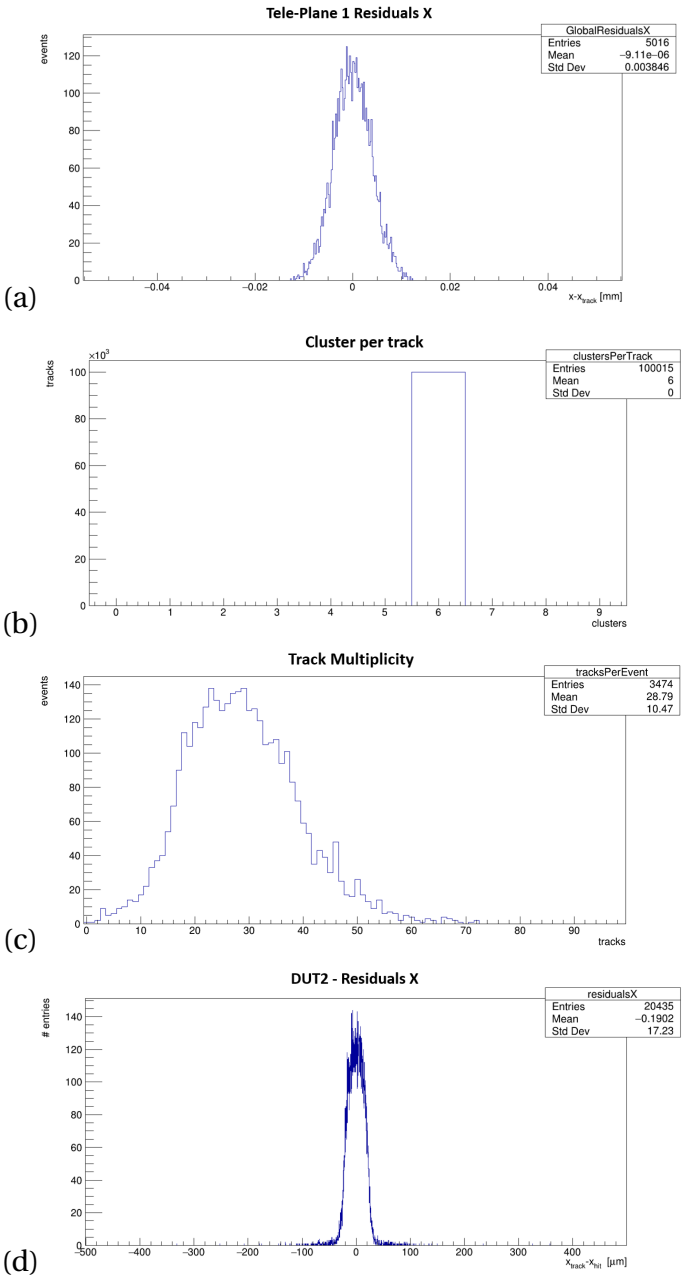

Figure 7.9: (a) The MIMOSA-26 first plane residuals in the x-direction after telescope alignment. The standard deviation indicates the expected intrinsic resolution of close to the optimum value of 3.25 μm. (b) The number of required clusters to construct one single track for telescope alignment. (c) Track multiplicity refers to the number of events that give rise to the reconstructed particle tracks in the telescope sensors. (d) The residual distribution of the second DUT in the test beam setup showing a convenient result for the telescope alignment with the residual RMS of 17.23 μm.

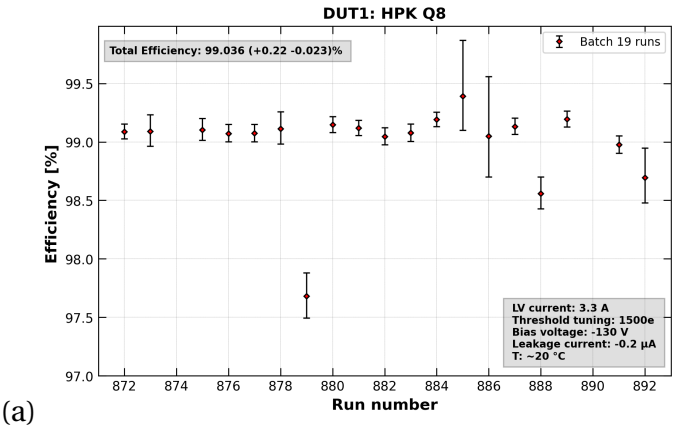

(a)

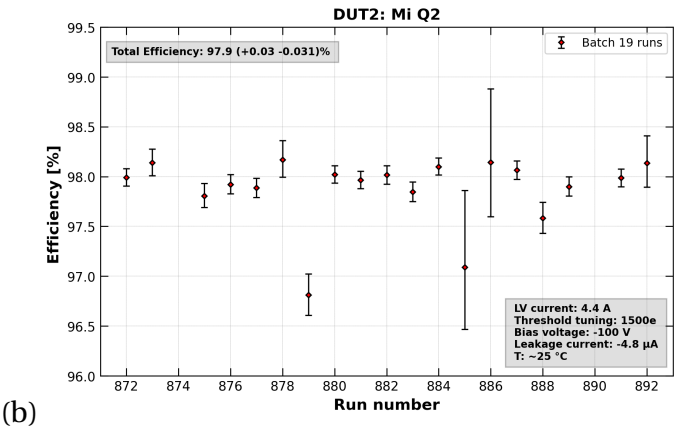

(b)

Figure 7.10: (a) Pixel-hit efficiency for unirradiated module operated with V_{bias} = -130 V with pixels threshold tuned on 1500e. The cumulative efficiency for all runs joined and analyzed collectively in batch 19 shows ϵ_{eff} = 99.034 ± 0.22 within the ITk planar sensors requirements. (b) Unirradiated DUT2 pixel-hit efficiency for the default-size pixel determined to be ϵ_{eff} = 97.9 ± 0.03 with an operating V_{bias} = -110 V, less than DUT1. The ϵ_{eff} score is less than the ITk requirements.

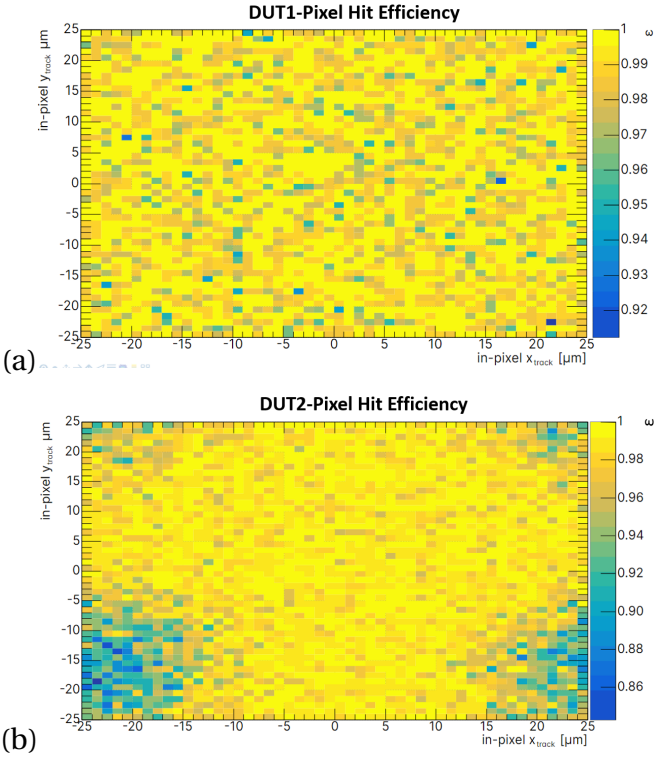

(a)

(b)

Figure 7.11: (a) In-pixel hit efficiency map for DUT1. (b) In-pixel hit efficiency map for DUT2 with low efficiencies at the sensor corners.

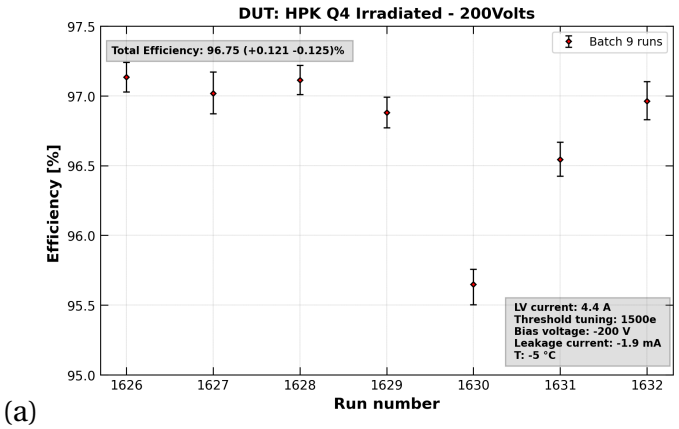

(a)

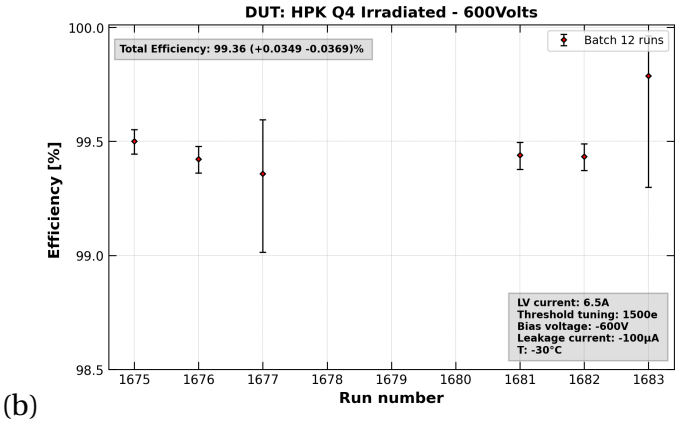

(b)

Figure 7.12: (a) Selected runs efficiencies for irradiated DUT3 with -200V bias. The ϵ_{eff} is less than the required ITk planar sensors recommendations. (b) Same irradiated modules with a different bias at -600 achieving higher efficiencies with recovering the in-pixel hit losses at the corners.

been found to be 96.75 ± 0.121 %, with efficiency losses in the pixels sensor edge as illustrated in Fig.7.13 (a). On the contrary, raising up the V_{bias} to -600 boosted the measured efficiency ϵ_{eff} = 99.36 ± 0.035% with significant improvements on the in-pixel hit efficiency map as in Fig.7.13 (b). Hence, for the irradiated module elevating the bias results in efficient recovery compared to the lower bias value. Considering the ITk requirements, the achieved ϵ_{eff} is within the vital limits with a uniform hit efficiency as in the unirradiated DUT1.

Apart from this, comparing residual distribution for the tested DUTs at different biases shows no difference in the expected RMS value as in Fig.7.14. Lastly, a summary of the outcome of the results with the DUTs attributed efficiencies is summarized in Tab.7.5.

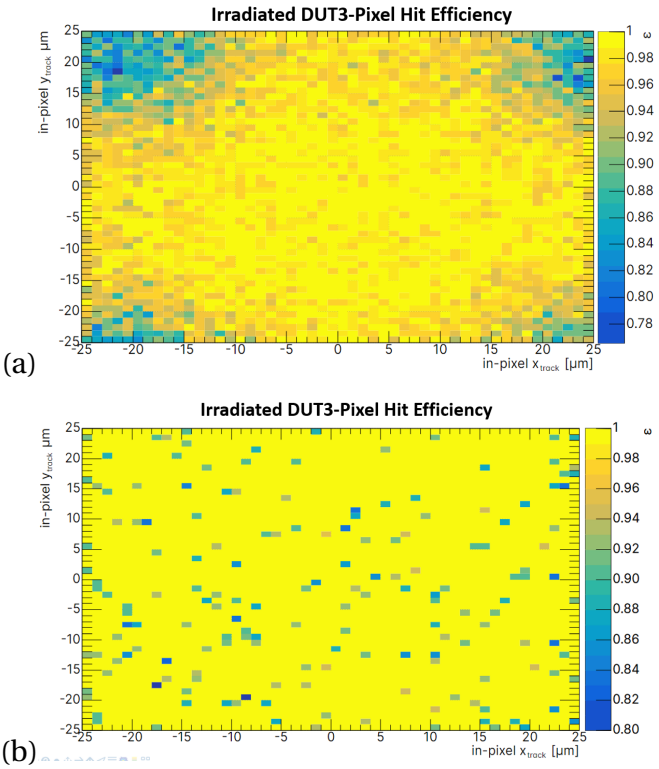

Figure 7.13: (a) Shows the hit efficiency as a function of the positions of the pixels at -200V bias voltages. (b) shows the in-pixel hit efficiency map at 600V.

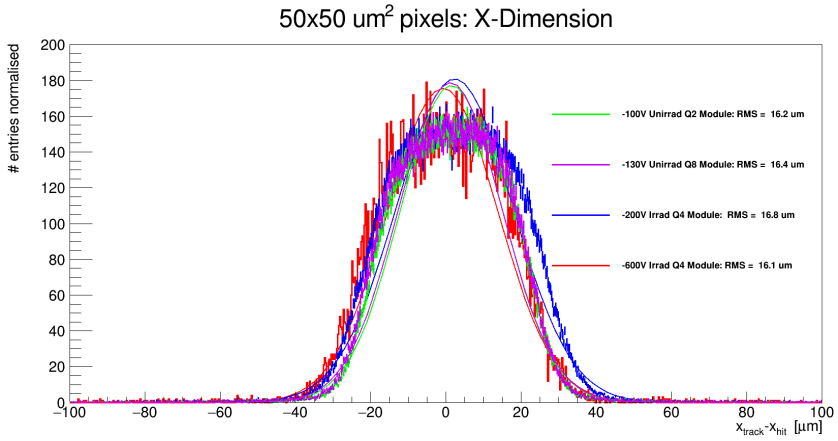

Figure 7.14: Summary of the DUTs residual distribution for the 50x50 μm^2 pixels in the x-direction that are compatible with the expectations for the given pixel size. However, for the irradiated DUT3 the distribution is disturbed with a slightly higher RMS value due to reduced charge sharing after irradiation.

Table 7.5: Operational conditions for three DUTs in different test beam campaigns.

DUT	V_{bias} [V]	I_{leak} [μA]	T [°C]	Threshold [e]	ϕ [$n_{eq}.cm^{-2}$]	ϵ_{eff}
Q8	-130	-0.2	20	1500	0	99.036±0.22%
Q2	-100	-4.8	25	1500	0	97.9±0.03%
Q4	-200, -600	1900,100	-5, -30	1500	5×10^{15}	96.75±0.121%, 99.36±0.035%

7.5 Conclusion and Remarks

In conclusion, our test beam setup allowed us to calculate the intrinsic resolution of the telescope planes, a crucial parameter for accurate particle tracking. Through meticulous analysis, we determined that the intrinsic resolution of the telescope planes was reliably estimated at 3.8 µm, which served as a pivotal input for subsequent analyses.

Furthermore, our efforts in achieving precise alignment between the RD53A quad modules and the telescope planes bore fruit, as evident in the achieved RMS residual distribution. This distribution, which represents the deviation between reconstructed tracks and actual hit positions, serves as a pivotal indicator of overall system performance. Remarkably, the meticulous alignment process yielded an RMS residual distribution well within the expected performance envelope, thereby validating the reliability and accuracy of our alignment methodology.These outcomes collectively reinforce the robustness and viability of the RD53A quad modules for potential integration into the intricate apparatus of high-energy physics experiments. By effectively characterizing intrinsic resolution and achieving favorable residual distribution outcomes, our test beam campaign has not only provided essential insights but has also bolstered confidence in the feasibility of these modules for the demanding requirements of ITk requirements.

In addition, our comprehensive test beam setup successfully evaluated the performance of three RD53A quad modules using the pion beam at the SPS. Among these modules, DUT1 and DUT2, both unirradiated, displayed robust pixel hit efficiency, aligning well with the RD53A SCC and adhering to the stringent requirements of the ITk planar sensor. It's noteworthy that DUT1 and DUT2, operated at different bias voltages, revealed superior performance in the in-pixel hit efficiency map when higher bias was employed.

However, DUT3, the irradiated module, presented distinct challenges due to its reduced charge-sharing properties resulting from irradiation effects. This necessitated testing at extremely low temperatures of up to -40°C to mitigate leakage current. Notably, when tested at lower bias, DUT3 exhibited shortcomings in meeting ITk requirements and suffered from diminished hit efficiency. Yet, a substantial increase in bias voltage led to remarkable improvements, effectively restoring hit efficiency and aligning with ITk standards.

Moreover, our test beam campaigns played a pivotal role in the development of the YARR software and the corresponding producers, essential components for the successful readout of RD53A quad

modules. This holistic assessment of module performance and the derived insights into bias voltage and temperature effects greatly contribute to advancing our understanding of these components and their suitability for the challenging demands of future high-energy physics experiments.

8

The Outer Barrel Demonstrator Project

The construction of the outer barrel demonstrator using RD53A quad modules represents a meticulously orchestrated endeavor with distinct stages, each contributing to a comprehensive evaluation of module performance and the establishment of a reliable quality control framework. This chapter embarks on a comprehensive journey through the key milestones and objectives achieved in this ambitious project.

The foundation of this work lies in the collaborative effort of acquiring assembled RD53A quad modules from multiple ITk cluster networks. These RD53A quad modules, serve as the fundamental building blocks of our demonstrator. The subsequent stages, however, delve into the intricate process of module calibration and assembly, involving five successive phases to ensure optimal performance before mounting in the demonstrator staves. Each module's performance is rigorously inspected at an individual level, encompassing a spectrum of electrical and optical analyses. These examinations, meticulously conducted, provide valuable insights into the consistency and stability of module behavior, thereby enhancing our understanding of their operational reliability. Moreover, a selected number of modules will undergo repeatability assessments, temperature, and voltage bias tests.

A pivotal aspect of this chapter centers around the innovative tool developed for quality control and yield evaluation. This novel tool, underpinned by a well-defined criteria set, meticulously identifies and quantifies open bumps, poorly tuned pixels, and subpar analog or digital performance. This analysis culminates in the computation of total defects, allowing us to effectively gauge the quality of the quad modules. Upon individual investigation, the modules converge to form a collective entity, stacked to offer an opportunity to identify trends in pixel defects. This interconnected examination contributes to a comprehensive understanding of potential systematic issues that may manifest in the assembled modules. An intriguing aspect of this study is the comparison between disconnected

bump scans and X-ray or source scans. This comparative analysis, involving all 114 chips of the outer barrel demonstrator, aims to ascertain the effectiveness of each scanning method for potential mass production deployment within the ITk framework.

As this chapter draws to a close, our journey culminates in a comprehensive conclusion, augmented by insightful remarks and recommendations that encapsulate the valuable lessons learned from the production line of the demonstrator quad modules process.

8.1 Overview of the ITk OB Construction Project

In the context of the broader ITk project, the outer barrel demonstrator serves as a pivotal component in the pursuit of a comprehensive validation of critical concepts and methodologies. Designed as an accurate emulation of the final detector setup, the demonstrator plays a crucial role in assessing and validating key elements, including the Data Acquisition Systems (DAQs), the innovative powering scheme SLDO (Serial Low Dropout Regulator), and the local loaded support structures that house the cell-loaded quad modules.

Central to the current phase of the demonstrator construction are the RD53A quad modules, carefully selected for their proven reliability and suitability for the task at hand. These modules embody a significant step toward realizing the ITk outer barrel's vision, encompassing sophisticated functionalities and attributes that align with the demanding operational requirements of high-energy physics experiments.

As we peer into the horizon of the ITk project's future, the impending production of the ITkPixV2 quad modules looms large. Anticipated to initiate during the early phases of the ITk outer barrel production, these modules will be sourced from an array of validated ITk clusters and laboratories. The scale of this endeavor is truly impressive, with an envisaged production target of approximately 4472 modules in the ITk outer barrel, accompanied by a corresponding number of meticulously engineered local loaded supports as seen in Tab.8.1, distributed in multiple layers of two main LLS structures.

Table 8.1: Summay of a total number of modules and local loaded supports in two different structures for the outer barrel ITk section. In this table, longerons are indicated by "lngrn" and inclined half rings with (IHR).

Layer	OB Flat Section			OB Inclined Section		
	# of lngrns	# of mod./lngrn	# of mod./layer	# of IHR	# of mod./IHR	# of mod./layer
2	16	36	576	24	16	384
3	22	36	792	32	22	704
4	28	36	1008	36	28	1008
Total	66	-	2376	92	-	2096

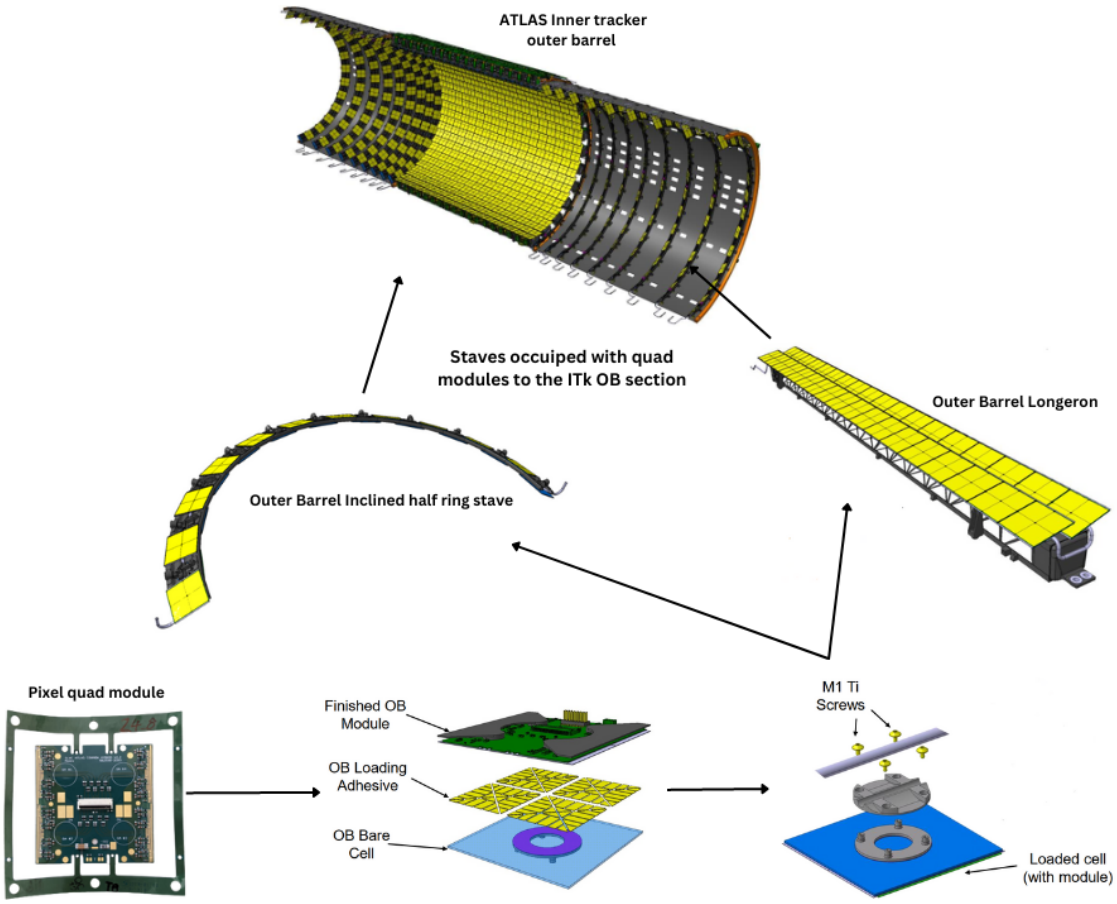

Figure 8.1: Overview of the ITk construction initiates with an assembled ITkPixV2 quad modules that are later loaded and cell-integrated on the local loaded supports. Images are edited and taken from [22]

8.2 Modules for the OB demonstrator

The construction of the Outer Barrel (OB) demonstrator modules represents a significant milestone for the demonstrator project. A total of 32 modules have been assembled, drawing on contributions from esteemed institutions and clusters worldwide. Among the contributors are the French cluster, KEK in Japan, CERN, Liverpool, Siegen, and Gottingen. The following sections delve into the intricacies of this construction process, one key aspect that stands out is the application of electrical scans to ensure the operational quality of each module and reliability. The utilization of electrical scans emerges as a crucial assurance measure in the construction of Outer Barrel demonstrator modules. These scans serve as an integrity test of each module before integration into the larger system. These electrical characteristics provide a comprehensive snapshot of the module's health, aiding us in identifying deviations and potential anomalies that could impede its optimal performance. A summary of the electrical testing procedures deployed as a regulation at all of the ITk cluster sites will be introduced in Sec.8.2.4. For comparability reasons, the electrical scans and visual inspection measures for all modules before and after arriving at the Pixel laboratory at CERN are identical. At CERN, the module will follow pre-defined production stages that will be discussed in detail. Within that, a repeatability test on Goe4 quad modules is introduced with temperature and bias studies on Paris6 quad modules in Sec.8.2.2 and Sec.8.2.3. Moreover, the OB demonstrator is briefly introduced with its associated on and off-detector systems in Sec.8.3, explaining the setup, testing plan, and summarizing the overall production performance of the Inclined Half Ring (IHR) modules. Finally, this section will be enclosed with a conclusion and remarks based on the contribution of testing 32 RD53a quad pixel modules, in Sec.8.4.

8.2.1 Module Electrical Scans Characteristics

As previously discussed, the electrical scans ensure the reliability of the module's performance. A large set of electrical scans are needed to characterize an individual module components functionality. As seen in Fig.8.2, the module consists of the sensor itself which is the active material for particle detection. While biased, the sensor features the IV curve characteristics, which based on the bias value poses a certain temperature-dependent leakage current. It is also worth mentioning that at some dedicated inspection scans, the sensor bias affects the ASIC electronics and vice versa. Moreover, ASIC electronics play a critical role in sensor pixel tuning, masking, and acquisition. The ASICs mainly consist of the analog circuit for preamplifing and shaping the signal, tuning the threshold of the pixels, and digitizing the hits in the digital domain. Nevertheless, the bump-bonding of the ASIC chip to the sensor pixels could cause issues, such as disconnections or short circuits to nearby pixels. The key point in the following testing procedure is to study either individually certain module functionalities, or collectively using a radioactive source or x-ray scan. The full testing

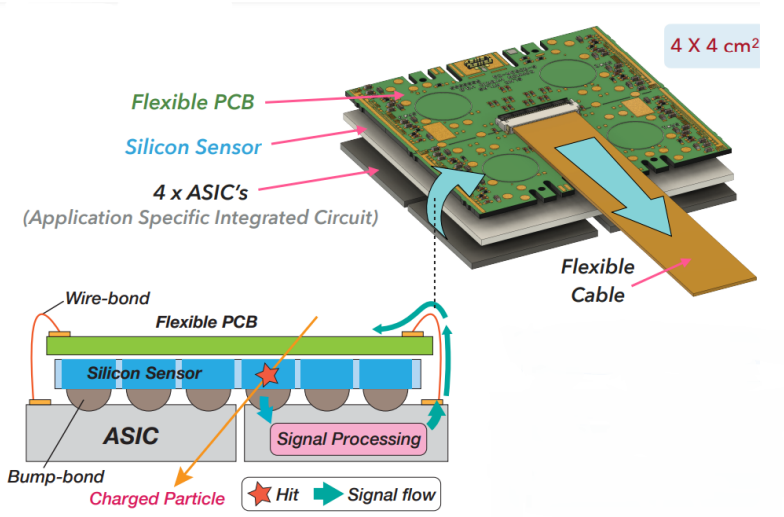

Figure 8.2: Overview of the RD53A quad module layout with a slice-view of the main components of the module layers. A particle hit originating at the sensor level would be preamplified and sent to the AFE domain to be digitized. The interconnection between the ASIC and sensor is done with the bump-bonding technique. The bumps work as an electrical connection that transfers the signal as illustrated in the cross-sectional view. Image edited and taken from [23].

procedure for RD53A quad modules is defined in [**?**] which in addition includes several thermal cycle tests in the temperature ranges between -55°C and 60°C to stress the module bumps and inspect any potential disconnections. An introduction to the electrical testing procedures with scans definition, inspection role, and chosen values are discussed.

Digital Scan: Involved fixed charge injection after the analog FE and before the digital core of the chip to check the connectivity in the form of occupancy per pixel. The response of the pixel digital FE is expected as the injection counts are known, and the performance response is evaluated based on the deviation from the anticipated value. For the OB demonstrator quad modules, the digital domain is tested with a fixed charge injection of 100e. Hence, if a deviation within $\pm 2e$ is detected, the pixel response is marked as good. Otherwise, more or less than $\pm 2e$ considers the pixel as a bad digital pixel. In case no response is measured with occupancy equaled to 0, the pixel digital part is referred to as digital $dead$.

Analog Scan: Similar to the digital test, the analog scan involved fixed calibration charge injection before the analog Front-End to check the time that the analog signal stays over the threshold. Based on the acquired charges after the threshold discriminator, the pixel analog FE will be categorized as either $good$, bad, or $dead$, similar to the digital analogy.

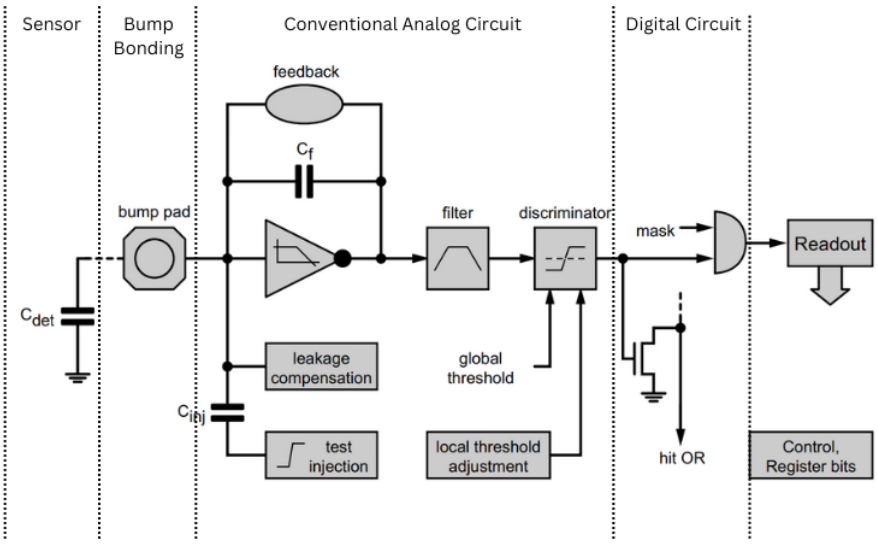

Figure 8.3: Conventional single pixel electronics circuit highlighting the main components of the analog and digital circuitry, bump-bonding connection, and the sensor treated as a capacitance. The electrical scans either test a single stage of this layout individually or collectively. Image taken and edited from [8], p. 135.

Threshold Scan: Is relevant to the analog circuitry by checking the threshold discriminator turn-on of the so-called S-curve. In an ideal case, a pixel response will remain off until the signal surpasses the defined threshold value, resulting in a step-function response. However, an attributed electronic noise is involved in smearing the step function which will result in shape distortions. Based on that, the scan is performed by injecting in steps a calibration charge before the analog FE to check the pixel response.

Whereas, the probability of having the S-curve signal as a function of the injected charge Q_{inj} is described by the convolution of a step-function with a Gaussian distribution, as follows:

$$S(Q_{inj}) = \frac{1}{2} erfc(\frac{Q_{thr} - Q_{inj}}{\sqrt{2}\sigma_{noise}}) \tag{8.1}$$

Where Q_{thr} is the S-curve mean turn-on position and the width defines the noise equivalent to the σ_{noise} induced electronic noise, and $Erfc$ is the complementary error function.

For the OB demonstrator modules, an identical response for similar AFE chip tuning values is used. The linear (Lin) and differential (Diff) AFEs will be tuned on $1500e$. However, the synchronous AFE will be tuned to $2500e$. Moreover, it must be noted that prior to chip tuning, a notable variance in pixel thresholds is always apparent. This discrepancy in threshold values is addressed through a dual approach encompassing both global and local threshold tuning. The global threshold tuning method serves to align pixels with higher and lower thresholds toward the desired target value. This is achieved by optimizing the settings of global digital-to-analog converters (DACs). In parallel,

the local threshold tuning technique involves adjusting the TDAC settings for each individual pixel. The objective here is to minimize the spread of threshold distribution per pixel, ensuring a tighter alignment around the specified target value with less noise.

Noise Scan: As previously introduced in the test beam analysis, prior masking of pixels that exhibit signals with no source of hits is essential. In which a routine of returning the pixels with a low threshold discriminator or disabling the pixel would be needed. A noise scan is done in advance before source or x-ray scans to mask untunable or noisy pixels. The method of doing so is based on trigger commands sent by the FE, in case a coexistence of noise and a trigger in a single bunch crossing, exceeds 10^{-6} hits, the pixel would be masked. In the case of the OB quad modules, the noise scan results would be attributed to the induced noise from the threshold S-curve width.

Time-Over-Threshold (ToT): Involves a fixed calibration of charge injection before the AFE to check the time that the analog signal stays over threshold. The time is measured in terms of bunch crossing (bc) of the HL-LHC beam.

Source or X-ray scan: With a radio-active or X-ray source it's possible to have the hit map of collected charges due to the particle interaction with the sensor. Regions with a lower number of hits – such as passive elements – could be easily visible. Hence, the Surface Mount Devices (SMD) will record much lower hits. The difference between working and non-working pixels would be large enough to readily identify disconnected Pixels. The results introduced in this thesis are done using X-ray scans distanced away from the quad module to have the beam covering the 4-chips with the three different AFEs. However, the noise scan is done before the X-ray scans to mask noisy pixels, while the X-ray scans last for at least 15mins. Furthermore, the X-ray scan plays a significant role in identifying dead pixels due to disconnection between the ASIC FE and the sensor due to the open bump. One can also imagine that X-ray scans testify to the complete circuitry of a single pixel as the hit originates in the sensors and is delivered by a bump connection to the FE for processing.

Cross-talk and Disconnected Bump Scans (DBS): Are used as a complementary scan method to identify open bumps based on specific criteria. As a non-edged single pixel is accommodated around adjacent pixels, a high charge injectioned sequentially in the 4 neighboring pixels, might result in an S-curve turn-on for the central pixel due to crosstalk. The information gained using this scan can be deduced to know if the pixel is connected by seeing charges read at the central pixel, or dead if no charge is detected. However, due to the fact that a high inter-pixel capacitance is used to isolate nearby pixels, a high charge injection is used for Syn AFE $25Ke$ value, with $40Ke$ for Lin, Diff AFEs to examine the connection of bump bonds. The injection pattern used for the OB modules is outlined in Fig.8.4. Moreover, the cross-talk scan is also used to detect merged bumps, this will be introduced in detail with the quality control (QC) Sec.8.5.1 studies. Moreover, the DBS uses the cross-talk scan approach to identify pixels without any crosstalk which is likely due to disconnected bumps. Based on analog scan with cross-talk mask. The DBS is evaluated by injecting in the neighboring pixels and checking the occupancy in the central pixel with fewer charges compared to the cross-talk scan.

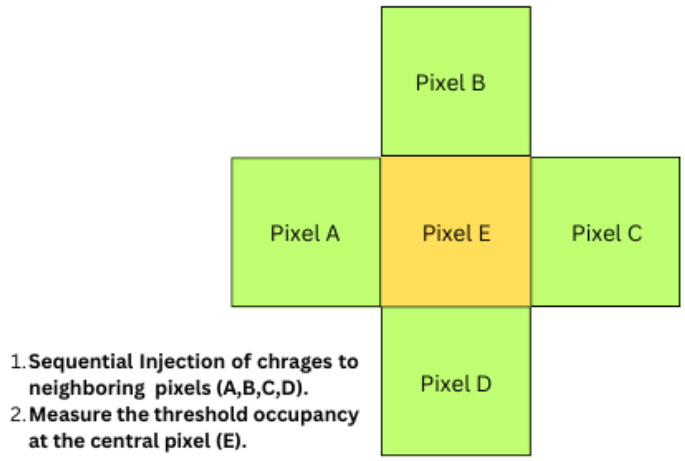

Figure 8.4: The injection pattern used to test the RD53A quad modules using the crosstalk scan. The nearby pixels in green are injected sequentially with high number of charges. Afterward, the threshold occupancy at the central pixel would be read to identify the presence of high charge sharing, known as high crosstalk, or to inspect if no charges are detected which could potentially indicate an open bump.

Forward Bias Scan (FWB): Is considered as an additional option to detect completely disconnected bumps. The methodology of FWB scan is based on the comparability of threshold and noise performance in HV bias to biasing the sensor with +1V or with no bias. While the pixels are biased with +1V, a shift in the pixel sensor capacitance would change the noise and the threshold of AFE charge amplifier. By comparing both measurements, the non-disconnected pixels would appear to have a shift in noise or threshold based on the AFE. However, disconnected pixels wouldn't react to the forward bias and are potentially considered disconnected. The noise power is typically proportional to the pixel capacitance and the pixel capacitance is dependent on the depletion zone. Hence, when the depletion zone shrinks the pixel capacitance increases, and thus the AFE noise and threshold increase. The relation describing this phenomenon is expressed as:

$$C(V) = \frac{\epsilon_0 \epsilon_{Si}}{W(V)} = \sqrt{\frac{e\epsilon_0 \epsilon_{Si} N}{2V}} \tag{8.2}$$

Where C pixel sensor capacitance, W is the depletion zone width, and N is the substrate doping concentration. One drawback of the FWB scan is the non-feasibility to conduct it on a serial power chain with multiple modules, as the modules would be damaged from high bias voltage created by the voltage drop measured between the last module at the chain and the power source ground.

Sensor IV curve: This is a fundamental characterization tool for pixel sensors, providing valuable insights into their electrical behavior and performance. By systematically varying the voltage

applied across the pixel sensor while measuring the resulting current, the IV curve unveils the relationship between these two critical parameters in addition to the leakage current dependency with temperature.

As the depletion region properties across the pixel sensor are affected by the increased or decreased bias, the corresponding response of the sensor at the full depletion is given by biasing at the plateau region. The IV curve not only reveals essential operational characteristics, such as breakdown voltage and leakage current but also offers a deeper understanding of the sensor's behavior under different voltage conditions including long-term irradiation effects.

For the RD53A quad modules, the IV curves were taken up to 200V with a step of 5V every few seconds. The compliance is set to $10\mu A$ to avoid any high current that could result in damaging the sensor. A comprehensive analysis of the IV curves in different production stages is done to assess the pixel sensor's overall health, identify potential anomalies, and optimize its performance within specific voltage ranges. Ultimately, the IV curve dependence on temperature is significant. A cornerstone in evaluating its performance would impose the need to normalize the IV-curves temperature and address uncertainties. Temperature corrections are done using the following expression:

$$I(T) = \frac{I(T_R)}{R(T)} \tag{8.3}$$

$$where \quad R(T) = (\frac{T_R}{T})^2.exp(\frac{-E_{eff}}{2k_B}(\frac{1}{T_R} - \frac{1}{T})) \tag{8.4}$$

In which the current is expressed as a function of temperature with T_R as the temperature to correct to, T is the acquired IV curve measurement, k_B is the Boltzmann constant, and E_{eff} is the effective Silicon band gap energy of $1.2eV$.

Module Turn-on temperature value: RD53A quad modules have a tendency to operate at a given temperature determined by testing when the chip communication is turned on. Hence, the turn-on behavior of the power domain using the SLDO is unstable and determined individually for the chips at a single quad module, due to the unreliability of the SLDO to provide a given voltage to the chip at all temperatures. Upon reception of the RD53A quad modules, execution of the VI scans procedure involves monitoring chip voltage against the input current from the power supply. The VI scan is conducted initially at -35°C, and if the results prove inconclusive, it is repeated at progressively higher temperatures in intervals of 15°C. The objective is to find the specific temperature threshold at which the readout chips achieve activation, ensuring an in-depth understanding of their operational characteristics under varying temperature conditions.

Apart from the electrical scans, functionality tests of chips upon module arrival are done. Including visual inspection of the wire bonding locations and quality of the module surface while transferred from the assembly site to the CERN pixel's lab.

Table 8.2: Summary of repeatable measurements with the operational conditions for Goe4 module.

Test	$T_{Chiller}$ [°C]	T_{NTC} [°C]	V_{bias} [V]	I_{leak} [μA]
1	15	31.5	-90	-1.279
2	15	31.4	-90	-1.29
3	15	32.1	-90	-1.356
4	10	28.3	-90	-1.02
5	17	34.2	-90	-1.5716
6	0	19.9	-90	-0.5167

8.2.2 Repeatability Measurements

Accurate characterization of pixel quad modules is important in ensuring the reliability and performance of these integral components by determining the ascertain of their consistency under similar conditions. One crucial facet of this comprehensive analysis is the undertaking of repeatability measurements. The significance of repeatability measurements transcends the confines of individual pixel quad modules and extends to the broader context of large-scale testing. Unearthing inconsistencies or variations in measurements at this early stage empowers us to anticipate challenges that might arise during extensive experimentation. This section focuses on the necessity and rationale behind conducting repeatability measurements using the Goe4 RD53A pixel quad module. To ensure the reproducibility of measurements and to preemptively identify any deviations or variations that might arise during testing, the Goe4 module was subjected to the following measurements as listed in Tab.8.2 using the setup indicated in Fig.8.5.

The overall measurements as indicated in the summary plots in Fig.8.6, and more detailed in Fig.8.7, show consistent behavior for the DBS, X-ray, noise, and threshold scans. However, deviations are seen at the lower temperature measurements for the threshold and noise distribution, which is expected and will be highlighted in detail in the next section. For the IV curve measurements, a correction to 25°C was done, it could be seen in Fig.8.5 (b) that, taking into account the error bars, the curves nicely overlay. The wider error bars for stage six measurement are due to the ±2°C of added uncertainty within the correction.

8.2.3 Temperature and Bias Voltage Measurements

The behavior of pixel quad modules is intertwined with the bias voltage applied to them and the temperature-rising effects. In this section, we focus on to the profound impact of bias voltage changes on the operational characteristics of a pixel quad module, all within the confines of a constant temperature environment. Paris6 quad module is to conduct this test while having its four chips working. Moreover, by systematically modulating the bias voltage between the ranges of [-115V,

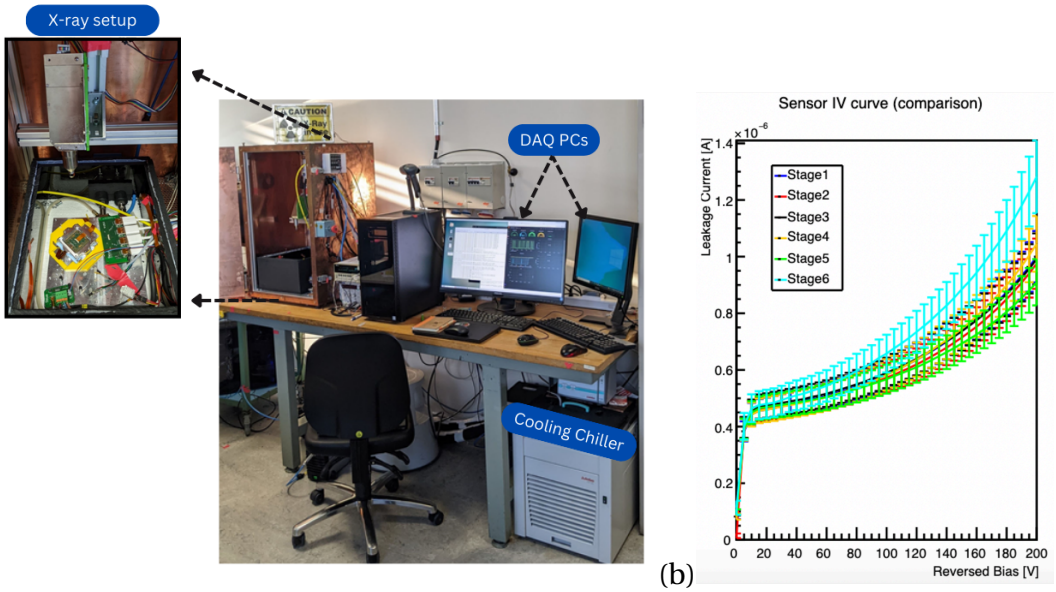

(a) (b)

Figure 8.5: (a) Testing setup for the RD53A quad module consisting of two PCs for DAQ with YARR, and the other for configuring the X-ray tube inside a thick aluminum box. The quad module is tested on a vacuum chuck cooled with a chiller, positioned under an x-ray tube, and distanced to have the beam on the total area of the quad module. (b) Summary of the IV curves measurements for Goe4 module with corrections to 25°C for comparability.

-100V, -80V, -60V, -40V, -20V] while keeping the temperature stable, we unravel the dynamic interplay between bias voltage and electrical scan behavior. This investigation not only sheds light on the responsiveness and sensitivity of the module to varying bias voltages but also serves as a pivotal step in comprehending its overall performance under controlled conditions.

Moreover, temperature fluctuations are an essential parameter of its operational envelope. Within this context, under the influence of varying temperatures between [30°C, 20°C, 10°C, 0°C, -15°C, -15°C] all while maintaining a constant high-voltage at -115V bias. The implications of temperature changes on the module's electrical characteristics, signal response, and noise levels come to the forefront. Moreover, the last stage of testing involved retuning the module at a low temperature before performing the electrical scans.

As seen in Fig.8.8 and Fig.8.9, voltage studies show a consistent output in all electrical scans, except for the DBS. As in Fig.8.8 (e), a slight increase in dead pixels is seen. On the other hand, temperature tests reveal more dependency on electrical scans. As the temperature goes down with a step of 10°C during testing stages, slight decreases in noise mean for the Lin and Diff AFE are seen up to stage five. At stage 6, new pixel tuning is done at -15°C, and electrical scans are performed. Whereas, the Syn AFE shows a significant increase in noise after tuning, compared to the same temperature value at stage 5. It also observed for other chips that retuning at -15°C increases the noise and gets the distribution tails wider. Fig.8.10 (e), illustrates the summary of noise performance

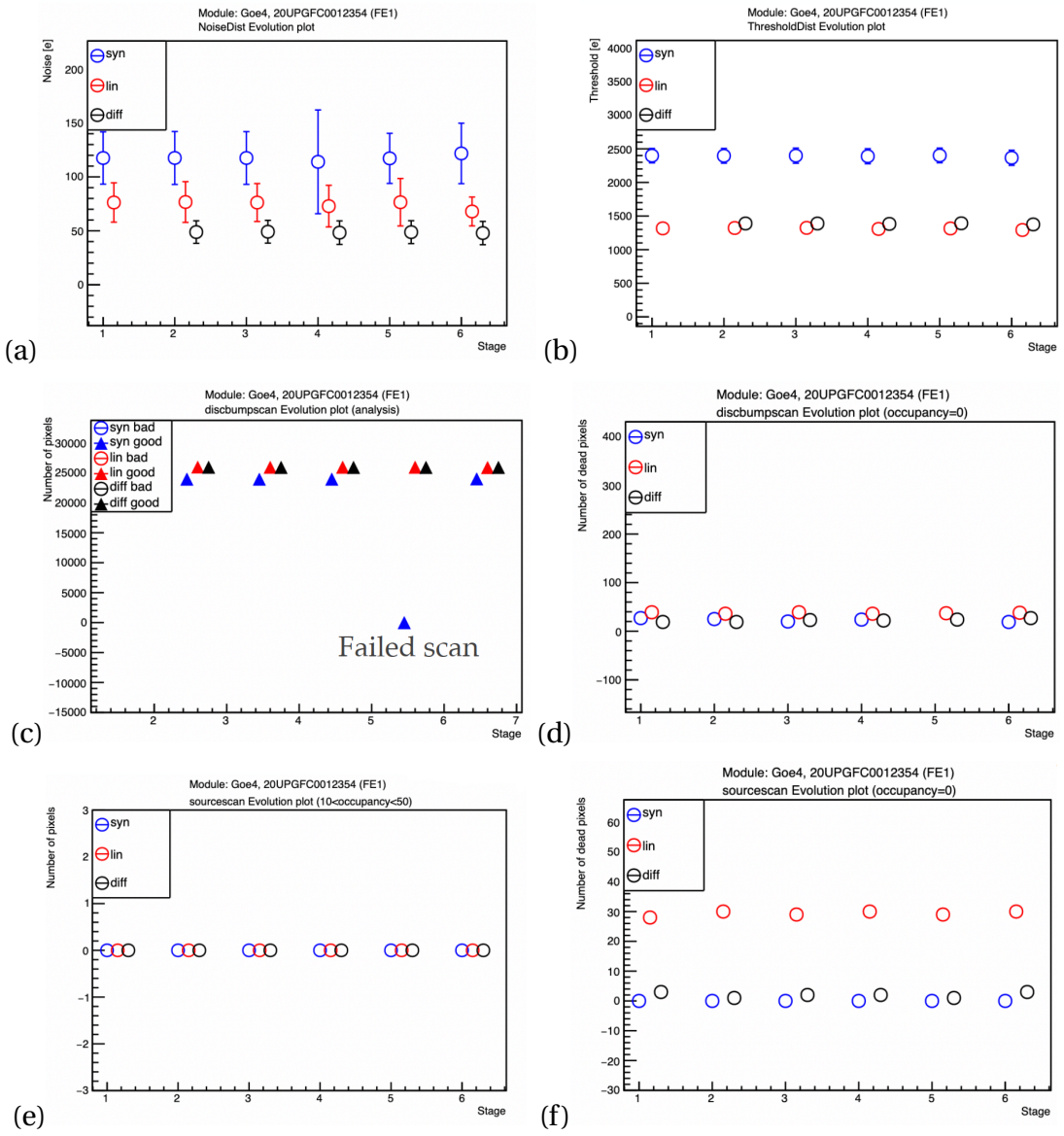

Figure 8.6: Collection of electrical scan repeatability results for Goe4 quad module based on the introduced setup measurements in table xyz. (a) Shows the noise in threshold scan evolution in the six tests, labeled as stages. The summary of the noise scans for only one chip is shown, where a failure in the noise scan is observed to be missing in the Diff AFE in stage one, however, as seen in stage six, noise is reduced due to lower temperature. Nevertheless, variations of ±3°C have barely any impact on the noise performance. (b) Presents the threshold scans featuring no variations on the acquired threshold means. Moreover, an inspection of the fitted threshold distribution and comments could be found in Figure xyz. (c) DBS summary for pixels performance in terms of the two categories, $good$, and bad. The summary indicates constant behavior across all stages. (d) DBS with dead pixels featuring occupancy equaled to zero are always present constantly through the stages. (e) X-ray scan summary for high occupancy that exhibits no fluctuations across the stages. However, in (f) Number of pixels with occupancy equaled to zero oscillates, with differences in a few more pixels found in stage six.

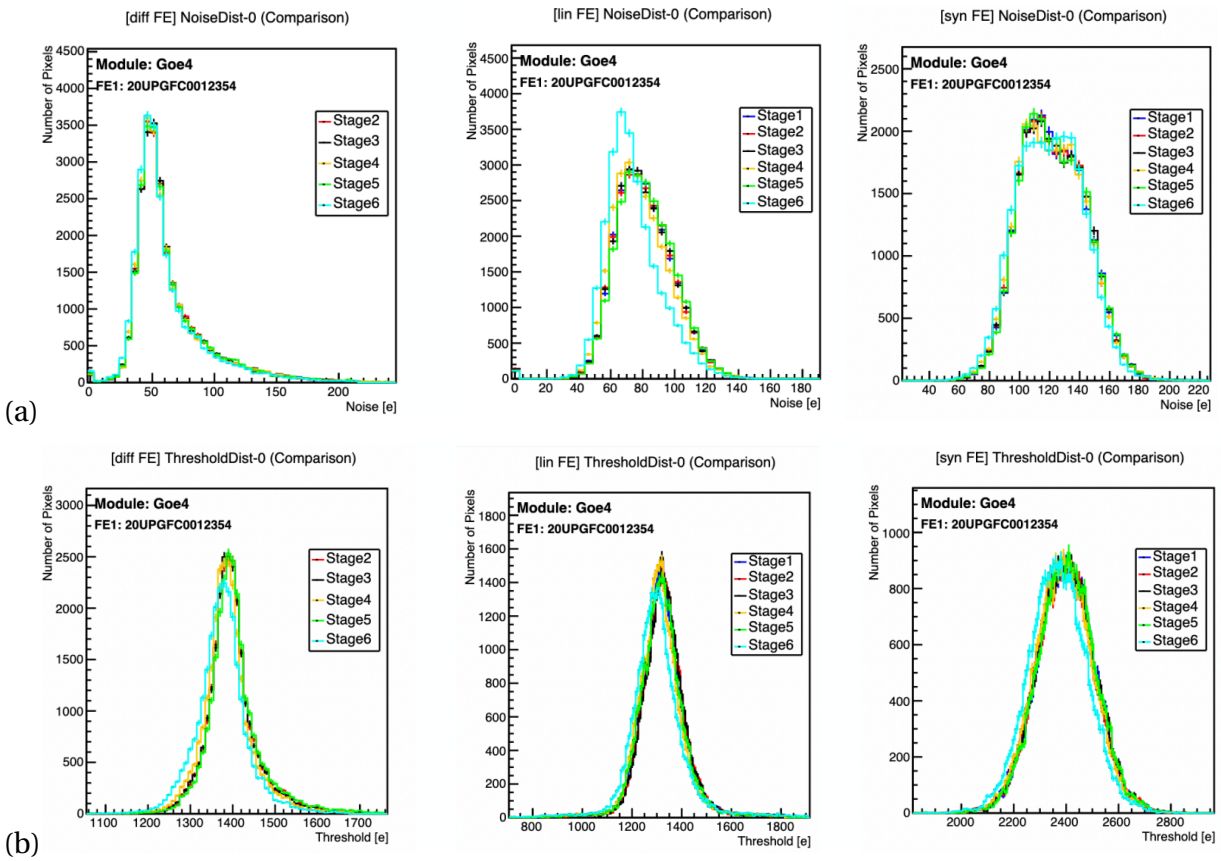

Figure 8.7: Summary of repeatability measurements of the noise and threshold distributions for the first chip in Goe4 quad module. (a) Three AFEs are presented, Syn, Lin, and Diff from right to left. Showing overlapping between measurements for the Syn and Diff AFE. However, for the Lin AFE, less noise is measured at stage six with a lower temperature test. (b) Threshold distributions overlap across testing stages. Nevertheless, at stage 6 it's observed to have a wider width compared to other measurements.

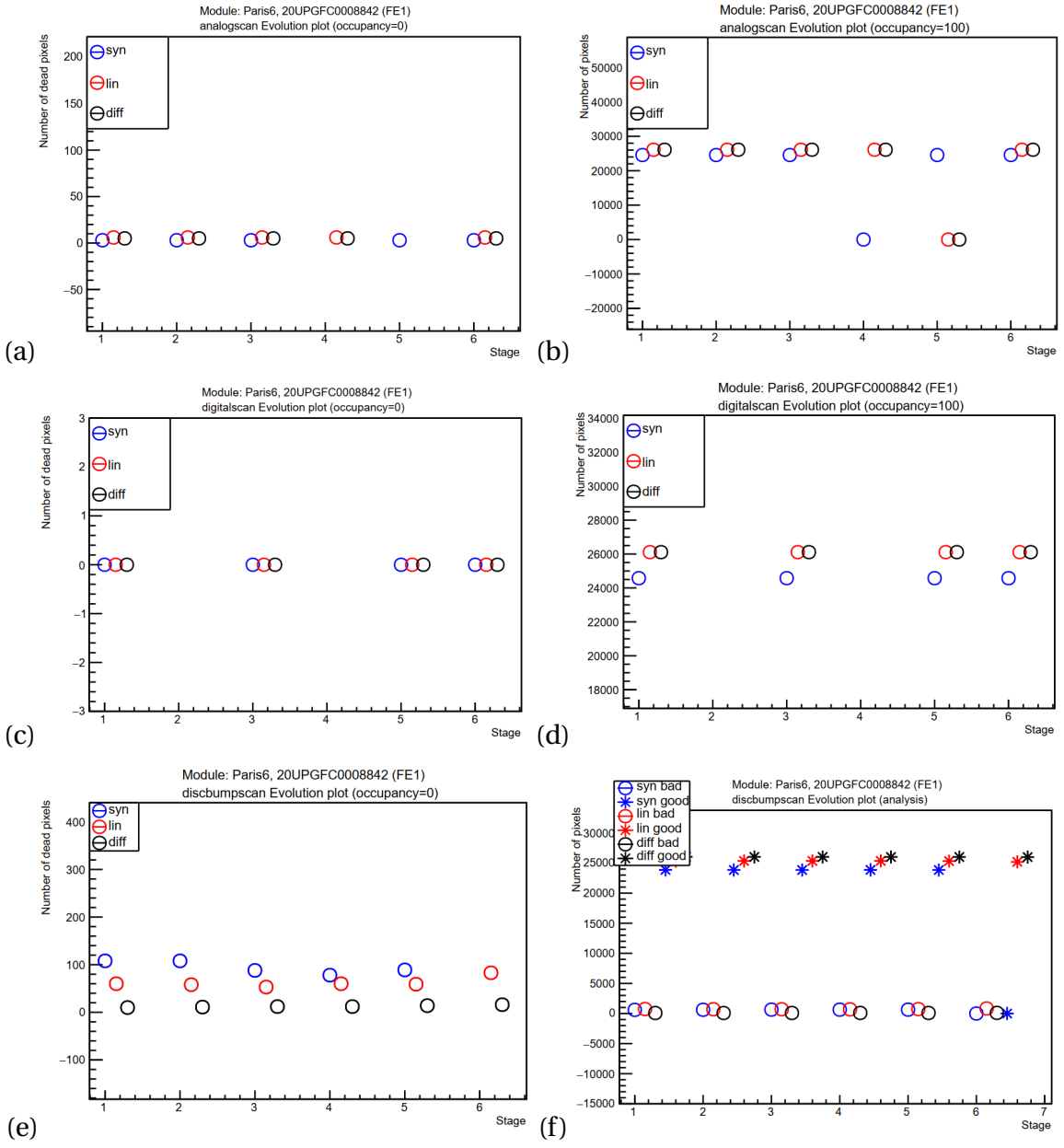

Figure 8.8: Summary of bias voltage variation results for the first chip of Paris6 quad module. (a) Shows the analog performance of dead pixels, and (b) for pixels with occupancy equaled to 100. Both plots show no significant change while ramping down the bias. However, at stage four a failure in the scan for Syn AFE is present. (c) and (d) highlights the evolution of dead digital pixels and pixels with occupancy equal to 100, with no effects seen due to changing the bias. Nevertheless, digital scans at stages two and four failed. In (e) and (f), a summary of the DBS shows a slight increase in the dead pixels, which is also seen in other chips. On the other hand, (f) shows the evolution of good and bad pixels.

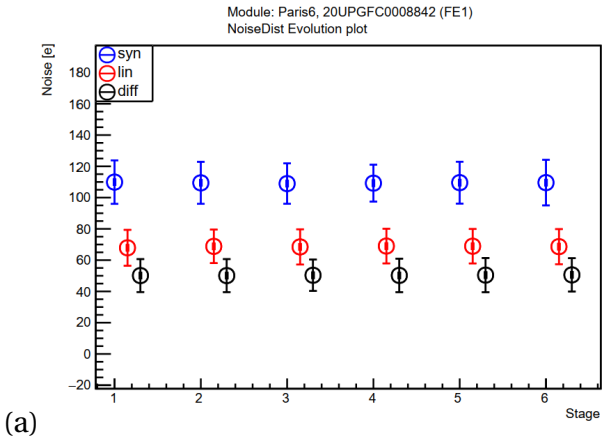

(a)

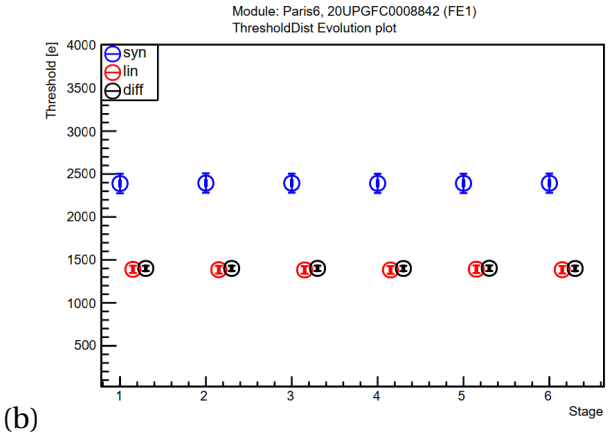

(b)

Figure 8.9: Bias voltage studies: (a) Indicates the noise in threshold scan for chip one with no variations seen while changing the bias voltage, in a well-controlled temperature environment. (b) Highlights the threshold scans which show consistent results in all stages.

with temperature, along with a fitting of the noise distributions for the three AFEs shown in Fig.8.11 (a). For the threshold scan, similar responses are depicted in the summary Fig.8.10 (f) along with the fits in Fig.8.11 (b) that reveal the distribution's dependency due to temperature and retuning at stage 6.

Furthermore, the DBS summary in Fig.8.10 (a) indicates increases in disconnected pixels which doesn't fit with the acquired results using the X-ray scan. In Fig.8.10 (c) and (d), two x-ray scans are done at high and low temperatures, which by comparing the disconnected pixels between both, reveals similar outputs.

8.2.4 Modules Production Flow

Characterizing the module performance with repeatability measurements, temperature, and bias voltage variation and related effects on the electrical scans output assisted in understanding in-depth the potential consequences. Moreover, in this section, an essential and important content of this thesis focuses on the 36 RD53A quad modules accomplished results at the presented production stages in production-line chart8.12. As previously mentioned, the followed procedure for studying the module's performance is consistent and repetitive in terms of the conducted electrical scans and production stages. The standardized QC measures across all production stages ensure direct inspections of any potential degradation by comparing the output to the previous and following stages.

The RD53A quad modules are received in a dedicated module carrier, as depicted in Fig.8.13 (a), with its dedicated configuration files parameters, initial electrical scans at the assembly site, and thermal cycled. This is the first stage considered for the production of the RD53A demonstrator project modules. The second stage at the CERN pixel laboratory is known as the reception stage where the quad module will check in terms of thermal calibrations using the FE negative temperature coefficient (NTC)[1] sensor, thermal cycled if not done at the assembly site, and conduct electrical scans to complement any missing studies. This stage doesn't involve any direct changes in the module characteristics, and any potential variations to the previous stage would be due to changing the testing setup environment or degradation related to transferring the module from one site to another. However, the third production stage involves the deposition of protection material on the module's wire bonds (WB). Coating the WB is important in protecting the signal flow, isolating the wires from short circuits due to module mishandling, and adding HV shielding between the sensor and the readout chip. The wire bonds at this stage will be visually inspected to ensure that they are connected based on the standardized production means. Afterward, the protection of the WB is done using the Sylgard, in the so-called potting stage. In principle, the material that would be used for the ITk project is Parylene because of the radiation hardness properties and mechanical robustness.

[1]At each chip in the quad module, an embedded NTC value could be read to obtain the temperature measurements.

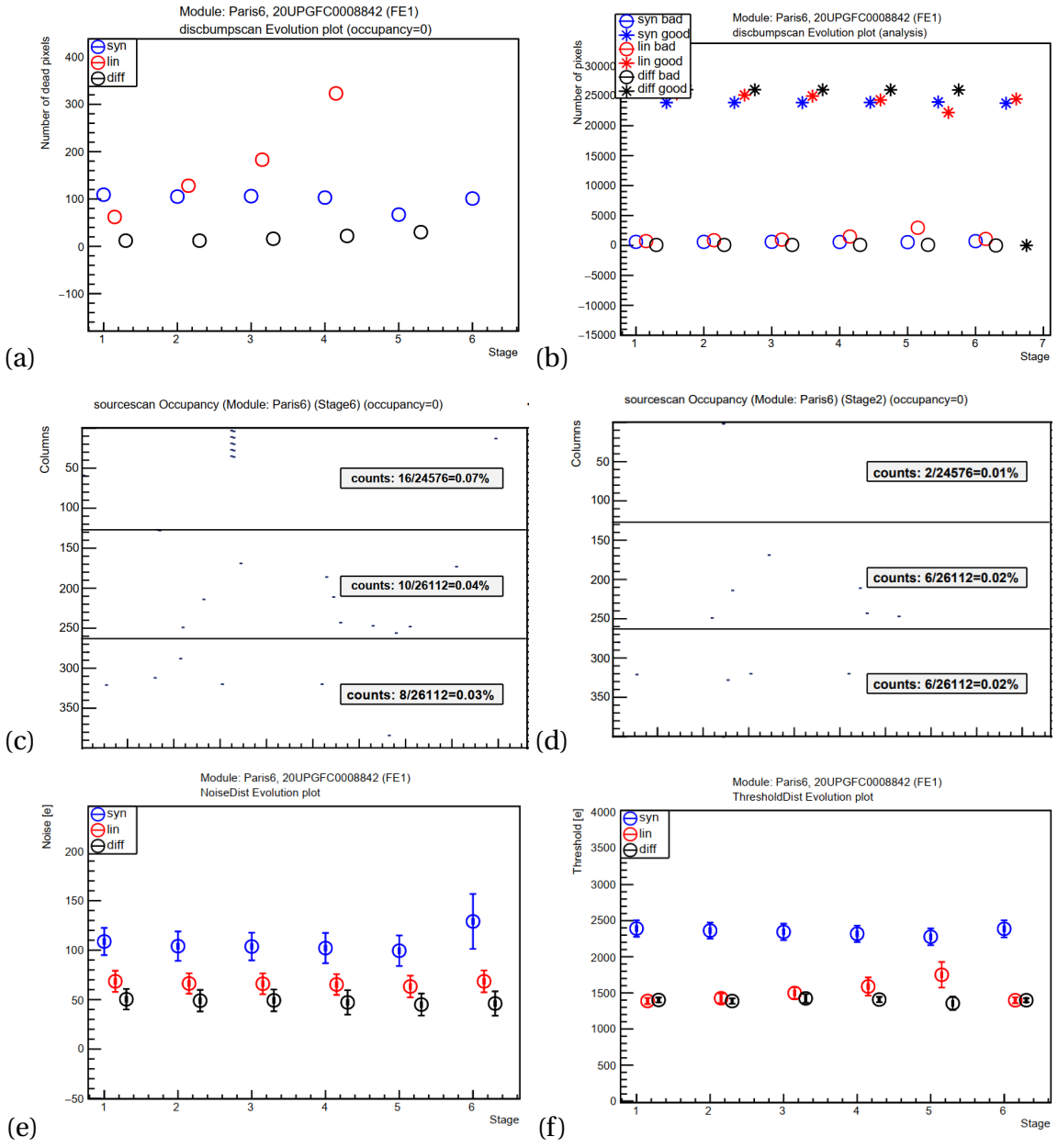

Figure 8.10: Temperature studies: (a) Indicates the DBS scan evolution with decreasing the temperature. It is apparent that Syn and Diff AFE shows more disconnected pixels. However, in (b) similar behavior is seen for the Lin AFE with more bad pixels increment up to stage 5. In (c) and (d) X-ray scans were done at 30°C and -4.7°C, respectively, to examine any disconnected bumps evolution. (e) Summarizes the noise scan evolution as indicated with a slight decrease until stage 5. At the retuning step, the noise increases for the three AFEs, while more for the Syn. (f) Shows the threshold scan summary. More information could be extracted from Figure 6.11 (b).

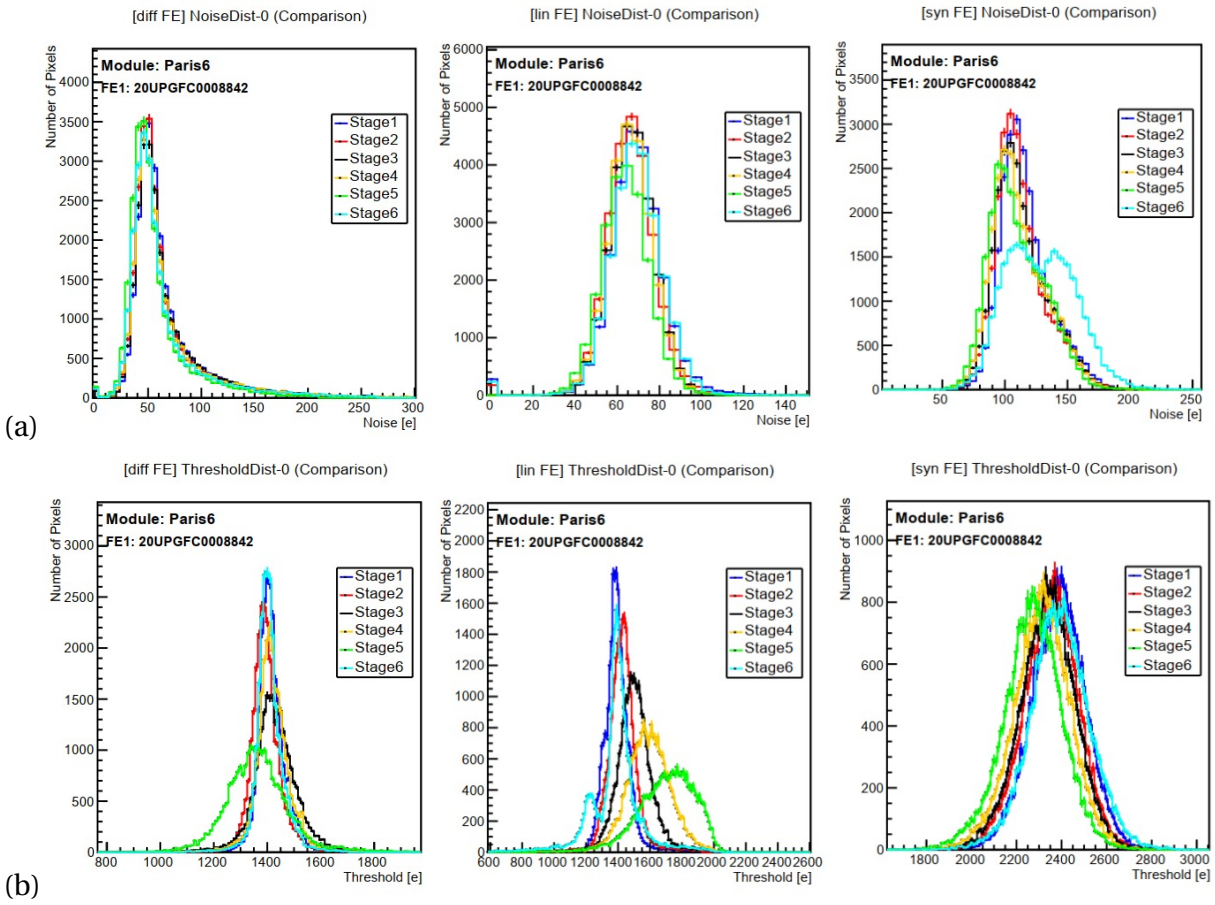

Figure 8.11: Temperature studies: (a) Indicates the noise distributions overlapped for the 6 stages. Syn AFE is largely affected by retuning at low temperatures and features a double peak Gaussian distribution. Other AFEs show a slight decrease in noise means. for chip one with no variations seen while changing the bias voltage, in a well-controlled temperature environment. (b) Shows the threshold distribution which indicates more AFE unique dependency with temperature. In Syn AFE, slight decreases in threshold mean are seen up to stage 5, in the retuning step the threshold poses similar characteristics as for stage 1. In Lin AFE threshold gradually increases and gets wider, resulting in fewer pixels tuned at the desired threshold. However, at stage 6 the pixels feature a double peaked-shaped threshold with similar tuning values as in stage 1. consistent results in all stages. Lastly, Diff AFE behaves similarly to Lin AFE, with less dependency on temperature.

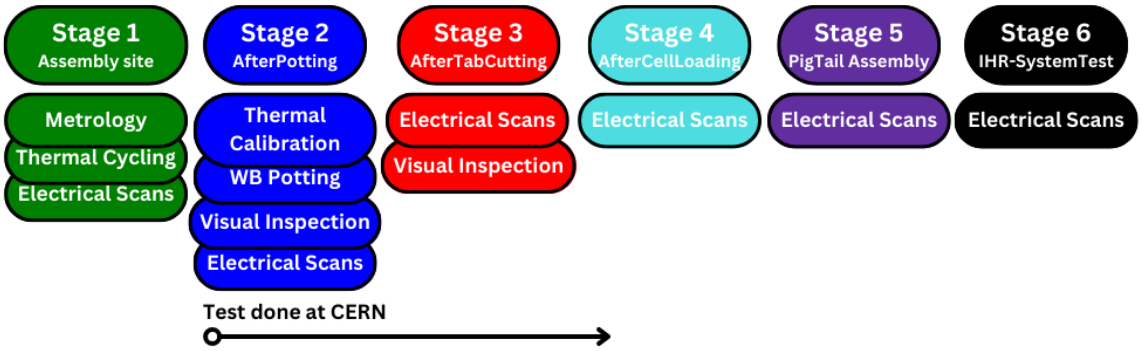

Figure 8.12: RD53A quad modules production line for the ITk OB demonstrator project.

Nevertheless, the module performance at this stage would be checked and tested to investigate any inherited changes with electrical scans. The following stage doesn't involve depositing or changing the module configuration, in stage 3 the module carrier would be changed to prepare it for stage 4. In stage 3, the module flex frame would be cut using scissors to remove the module inactive handling connections. This stage is known as Tab cutting, which will pave the way to stage 5, which could potentially cause changes to the module performance.

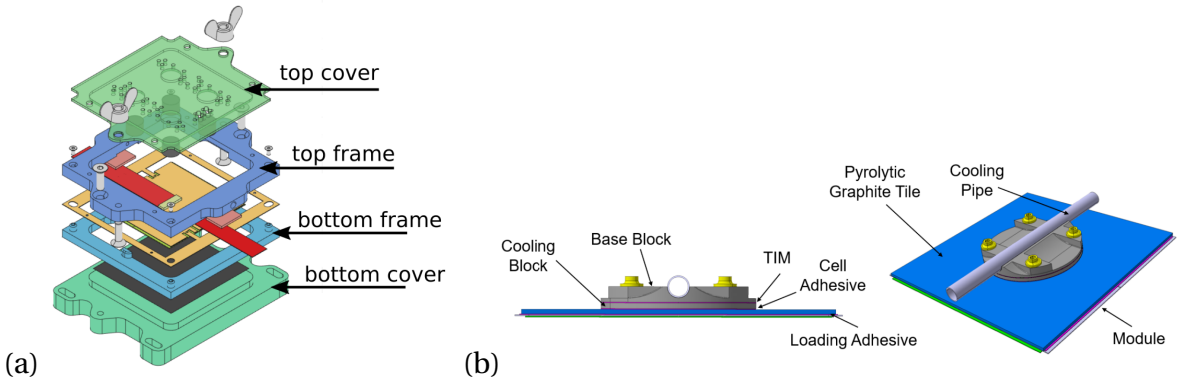

Figure 8.13: (a) Module carrier for the RD53A quad modules. (b) Presents the cell-loading schematics with an expected ≈4mm distance between the cooling pipe and the top part of the module.

The cell-loading stage involved transferring the module to a validated cell-loading site, for example in the University of Geneva or CPPM. In which the module structure will involve adding an extra mechanical frame cooling block made up of Aluminium-graphite, known as the bare cell using the loading tooling and glued to a Pyrolytic Graphite Tile (PGT), more information on cell-loading is found at Ref.[**??**, p. 46]. Both would be bonded using a conductive adhesive CT-303, resulting in a cell assembly to the module backside. The cell-loading stage is an essential part of the production flow that would allow the module integration on the demonstrator staves. The bare cell mechanical

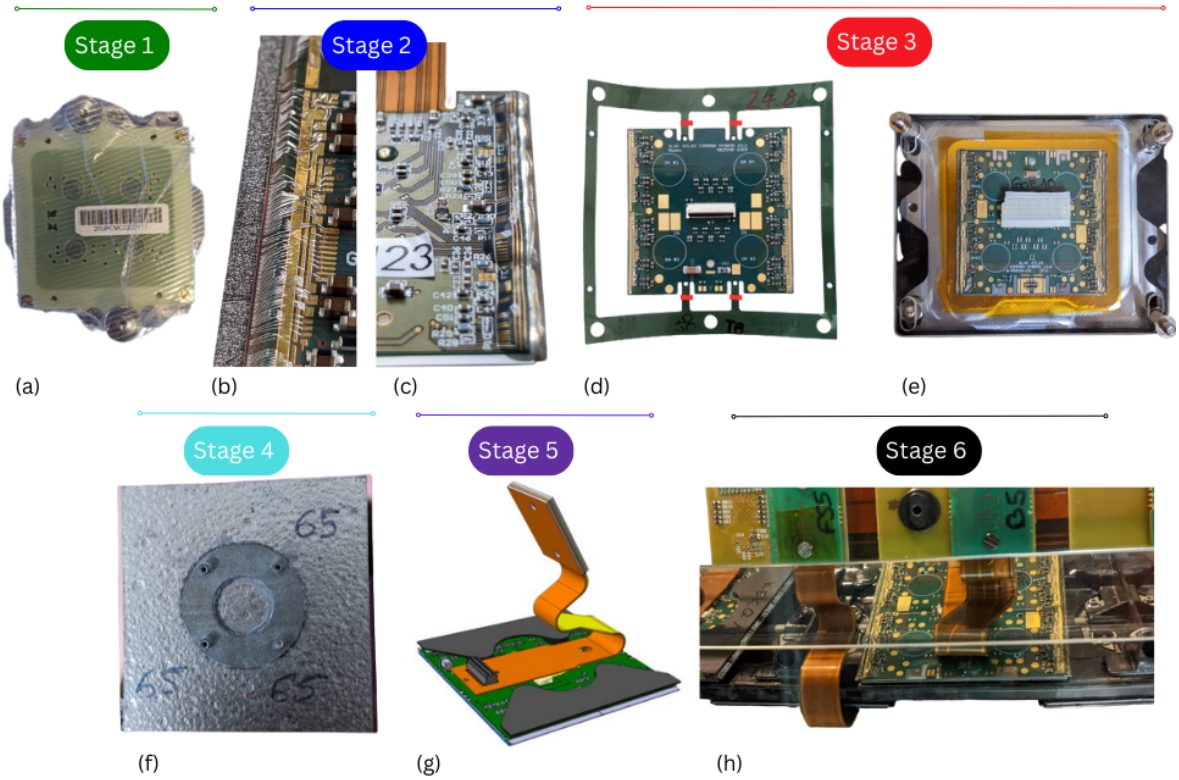

Figure 8.14: Summary of RD53A production stages: (a) Reception of quad module enclosed and protected inside a carrier. (b) Indicates the non-coated WB, in (c) stage 2 of potting the WB with Sylgard is shown. In (d), the module is attached with the bare flex using the tabs dashed with red lines. In (e), the tabs get cut and the module is placed in a new carrier. (f) Shows a picture of the module back, cell loaded with the circular Aluminium-graphite glued to the module. (g) Present a CAD view of a quad module loaded with the pigtail connection assembled. Lastly, (h) introduce the quad modules loaded on the IHR stave, with the pigtail connections attached to PP0 line.

and thermal characteristics were studied to ensure mechanical reliability and ease of functionality of loading. In addition to that, the thermal conductivity plays a vital role as during module cell integration on the staves, the module would be cooled by CO_2 plant pipes that are connected to the cells, being as the thermal interface. At this stage, one can imagine that adding a new layer of materials to the module could introduce changes in the thermal expansion coefficient. To ensure the assembled cell reliability the electrical scans are once again performed to track the performance evolution. With the modules cell-loaded and tested, they are received once again at CERN to be transferred to the SR1 facility for cell integration on staves and assemble dedicated Pigtail connectors. In this fifth stage, another round of scans is performed before the last stage of testing the loaded modules using the demonstrator setup. The system test using the ITk OB demonstrator would feature different DAQ systems, CO_2 cooling, SLDO serial powering chains, and collective module

testing. In this thesis, the Inclined Half Ring (IHR) testing would be presented to conclude the overall performance in the six different discussed stages. It must be noted that due to the demonstrator readout limitations, the signed-up modules for the cell integration on staves must have chips 2 and 4 functioning. A summary of 36 RD53A quad modules produced along the presented sequence of stages reveals modules with high start-up temperatures which are hard to manipulate. In addition, several modules have been shown to have more than a single chip failure and up to three chips in a single quad module. The summary of results in the six production stages will be highlighted after introducing the demonstrator setup in Sec.8.3.3. Besides, a dedicated QC study for the cell-loaded modules would be presented with a detailed motivation, QC criteria, and analysis in Sec.8.5. The stared modules (*) in Tab.8.3 are implemented for the special QC study.

8.2.4.1 Visual Inspection: Ensuring Integrity and Quality

The process of receiving modules from various ITk assembly sites plays a pivotal role in the overall integrity and quality of our pixel quad modules. However, an inherent challenge arises from the differing packaging practices employed during transportation. This section sheds light on the implications of varied packaging methods and the vital necessity of a comprehensive visual inspection process upon module arrival.

A rising cause of concern in the modules arriving from different ITk assembly sites often exhibits a wide spectrum of packaging methods. Some modules are diligently packaged within well-maintained cardboard boxes, meticulously safeguarding them during transit. Conversely, others are encountered wrapped in plastic bags without adequate protection, leaving them vulnerable to potential damage. Furthermore, inconsistencies in the tightness of the module carriers contribute to an added layer of variability, where some carriers may prove inadequate in securely holding the modules in place.

The potential defects and damages of inappropriate packaging practices can extend far beyond initial appearances. Modules subjected to inadequate packaging are susceptible to a range of potential issues, including but not limited to major defects, scratches, and dead chips. Moreover, the wire bonds, which are as thin as human hair, face the peril of being pressed and damaged due to insufficient protection during transportation, in which such damage is irreversible. Thus, a comprehensive visual inspection process is essential before proceeding with production and wire bond coating to identify and mitigate any defects or damages that may have occurred during transit. Collective visual inspection photographs are accompanied by descriptions in Fig.8.15, we will underscore the significance of this crucial step in our pursuit of excellence in pixel module assembly and research endeavors.

Table 8.3: Summary of 36 tested modules for the OB demonstrator project indicating the start-up temperature and number of working chips. (*) Indicates the chips used for the Deep QC analysis in Sec.8.5.

Module	4FE Working	3FE Working	Cold Start-Up [C°]	Other
Goe4*	x		10,10,10,10	
Goe5*		x	-35, ,-25,-35	Chip 2 is dead
Goe7*	x		-3,-3,-3,8	
Goe9*	x	x	-35,-35„-35	Chip 3 is dead
Goe10*	x		-35,-35,-35,-35	
Siegen1*	x		-35,-35,-35,-20	
Siegen2*	x		-35,-35,-35,-35	
Siegen3*	x		-35,-35,-35,-10	
Siegen4*	x		-35,-35,-35,-35	
CERNQ4*		x	-35,-35,-35,-35	Chip 1 is dead
CERNQ6	x		10,10,-5,10	
CERNQ8			-35,-35„	Chip 3,4 are dead
CERNQ9	x		-35,-35„	Chip 3,4 are dead
CERNQ10*		x	,-35,-35,-35	Chip 1 is dead
CERNQ11*	x		-35,-35,-35,-35	
Paris2*		x	,-35,-35,-35	Chip 1 is dead
Paris3*	x		-20,-21,-21,-21	
Paris6*	x		-24,1,-9,1	
Paris7*		x	,-26,-26,-26	Chip 1 is dead
Paris8*			„,-26	Chip 1,2,3 are dead
Paris9*		x	-35,-35,-20	Chip 3 is dead

Table 8.4: Summary of 36 tested modules for the OB demonstrator project indicating the start-up temperature and number of working chips. (*) Indicates the chips used for the Deep QC analysis in Sec.8.5.

Module	4FE Working	3FE Working	Cold Start-Up [C°]	Other
Paris10*		x	-26,-26,-26,	Chip 4 is dead
Paris11*		x	-23,-23,-14,-14	Chip 3 not tunable
Paris12*		x	-31,-31,-31,-30	
Paris13*		x	,-30,-30,-20	Chip 1 is dead
Paris15*			-29,,-29,	Chip 2,4 are dead
Paris16*	x		-13,-24,-13,-13	
Paris17*	x		-26,-12,-26,0	
Paris18*		x	,-30,-30,-30	Chip 1 is dead
KEK19*	x		-20,-35,10,10	
KEK20*	x		-35,-35,-35,-20	
KEK22*			,,-35,-35	Chip 1,2 are dead
KEK24*	x		10,10,10,10	
KEK25*		x	-35,-35,-35,-35	
Liv5*	x		-35,-35,-35,-35	
Liv8*	x		-35,-35,-35,-35	

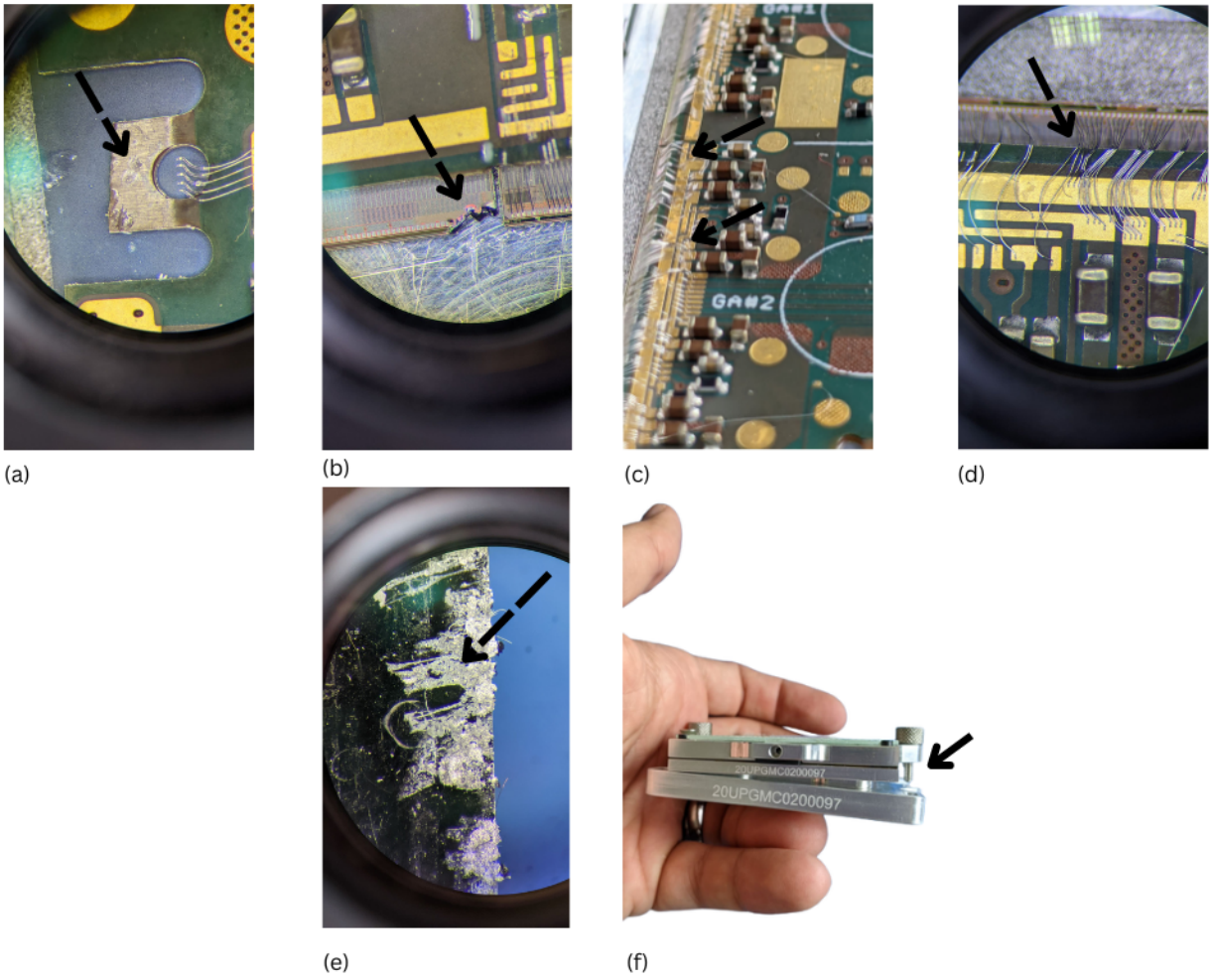

Figure 8.15: Various visual inspection outcomes for a sample of received RD53A quad modules. (a) and (b) shows broken edges of active and inactive parts of the module FE. In (c) and (d) the wire bonds are damaged, short-circuited, and pressed to a level that the induced damage couldn't be fixed. (e) Introduced serious scratches to the module's backside which could potentially change the module's electrical characteristics. Lastly, (f) presents one of the received modules not tightly secured, due to a screw that isn't long enough to hold tight the far top and bottom layers.

Table 8.5: OB demonstrator loading structures with the number of modules per flavor, serial power chains, and HV lines.

Stave Structure Flavor	# of Modules	SP Chains	HV Channels
Longeron (M6)	6	1	2
Longeron (M12)	12	1	2
Inclined Half Ring	11	1	2

8.3 Outer Barrel Demonstrator Project

The Outer Barrel Demonstrator Project is designed to validate and proof the foundational concepts necessary for the construction of the larger Inner Tracker (ITk) detector. This initiative serves as a crucial step toward ensuring the feasibility and effectiveness of essential components, methodologies, and systems that will culminate in the realization of a cutting-edge particle detection system.

One of the primary objectives of the Outer Barrel demonstrator project is to validate loading concepts integral to the ITk detector's construction. This validation process is accomplished through the utilization of prototypes equipped with RD53A electronics, enabling the assessment of loading structures such as the longerons and inclined half-rings. These structures serve as a mechanical constitution to enable the required cabling, cooling, and functionality of the ITk detector, which are evaluated using the RD53A electronics as a proxy for the upcoming ITkPixV2 electronics.

The scope of the demonstrator project extends beyond structural validation alone. It encompasses a comprehensive examination of critical concepts, including the validation of the Data Acquisition (DAQ) systems, interlock mechanisms, and the conversion of electrical data to optical signals. Moreover, the project seeks to validate the transfer of readout electrical scans through an extended 60-meter cable, mirroring the high luminosity conditions of the new all-Silicon tracker. Moreover, to optimize the overall design and performance of the ITk detector, innovative strategies are employed. The implementation of Single Low Dropout (SLDO) powering for front ends is introduced to minimize inactive material and mitigate scattering. Furthermore, specific High Voltage (HV) power chains are devised for connecting modules on the staves, contributing to enhanced functionality and streamlined operation.

This thesis focuses on the testing and validation of the Inclined Half-Ring (IHR) stave structure. Comprising 11 modules, this arced-shaped stave features a single serial power chain and two HV lines. The IHR stave structure serves as a focal point for assessing the production of RD53A modules, thereby completing the final stage of the demonstrator's testing program to assure the performance of the module across all stages, including the cell-integration and testing with developed infrastructure in SR1 facility, as illustrated by the demonstrator setup in Fig.8.17.

In the subsequent sections of this thesis, we will introduce in detail the IHR, highlighting the innovative concept of serial power chains, the demonstrator's setup and configuration, and the

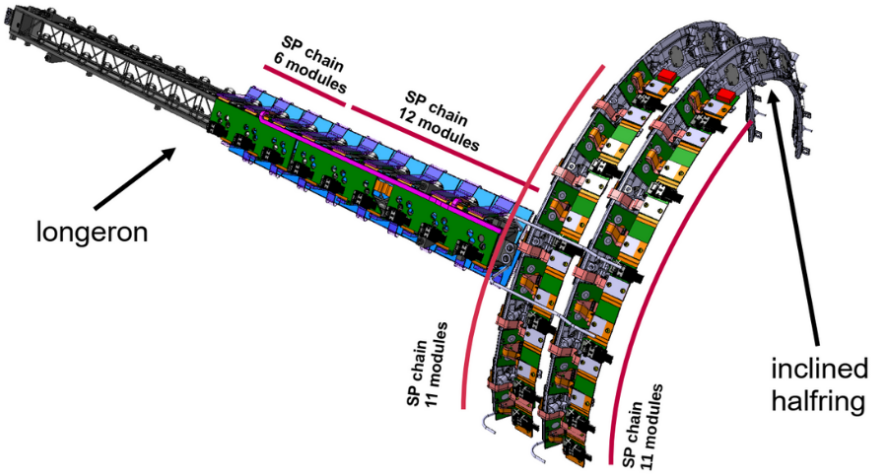

Figure 8.16: OB demonstrator configuration consisting of two main stave units, the longerons, and the inclined half rings.

comprehensive testing program to prove the final design report (FDR) that was accomplished earlier in 2023.

8.3.1 Demonstrator Setup and Associated Sub-systems

The demonstrator setup consists mainly of two main interconnected systems. Firstly, the on-detector services connecting the modules to the overall system structures. It consists of the detector module's power supplies, with long Type-3 cables of 60m to a dedicated rack area. Besides, the CO_2 evaporative cooling plant that flows in a devoted Titanium cooling popes, utilizes special monitoring information for warnings and error flags highlighting the operational status of the cooling plant. Moreover, a developed system to trace the power channels of individual modules, and their corresponding temperature read using NTC, known as the Monitoring Of Pixel System (MOPS) is added. The new innovative serial powering scheme groups up the module into chains powered with a constant current source. In each individual module, the chips are powered in parallel. However, the modules globally draw a constant current using the serial input line and shunt any excess using the SLDO regulators.

The off-detector services are made up of the cable plant, aiming to test the realistic set of cables, for example, the type-1 bundles, patch panels 1, 2, and type-3 cabling for LV, HV, DCS, and interlock. The large set of cabling used is however reduced due to the implementation of serial powering. Regarding data transmission and command signals, the electrical services route and plays the role of an interface between the modules and the Opto-converters. Using the Opto-box, the electrical to optical conversion occurs outside the test box with signal aggregation, as will be done in the ITk, for radiation protection and ease of accessibility to the optical elements. To cope with the transmission of large data sets for multiple modules, fibers are used with dedicated 1.28Gb/s in uplinks for each

quad module. The demonstrator as well needs to address the overall functionality of the off-detector services. Bandwidth stress tests and reliability of data transmission are only feasible while using the realistic length of cables.

To further optimize the experimental setup, the detector components including the loaded local supports are housed within a specially designed large test box crafted to allow electrical and thermal tests. The test box is lightproof, enclosed with sensitive sensors from extraneous light interference while also facilitating controlled air flushing to maintain low humidity levels with the due point of less than 15°C to the actual CO_2 cooling temperature, thereby ensuring optimal operation conditions. A collection of sensors and switches are implemented for monitoring thermal, humidity, light, and contact closure properties in the cold box. An overview of the essential components indispensable for the operational and testing inspections of the loaded local support, encapsulating the Quality Control (QC) setups is shown in Fig.8.17. Different colored lines serve to differentiate the nature of connections between these components, encompassing DAQ, Interlock, monitoring, and power interactions.

Moreover, the complexity of the setup imposes concerns on the interdependences of different sub-systems, sequence of operation, and safety of the loaded staves. To tackle that, a Detector Control System (DCS) pilots the setup to control and monitor the environmental sensors, cooling plant, interlock crate, MOPS, Opto-box, and loaded staves. Furthermore, a dedicated DAQ system known as Front-End Link eXchange (FELIX) [94] has been developed exclusively for the future ITk pixel sensors [95]. Being a centralized system, it allows for safe operation and ease of testing to prevent users from creating mistakes, using a finite state machine and warning flags. The powering sequence of the total setup and detector components could be manipulated through the interlock graphical user interface (GUI). The overall strategic arrangements and complexity in the assembly of the demonstrator underscore the collective work of many institutions, and the unwavering commitment to precision, and reliability, to commission the demonstrator.

The testing program for the demonstrator highlighted in this thesis focuses on two main conceptual thermal and electrical tests. It is essential to highlight any potential problems arising from the cell-integration step and trace the performance of the modules in all QC stages introduced in Fig.8.12. Along with this, the system-related aspects of the demonstrator setup need to be validated, mentioning the MOPS system, serial powering, and the cooling method used with the base cooling block, to test the effectiveness of thermal conduction to cool down the modules and mark any inconsistencies in the NTC measurements.

8.3.2 Overview of Inclined Half Ring

Local loaded supports specify the module position to relative global coordinates in the overall detector volume and provide mechanical standpoints around the beam pipe IP. The importance of validating the IHR necessity implementation of meteorology studies on the thickness of glue used to

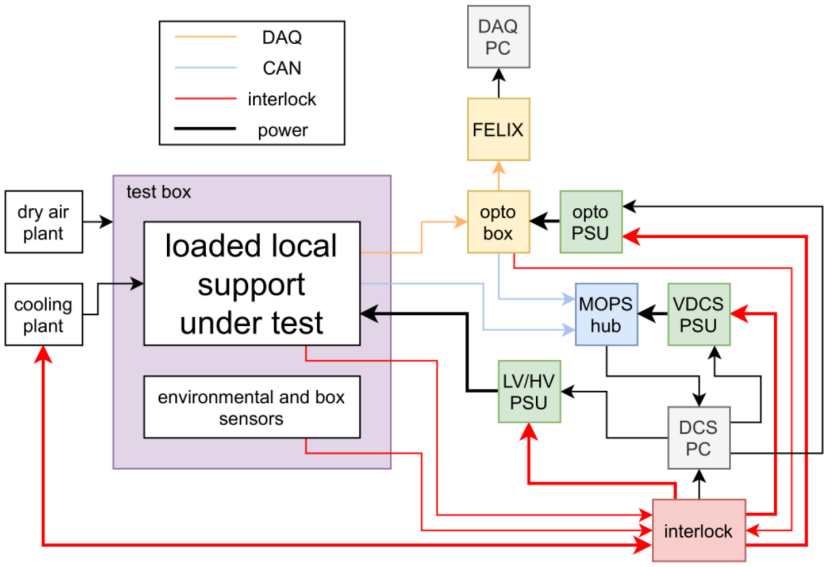

Figure 8.17: Overview of the main on/off detector systems for the OB demonstrator testing setup.

attach the cells on modules. Any increase of unnecessary glue will distance away the modules from the stave and minimizes heat interface spreading. The main key elements in the IHR geometrical elements are shown in Fig.8.18 (a). The four pillars include the thin-walled titanium tube to circulate the CO_2 boiling fluid, a series of base cooling blocks attached to discrete locations on the staves to hold the cell-loaded modules and create a thermally conductive interface to the CO_2 cooling pipe. Moreover, carbon fiber-reinforced plastic (CFRP) holds the overall structure. The properties of CFRP enable minimum thermo-elastic stresses induced due to the temperature variations and stiff for simplicity handling.

The IHR houses 11 modules listed in Tab.8.6 with the positions relative to the patch panel (PP0) in Fig.8.18 (b), the maximum attained bias, and the HV channel chain with start-up temperature. The IHR features a semi-annular structure on two sides for module loading to provide hermetic coverage. The front and back sides were occupied with five and six modules respectively, each connected to a dedicated HV channel for one side. In the following results summary, only chip 4 is read from its associated modules due to a lack of data merging in the RD53A chip. However, it could be observed that KEKQ19 and KEKQ24 modules gave relatively high start-up temperature values, which will cause problems in cold testing. Moreover, the bias voltages for the two HV chains were set to be 83V for HV1, and 85V for HV2.

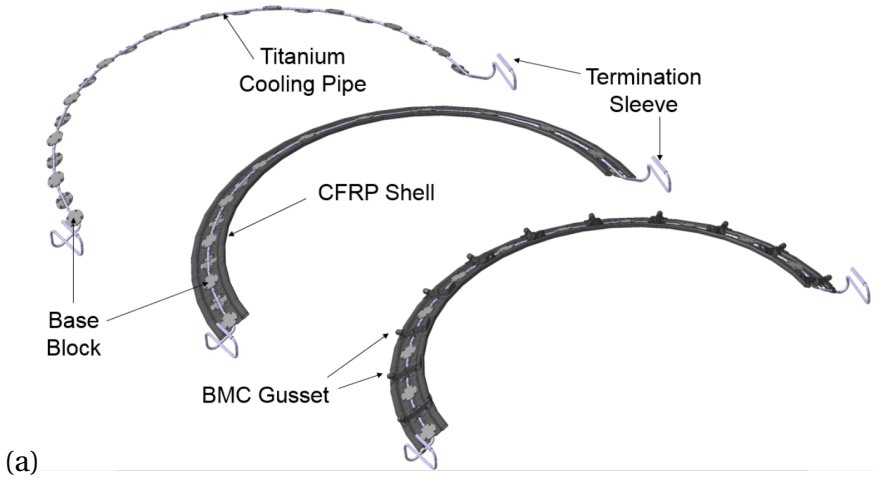

(a)

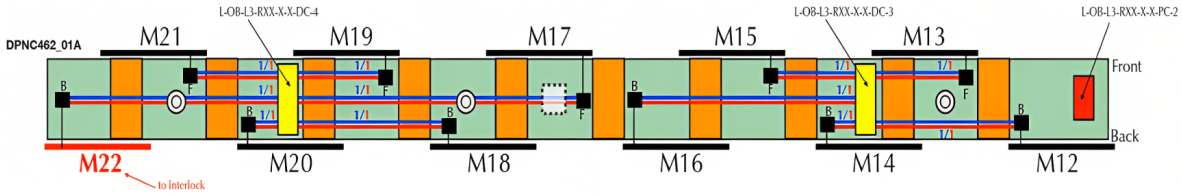

(b)

Figure 8.18: CAD view of the CFRP structure, the titanium cooling pipes, and the base blocks [24].

Table 8.6: IHR fully loaded with 11 modules in SP chain and two HV chains. The indicated module measurements are relevant for chip 4.

Module ID	PP0 Position	HV range [V]	HC Channel	Start-up Temperature [C°] - Chip4
KEKQ22	M12-back	10-100	HV1	-35
KEKQ24	M13-front	10-150	HV2	10
KEKQ25	M14-back	10-200	HV1	-35
Liv8	M15-front	20-180	HV2	-35
KEKQ19	M16-back	20-150	HV1	10
Paris6	M17-front	20-200	HV2	1
Goe5	M18-back	10-200	HV1	-35
Paris16	M19-front	10-160	HV2	-13
Paris11	M20-back	20-160	HV1	-14
Goe7	M21-front	20-80	HV2	8
Paris8	M22-back	20-200	HV1	-26

(a) 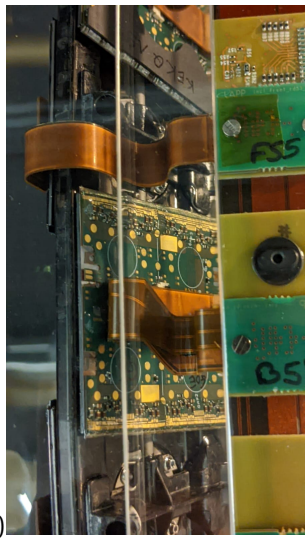 (b) 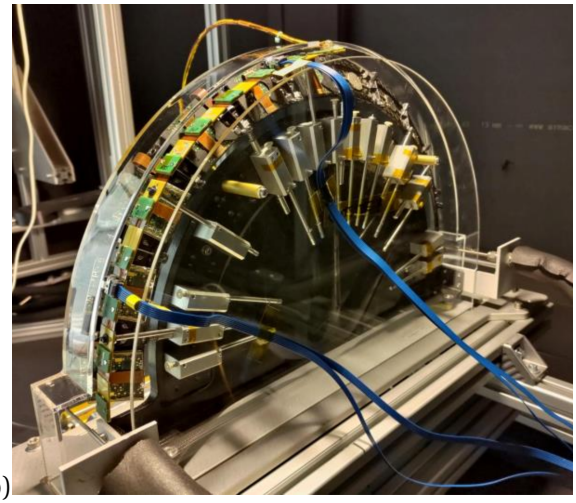

Figure 8.19: (a) IHR stave installed inside the test box and mounted with (b) showing part of the 11 cell-loaded RD53A quad modules attached with pig-tail cables to patch panel 0 (PP0).

8.3.3 Inclined Half Ring Testing Program and Results

The measurements to validate the IHR and services setup are done at different configurations and conditions to cover as much as possible the potential differences that could arise due to the systematic differences in the infrastructure or to variations due to temperature. The overall summary of tests conducted on the IHR are as follows:

- **Electrical scans**: Analog, digital, ToT, crosstalk, DBS, IV, and VI scans with the associated number of failed communication to chips.
- **Temperature tests**: To quantify the IHR modules performance, the CO_2 cooling plant was set to obtain the module's NTCs at 20°C, and 0°C. At each temperature value, the previously indicated list of scans is done and compared.
- **Data Acquisition (DAQ) System** : Three potential promising DAQs were developed exclusively for the demonstrator program, in this section, a comparison-based study using the electrical scans is evaluated to understand the potential induced changes by the DAQs on the module performance.
- **Thermal validation of cell-loaded modules** : One can envisage in collective testing of modules on the stave to have heated-up CO_2 fluid in the modules end of the cooling chain, due to the dissipated heat earlier by modules at beginning positions. Besides, cell-loaded modules, as introduced before, have an added set of mechanical supports to mount on the stave with an additional layer of glue. The impact of the previously opened concerns is evaluated by

means of comparing the NTC value at single tests and on the CO_2 cooling pipe, to evaluate the effectiveness of base-cooling block thermal conductivity and CO_2 cooling.

The first studies were conducted with an ambient temperature using CO_2 set at 10°C, followed by another cold test at -10°C. All electrical measurements and thermal performance evaluation are in prospect, however, due to geometrical reasons, no radioactive source scans were done. **IV curves** were taken for both channels, where two sets of plots are presented for comparability in individual IV scans at stage 5, and stage 6 on the demonstrator. Moreover, temperature corrections were applied to have a similar NTC value as in the demonstrator test for 22°C. While Fig.8.20 (a) shows both individual channels, Fig.8.20 (b) indicates the IV scan for Channel-1 in stage 6, to have a large discrepancy and early break-down voltage. In contrast, channel-2 shows an agreement with the individual IV scans. Further inspections at channel-1 reveal that early breakdown voltage occurred due to the KEKQ19 module ohmic behavior, which has no clear plateau region for operation, and the current increases rapidly after 10V. By looking at the channel-1 IV curve, one can envisage the resultant IV scan as a collective behavior of the entire used modules. It must be noted, however, that the module location for each channel isn't arbitrary and therefore chosen based on each individual IV curve characteristic.

As mentioned before, warm-to-cold tests were compared and illustrated the IV curves of channel-1 and 2, with 3°C for the cold test, and 22°C for the warm test. In which a consistent temperature to current dependency in both channels with its attributed bias range scans. Following the IV curve, an investigation of **VI characteristics** by the LV supplied to the chips and the number of working modules are drawn. Fig.8.21 (a), clarifies the number of failures to operate the modules while going down with the LV power supply at both warm and cold tests joined. The relation is trivial for the VI characteristics derived from the MOPS system, as indicated, by the input current and voltages of different modules in the SP chain it is possible to extract when the module communication stops. Moreover, it could be observed that the number of starting modules at the cold test is less, due to the high-temperature start-up of KEKQ19, as previously indicated in Tab.8.6.

Apart from this, VI at each input stage could be measured directly using MOPS system even if no communication is established to speculate voltage drops at each module and the potential effects of different grounds to the return line of the LV power supply. As seen in Fig.8.21 (b), the local grounds of each module are an input potential to the next module in the SP chain, while any over-current is shunted with the SLDO regulators. However, there is an unobserved nonlinearity for the V-I curve.

Concerning **electrical scans**, with the demonstrator a comparative analysis to embark on the QC assessments conducted on the individual modules prior to their standalone testing, with the comprehensive evaluation achieved through the system test using the demonstrator. This comparative study seeks to unveil the differences and potential synergies between these two distinct approaches, shedding light on the comprehensive insights gained by examining the modules collectively within the demonstrator framework.

The **noise scan** extracted from the width of threshold scans is presented in Fig.8.22 (a), with

systematic errors width of measurements in Fig.8.22 (b). For each AFE architecture, the noise scan is indicated with its attributed module for the 6 stages. The results obtained at different stages for the IHR show coherent noise for the Syn, Lin, and Diff AFEs for the overall modules across all stages. Furthermore, some modules reveal higher noise output at the initial test which isn't consistent with later stages, as in the KEKQ19 module. Though this could be a result of higher NTC value. However, the overall behavior across stages proves that there were no disagreements in measurements.

Similarly, in Fig.8.22 (c) and (d), **threshold scans** impart significant agreement for all tested stages regarding the Lin and Diff AFEs. In contrast, Syn AFES shows a slight increase in the measured tuning value for all modules, despite having a consistent output compared to the earlier testing stages. In stage 6, measured growth is detected of about 50e for the Syn AFE.

In addition, **DBS** reveals unprecedented growth in open bumps for the Diff AFE in all modules at the last testing stage with the demonstrator, in respect to the previous stages, clarified in Fig.8.23 (a). However, to inspect other AFE, Fig.8.23 (b) neglects the last Diff testing stage. Several inspections have been carried out to investigate the origin of the faults detected, including changing the DAQ systematics. Moreover, the growth of open bumps in the Diff AFE using a dedicated developed DAQ known as the VakYarr is seen in Fig.8.23 (c-left), in contrast, using the YARR DAQ Fig.8.23 (c-right) optimized for the collectivist IHR modules scan, the open bumps vanished. A clear comparison of both DAQs for the DBS could be seen in Fig.8.23 (d).

Regarding **other electrical scans** comparison for the total QC production stages, a summary of the time-over-threshold (ToT), digital, analog, crosstalk, and a fit of threshold and noise scan could be inspected in Fig.8.24. Whereas those results are for chip 4 in Goe5, other IHR modules indicate similar performance.

Following that, **warm to cold tests** are compared on the module's electrical scans as indicated by Tab.8.7 is evaluated and compared to earlier results by warm tests. Besides, one of the consequences of the cold test was losing the opportunity to test the KEKQ24 module. In fact, due to its high start-up temperature value, the communication failed to start. However, surprisingly KEKQ19 succeeded in starting the cold test. Hence, 9 modules out of the 11 in the IHR will be compared to the warm tests. Moreover, the inspection of noise and threshold scans, similar to the previous results, are introduced in Fig.8.25 (a) and (c) respectively. Furthermore, noise scans show in general less noise measured for all AFEs with few exceptions in a bit higher noise observed. On the other hand, threshold scans in Syn AFEs shows a slightly lower threshold obtained at cold temperatures, while in Lin and Diff AFEs the performance is preserved. Other electrical scan summaries are presented in Fig.8.26, keeping in mind that the warm test is referred to as stage 1, and stage 2 for the cold test.

Evaluation of temperature variations before and after cell integration is crucial as previously discussed. The added layers, while serving as an interface, have the potential to introduce variations that reverberate through the efficiency of the cooling process by CO_2 cooling plant. A critical juncture in this exploration is the module's integration into the stave, a stage marked by cell-loading. To

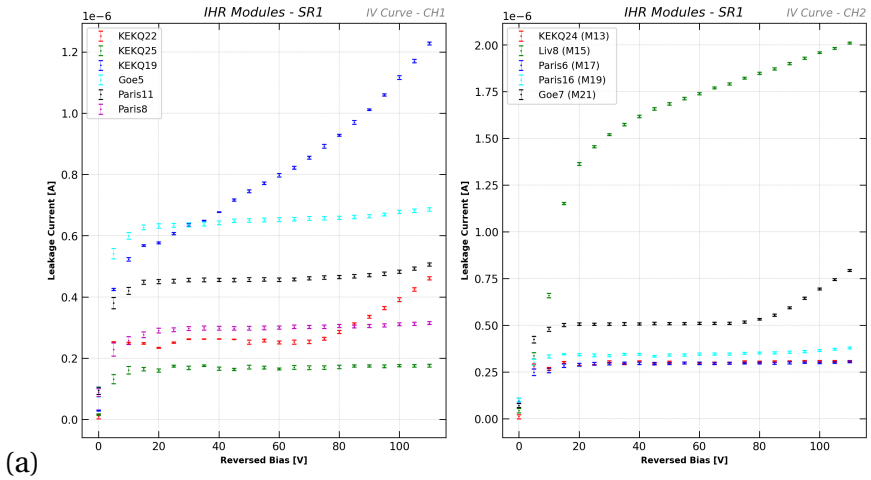

(a)

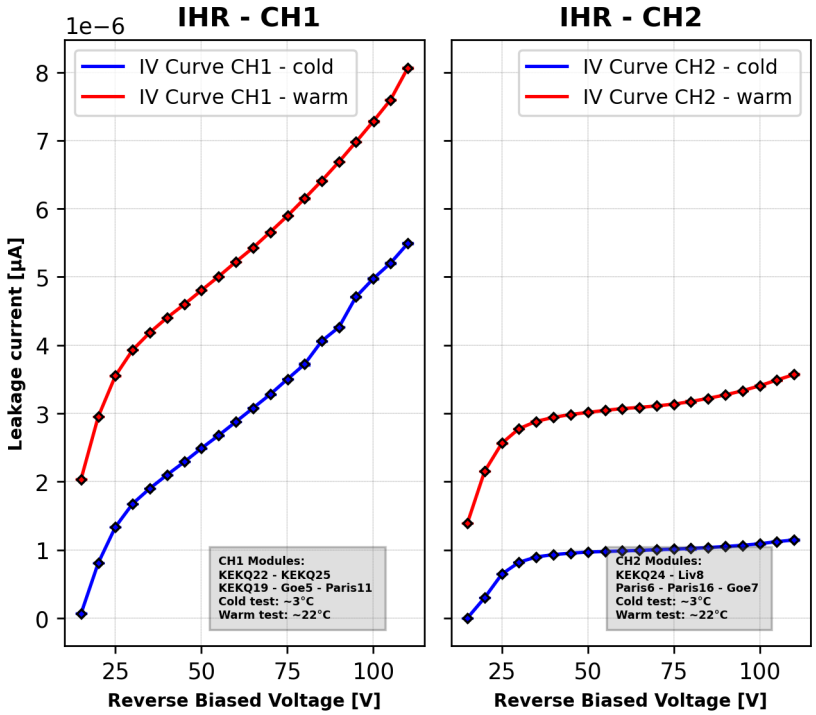

(b)

Figure 8.20: IV curves extracted at similar temperature value. (a) Indicates corrected IV curves for channel-1 and 2 modules at the individual tests in stage 5. (b) Shows the IV curves with the demonstrator test at both cold and warm tests.

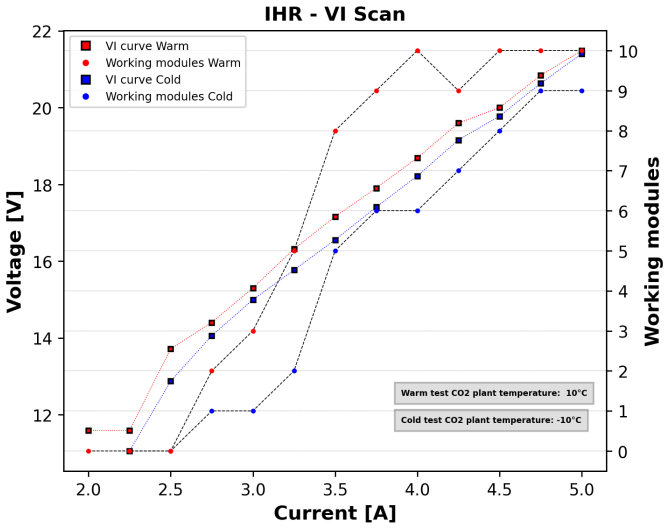

(a)

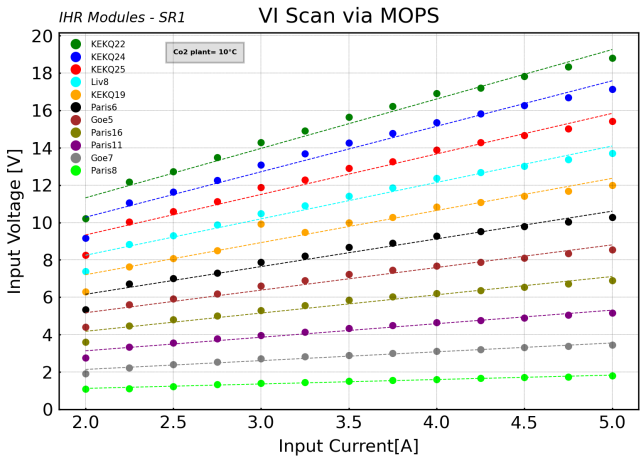

(b)

Figure 8.21: (a) Illustrates the number of working IHR modules while ramping down the current in both warm and cold measurements. (b) Presents the VI curves measured at each module in the IHR demonstrator using the MOPS system.

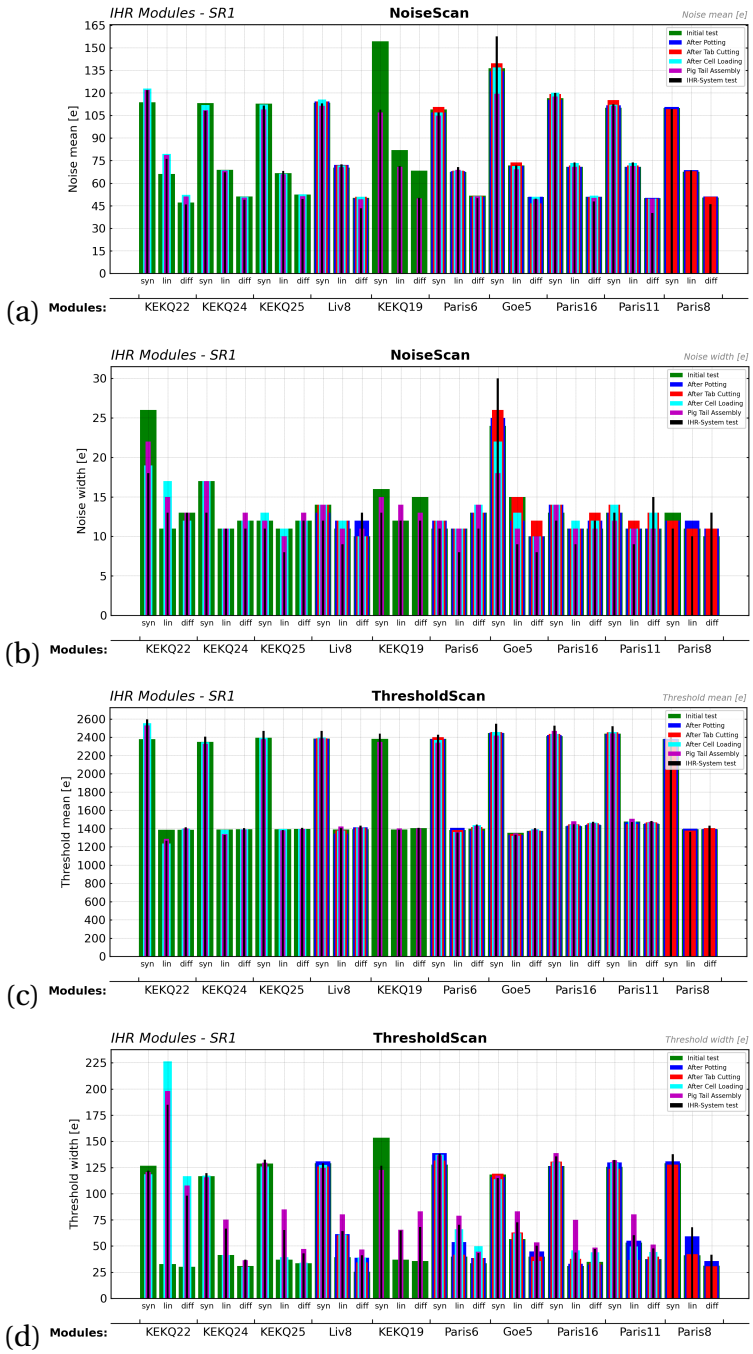

Figure 8.22: Overall QC stages of the RD53A OB demonstrator program: (a) Shows the noise scan performance across all stages, indicating consistent behavior for the IHR modules, with a bit of increase seen in the KEKQ19 module at the initial tests in Japan, and a further increase in Goe5 Syn AFE at stage 6. (b) Indicates the width of noise measurements. (c) Expresses the threshold scan progress up to the final test at the IHR stave in the demonstrator setup. A bit of increase is observed for Syn AEF at stage 6, and (d) introduces the width of the measurement.

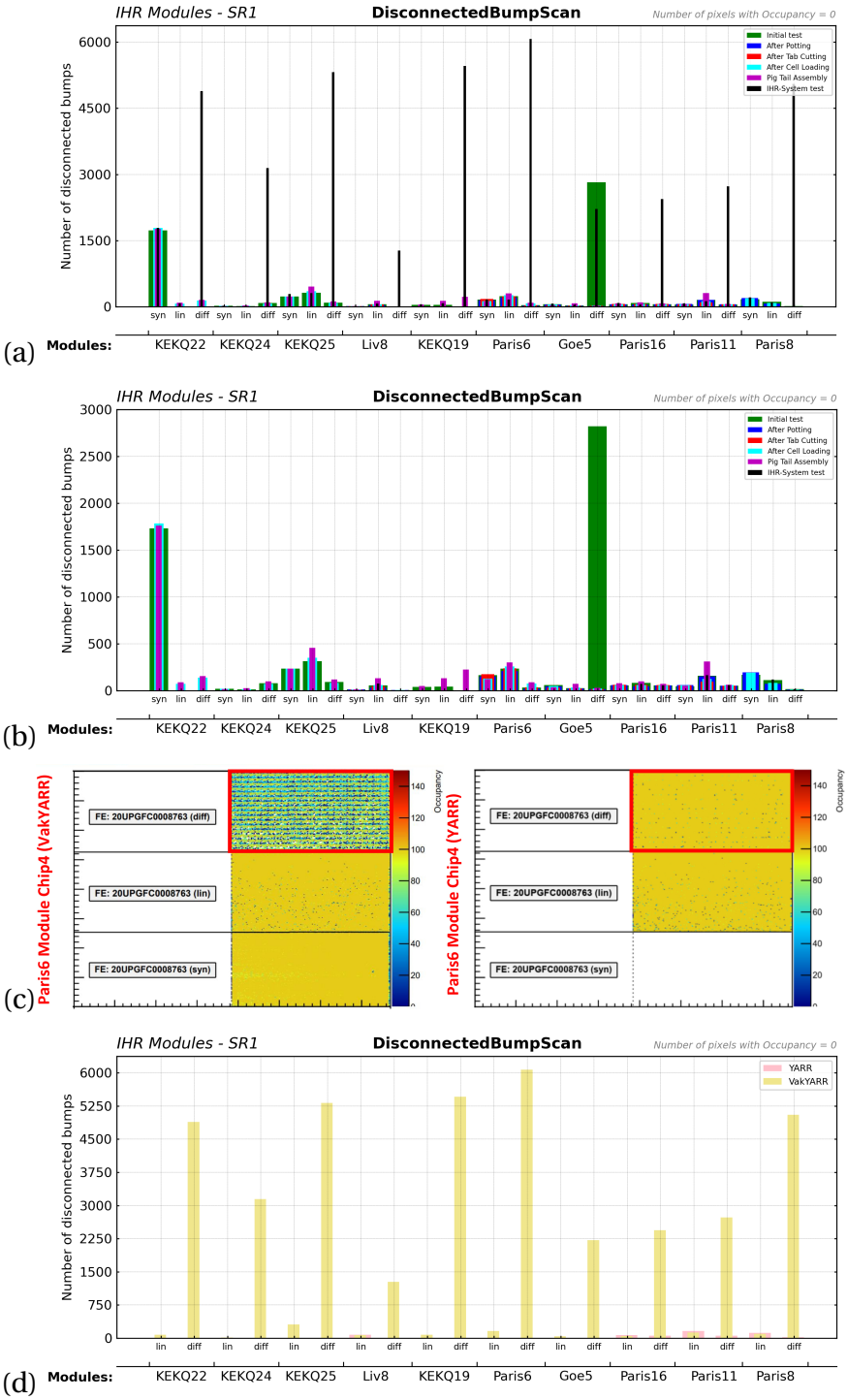

Figure 8.23: Overall QC stages of the RD53A OB demonstrator program: (a) Shows the DBS evolution with a large increase of open bumps at stage 6, using the VakYarr DAQ. In contrast, (b) indicates a similar scan using the YARR DAQ that stipulates a fall-off in open bumps counts, compatible with other QC stages. In (c), an occupancy of counts measured for each individual pixel is shown. In Diff AFE using the VakYarr (left) shows dead pixels in patterned behavior. However, with YARR DAQ (right) the observed pattern disappears. (d) shows a comparison between both DAQs in DBS.

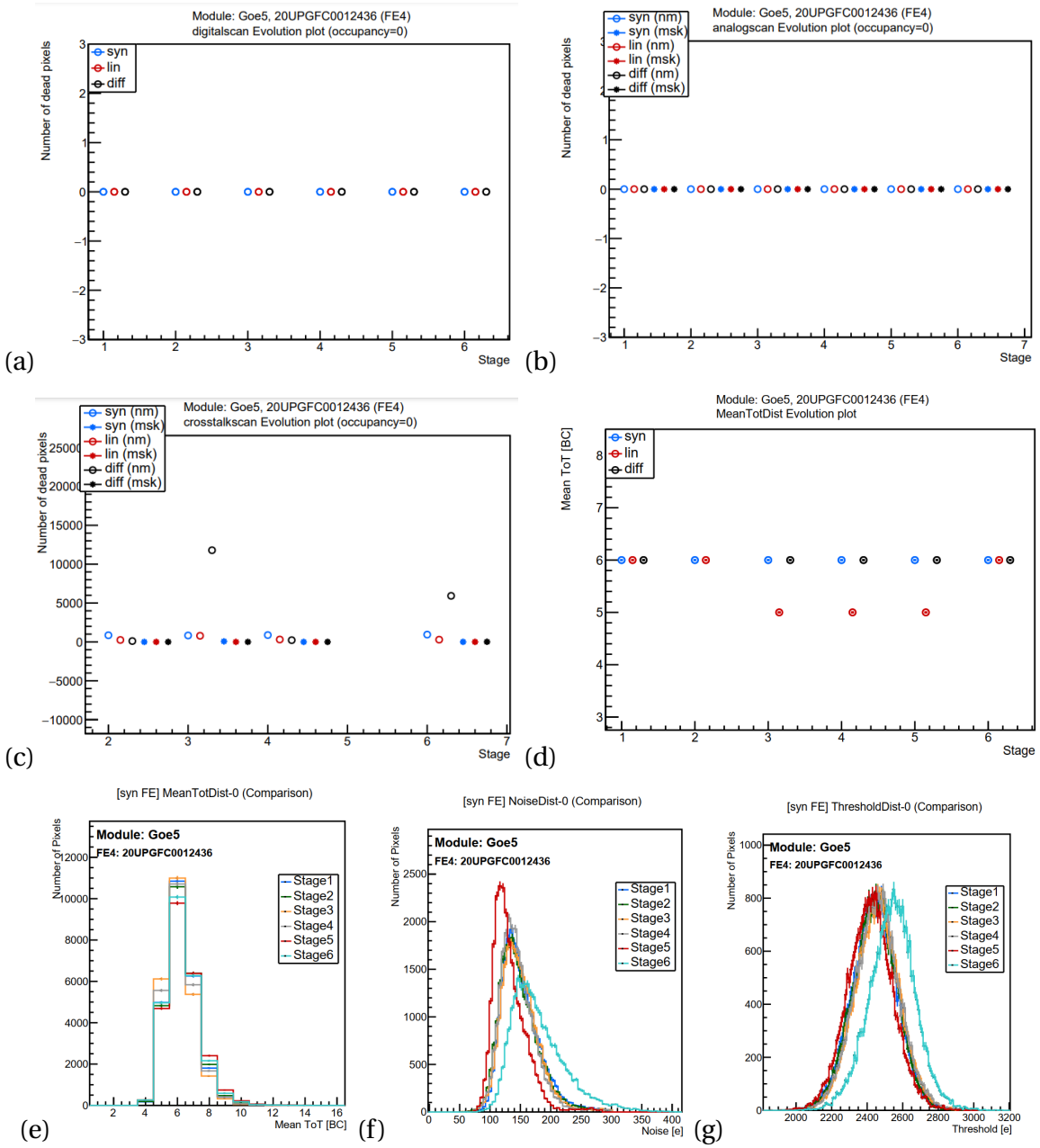

Figure 8.24: Summary of all QC production stages for Goe5 chip 4, in (a) and (b), the digital and analog, respectively, dead pixels are consistent. (c) shows the dead pixels in the crosstalk scan with a bit of increase in the Diff AFE. However, other stages and AFEs are compatible with previous stages. In (d) a summary of TOT is evaluated, with a kept-up performance during all stages. It could be also further inspected in (e) indicating a well-preserved performance. Finally, (f) and (g) show the noise and threshold scans respectively. As previously discussed, an increase in both measurements is found.

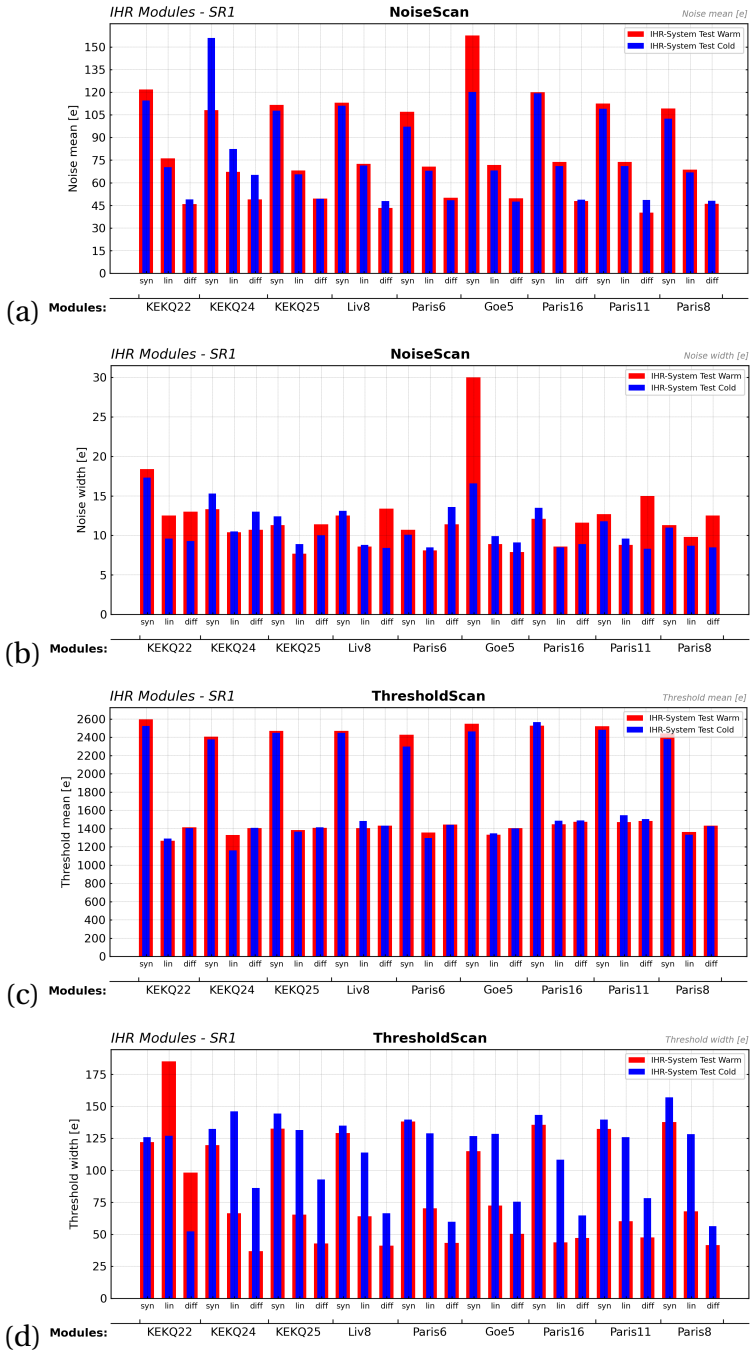

Figure 8.25: Temperature tests comparisons on the IHR demonstrator setup: (a) and (b) introduce the noise mean and width, respectively. In which the overall performance indicates lower noise measured due to a difference of ≈20°C. In addition, (a) presents threshold findings with lower measurements in cold temperatures, with its corresponding threshold width at (d).

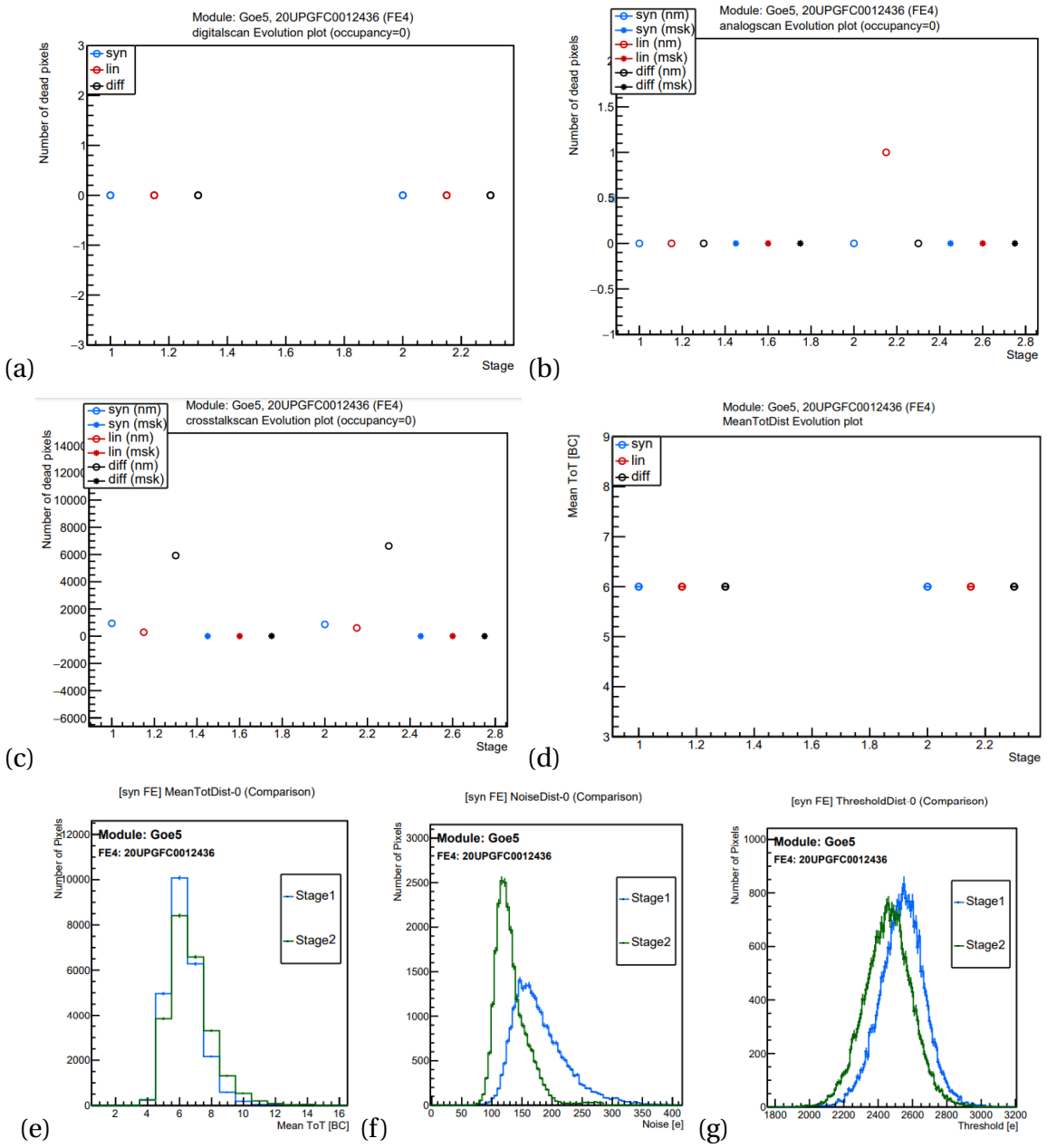

Figure 8.26: Temperature tests comparisons on the IHR demonstrator setup: Digital and analog scans reveal no differences as indicated in (a) and (b) respectively. Similar outcomes are seen also in crosstalk scan and ToT in (c) and (b), correspondingly. However, in (e) by examining the ToT fit an increase of the mean ToT is slightly noticed. Moreover, (f) shows less noise for the Syn AFE at stage 2 (cold test) and similar results in threshold scan in (g)

Table 8.7: IHR modules NTC measurements at two different CO_2 temperature tests. The LV in both cases was set to I =4.6A and V =20.9V for the total SP chain.

Module ID	Warm Test at CO_2 = 10řC, NTC in [°C]	Cold Test at CO_2 = −10řC, NTC in [°C]
KEKQ22	20.3	-0.42
KEKQ24	21.8	1.15
KEKQ25	20.1	-1.9
Liv8	24.2	1.9
KEKQ19	23.3	1.75
Paris6	22.4	2.3
Goe5	22	2.54
Paris16	23.3	3.8
Paris11	22.2	2.9
Goe7	21.1	2.5
Paris8	21.5	1.87

investigate any possible issues, a temperature comparison of single modules on a cooling jig at different temperatures and to the IHR demonstrator setup is introduced. While having the LV on, the jig and set-point of CO_2 cooling pipe are measured, with the relevant module NTC temperature through the MOPS chip. In Fig.8.27 (a), three set-points of temperature are introduced for the cooling jig at 20°C, 10°C, and -10°C. On the other hand, in the demonstrator setup set points of 10°C, 0°C, -10°C, -20°C, and -28°C were extracted. The results display variations in the 11-module NTC at the same set-point, either by the jig or CO_2 cooling pipe. This clarifies initial discrepancies in the module NTC behavior, furthermore, the overall performance indicates an offset of ≈5°C between both tests, indicating that the NTC temperature value tends to be closer to the jig set-point. However, as in the cooling pipe dissipation of heat is presented due to the serial cooling method of other modules in the chain, the CO_2 succeeded in maintaining the offset constant with respect to the jig. In addition, the thermal behavior at other set points is clearly reproduced with the inlet and exhaust being similar.

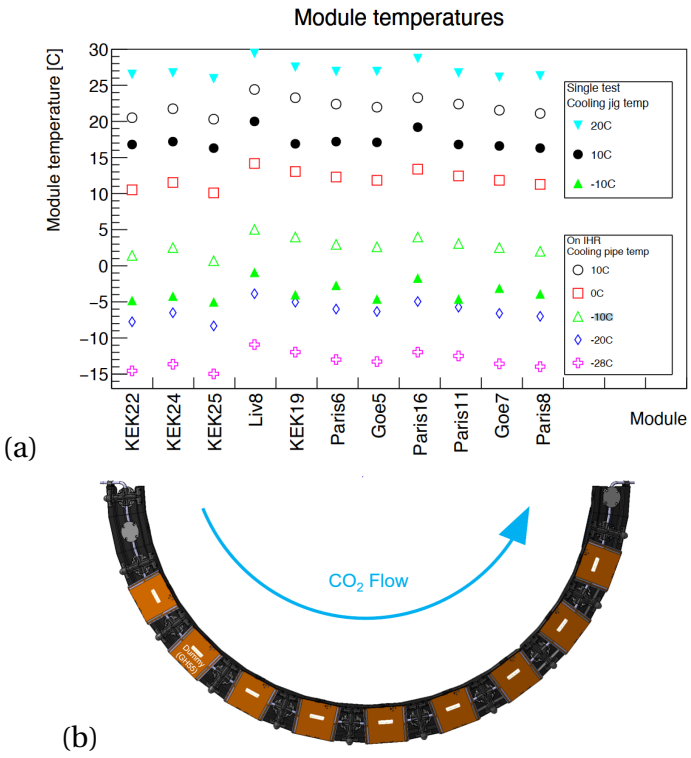

Figure 8.27: (a) Thermal variations between the NTC measured temperature value between a single module test with a cooling jig, and the obtained NTC measurement through MOPS by CO_2 cooling pipe. (b) Shows the IHR with CO_2 fluid inlet (left) to exhaust (right) as listed in (a).

8.4 Conclusion and Remarks with lessons learned

Several studies have been introduced to elaborate on the module performance, highlighting the main features of each testing setup, the potential impact on the QC procedures, and the overall performance using the 6 stages that ended with the realistic system test setup using the OB demonstrator. Starting with module production at CERN Pixel's lab, the testing stages starting with the initial tests at the assembly site and up to the system tests at the SR1 facility, proved of a very good performance with no potential degradation, while preserving the module's characteristics. The validation of the module production measures and the tooling methods, along with cell-loading demonstrated the final design report to be successful. The results obtained via the demonstrator setup have validated the concept of design, the key elements of the system test including on and off detector components, and the local loaded supports used. The studies performed with repeatability measurements proved to have a consistent output, enough to rely on the reproducibility of electrical scans. Furthermore, voltage and temperature inspections on Paris6 module clarified the expected electrical scan variations and related dependencies.

Moreover, the 32 received RD53A quad modules from the ITk clusters indicated several differences in electrical scan outputs. During the QC and production measures, few modules were received with a limited number of chips available for testing and some others have shown surprising start-up temperature values compared to what is expected. As indicated in the previous sections, only chips 2 and 4 were essential to be used for the demonstrator loading and testing. As in the case of the IHR, the modules have revealed no degradation of the readout performance. But, as was seen in HV channel-1, due to the early breakdown voltage of KEKQ19 the overall collective IV scan was not satisfactory.

On the other hand, the CO_2 cooling plant methodology with the associated loading components proved to be effective in providing adequate performance. Validating once again, the thermal functionality of cell-loading and gluing. Throughout testing, the OB demonstrator has proved to be a reliable setup to cope with the upcoming challenges in ITk construction. The international collective efforts bear fruit in designing and authenticating the demonstrator components and validating the designs of the local loaded supports and the module production stages. The demonstrator MOPS system, opto-boards, FELIX readout system, CO_2 cooling plant, interlock, and other sub-systems have proved to be able to mimic the real detector concepts and tackle the challenges encountered during multiple stages of commissioning in the SR1 facility.

However, many lessons were learned during the module production with a broad range of modules arriving from multiple institutes. It has been observed at many stages that human-induced errors in handling the module and non-fulfillment of precautions caused a lower yield in the number of working chips. Moreover, a limited number of modules have revealed areas of disconnectivity due to open bumps caused by improper handling of the module. Other modules revealed bad performance due to misconfigured register values provided by the assembly site that is not in agreement with the standardized configurations. Through this, it could be highlighted that proper training of personnel is essential to meet the required quality of module production. In addition, better coordination with the assembly sites is needed, while sharing similar standardized configuration of tests.

In the systematic levels of measurement, the 34 quad modules presented a broad range of inconsistencies in the AFE levels, IV curves, dissipated power, and thermal behavior. Those were proven to be the case for the OB modules, and as the envisaged ITk production would yield a total of 4472 ITkPixV2 quad modules for the outer barrel region, a methodology of determining the overall performance of an individual module to others, and a single stave to the total produced staves, with the targeted physics demands, must be kept in mind. In other words, a grading approach based on QC criteria has to be implemented to yield optimum physics demands. The previously introduced approach for the OB modules production QC proved to fulfill the OB demonstrator project targets and demonstrated no potential degradation after 6 stages. But, as the QC measures were limited to observing any inconsistent measurements in testing stages, it doesn't pose a combined analysis of electrical scans for an individual stage, to point at the cause of faults. To tackle this, a novel QC

assessment tool to quantify the production yield of the RD53A quad-pixel modules is introduced in the following section in addition to stacking the 32 quad modules to investigate the pixel defects trends.

8.5 Towards Deeper Module QC Analysis

In the domain of constructing tracking detector systems, the complexities of module production become paramount. Take, for instance, the Insertable B-Layer (IBL) [**?**] at ATLAS, where numerous modules are crafted for integration into the innermost detector layer. Yet, a broad spectrum of performance inconsistencies emerges among these modules. Compounded by potential degradation during production, determining whether such modules should be incorporated becomes a critical challenge.

To address these complexities, a rigorous quality control (QC) regimen is imperative. Establishing grading criteria becomes pivotal in assessing module performance, employing a multifaceted approach involving electrical scans, thermal behaviors, and IV curves. This selection process ensures only qualified modules proceed to cell loading and subsequent stave integration, guaranteeing optimal performance within the ATLAS framework.

Delving deeper, in this section we'll explore the identification, classification, and origin of defects unearthed by combining electrical scans. This intricate analysis paves the way for a novel QC assessment tool, meticulously developed and applied to the Outer Barrel demonstrator modules. This tool not only examines the performance and yield of 32 quad modules but also assesses the functionality of 114 chips up to the cell-loading stage introduced earlier. By navigating these vital aspects, this section illuminates the indispensable role of QC in constructing tracking detector systems, ensuring precision, reliability, and peak performance.

8.5.1 QC Analysis Strategy

A hybrid pixel detector consists of three main parts of particle detection, identification, and signal processing. The sensor works as the active area of detection, the bump bonding that enables the transfer of the single by flip-chip bump process on specific locations, and the chip FE. Each region of the detector features a certain desired performance that must be fulfilled. However, rising issues have been always a concern in detector R&D and mass-scale production. Therefore, the pixel defects [1] could be categorized into two major classes, as follows:

1. Defects in the readout electronics:

[1] It must be boted that other defects can be related to sensor leakage current, capacitive behavior.. etc, that are not included in this study.

(a) Digital dead or bad response.

(b) Analog dead or bad response.

(c) Failing to tune or bad-tuned pixel.

(d) High AFE noise.

2. Defects in Bump-bond

(a) Merged bump or shorted-pixel.

(b) Open bump.

Furthermore, the electrical scans previously introduced in Sec.8.2.1 enable to finding of unwanted performance, but, due to the complexity of the pixel detector architecture and electrical scans limitations, it is necessary to integrate and merge the output of the scans to reason out the cause of the faults that the pixel features due to the dependable functionality. For that reason, a combined analysis of electrical pixel scans would assist in finding the reason for detected defects. Keeping in mind, that the failure identification is exclusive, which means that only one category of pixel defect would be assessed per pixel based on the following order of failures exclusion in Tab.8.8.

As listed, the failure ID with the scan method implemented and the criteria of each classification can directly give an indication of faults. Digital and Analog scans[1] are based on a known injection of charges that in case of no faults would be received the same. In case a dead or bad response is found, the pixel would be masked and classified based on the criteria set. Contrarily, the loop will continue to examine the merged pixel class cooperating with the analog scan of a bad response and the perception of a turn-on of the S-curve by finding a low threshold occupancy. The threshold occupancy at the crosstalk scan is an indication of the received charges via the bump-bond to the central pixel based on the injection pattern introduced previously in Fig.8.4. The comprehension here denotes less than 10% of known injection charge[2] that resulted in a turn-on of the S-curve, due to shorted pixels. Besides, it must be mentioned that a threshold occupancy equal to zero is not accounted for as this might be an open bump. Moreover, the contrary in the case of the absence of a merged bump would show a turn-on of the S-curve at much higher values close to the injected, which in principle means, that after so many injected charges we started to see them in the central pixel. This definition of merged bumps is assisted by the analog bad response due to the fact in crosstalk scans, the injection is based on the analog domain.

However, if the loop doesn't find a hint about the last category, it starts to examine the threshold scans to detect untunable pixels and tuning bad pixels. Following the absence of it, the noisy pixels are examined by looking at the total mean of the individual AFE pixel and checking whether it is far away by 3σ. Lastly, the disconnection of the bump is difficult to find, even after discriminating

[1] Test injections for digital and analog scans are fixed to 100e.

[2] Total injections in crosstalk scan are 25Ke for Syn AFE, and 40Ke for the Lin, Diff AFEs.

Table 8.8: Pixel defects organized by the order of exclusion for RD53A quad modules with the relevant cut-values for each electrical scan.

Failure ID	Scan Type	Criteria Conditions
Digital Dead	Digital	Occupancy = 0
Digital Bad	Digital	Occupancy > 98 or 102 < Occupancy
Analog Dead	Analog	Occupancy = 0
Analog Bad	Analog	Occupancy > 98 or 102 < Occupancy
Merged Bump	Crosstalk and Analog	Analog bad and Threshold Occupancy < 10% of the total injections and Threshold Occupancy $\neq$ 0
Tuning Failed	Threshold	Threshold Occupancy = 0 (S-cruve Failed)
Tuning Bad	Threshold	| Pixel Threshold - Threshold mean | > 5 σ
Noisy Pixel	Noise	| Pixel Noise - Noise mean | > 3 σ
Open Bump	X-ray and Crosstalk	X-ray Occupancy = 0 and Crosstalk Threshold Occupancy = 0

other categories because of time constraints of demanded 15mins of X-ray scan tests and low hits originating in the sensor below the Surface Mount Devices (SMD). To assist with this, an implementation of the crosstalk scan of which both scans must identify a number of hits and threshold occupancy equaled to zero. Although, a comparison between the crosstalk-based scan known as the disconnected bump scan (DBS) and X-ray scan, to identify open bumps will come in Sec.8.5.4, after introducing the previously discussed procedures with examples. Moreover, an investigation-based study on open-bump-related effects on the AFEs noise and threshold will be introduced accordingly in Sec.8.5.2.

8.5.2 Feedback from QC Analysis

The introduced QC tool in the flow chart.8.28 was applied on KEKQ22 and Paris8 RD53A quad pixel modules. KEKQ22 is a module known with a region of open bumps in the corner of chip1, as seen in the X-ray scan Fig.8.29 (a), the sensor doesn't receive any hits and features ≈1300 open bumps. Examining the digital and analog scans reveals a persistent good response, but, with noise and threshold scans, the area of disconnected bumps shows a shift toward lower noise and tuned threshold values. Similarly, inspecting the crosstalk scan shows also threshold occupancy equaled to zero. Merging those scans based on the criteria discussed gives the pixel defects summary for the KEKQ22 quad module as in Fig.8.29 (b). This is an example of having defects in the bump bonding, and the potential aspects related to increased pixel capacitance are shown in the noise and threshold scans distributions in Fig.8.30 (a) and (b). In the analysis flow, an exclusive selection for disconnected pixels at KEKQ22 Syn AFE was done to filter out the associated noise and threshold values and plotted to the non-disconnected pixels. As depicted in the figures, the open pixels noise and threshold are located in the lower tail of the distributions deviating away from the means.

Furthermore, Paris8 module poses a certain bad response in the FE chip affecting other scan

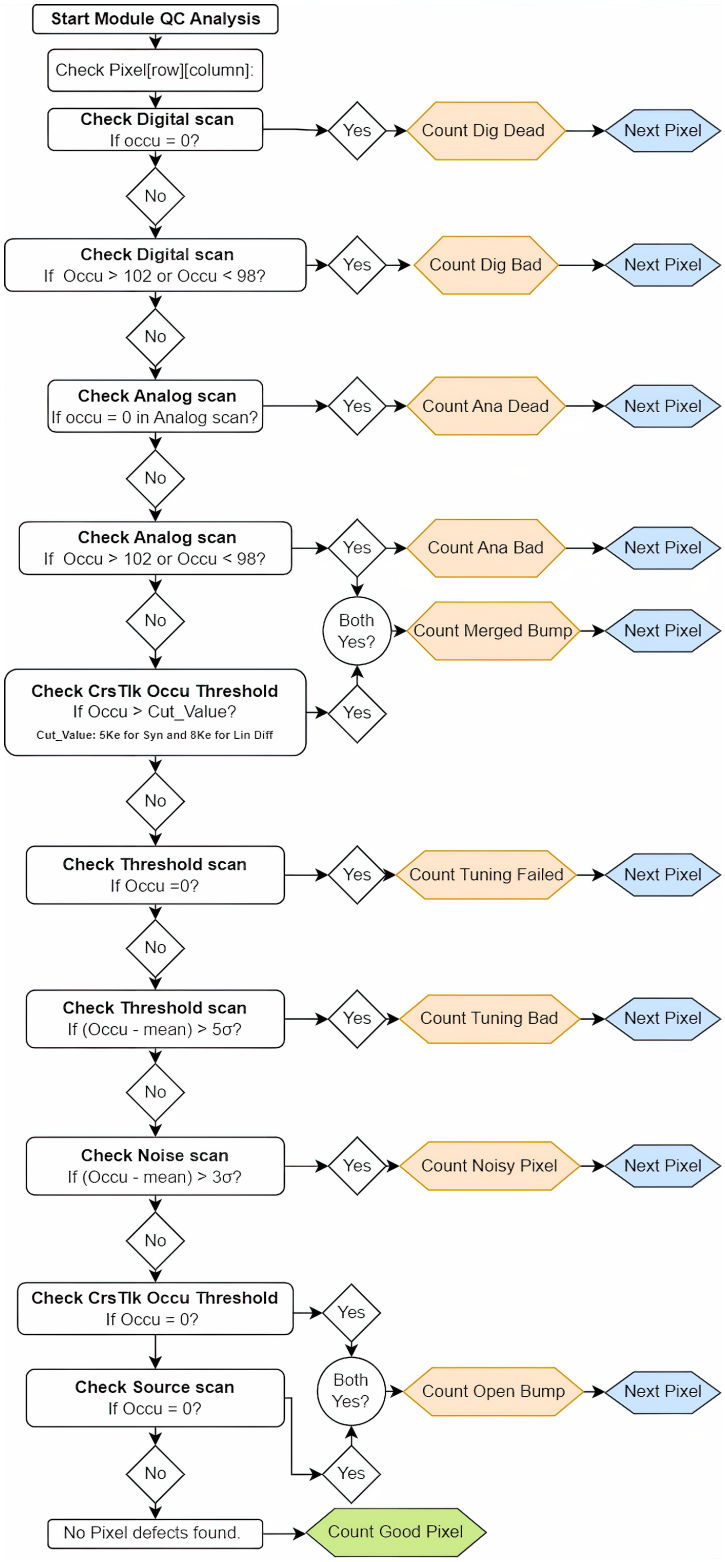

Figure 8.28: Pixel defects analysis categorization and criteria flow chart.

information. It can be observed in Fig.8.31 (a) the various unseen responses in the noise, threshold, crosstalk, and X-ray scans. In Fig.8.31 (b), the pixel defects summary shows a major fault seen as a column in the Lin AFE by the digital scan.

Applying this methodology to the 10 previously studied IHR OB demonstrator modules is apparent in Fig.8.32 (a) and (b). Whereas, due to the lack of X-ray or source scans in stage 6, the QC measures were applied at the cell-loading stage 4. It is evident that the majority of faults related to the modules are due to tuning failed and noisy pixels. With a fraction of other defect categories as explained for Paris8 and KEKQ22 modules. However, what is perceived at first sight in Lin AFE is more noisy pixels and a more untunable threshold in the Diff AFE. As this is a problematic issue, an investigation of 32 quad modules for the OB demonstrator project will be introduced in the following Sec.8.5.3.

8.5.3 32 Quad Modules Stacking

Using the QC methodology introduced, an exploration of 32 quad-pixel modules are ingeniously stacked atop one another. This approach holds a profound purpose: to unravel potential failures that these modules might harbor during production and relate the potential defects or faults to the pixel location. By merging the outcomes of comprehensive electrical scans with the functioning chips, a remarkable map emerges summarizing the overall performance. This map will assist in finding problematic locations where the pixel matrix tends to have specific undesirable behavior by resembling a map of each pixel defect location.

In essence, this method unveils a novel way of obtaining electrical scans for each AFE type in the chip for each module and joining it via a loop over 114 working chips in 32 quad modules for the same pixel location. Potentially, this analysis obtains at the core of AFE of each module produced for the OB demonstrator project valuable information on the overall functionality of the chips and the corresponding yield of good pixels. Fig.8.33 (a) illustrates the number of discovered digital bad pixels for 114 chips, showing only 1 chip exhibiting a digital bad response due to Paris8 as shown in the previous section. Following that, Fig.8.33 (b) demonstrates the digital dead findings in the Diff AFE featuring also 1 chip, with no particular location that tends to have major faults.

However, the digital bad and dead pixels for the 114 chips have the property of being in clusters, as the findings proved for 32 tested modules. Moreover, Fig.8.33(c) displays the analog bad class showing collective faults from 4 chips in the Diff AFE. In fact, the displayed analog bad response was found in the SiegenQ2 quad module due to bad tuning of the $Diff - LCC$ register value. Moreover, Fig.8.34 (a) shows a limited number of tuning bad pixels, and (b) surprisingly indicates a large fraction of chips exhibiting a pattern of tuning failed pixels in Diff AFE, with a maximum mutual matching of 35 chips in an individual location. However, Syn and Lin AFEs show a small amount distributed among the pixel matrix. Nevertheless, in Fig.8.34 (c) the same pattern seen in the Diff AFE is found for the noisy pixels class, with randomly distributed noisy pixels in Lin AFE, and a very limited number

in Syn AFE. In spite of that, 40 merged bumps have been found in 114 chips based on the cut values introduced in Tab.8.8. The location has no particular feature of matching between chips but tends to be in module edges, as seen in Fig.8.34 (d). Lastly, the open bumps locations are evaluated in Fig.8.35 using the complete layout of the RD53A quad module. Through the figure, the locations are displayed where the chips are exhibiting disconnected pixels. At chips 2 and 4, major disconnections are seen near the sensor edge for two individual chips, out of the 114 chips stacked. It must be noted that the maximum correlative of chips in an individual pixel location is only three open bumps.

Moreover, more information is gained by combining the FE-related defects, known as the non-disconnection pixel defects. By joining the faults found in digital and analog bad and dead responses, noisy, bad, and failed tuned pixels, the AFE-related problems are obtained. It is clearly seen in Fig.8.36 (a) that a higher number of consistent faults are found in the Diff AFE, while much less in the Lin and Syn AFEs. Moreover, a comprehensive summary for 8.75M pixels tested in the 114 chips is expressed in Fig.8.36 (b) indicating the AFE type and classes of pixel failures. The categories where defects were found significant are related to the tuning failure and noisy pixels, significantly observed in the Diff and Lin AFE. Open bumps for the three AFEs represent collectively 0.29% of disconnections out of the total 114 chips and only 30 merged bumps. The analog, digital, and tuning bad pixels are negligible and constitute a fraction of the pixel defects. Furthermore, the concluded summary yields 95,41% of good pixels with no defects and 4,58% with failures summarized in percentage aside from the AFE type in Fig.8.37. Moreover, it must be noted that the percentage of findings doesn't include the non-functioning chips. For the 32 quads made up of 128 chips, 14 weren't working. However, this yield is satisfying for the OB demonstrator project while using RD53A electronics, as it enriches our understanding of the performance and also offers a new perspective on addressing challenges and refining our techniques for producing robust and reliable modules. As those results are also taken from the cell-loading stage, a percentage of open bumps were due to bad handling. In the next section, a brief summary of outcomes by comparing the disconnected bump and X-ray scans is presented.

8.5.4 X-ray Vs. Disconnected-Bump Scans (DBS)

Different electrical scans are used to identify potentially open bumps. The X-ray scan depends on real particle interaction with the sensor and is efficient in giving a sufficient number of hits by prolonging the time of irradiation. But, consumes time in masking, and requires 15 minutes at least to acquire the desired number of hits. However, the limitations in such a method come in the SMD components as lower hits are expected. On the other hand, DBS relies on the neighboring pixels and is fast compared to X-ray. But, there is a chance of not catching all disconnected pixels, especially in the module edge. In addition, limitations exists in finding open bumps at couple-pixels-structure in case one of them is already opened. Nevertheless, the forward bias scan is faster, more effective, and more reliable if compared to reverse-biased noise and threshold scans. One drawback is in biasing

positive voltages in HV chains while testing on staves, which will then lack the comparability to previous stages in individual tests. Therefore, an investigation using the 114 chips is performed to compare the X-ray scan with DBS, to evaluate the discrepancies in finding the disconnected pixels. However, it must be noted that those methods are generally complementary, and none of them has a 100% agreement, e.a., The X-ray scan is not consistent every time with itself. In the following analysis methodology, the previously discussed QC measures are optimized in two different branches for identifying open bumps. The first is based on using exclusively the X-ray scan and classifying pixels with hits equal to zero as open bumps. The second deploys the DBS and considers an open pixel in case no charge was measured, similar to the occupancy of X-ray. Moreover, as matching is expected to be found, the open bump as in Fig.8.38, would be labeled as open in both scans. Finally, the two branches would be applied to the OB demonstrator modules to observe any discrepancies.

The analysis approach is applied, once again, on the KEKQ22 quad module with the edged disconnected pixels. The white pixels indicate the non-open but faulty due to other classifications. Yellow labeled pixels indicate open bumps seen via X-ray, and red to open bumps found by the DBS. In case of a matching between both, the pixel is labeled in black. Nevertheless, good pixels are indicated in green which manifests perfect behavior based on the QC strategy cut values for both scans. Inspecting the regions of disconnection reveals confirmations of open bumps in both scans in Fig.8.38 (a), however, the DBS shows more open bumps away from the edged pixels intercepted with confirmations of both scans. Moreover, the junctions between the three different AFEs pose an open bump seen at many chips, which is consistent in the column between Syn and Lin AFEs and along row zero. Furthermore, the overall performance of both scans is evaluated in Fig.8.39 with a notable figure that the matching between both scans is restricted by the X-ray findings and more open bumps are seen at the DBS for each AFE type.

8.5.5 Conclusion

In the journey toward summarising the RD53A quad module's performance, the implementation of a novel and useful tool emerges to be valuable for gaining insights. This tool has harvested within the context of the OB demonstrator project the main features and potential defects for 114. Making the first milestone of yield evaluation for large set of chips and their associated performance.

Using the implemented tool, the defects and faults have been evaluated to understand the origin of faults and their associated effects in other means, uncovering the connectivity of the module performance with the available electrical scans. The most problematic figures have been studied for both the FE and the bump connectivity. Exploring the likelihood of locations that have a trend of defects.

The augmentation of 32 selected RD53A quad modules forms the basis of this study and has served as a canvas upon which we paint a vivid picture of the module's behavior. This canvas reveals not only expected faults but also provides a road map for investigating the very essence of the

challenges that arise. This endeavor, marked by ingenuity, employs a unique approach of stacking 32 quad modules. In doing so, it illuminates the main pixel trends and identifies regions that are predisposed to potential faults, offering an unparalleled insight into the underlying complexities.

Moreover, the spotlight was cast upon an open bumps region of the chip, unraveling a fascinating revelation. Within this region, we observed a shift in threshold and noise, where these values exhibited a marked decrease in comparison to the noise or threshold-tuned values of the overall regions. This discovery serves as a testament to the tool's capability to locate and uncover anomalies that could otherwise remain concealed.

Furthermore, the study has examined the Diff FE, unearthing a pattern consistent across multiple modules. This observation suggests that certain pixels within these modules exhibit a more problematic nature, forming a common thread that binds them together. This intricate pattern underscores the interconnectedness of these modules and paves the way for targeted interventions and refinements, especially for threshold tuning and noise control.

Moreover, a comparison between the two scans capabilities to discover open bumps has been studied and sorted out. The DBS, even with its better easiness and speed of use along with no required development of a dedicated irradiation setup, poses over estimated number of open bumps compared to the X-ray scan. The DBS has shown limitations in finding open bumps and a tendency to resolve the pixel's information in certain columns to be disconnected, a drawback that the X-ray scan didn't run into.

In conclusion, the implementation of this tool marks a pivotal juncture in our research, fostering a deeper understanding of module behavior and uncovering a spectrum of potential improvements. As we move forward, armed with these insights, we set our sights on pushing the boundaries of this tool that could potentially be implemented for the ITkPixV2 pixel modules knowledge by probing the RD53A quad modules.

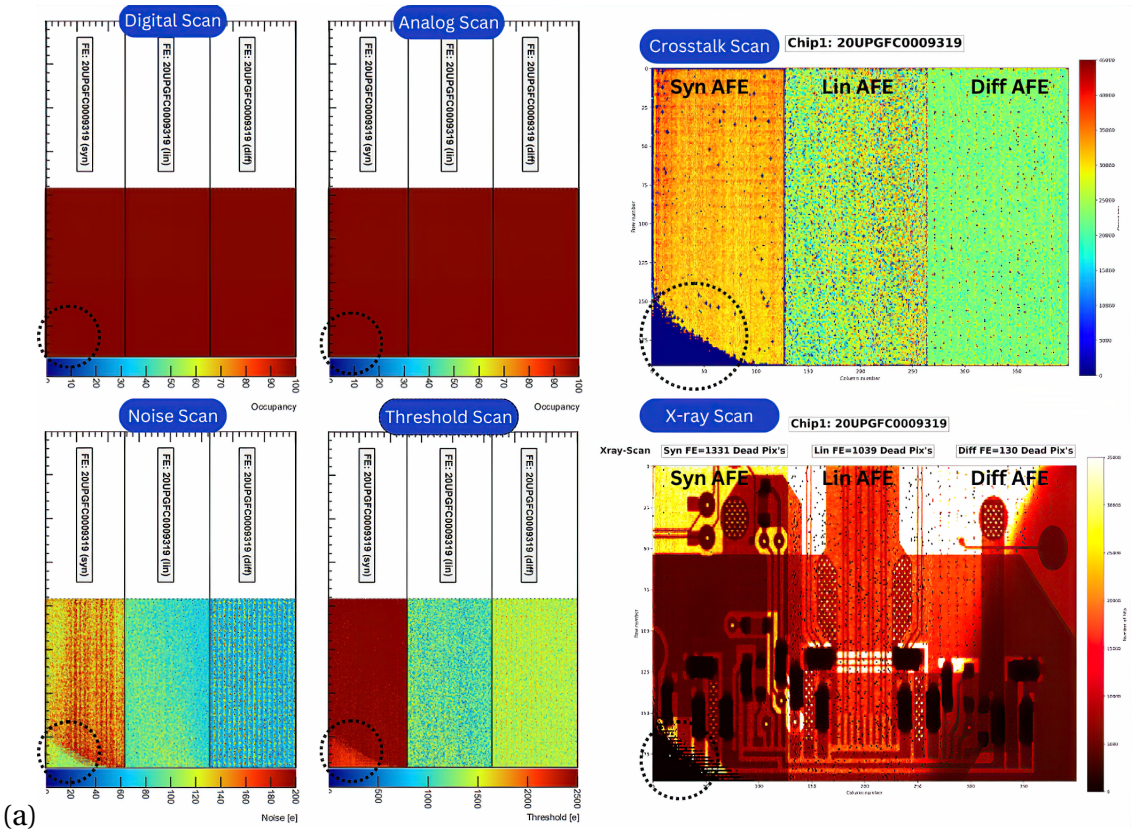

(a)

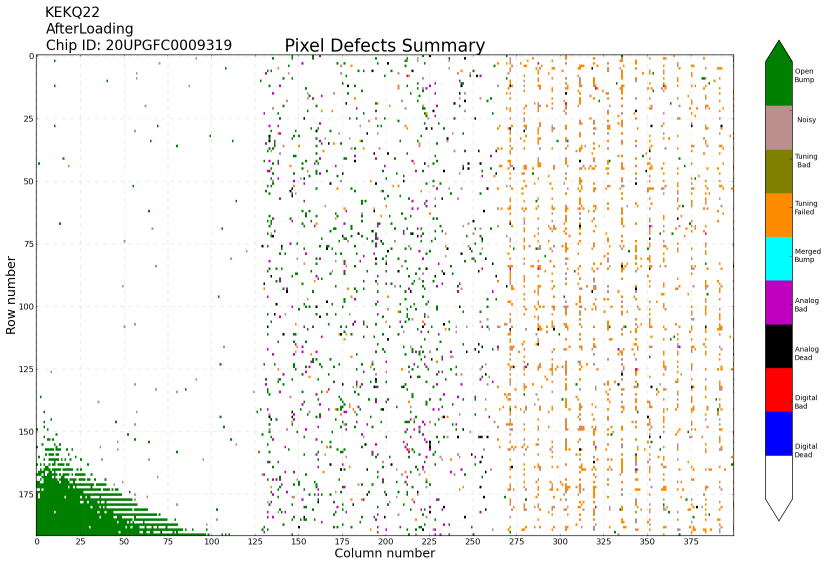

(b)

Figure 8.29: (a) All basic electrical scans for KEKQ22 chip 1 reveal an open bump area at the edge of the Syn AFE. (b) Summarizes the information obtained for combining electrical scan output using the QC method with the labels of each pixel defect found.

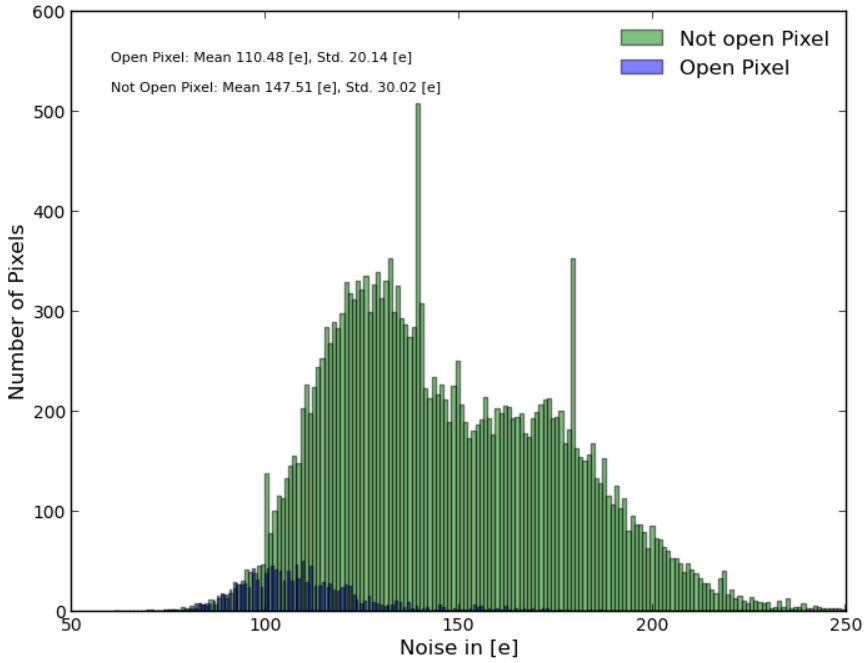

(a)

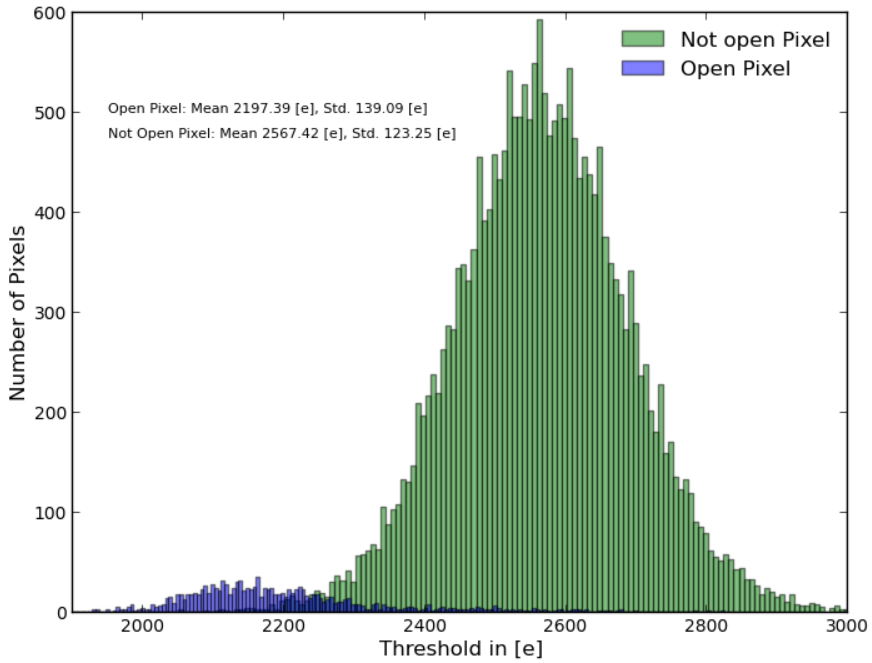

(b)

Figure 8.30: (a) Syn AFE Noise scan for KEKQ22 module showing the potentially disconnected bumps with the associated pixels noise to be lower and deviating from the mean. (b) Syn AFE threshold scan for the open bump pixels deviating from the tuned threshold value at 2500e.

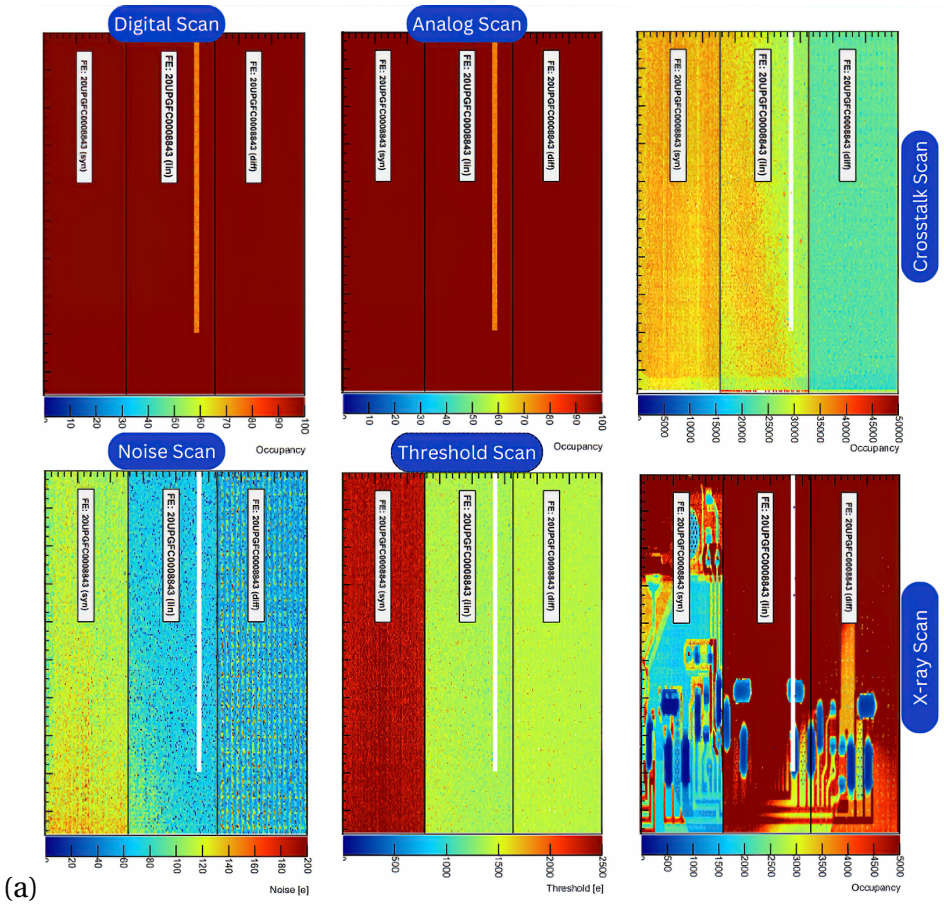

(a)

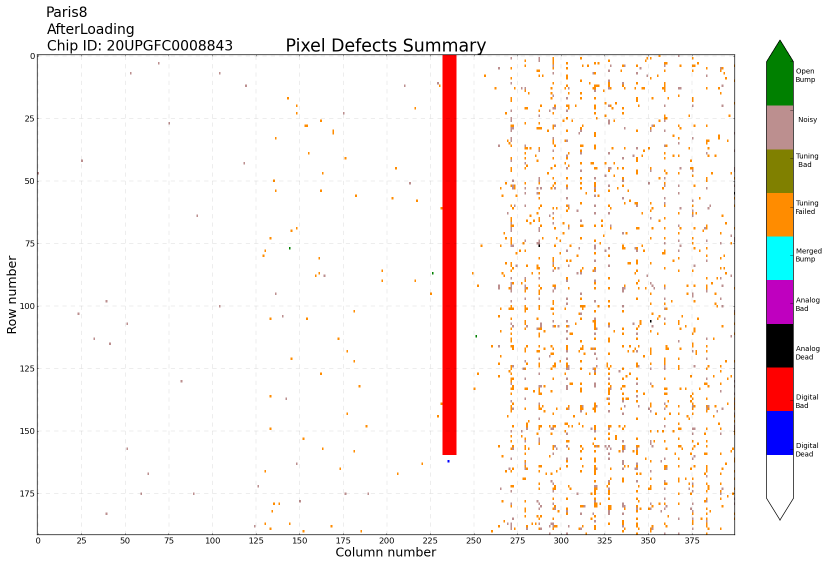

(b)

Figure 8.31: (a) All basic electrical scans for Paris8 chip 4 showing a bad response in both analog and digital scans for an identified column in the Lin AFE. (b) Summarizes the information got for combining electrical scans output using the QC method with the labels of each pixel defect found.

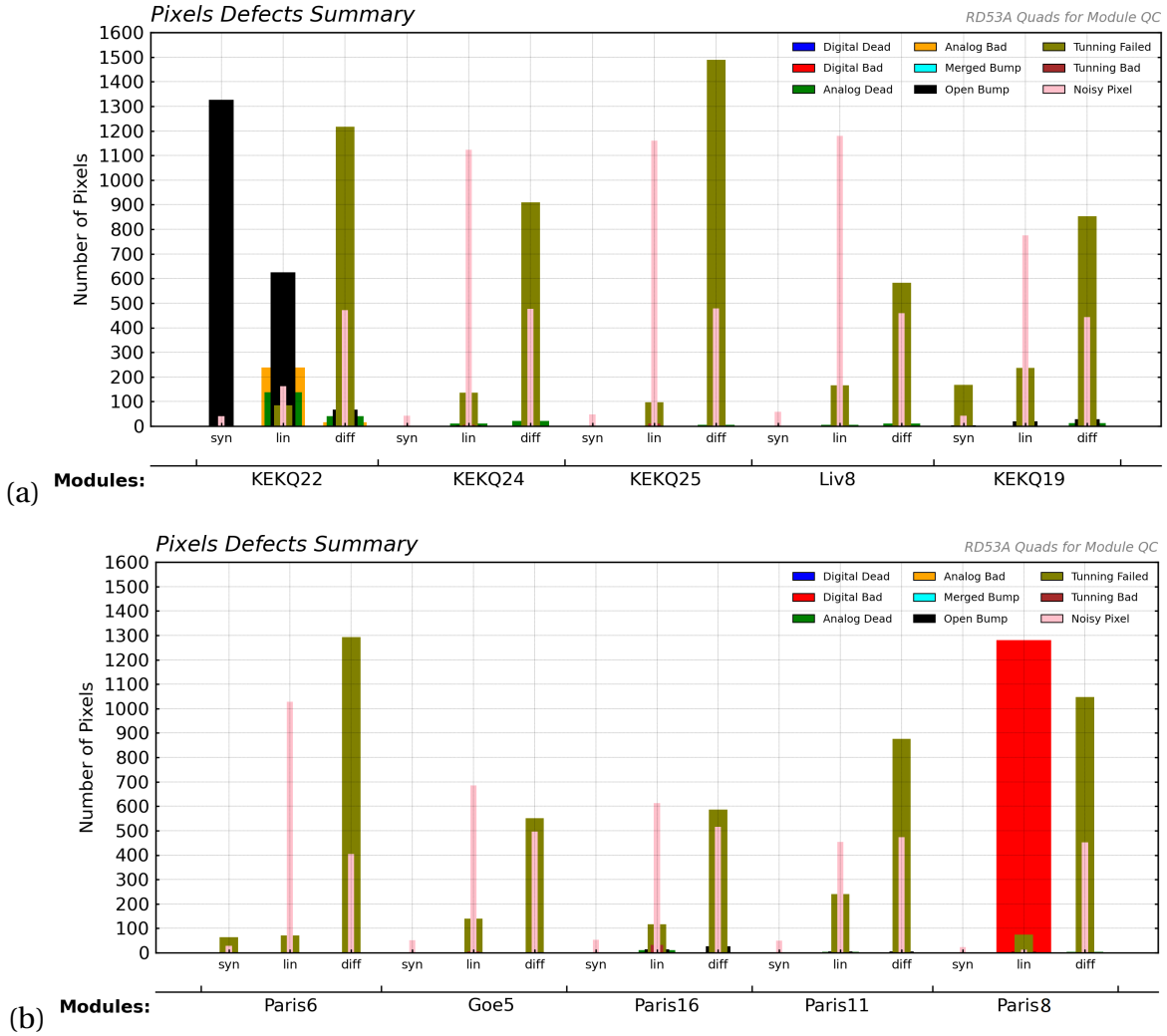

Figure 8.32: Summary of the QC procedure to identify and classify pixel faults in the used modules for the IHR stave. Electrical tests are gathered from stage 5, at the cell-loading.

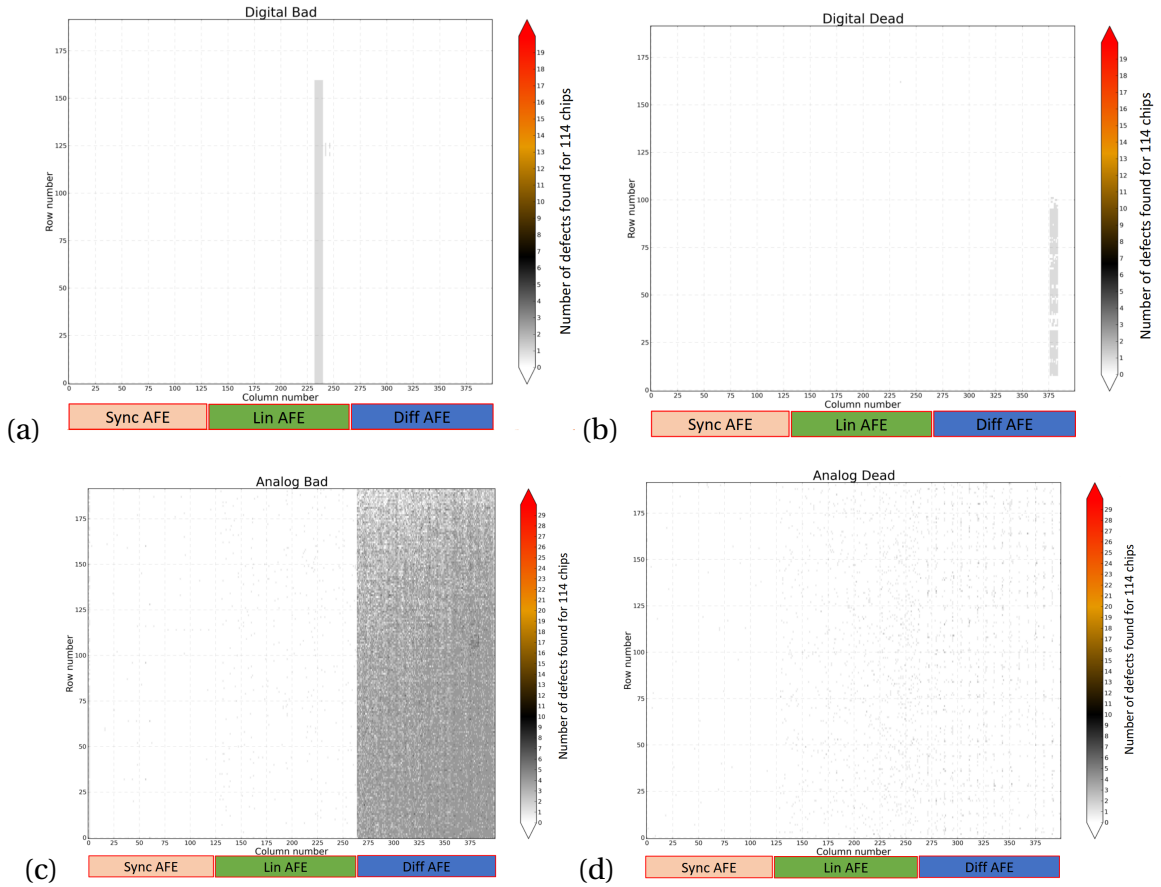

Figure 8.33: (a) Shows the digital bad response found for 114 chips, indicating 1 chip that features a column of bad response. (b) Indicates the digital dead pixel of occupancy equaled to zero for only 1 chip. (c) Displays the analog bad response showing that the Diff AFE has the majority of its pixels with 4 chips indicating the pixel defect class. (d) Illustrates a limited number of analog dead pixels.

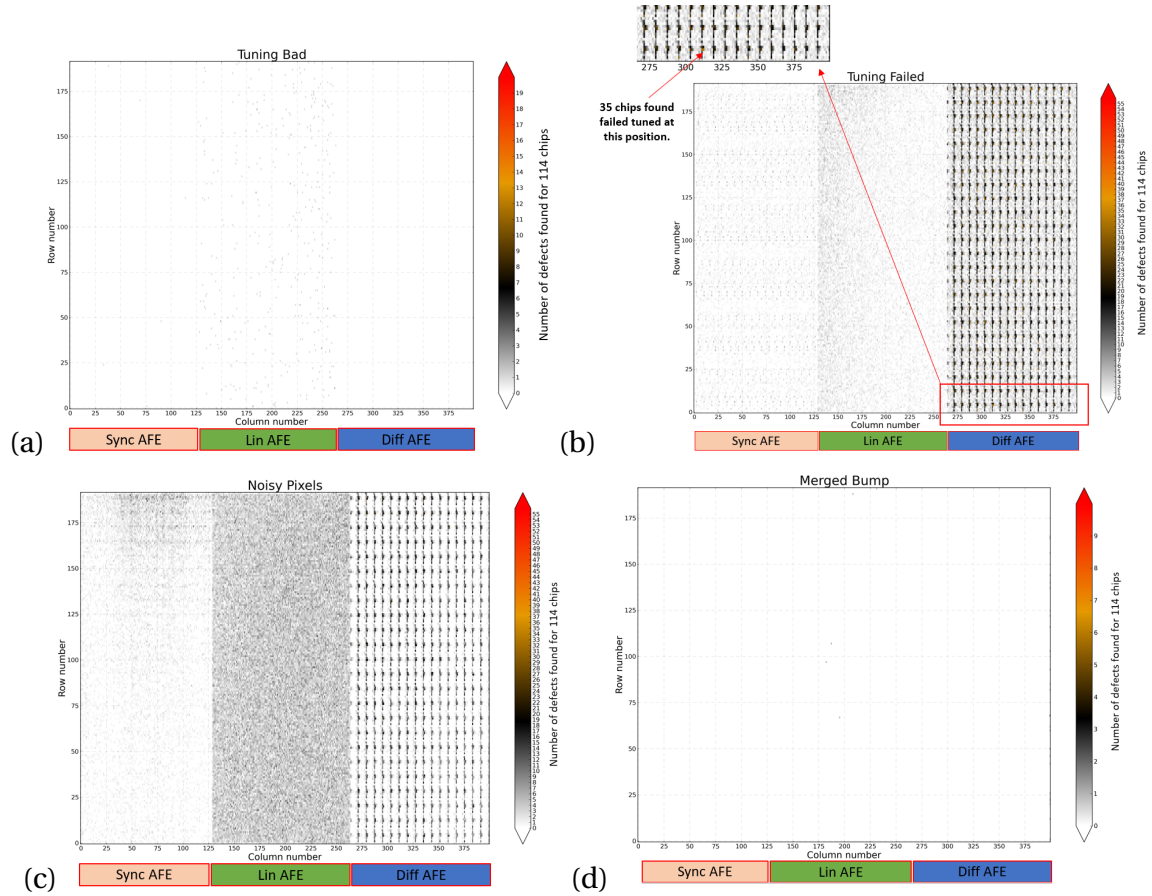

Figure 8.34: (a) Features the pixels with more than 5σ of threshold deviation from the mean. (b) Shows the failed tuned pixels with a large number of pixels in the Diff AFE with a pattern and mutual confirmation at a maximum of 35 chips at the same location. (c) Displays the noisy pixels with a pattern similar to (b) but with fewer chips at the same location. (d) Indicates a very low number of merged bumps found across 114 chips.

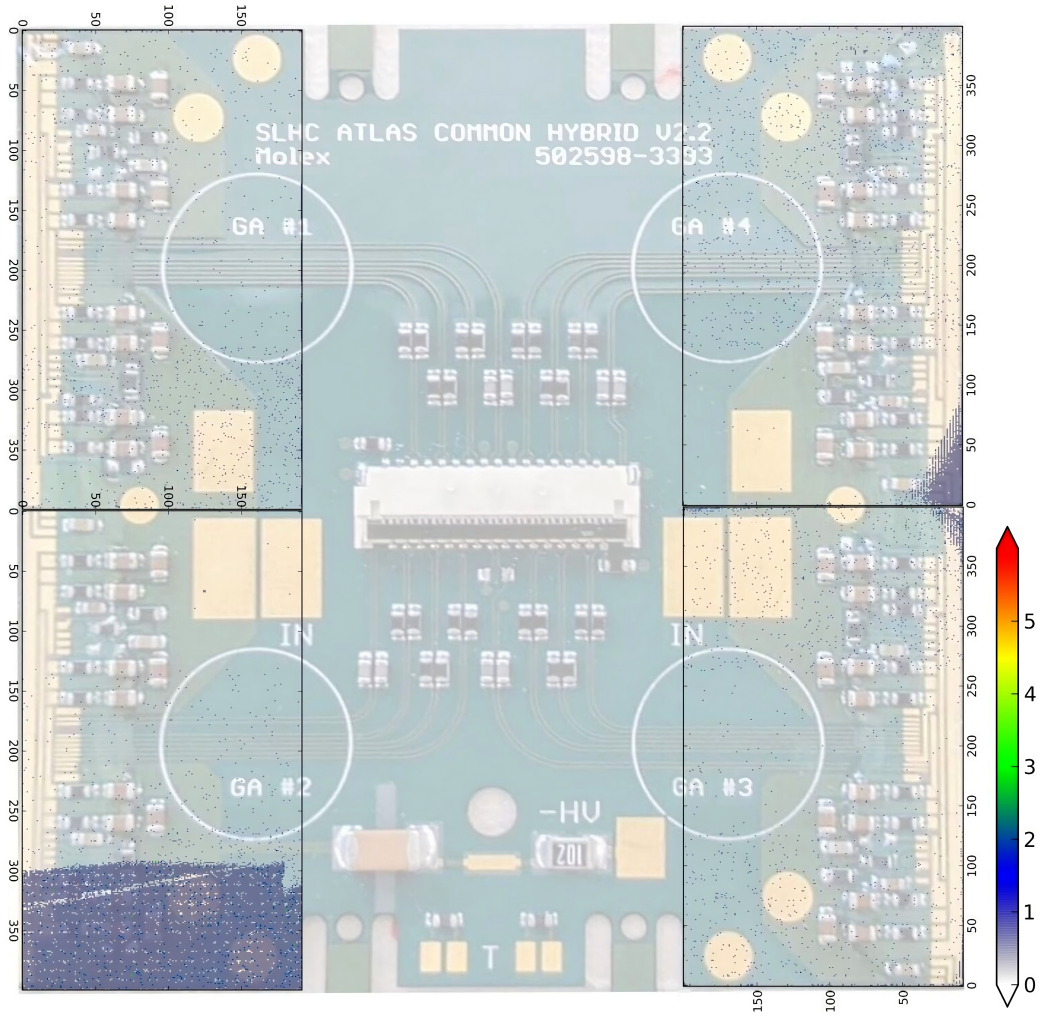

Figure 8.35: Quad module view of the open bumps locations found for 114 chips distributed based on the chip number, with the legend indicating the number of open bumps findings. The top left chip, known as chip 1, is made up of 26 chips. Chip 2, on the bottom left side, is constituted of 29 chips stacked and featuring a region of disconnected pixels at the Diff AFE, with a maximum location mutual agreement of 3 open bumps. The bottom right, referred to as chip 3 is made up of 29 stacked chips, indicating a small region of open bumps at Diff AFE at the edge of the sensor. However, the last region of 30 stacked chips at the top right of the module has open bumps at the Syn AFE that were previously discussed for the KEKQ22 module. The collective behaviour as seen in the 4 different regions in the sensor indicates a trend to have large disconnection areas at the sensor edge sides.

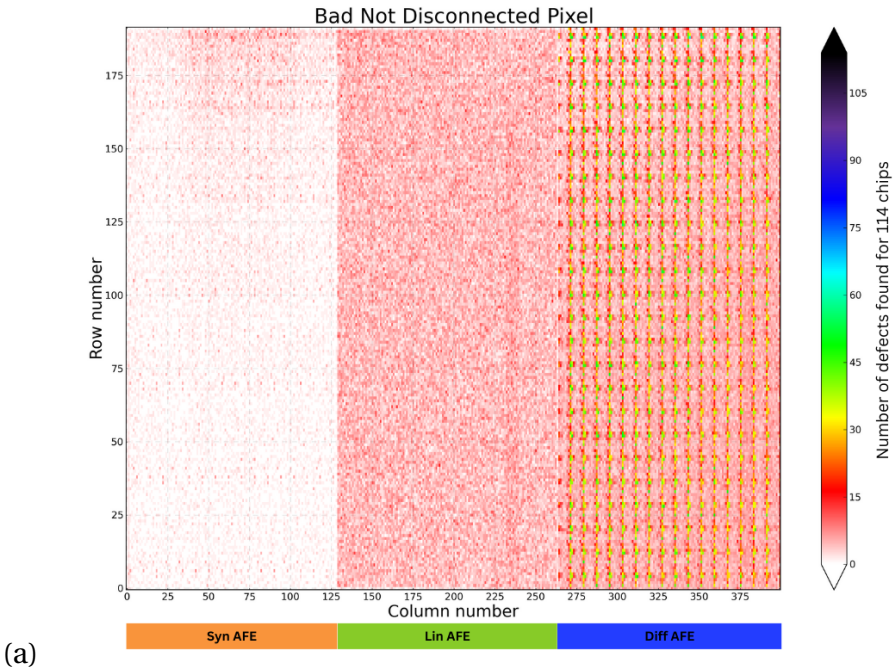

(a)

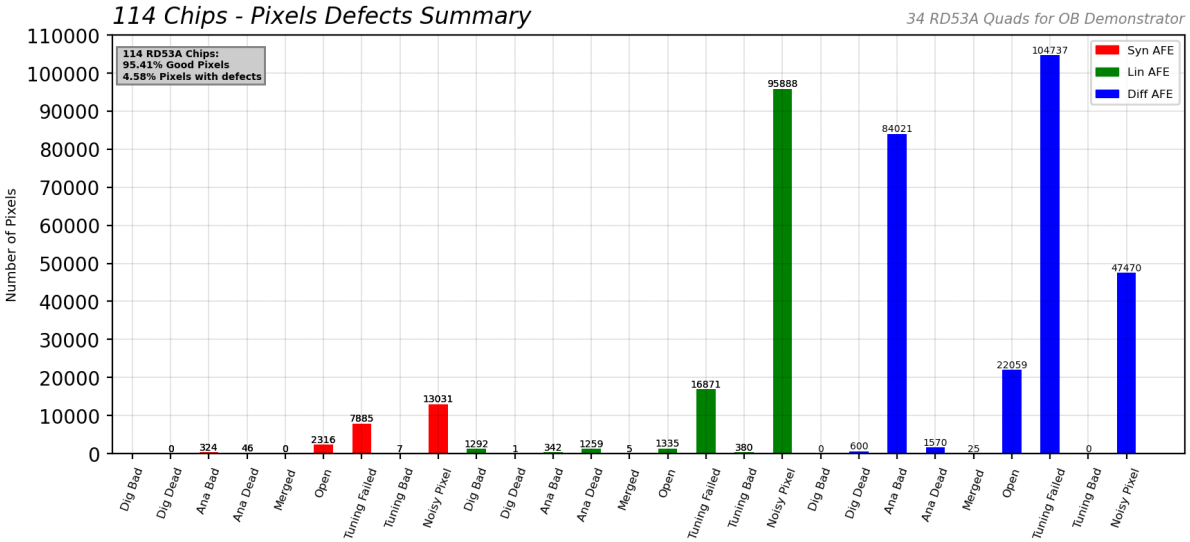

(b)

Figure 8.36: (a) Represents all observed failures not including the disconnected and merged bumps for 114 chips. The Diff AFE poses the highest number of faults and consistencies between chips in specific locations. (b) Indicates an inclusive view of all counted defects in the three AFE of RD53A quad modules.

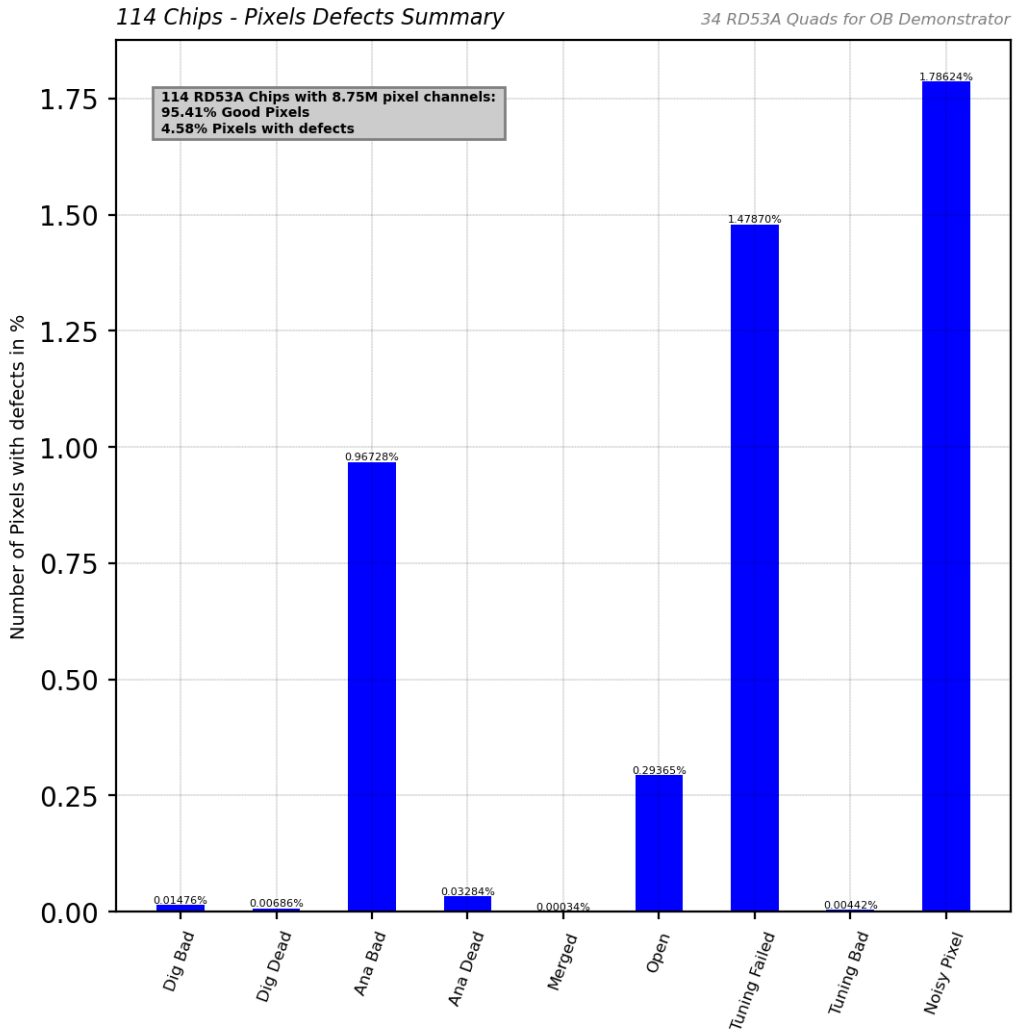

Figure 8.37: Expresses the summary of gathered information on pixel defects not accounting for the AFE type. The percentage of each bar presents the amount of failures out of 8.75M pixels.

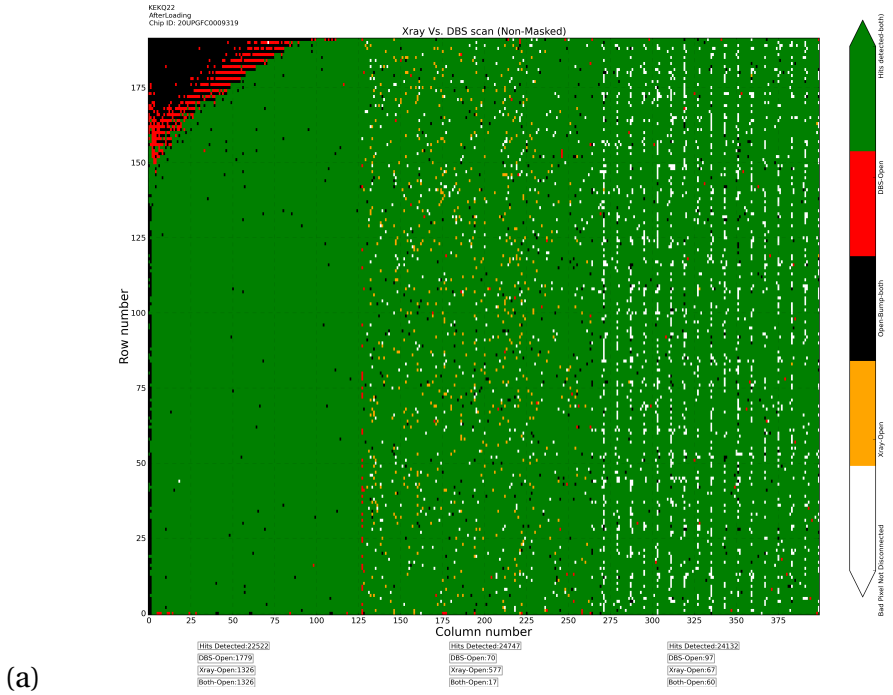

(a)

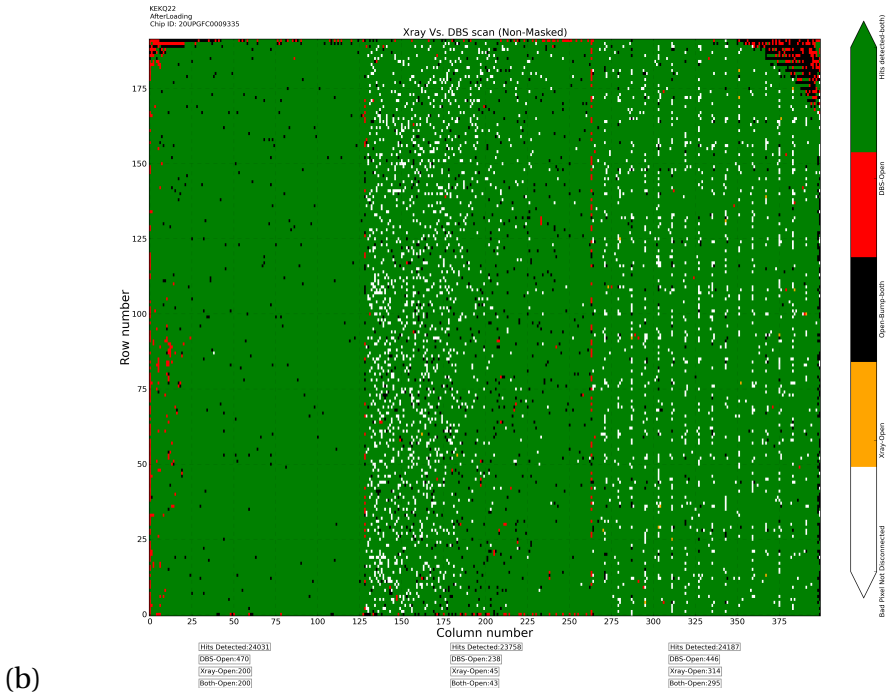

(b)

Figure 8.38: Pixel map showing open bumps findings in both scans with mutual agreements: (a) Indicates the region of disconnection seen at the pixel edge. (b) Highlights the location of open bumps by both scans and more for the DBS at the intersection between Lin and Diff AFE.

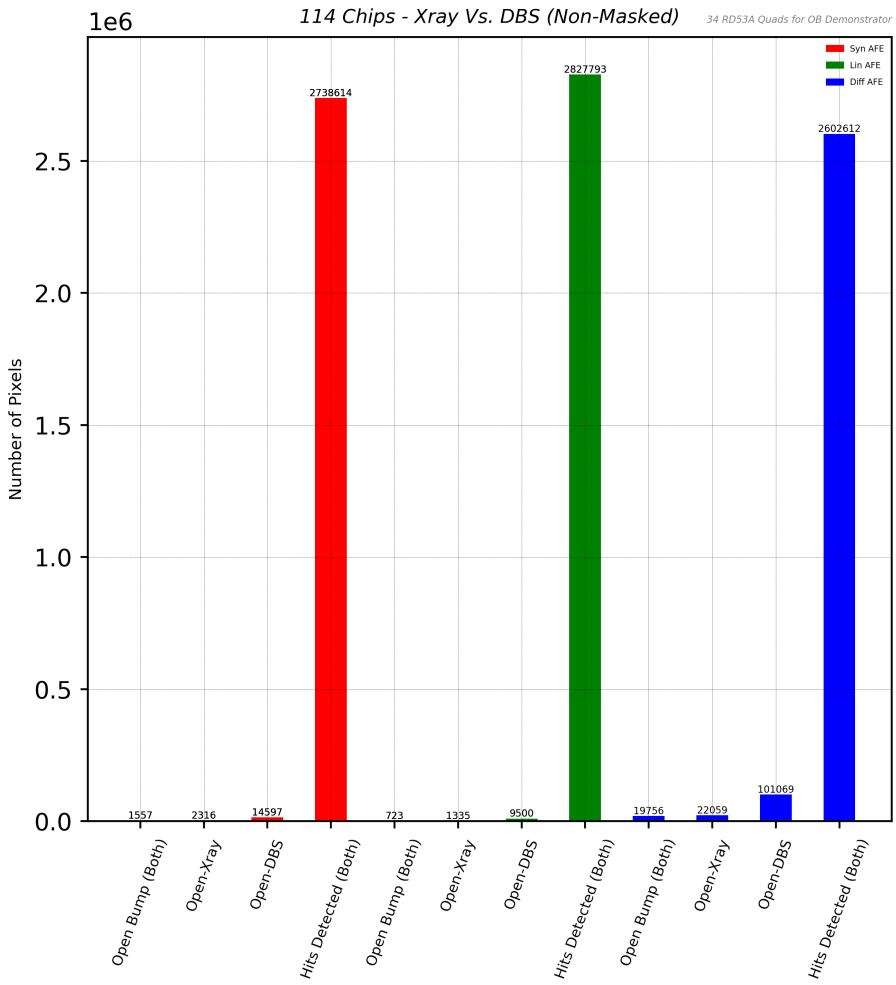

Figure 8.39: Summary of X-ray Vs. DBS open bumps findings for the 114 chips by using the QC methodology to eliminate other pixel failure categories.

9

Conclusion and Outlook

The studied aspects of the thesis have covered a wide range of R&D programs encapsulated in the front-end electronics validation and testing and the evaluation of the produced pixel quad modules, within the ITk project in the ATLAS experiment. The comprehensive exploration of various aspects of the development took place at several levels to tackle the rising challenges due to the high luminosity phase. The undertaken irradiation campaigns have provided valuable insights into the chip's performance under harsh radiation conditions, showcasing its resilience against total ionizing dose (TID) up to 500 Mrad. The investigations into the effects of irradiation and subsequent annealing on ring oscillators have revealed degradation and partial recovery, offering crucial information for chip stability.

Moreover, simulation-validation efforts have aligned with experimental data, marking a significant achievement in characterizing ring oscillators accurately. The testing conducted at the proton synchrotron, employing the IRRAD facility, has shed light on single event upsets (SEUs) and memory storage reliability in the readout chip under proton flux similar to what is envisaged in the HL-LHC. The calculated SEU cross-section has added to the understanding of chip behavior in challenging environments and proved to be within the design standards.

In parallel, the thesis delved into test beam setups and studies involving quad pixel modules, employing the Super proton synchrotron at CERN. By exposing irradiated and unirradiated modules to energetic pion beams, the efficiency, charge collection, and resolution of the detector were thoroughly examined. The outcomes demonstrated that the quad modules met expectations under specific voltage biases, offering valuable insights for further developments. Within testing, the unirradiated modules scored within -100V and -130V a corresponding pixel hit efficiency ϵ_{eff} of 97,9% and 99%, respectively. In contrast, irradiated modules were more challenging in maintaining a nominal

leakage current at a higher voltage bias. Depleted with -200 and -600 volts, the bias voltage proved to be a key player in improving ϵ_{eff} to reach 96,75% and 99,36%, respectively.

Regarding the upcoming mass production of pixel quad modules, efforts have been made within the pixel lab at CERN to assist and contribute to the production and quality control of RD53A modules that played a pivotal role in the outer barrel (OB) demonstrator project. Through meticulous checks and testing, 32 quad modules undergo several production steps while being studied at each stage. The modules exhibited high performance and durability and showed beyond doubt a high production yield that is, out of 32 modules only 14 chips were found to be non-functional. Moreover, several recommendations and insights were also raised. Nevertheless, at the final testing stage, the inclined half-ring (IHR) mounting stave showcased exceptional stability, and the collaborative efforts in constructing the demonstrator system facilitated the commissioning of on and off-detector systems. The CO_2 cooling method proved to be reliable through the attained NTC values after module cell-loading and validated the thermal behavior, thus, the cell-loading method with local loaded support structure.

Moving ahead with the testing data of OB demonstrator modules, an innovative quality control approach was introduced, involving combined electrical scans and data analysis to identify and classify pixel defects. This process allowed for the categorization and localization of defects within the pixel matrix. The evaluation of 114 chips further refined the understanding of pixel defect trends, revealing that the majority of chips exhibited good performance, while a fraction displayed defects mostly related to AFE tuning and noise. Additionally, the study uncovered trends related to specific pixel locations and differential analog front ends.

In essence, this thesis encapsulates a range of pivotal contributions to the advancement of pixel front-end chip electronics for the ITk detector. Through meticulous testing, quality control, and collaboration, the work presented here has significantly enriched our understanding of the performance and reliability of these crucial components in the pursuit of the ITk development and construction phases.

Looking ahead, it's important to acknowledge the work that was planned but faced challenges due to time constraints. One of the areas that required further exploration was the X-ray irradiation simulation framework. While initial simulations using the rad-model 2019 from Cadence were carried out, the results did not align with the data obtained from actual irradiation. As a result, the simulation model would need optimization based on the insights gained from the experimental data. The optimization of the simulation model was initially considered during the first year of the thesis, particularly during the Covid-19 pandemic. However, these efforts were temporarily paused to prioritize test beam campaigns and analysis.

Additionally, the quality control (QC) method introduced in Ch.8 was intended to be further developed. The plan was to expand the methodology beyond electrical scans, incorporating IV curve analysis and evaluating critical factors such as breakdown voltage, leakage current at defined

bias voltages, and the suitable bias range for modules. Thermal behavior also posed an important aspect for evaluation. The vision was to create a comprehensive QC process that integrates electrical, thermal, and IV curve scans. This comprehensive approach would help determine the module's position on the staves, prioritizing modules with higher power dissipation or leakage current for appropriate cooling strategies. The selection criteria for high-voltage channels would be refined to ensure feasible IV curves for effective module depletion. This strategy would be particularly important for addressing early breakdown voltages observed in certain channels, as shown in Ch.8.

Nonetheless, it's essential to acknowledge the complexity of implementing a grading methodology for modules and loaded staves. With a considerable number of quad modules for the ITk outer barrel, totaling 4472, arranging staves on the global supports within the ITk structure as a function of the pseudorapidity requires a sophisticated approach to meet the demands of physics experiments. As this thesis was conducted during the research and development phase, it's with confidence that the future generations of PhD researchers and scientists will continue to build on these efforts. The ITk project is a monumental undertaking, and the ongoing dedication of researchers will undoubtedly lead to further advancements and innovative solutions in this remarkable endeavor.

As we bring this humble work to a close, we do so with the belief that every small contribution, every meticulously tested sensor, and every successful experiment, no matter how modest it may seem, furthers our collective journey of exploration and discovery. This work is dedicated to the shared goal of understanding the cosmos, and I look forward to the next chapter of collaboration and discovery in the field of particle physics.

In the spirit of Lederman's vision (See quote at p. 26), we continue to push the boundaries of our knowledge, driven by curiosity and guided by the collaboration between theory and experiment. The journey is far from over, and together, we will continue to unravel the mysteries of the universe.

Bibliography

[1] P. Pralavorio, "Particle Physics and Cosmology", in *100e Ecole d'Ete de Physique: Post-Planck Cosmology*, pp. 353–405. 2015. arXiv:1311.1769 [hep-ph].

[2] P. D. Group and Workman, "Review of Particle Physics", *Progress of Theoretical and Experimental Physics* **2022** (2022) 083C01.

[3] **ATLAS** Collaboration, "Standard Model Summary Plots February 2022",.

[4] W. A. Barletta *et al.*, "Planning the Future of U.S. Particle Physics (Snowmass 2013): Chapter 6: Accelerator Capabilities", in *Snowmass 2013: Snowmass on the Mississippi*. 1, 2014. arXiv:1401.6114 [hep-ex].

[5] H. M. Gray, "Future colliders for the high-energy frontier", *Reviews in Physics* **6** (2021) 100053. https://www.sciencedirect.com/science/article/pii/S2405428321000022.

[6] "The CERN accelerator complex",. https://cds.cern.ch/images/CERN-GRAPHICS-2022-001-1.

[7] **CDF** Collaboration, R. D. Field, "The Underlying Event in Hard Scattering Processes", *eConf* **C010630** (2001) P501, arXiv:hep-ph/0201192.

[8] L. Rossi, P. Fischer, T. Rohe, and N. Wermes, *Pixel detectors: from fundamentals to applications*. Particle acceleration and detection. Springer, Berlin, 2006. https://cds.cern.ch/record/976471.

[9] **ATLAS** Collaboration, G. Aad *et al.*, "The ATLAS Experiment at the CERN Large Hadron Collider", *JINST* **3** (2008) S08003.

[10] Krämer, M and Soler, F J P, *57th Scottish Universities Summer School in Physics on Large Hadron Collider Phenomenology* . Krämer, M and Soler, F J P, Bristol, 2005. https://cds.cern.ch/record/602552.

[11] B. A. I. *et al.*, *High-Luminosity Large Hadron Collider (HL-LHC): Technical Design Report V. 0.1*. CERN Yellow Reports: Monographs. CERN, Geneva, 2017. https://cds.cern.ch/record/2284929.

[12] **ATLAS** Collaboration, "Technical Design Report for the ATLAS Inner Tracker Pixel Detector", tech. rep., CERN, Geneva, 2017. https://cds.cern.ch/record/2285585.

[13] W. Commons, "File:pn-junction-equilibrium-graphs.png — wikimedia commons, the free media repository", 2020. https://commons.wikimedia.org/w/index.php?title=File:Pn-junction-equilibrium-graphs.png&oldid=451423606. [Online; accessed 4-September-2023].

[14] K. Olive, "Review of particle physics", *Chinese Physics C* **38** no. 9, (Aug, 2014) 090001. https://dx.doi.org/10.1088/1674-1137/38/9/090001.

[15] M. Moll, *Radiation damage in silicon particle detectors: Microscopic defects and macroscopic properties*. PhD thesis, Hamburg U., 1999.

[16] H. Kolanoski and N. Wermes, *Particle Detectors: Fundamentals and Applications*. Oxford University Press, 06, 2020. https://doi.org/10.1093/oso/9780198858362.001.0001.

[17] A. Dimitrievska and A. Stiller, "Rd53a: A large-scale prototype chip for the phase ii upgrade in the serially powered hl-lhc pixel detectors", *Nuclear Instruments and Methods in Physics Research Section A: Accelerators, Spectrometers, Detectors and Associated Equipment* **958** (2020) 162091. https://www.sciencedirect.com/science/article/pii/S0168900219305029. Proceedings of the Vienna Conference on Instrumentation 2019.

[18] **RD53** Collaboration, M. Garcia-Sciveres, "The RD53A Integrated Circuit", tech. rep., CERN, Geneva, 2017. https://cds.cern.ch/record/2287593.

[19] J. R. Schwank, M. R. Shaneyfelt, D. M. Fleetwood, J. A. Felix, P. E. Dodd, P. Paillet, and V. Ferlet-Cavrois, "Radiation effects in mos oxides", *IEEE Transactions on Nuclear Science* **55** no. 4, (2008) 1833–1853.

[20] F. Wang and V. D. Agrawal, "Single event upset: An embedded tutorial", in *21st International Conference on VLSI Design (VLSID 2008)*, pp. 429–434. 2008.

[21] M. Menouni, P. Barrillon, L. Flores, D. Fougeron, T. Hemperek, E. Joly, J. Lalic, and T. Strebler, "Single event effects testing of the rd53b chip", *Journal of Physics: Conference Series* **2374** no. 1, (Nov, 2022) 012084. https://dx.doi.org/10.1088/1742-6596/2374/1/012084.

[22] **ATLAS** Collaboration, F. Munoz Sanchez, "Carbon based local supports for the ATLAS ITk-pixel detector", tech. rep., CERN, Geneva, 2023. https://cds.cern.ch/record/2847861.

[23] L. WICKREMASINGHE, "Development and qa/qc of new pixel detectors for upgrading the lhc atlas experiment", 2021. https://zimbra.in2p3.fr/service/home/~/?auth=co&loc=en_GB&id=9472&part=2.

[24] F. B. J. D. Diego Álvarez, Christophe Bault, "Design Overview of the Bare Local Supports for the ITk Pixel Outer Barrel",. https://edms.cern.ch/nav/D:2632352:V1/D:2632352:V1.

[25] I. Perić, L. Blanquart, G. Comes, P. Denes, K. Einsweiler, P. Fischer, E. Mandelli, and G. Meddeler, "The fei3 readout chip for the atlas pixel detector", *Nucl. Instrum. Methods. Phys. Res. B* **565** no. 1, (2006) 178–187. https://www.sciencedirect.com/science/article/pii/S0168900206007649. Proceedings of the International Workshop on Semiconductor Pixel Detectors for Particles and Imaging.

[26] M. Garcia-Sciveres, D. Arutinov, M. Barbero, R. Beccherle, S. Dube, D. Elledge, J. Fleury, D. Fougeron, F. Gensolen, D. Gnani, V. Gromov, T. Hemperek, M. Karagounis, R. Kluit, A. Kruth, A. Mekkaoui, M. Menouni, and J.-D. Schipper, "The fe-i4 pixel readout integrated circuit", *Nuclear Instruments and Methods in Physics Research Section A: Accelerators, Spectrometers,*

Detectors and Associated Equipment **636** no. 1, Supplement, (2011) S155–S159. https://www.sciencedirect.com/science/article/pii/S0168900210009551. 7th International Hiroshima Symposium on the Development and Application of Semiconductor Tracking Detectors.

[27] **RD53collaboration** Collaboration, M. Garcia-Sciveres, F. Loddo, and J. Christiansen, "RD53B Manual", tech. rep., CERN, Geneva, 2019. https://cds.cern.ch/record/2665301.

[28] H. Jansen *et al.*, "Performance of the EUDET-type beam telescopes", *EPJ Tech. Instrum.* **3** no. 1, (2016) 7, arXiv:1603.09669 [physics.ins-det].

[29] P. D. Group, " Atomic Nuclear Properties of Materials",. https://pdg.lbl.gov/2017/AtomicNuclearProperties/.

[30] G. 't Hooft, *In Search of the Ultimate Building Blocks*. Cambridge University Press, 1996.

[31] J. J. T. M. F.R.S., "Xl. cathode rays", *The London, Edinburgh, and Dublin Philosophical Magazine and Journal of Science* **44** no. 269, (1897) 293–316, https://doi.org/10.1080/14786449708621070.

[32] S. F. Novaes, "Standard model: An Introduction", in *10th Jorge Andre Swieca Summer School: Particle and Fields*, pp. 5–102. 1, 1999. arXiv:hep-ph/0001283.

[33] G. Dissertori, "The Determination of the Strong Coupling Constant", arXiv:1506.05407. https://cds.cern.ch/record/2028490. Comments: A contribution to: The Standard Theory up to the Higgs discovery - 60 years of CERN, L. Maiani and G. Rolandi, eds.

[34] A. Collaboration, "Observation of a new particle in the search for the standard model higgs boson with the atlas detector at the lhc", *Physics Letters B* **716** no. 1, (2012) 1–29. https://www.sciencedirect.com/science/article/pii/S037026931200857X.

[35] C. collaboartion, "Observation of a new boson at a mass of 125 gev with the cms experiment at the lhc", *Physics Letters B* **716** no. 1, (2012) 30–61. https://www.sciencedirect.com/science/article/pii/S0370269312008581.

[36] L. M. Lederman and D. Teresi, *The God particle: If the universe is the answer, what is the question?* Houghton Mifflin Harcourt, 2006.

[37] **CKMfitter Group** Collaboration, J. Charles, A. Hocker, H. Lacker, S. Laplace, F. R. Le Diberder, J. Malcles, J. Ocariz, M. Pivk, and L. Roos, "CP violation and the CKM matrix: Assessing the impact of the asymmetric *B* factories", *Eur. Phys. J. C* **41** no. 1, (2005) 1–131, arXiv:hep-ph/0406184.

[38] P. W. Higgs, "Broken symmetries and the masses of gauge bosons", *Phys. Rev. Lett.* **13** (Oct, 1964) 508–509. https://link.aps.org/doi/10.1103/PhysRevLett.13.508.

[39] *Fundamental Physics at the Intensity Frontier*. 5, 2012. arXiv:1205.2671 [hep-ex].

[40] M. S. Safronova, D. Budker, D. DeMille, D. F. J. Kimball, A. Derevianko, and C. W. Clark, "Search for New Physics with Atoms and Molecules", *Rev. Mod. Phys.* **90** no. 2, (2018) 025008, arXiv:1710.01833 [physics.atom-ph].

[41] A. Cho, "Physicists' nightmare scenario: The higgs and nothing else", *Science* **315** no. 5819, (2007) 1657–1658. https://www.science.org/doi/abs/10.1126/science.315.5819.1657.

[42] A. Crivellin and B. Mellado, "Anomalies in Particle Physics", arXiv:2309.03870 [hep-ph].

[43] "LHC Machine", *JINST* **3** (2008) S08001.

[44] J. Coupard *et al.*, "LHC Injectors Upgrade, Technical Design Report: v.2: Ions",.

[45] A. Collaboration, "Luminosity public results run 2",. https://twiki.cern.ch/twiki/bin/view/AtlasPublic/LuminosityPublicResultsRun2(visitedonOct.11,2022).

[46] **Particle Data Group** Collaboration, Beringe., "Review of particle physics", *Phys. Rev. D* **86** (Jul, 2012) 010001. https://link.aps.org/doi/10.1103/PhysRevD.86.010001.

[47] L. D. Lella and C. Rubbia, *The Discovery of the W and Z Particles*, pp. 137–163. https://www.worldscientific.com/doi/pdf/10.1142/9789814644150_0006. https://www.worldscientific.com/doi/abs/10.1142/9789814644150_0006.

[48] **Super-Kamiokande** Collaboration, Y. Fukuda *et al.*, "Evidence for oscillation of atmospheric neutrinos", *Phys. Rev. Lett.* **81** (1998) 1562–1567, arXiv:hep-ex/9807003.

[49] A. Collaboration, "Atlas pixel detector electronics and sensors", *Journal of Instrumentation* **3** no. 07, (Jul, 2008) P07007. https://dx.doi.org/10.1088/1748-0221/3/07/P07007.

[50] **ATLAS** Collaboration, *ATLAS central solenoid: Technical Design Report*. Technical design report. ATLAS. CERN, Geneva, 1997. https://cds.cern.ch/record/331067.

[51] **ATLAS** Collaboration, M. Capeans, G. Darbo, K. Einsweiller, M. Elsing, T. Flick, M. Garcia-Sciveres, C. Gemme, H. Pernegger, O. Rohne, and R. Vuillermet, "ATLAS Insertable B-Layer Technical Design Report", tech. rep., 2010. https://cds.cern.ch/record/1291633.

[52] Y. Unno, "Atlas silicon microstrip semiconductor tracker (sct)", *Nuclear Instruments and Methods in Physics Research Section A: Accelerators, Spectrometers, Detectors and Associated Equipment* **453** no. 1, (2000) 109–120. https://www.sciencedirect.com/science/article/pii/S016890020000615X. Proc. 7th Int. Conf on Instrumentation for colliding Beam Physics.

[53] A. Collaboration, "The atlas trt barrel detector", *Journal of Instrumentation* **3** no. 02, (Feb, 2008) P02014. https://dx.doi.org/10.1088/1748-0221/3/02/P02014.

[54] D. Perkins, *Introduction to High Energy Physics*. Cambridge University Press, 2000. https://books.google.ps/books?id=e63cNigcmOUC.

[55] **ATLAS** Collaboration, *ATLAS liquid-argon calorimeter: Technical Design Report*. Technical design report. ATLAS. CERN, Geneva, 1996. https://cds.cern.ch/record/331061.

[56] F. Cavallari, "Performance of calorimeters at the lhc", *Journal of Physics: Conference Series* **293** no. 1, (Apr, 2011) 012001. https://dx.doi.org/10.1088/1742-6596/293/1/012001.

[57] **ATLAS Collaboration** Collaboration, A. M. Henriques Correia, "The ATLAS Tile Calorimeter", tech. rep., CERN, Geneva, 2015. https://cds.cern.ch/record/2004868.

[58] A. Ruiz-Martinez and A. Collaboration, "The Run-2 ATLAS Trigger System",. https://cds.cern.ch/record/2125783.

[59] CERN, *High-Luminosity Large Hadron Collider (HL-LHC): Technical design report*. CERN Yellow Reports: Monographs. CERN, Geneva, 2020. https://cds.cern.ch/record/2749422.

[60] G. Apollinari, O. Brüning, T. Nakamoto, and L. Rossi, "Chapter 1: High Luminosity Large Hadron Collider HL-LHC. High Luminosity Large Hadron Collider HL-LHC", *CERN Yellow Report* no. 5, (2015) 1–19, arXiv:1705.08830. https://cds.cern.ch/record/2120673.

[61] **ATLAS** Collaboration, L. Meng and A. Collaboration, "Module and System Test Development for the Phase-2 ATLAS ITk Pixel Upgrade", tech. rep., CERN, Geneva, 2020. https://cds.cern.ch/record/2693319.

[62] N. Apadula *et al.*, "Monolithic Active Pixel Sensors on CMOS technologies", in *Snowmass 2021*. 3, 2022. arXiv:2203.07626 [physics.ins-det].

[63] **ATLAS** Collaboration, G. Calderini, "The ATLAS ITk detector for High Luminosity LHC Upgrade", tech. rep., CERN, Geneva, 2022. https://cds.cern.ch/record/2798838.

[64] **ATLAS** Collaboration, L. Franconi, "The Opto-electrical conversion system for the data transmission chain of the ATLAS ITk Pixel detector upgrade for the HL-LHC", Tech. Rep. 1, CERN, Geneva, 2022. https://cds.cern.ch/record/2773360.

[65] **ATLAS** Collaboration, A. I. Collaboration, "Technical Specification and Acceptance Criteria for the Planar Pixel Sensors for the ITK project", Tech. Rep. 1, CERN, Geneva, 2017. https://edms.cern.ch/document/1817538/1.

[66] S. Terzo, J. Carlotto, S. Grinstein, M. Manna, G. Pellegrini, and D. Quirion, "Performance of radiation hard 3d pixel sensors for the upgrade of the atlas inner tracker", *Journal of Physics: Conference Series* **2374** no. 1, (Nov, 2022) 012168. https://dx.doi.org/10.1088/1742-6596/2374/1/012168.

[67] D. M. S. Sultan, M. A. Samy, J. Ye, M. Boscardin, F. Ficorella, S. Ronchin, and G.-F. D. Betta, "Quality control (qc) of fbk preproduction 3d si sensors for atlas hl-lhc upgrades", *Journal of Instrumentation* **17** no. 12, (Dec, 2022) C12016. https://dx.doi.org/10.1088/1748-0221/17/12/C12016.

[68] **RD53** Collaboration, R. Collaboration, "RD53 analog front-end processors for the ATLAS and CMS experiments at the High-Luminosity LHC", *PoS* **Vertex2019** (2020) 021. https://cds.cern.ch/record/2747750.

[69] G. J. Schlenvogt, H. J. Barnaby, J. Wilkinson, S. Morrison, and L. Tyler, "Simulation of tid effects in a high voltage ring oscillator", *IEEE Transactions on Nuclear Science* **60** (2013) 4547–4554. https://api.semanticscholar.org/CorpusID:37463953.

[70] F. Faccio, C. Detcheverry, and M. Huhtinen, "Estimate of the single event upset (SEU) rate in CMS",. https://cds.cern.ch/record/405088.

[71] **ATLAS** Collaboration, Y. Takubo, "Single Event Upsets in the ATLAS IBL Frontend ASICs", Tech. Rep. 11, CERN, Geneva, 2019. https://cds.cern.ch/record/2663244.

[72] S. Bonacini, K. Kloukinas, and A. Marchioro, "Development of SEU-robust, radiation-tolerant and industry-compatible programmable logic components", *JINST* **2** (2007) P09009. https://cds.cern.ch/record/1061594.

[73] **ATLAS** Collaboration, L. Meng, "ATLAS ITk Pixel Detector Overview", in *International Workshop on Future Linear Colliders*. 5, 2021. arXiv:2105.10367 [physics.ins-det].

[74] J. M. Rabaey, *Digital Integrated Circuits: A Design Perspective*. Prentice-Hall, Inc., USA, 1996.

[75] N. Weste and D. Harris, *CMOS VLSI Design: A Circuits and Systems Perspective*. Addison Wesley, 2011. https://books.google.ps/books?id=sv8OQgAACAAJ.

[76] R. Kumar and V. Kursun, "Reversed temperature-dependent propagation delay characteristics in nanometer cmos circuits", *IEEE Transactions on Circuits and Systems II: Express Briefs* **53** no. 10, (2006) 1078–1082.

[77] P. Chen, C.-C. Chen, C.-C. Tsai, and W.-F. Lu, "A time-to-digital-converter-based cmos smart temperature sensor", *IEEE Journal of Solid-State Circuits* **40** no. 8, (2005) 1642–1648.

[78] C.-M. Zhang, F. Jazaeri, G. Borghello, S. Mattiazzo, A. Baschirotto, and C. Enz, "A generalized ekv charge-based mosfet model including oxide and interface traps", *Solid-State Electronics* **177** (2021) 107951. https://www.sciencedirect.com/science/article/pii/S0038110120304184.

[79] C. Lee, G. Cho, T. Unruh, S. Hur, and I. Kwon, "Integrated circuit design for radiation-hardened charge-sensitive amplifier survived up to 2 mrad", *Sensors* **20** no. 10, (2020) . https://www.mdpi.com/1424-8220/20/10/2765.

[80] G. Yan, J. Bi, G. Xu, K. Xi, B. Li, L. Fan, and H. Yin, "Simulation of total ionizing dose (tid) effects mitigation technique for 22 nm fully-depleted silicon-on-insulator (fdsoi) transistor", *IEEE Access* **8** (2020) 154898–154905.

[81] **CERN** Collaboration, A. Caratelli, "CERN ASIC support News and Radiation Tolerant device models for 65nm technology", tech. rep., TWEPP, 2019. https://indico.cern.ch/event/799025/contributions/3537494/attachments/1902331/3140743/2019-09-02_MUG_News.pdf.

[82] A. Sharma, "Xray irradiation at cern", tech. rep., 2021. https://indico.cern.ch/event/1011942/contributions/4286567/attachments/2215047/3749742/ASharma_RD53BMeeting_2021_03_24.pdf,.

[83] M. Menouni, D. Arutinov, M. Backhaus, M. Barbero, R. Beccherle, P. Breugnon, L. Caminada, S. Dube, G. Darbo, J. Fleury, D. Fougeron, M. Garcia-Sciveres, F. Gensolen, D. Gnani, L. Gonella, V. Gromov, T. Hemperek, F. Jensen, M. karagounis, R. Kluit, G. Krüger, A. Kruth, Y. Lu, A. Mekkaoui, A. Rozanov, J. Schipper, and V. Zivkovic, "SEU tolerant memory design for the ATLAS pixel readout chip", *JINST* **8** (2013) C02026. https://cds.cern.ch/record/1997618.

[84] S. Miryala, T. Hemperek, and M. Menouni, "Characterization of Soft Error Rate Against Memory Elements Spacing and Clock Skew in a Logic with Triple Modular Redundancy in a 65nm Process", *PoS* **TWEPP2018** (2019) 029.

[85] I. Efthymiopoulos, " Target Station T4 Wobbling – Explained",. https://sba.web.cern.ch/sba/Documentations/Target/T4/T4Wobbling3.pdf.

[86] J. Baudot, G. Bertolone, A. Brogna, G. Claus, C. Colledani, Y. Degerli, R. De Masi, A. Dorokhov, G. Dozière, W. Dulinski, M. Gelin, M. Goffe, A. Himmi, F. Guilloux, C. Hu-Guo, K. Jaaskelainen, M. Koziel, F. Morel, F. Orsini, M. Specht, I. Valin, G. Voutsinas, and M. Winter, "First test results of mimosa-26, a fast cmos sensor with integrated zero suppression and digitized output", in *2009 IEEE Nuclear Science Symposium Conference Record (NSS/MIC)*, pp. 1169–1173. 2009.

[87] T. Heim, "Performance of the Insertable B-Layer for the ATLAS Pixel Detector during Quality Assurance and a Novel Pixel Detector Readout Concept based on PCIe", 2016. https://cds.cern.ch/record/2206274. Presented 28 Aug 2015.

[88] M. Backhaus, M. Barbero, L. Gonella, J. Große-Knetter, F. Hügging, H. Krüger, J. Weingarten, and N. Wermes, "Development of a versatile and modular test system for atlas hybrid pixel detectors", *Nuclear Instruments and Methods in Physics Research Section A: Accelerators, Spectrometers, Detectors and Associated Equipment* **650** no. 1, (2011) 37–40. https://www.sciencedirect.com/science/article/pii/S0168900210028676. International Workshop on Semiconductor Pixel Detectors for Particles and Imaging 2010.

[89] P. Ahlburg, S. Arfaoui, J.-H. Arling, H. Augustin, D. Barney, M. Benoit, T. Bisanz, E. Corrin, D. Cussans, D. Dannheim, J. Dreyling-Eschweiler, T. Eichhorn, A. Fiergolski, I.-M. Gregor, J. Grosse-Knetter, D. Haas, L. Huth, A. Irles, H. Jansen, J. Janssen, M. Keil, J. Keller, M. Kiehn, H. Kim, J. Kroll, K. Krüger, S. Kulis, J. Kvasnicka, J. Lange, Y. Liu, F. Lütticke, C. Marinas, P. Martinengo, A. Nurnberg, B. Paschen, H. Perrey, R. Peschke, D. Pitzl, D.-L. Pohl, A. Quadt, T. Quast, F. Reidt, E. Rossi, I. Rubinsky, A. Rummler, H. Schreeck, P. Schütze, B. Schwenker, S. Spannagel, M. Stanitzki, U. Stolzenberg, T. Suehara, M. Suljic, G. Troska, M. Varga-Kofarago, J. Weingarten, and P. Wieduwilt, "Eudaq—a data acquisition software framework for common beam telescopes", *Journal of Instrumentation* **15** no. 01, (Jan, 2020) P01038. https://dx.doi.org/10.1088/1748-0221/15/01/P01038.

[90] **CLICdp** Collaboration, J. Kröger, S. Spannagel, and M. Williams, "User Manual for the Corryvreckan Test Beam Data Reconstruction Framework, Version 1.0", `arXiv:1912.00856 [physics.ins-det]`.

[91] E. Belau, R. Klanner, G. Lutz, E. Neugebauer, H. Seebrunner, A. Wylie, T. Böhringer, L. Hubbeling, P. Weilhammer, J. Kemmer, U. Kötz, and M. Riebesell, "Charge collection in silicon strip detectors", *Nuclear Instruments and Methods in Physics Research* **214** no. 2, (1983) 253–260. https://www.sciencedirect.com/science/article/pii/0167508783905914.

[92] F. James and M. Roos, "Minuit - a system for function minimization and analysis of the parameter errors and correlations", *Computer Physics Communications* **10** no. 6, (1975) 343–367. https://www.sciencedirect.com/science/article/pii/0010465575900399.

[93] V. Blobel, C. Kleinwort, and F. Meier, "Fast alignment of a complex tracking detector using advanced track models", *Comput. Phys. Commun.* **182** (2011) 1760–1763, `arXiv:1103.3909 [physics.ins-det]`.

[94] C. S. Sanchez and on behalf of the ATLAS Collaboration, "The felix detector interface for the atlas tdaq upgrades and its deployment in the itk demonstrator setup", *Journal of Physics: Conference Series* **1525** no. 1, (Apr, 2020) 012033. https://dx.doi.org/10.1088/1742-6596/1525/1/012033.

[95] W. Wu, H. Chen, K. Chen, F. Lanni, S. Stucci, S. Tang, and E. Zhivun, "Development of a felix based readout system for itk strip hybrid module demonstrator for atlas phase-ii upgrade", *Journal of Instrumentation* **15** no. 03, (Mar, 2020) P03013. https://dx.doi.org/10.1088/1748-0221/15/03/P03013.